Title

STRANGE-PARTICLE PRODUCTION IN n-p INTERACTIONS FROM 1.5 TO 4.2 BeV/c. Part I. THREE-AND-MORE-BODY FINAL STATES

Authors

Dahl, Orin Z.
Hardy, Lyndon M.
Hess, Richard I.
et al.

Publication Date

1967

UCRL-16978

University of California

Ernest O. Lawrence Radiation Laboratory

STRANGE-PARTICLE PRODUCTION IN
π^-p INTERACTIONS FROM 1.5 TO 4.2 BeV/c

PART I. THREE-AND-MORE-BODY FINAL STATES

DISCLAIMER

Submitted to the Physical Review

UCRL-16978
Preprint

UNIVERSITY OF CALIFORNIA

Lawrence Radiation Laboratory
Berkeley, California

AEC Contract No. W-7405-eng-48

STRANGE-PARTICLE PRODUCTION IN π^-p INTERACTIONS FROM 1.5 TO 4.2 BeV/c PART I. THREE-AND-MORE-BODY FINAL STATES

Orin I. Dahl, Lyndon M. Hardy, Richard I. Hess,
Janos Kirz, and Donald H. Miller

January 1967

Strange-Particle Production in π^-p Interactions from 1.5 to 4.2 BeV/c.*

Part I. Three-and-More-Body Final States

Orin I. Dahl, Lyndon M. Hardy,†‡
Richard I. Hess†**, Janos Kirz, and Donald H. Miller

Department of Physics and Lawrence Radiation Laboratory
University of California, Berkeley, California

January 1967

ABSTRACT

We have investigated π^-p interactions from 1.5 to 4.2 BeV/c in the 72-in. hydrogen bubble chamber. This report describes the procedures for identifying and analyzing the reactions involving strange-particle production.

Experimental results on the invariant mass distributions, cross sections, and angular correlations are given for three- and four-body final states, which are shown to be rich in resonances. Production and decay of these resonant states is discussed. Results on five-body final states and Ξ production are also presented.

I. INTRODUCTION

We present here results of an experimental program designed to investigate strange-particle production in $\pi^- p$ interactions between 1.5 and 4.2 BeV/c.

The low-BeV range of incident momentum for πp and Kp interactions has proven to be so rich in interesting physical phenomena that it has been possible to conduct bubble-chamber experiments with no specific or detailed objective in mind. Instead, the data are collected and reduced in a systematic way. If the experimenters are fortunate, and in most cases they are, this first step in the analysis will indicate promising directions that can be pursued in detail fruitfully. This exploratory approach was the guiding principle for the collection of data analyzed and presented here. As a result the conclusions that we reach cover a variety of topics rather than definitive statements about any particular physical problem. We did not attempt to independently determine the masses, lifetimes, and branching ratios of the hyperons and K mesons. Rather, we used these relatively well-determined quantities to study possible biases in the data.

Several experimental groups have explored $\pi^- p$ interactions leading to three-or-more-body-final states involving strange particles.[1-12] The data which form the subject of this report were collected at the Bevatron, with the 72-in. bubble chamber. The analysis is based on 890,000 photographs, in which 50,000 events involving strange particles were found. The first set of 240,000 pictures was collected in 1961-62. Some results based on this exposure have already been published[13-20]. We shall refer to this exposure as "π72". The rest of the film was taken in 1963-64. Preliminary results from this exposure (to be referred to as "π63") are also available in the literature[21-27].

The events were scanned and measured independently for the two sets of pictures. We merged the data in most cases, in order to gain statistical significance. Cross sections, however, were determined independently, and we shall merely quote the values given by Schwartz for $\pi 72$.[28-29]

In this report we discuss first the procedures for analyzing the data, then turn to the determination of the cross sections for the various reactions. This is followed by the results on the three- and four-body final states. We present evidence for the presence of several resonant states, and discuss their production and decay. Our results concerning the Ξ hyperon are given before the closing section, in which we briefly summarize the results. The two-body final states ΛK^0, $\Sigma^0 K^0$, and $\Sigma^- K^+$, are discussed in a separate report.[30]

The paper is organized into the following sections;

II. EXPERIMENTAL PROCEDURE

A. Scanning and Measuring

Each set of stereo pictures was examined by trained scanners for interactions involving strange-particle production, and the indicative data for these events was recorded on a masterlist. The topologies which were sought are shown in Fig. 1. Figure 2 shows the number of detected events involving strange particles as a function of beam momentum for the π72 and π63 exposures. Most data are contained in three broad groupings of beam momentum: 1.6 to 2.4 BeV/c (32.5 events per μb), 2.9 to 3.3 BeV/c (12.8 events per μb), and 3.8 to 4.2 BeV/c (5.6 events per μb). The number of events found as a function of topology and beam momentum is given in Table I.

Rare interactions of interest such as possible Ξ productions, were recorded separately and did not proceed through the normal processing described below. Each event was measured on a Franckenstein or a scanning-and-measuring projector (SMP).[31]

B. Event Reconstruction and Kinematic Fitting

The data from each measurement were fed into a standard chain of Alvarez-group computer programs[31] which reconstructed the topology in three dimensions and tried to fit a preselected set of reaction hypotheses to the event. The attempted interactions are given in Table II. For each hypothesis, a four-vector of the "missing momentum" was calculated with the formula

$$\underset{\sim}{P}_{MM} \equiv \underset{\sim}{P}_{inc} + \underset{\sim}{P}_{targ} - \sum_i \underset{\sim}{P}_i , \tag{1}$$

where $\underset{\sim}{P}_{inc}$, $\underset{\sim}{P}_{targ}$, and the $\underset{\sim}{P}_i$ are measured (unfitted) values of the four-momenta of the incident pion, target proton, and observed final-state particles (including neutrals with observed decays). The missing mass is defined by

$$(mm)^2 = (\underset{\sim}{P}_{MM})^2. \tag{2}$$

C. Separation of Hypotheses

For a given event, each hypothesis with nonzero constraints is assigned a confidence level that measures the extent to which energy and momentum are conserved in the interactions. Presumably, events that do not proceed via the proposed interactions will have a low confidence level, and therefore can be eliminated from consideration by imposing a minimum cutoff in this variable. The value chosen must be low enough to include desired interactions, yet high enough to exclude unwanted events, and in practice it is selected with some degree of uncertainty. In this analysis, a hypothesis with nonzero constraints was considered acceptable if it had a confidence level greater than 0.005. Events with no acceptable constrained production hypothesis

but consistent with at least two missing neutrals at the production interaction were accepted as missing-mass hypotheses. In Table II the two or more missing neutrals are designated mm.

An event for which more than one hypothesis is acceptable was termed ambiguous. Ambiguous events which in principle could be resolved by an examination of the bubble density of one or more tracks were selected by a computer program and examined on a scanning table. Hypotheses inconsistent with the observed densities were eliminated.

The ambiguities remaining after scanning-table examination are conventionally resolved by selecting the hypothesis with the highest confidence level. For many events we attempt to choose between hypotheses of different constraint classes, however, and it is not clear that a confidence-level criterion is the correct selection to use here. Instead the problems associated with each constraint class are examined in turn.

Resolution of Λ and K^0 decays is quite good. For events with a neutral decay nearly all ambiguities occur between production hypotheses involving the same observed neutral. In all cases, therefore, we examined only the constraint classes associated with production, of which there are four types: no missing neutrals (four constraints), Σ^0 production (two constraints), one missing neutral (one constraint), and two or more missing neutrals (zero constraints).

1. Four-Constraint Fits

We expect events with an acceptable four-constraint fit to constitute a pure sample of four-constraint interactions. It is unlikely that events from other processes can simultaneously satisfy energy

and momentum conservation to a sufficient degree to yield an acceptable confidence level. It is possible, however, that measurement errors will be large enough that four-constraint events will give a high confidence level to hypotheses with only one or two constraints. Selection on the basis of confidence level will produce a pure sample of four-constraint events but not necessarily a complete one.

In this experiment the number of events that have both acceptable four-constraint and one-constraint hypotheses is small, and a test of our expectations is hard to perform because of the statistical limitations. There are however, a large number of events that are ambiguous between four and two constraints; as an example we consider two-prong vee events (topology b of Fig. 1) with the hypotheses $\pi^- p \rightarrow \Lambda K^+ \pi^-$ and $\pi^- p \rightarrow \Sigma^0 K^+ \pi^-$ with $\Sigma^0 \rightarrow \Lambda\gamma$. Events that proceed via the second reaction should show an isotropic decay of the Σ^0 in its rest frame, whereas misidentified events of the first type need not do so. Figure 3a shows the decay distribution for the decay gamma ray relative to the normal of the production plane for events that pass only Σ^0 production. We see the expected isotropic distribution. Events that have a best confidence level as Σ^0 production but also an acceptable fit to Λ production are shown in Fig. 3b. Here we see a striking peaking in the production plane. Figure 3c shows the same plot for a sample of events that have a best fit as Λ production but also an acceptable Σ^0 fit. We believe events in the third category to be true Λ events because of the stringent requirements of the four-constraint fit. The characteristics of the events in the second category are very similar to those of the third, and we will not have an isotropic Σ^0 decay distribution if many of the events of the second category are

accepted as Σ^0 production. We conclude that the majority of the events in the second category are from Λ production.

A similar argument shows that events ambiguous between four- and one-constraint hypotheses should also be assigned to the four-constraint hypothesis. In this experiment, events that have an acceptable four-constraint fit were unambiguously chosen as such, regardless of the confidence levels of other hypotheses. (In the few cases where there was more than one acceptable four-constraint fit, the event was assigned to the hypothesis with the higher confidence level.) We believe that this procedure yields practically pure and complete samples of four-constraint events.

2. Two-Constraint Fits

Upon examining the two-constraint hypothesis $\pi^- p \rightarrow \Sigma^0 K^+ \pi^-$; $\Sigma^0 \rightarrow \Lambda\gamma$ after the removal of ambiguous $\Lambda K^+ \pi^-$ events, we find a significant number of ambiguities only with the final-state $\Lambda K^+ \pi^- \pi^0$. Since the Σ^0 decays rapidly, the process could be viewed as $\pi^- p \rightarrow \Lambda K^+ \pi^- \gamma$. The experimental resolution is such that it is hard to distinguish between a γ and a π^0 by examination of the missing mass at the production vertex. We can use the additional fact, however, that for true Σ^0-production events, the effective mass squared of the Λ and missing mass, $M^2(\Lambda mm) = (\underset{\sim}{P}_\Lambda + \underset{\sim}{P}_{mm})^2$, should peak at $M^2(\Sigma^0)$, whereas for $\Lambda\pi^0$ production events, this quantity should lie above the kinematic threshold of 1.56 BeV^2. Figure 4a is a scatter plot of $M^2(mm)$ versus $M^2(\Lambda mm)$ for events that fit only $\pi^- p \rightarrow \Sigma^0 K^+ \pi^-$. Figure 4b is the same plot for events that pass only $\pi^- p \rightarrow \Lambda K^+ \pi^- \pi^0$. In Figure 4c are plotted those events that have acceptable fits for both hypotheses, but for which the Σ^0 hypothesis has a higher confidence

level. Figure 4d contains ambiguous events with a higher confidence level for $\Lambda\pi^0$ production. In general a selection on the basis of confidence level seems to do well in separating the hypotheses, but the distribution of points suggest that there is some misassignment. Therefore, ambiguous events were assigned, using $M^2(\Lambda mm)$ as a criterion. Events with $M^2(\Lambda mm) \geq 1.56$ BeV^2 were assigned to the $\Lambda\pi^0$-production hypotheses; events with $M^2(\Lambda mm) < 1.56$ BeV^2 were assigned to the Σ^0 production hypothesis. The cross contamination of these two channels is then quite small. The same criterion was applied to the separation of $\Lambda K^0\pi^0$ from $\Sigma^0 K^0$ for zero-prong, two-vee events.

3. One-Constraint Fits

After resolution of ambiguity between one-constraint fits and hypotheses of a higher constraint class, four types of ambiguity remained: (a) ambiguities between ΛK^0 and $\Sigma^0 K^0$, when only the Λ or the K^0 decay is observed; (b) ambiguities between $K^0\pi^+$ and $K^+\pi^0$, or $K^0\pi^-$ and $K^-\pi^0$; (c) ambiguities between $\Lambda K^0\pi^+\pi^-$, $\Sigma^0 K^0\pi^+\pi^-$, and $nK^\pm K^0\pi^\mp$ from events in which only the K^0 decay is observed; (d) ambiguities among the final states nK^+K^-, $\Lambda K^+\pi^-$, $\Sigma^0 K^+\pi^-$ or $pK^+K^-\pi^0\pi^-$, $nK^+K^-\pi^+\pi^-$, $\Lambda K^+\pi^+\pi^-\pi^-$ and $\Sigma^0 K^+\pi^+\pi^-\pi^-$ where one $K^\pm$ decay but no neutral decay is observed.

For each one-constraint hypothesis that involves production of a single missing neutral, there exists another reaction with the same observed particles but with two or more missing neutrals. In general, the kinematic threshold for the effective mass of two missing neutrals is sufficiently removed from the mass of the single neutral so that separation can be achieved by an examination of the missing mass at the production interaction. Contamination of one-constraint events is

typically <5%. For one-constraint hypotheses involving observed Λ decays, however, we must discriminate between Λ production reactions and corresponding reactions with a Σ^0 produced instead of a Λ. In the former case the missing-mass spectrum will show a peak at the mass of the missing neutral with a width characteristic of the experimental resolution. In the latter case the missing mass will be the effective mass of the neutral and the γ from Σ^0 decay and will range upward from a threshold near the mass of the neutral. Hence, there is no clear-cut separation of the two channels, and we must accept a contamination in the Λ final state.

This problem is most severe in the separation of the ΛK^0 events from the $\Sigma^0 K^0$ events, in which only the Λ decay is observed.[32] Fortunately we have available practically pure samples of ΛK^0 and $\Sigma^0 K^0$ events in which both the Λ and K^0 decays are seen. By suppressing information about the K^0 decay and processing these two-vee events through our data-reduction system, we determined the degree of contamination present in the ΛK^0 final state.

We also used this sample of two-vee events with Λ decay information neglected to investigate the cross contaminations of ΛK^0 and $\Sigma^0 K^0$ events in which only the K^0 decay is observed. Figure 5 is a plot of the missing mass squared for events accepted as either ΛK^0, $\Sigma^0 K^0$, or K^0mm. We found that our total sample of events for the final-state ΛK^0 has a contamination of approximately 6% at all momenta. The $\Sigma^0 K^0$ final-state contamination ranges from 1% at low momenta to 8% at high momenta. Cross-section determinations were corrected for these cross contaminations.

The hypotheses in category (b)--$\Lambda\pi^- K^+\pi^0$ and $\Lambda\pi^- K^0\pi^+$, $\Sigma^- K^+\pi^0$ and $\Sigma^- K^0\pi^+$, $\Sigma^+\pi^-\pi^- K^+\pi^0$ and $\Sigma^+\pi^-\pi^- K^0\pi^+$, $\Sigma^-\pi^+\pi^- K^+\pi^0$ and $\Sigma^-\pi^+\pi^- K^0\pi^+$, or $pK^0\overline{K^0}\pi^-$ and $pK^0K^-\pi^0$--are all approximately 25% ambiguous. A plot of the confidence level of one hypothesis versus the other for events ambiguous between $\Lambda\pi^- K^+\pi^0$ and $\Lambda\pi^- K^0\pi^+$ is shown in Fig. 6. There exists no clear-cut division of the events. The plots for the other ambiguous hypothesis pairs are similar. For the final state $\Lambda K^0\pi^+\pi^-$ we can use the number of four-constraint events that have both observed Λ and K^0 decays to calculate how many one-constraint events we should see (all properly weighed as discussed in Section III). We find that allocating the ambiguous events by the usual procedure of higher confidence level gives a number of one-constraint $\Lambda\pi^- K^0\pi^+$ events consistent with our expectation. This observation does not test the possibility of cross contamination of events, however.

Events of the final states $\Lambda\pi^- K^0\pi^+$ and $\Lambda\pi^- K^+\pi^0$, $\Sigma^- K^+\pi^0$ and $\Sigma^- K^0\pi^+$, $pK^0\overline{K^0}\pi^-$ and $pK^0K^-\pi^0$ were generated using the Monte Carlo program FAKE [33] and processed through the fitting programs in the same way as the actual events in the experiment. Assigning events on the basis of higher confidence level for these samples resulted in a cross contamination of approximately 4% at 2.9 to 3.3 BeV/c and approximately 8% at 3.8 to 4.2 BeV/c. Effective-mass plots for both unambiguous and ambiguous events for these six final states were examined separately, and no statistically significant differences were observed.

Rather than discard a quarter of the events for the final states in category (b), we assigned ambiguous events on the basis of confidence level and accepted the contamination.

Events in category (c) are about 40% ambiguous and present an even more difficult separation problem than those in category (b). Since we have available $\Lambda K^0\pi^+\pi^-$ and $\Sigma^0 K^0\pi^+\pi^-$ events in which both the Λ and the K^0 decays are seen, we choose not to use the events with only a K^0 decay observed for these final states. Events with a $nK^+\overline{K^0}\pi^-$ or $nK^0K^-\pi^+$ fit come only from this category, however. Monte Carlo events were generated by FAKE for these final states, and from these events we conclude that assignment on the basis of highest confidence level contaminates the $nK^+\overline{K^0}\pi^-$ and $nK^0K^-\pi^+$ final states about 13% at 3-BeV/c incident-pion momentum and about 17% at 4 BeV/c. On the other hand approximately 15% (31%) of the valid events are misassigned to other final states at 3 BeV/c (4 BeV/c).

Events detected only through the presence of a charged K decay are usually ambiguous. The $pK^+K^-\pi^-$ final states are fitted by four constraints; so they are an exception. The nK^+K^- events are particularly difficult to analyze, especially those with beam momentum above 2.3-BeV/c. In order for an event to be tried for such a final state, one of the two charged kaons must decay in the chamber. Furthermore, the lengths and curvatures of the two kaon tracks must be such that the momentum of each track can be measured reasonably accurately. Consequently our sample is biased in favor of events with low K momentum. Events for which the nK^+K^- final state was the best fit were examined on the scan table to check for consistency with that hypothesis. At the higher momenta this procedure was less effective because the bubble densities of tracks were usually close to minimum. At the low beam momentum (1.5 to 2.3 BeV/c), about 50% of the events were discarded. Usually it could be shown that the track with a momentum

change was made by a $\Sigma^{\pm}$ decay or by a $\pi^{\pm}$, which scattered on a proton without the recoil proton being detected. At the higher beam momenta about 40% of the events were discarded. To try to reduce the background still farther, we used only the unambiguous events in the subsequent analysis. We believe that the contamination in the accepted nK^+K^- events at low momentum is less than 10%; at high momentum it could be as much as 50%.

The $\Lambda K^+\pi^-$, $\Sigma^0 K^+\pi^-$, $\Lambda K^+\pi^+\pi^-\pi^-$, $\Sigma^0 K^+\pi^+\pi^-\pi^-$, $nK^+K^-\pi^+\pi^-$, and $pK^+K^-\pi^0\pi^-$ final states, without a visible Λ decay were so ambiguous that no further analysis was attempted on these events.

4. Zero-Constraint Events

Except for the final states ΛK^0mm and $\Lambda K^0\pi^+\pi^-$mm, missing-mass hypotheses for a given topology are ambiguous. An examination of bubble densities eliminated ambiguity in some instances, but most zero-constraint events have more than one missing-mass interpretation consistent with all of the information at our disposal. The final-state ΛK^0mm is discussed in Section IVH.; other missing-mass hypotheses were not examined for this report.

5. Primary Data Reduction

Most events found by the scanners were measured and then processed by the fitting programs. A small percentage were classified as unmeasurable and, for cross-section calculations, distributed in a manner proportional to events that were fully processed. Events were unmeasurable for a variety of reasons. A vertex could have been obscured in one or more views, or a track could have been distorted by turbulence, for example. Into this category also went events for which the measurement was never performed because of bookkeeping oversights or unavailability of the appropriate film.

Events that were recorded by mistake (not one of the topologies in Fig. 1) were placed in a reject category when examined on the measuring device by the more experienced scanners. In subsequent states of processing, more interactions were transferred to this category.

Hypothesis failures--events for which no hypothesis had an acceptable fit--were remeasured, since many of the failures were the result of operator oversights and poor measuring techniques. Events that failed twice were reexamined by specially trained scanners and physicists to ascertain the cause of failure. Most of these examined events were found not to involve strange-particle production and were rejected, some were good events that had to be remeasured with special care, and some were left as unexplained failures.

Table III shows the status of the events in the experiment at the conclusion of the present analysis. Almost all events have been assigned a good interpretation or rejected. The residual of failing events amounts to only 4% of the total sample. Part of this sample is desirable events with confidence levels below 0.005, and a more intensive and sophisticated analysis would probably discover the reason for failure of the rest. An effort to clean up this residual would have negligible effect on the results obtained for the copiously produced final states discussed in this report. Cross-section values were corrected for the estimated number of good events with confidence levels below 0.005.

III. CROSS SECTIONS

A. Cross-Section Scan

Cross sections for reactions involving strange particles were found by using the data from a special cross-section scan performed on the film and the total π^-p cross sections from counter experiments.[34,35] We describe here the procedure used on the second part of the exposure (π63). The first part was treated in a similar manner.

The film was divided into a series of intervals over which the experimental conditions were relatively constant, rolls of film were selected at random from each interval, and every fifth frame was examined by scanners. The scanners recorded the total number of observed interactions of all types as well as the number of incoming beam tracks at the entrance window, and checked to see that their difference was the number of outgoing tracks at the end of the chamber. This check insured that no zero-prong interactions were missed. The number of interactions involving strange particles, the number of zero prongs, the number of two prongs, and the number of four- and six-prong interactions were also recorded. These data from intervals with the same incident momentum were then grouped together.

Of course, the interactions observed by the scanners are subject to the usual scanning biases associated with a bubble-chamber experiment. By far the greatest number of missed events came from very-small-angle elastic scatters that were recorded as noninteracting beam tracks. An analysis of elastic-scatter events from this exposure by Jacobs[36] indicates a correction of $1.10 \pm .02$ to the number of observed two prongs at all momenta. From the total cross section, taken from counter experiments, the total path length, and the number of

strong interactions that we observe, we determine our μ contamination to be approximately 5% at all momenta.[37] Cross sections of interest in a given momentum interval were determined using the formula

$$\sigma_i = \sigma_{tot} \frac{N_s}{N_{tot}} \frac{N_i}{N_{m\ell}} = a N_i. \quad (3)$$

Here σ_{tot} is the total $\pi^- p$ cross section, N_s the number of strange-particle interactions found in the cross-section scan, N_{tot} the total number of interactions corrected for missed elastic scatters in the cross-section scan, $N_{m\ell}$ the number of strange-particle events recorded in the general scan, N_i the number of events of interest, and a the path length in units of μb/event. With this method the large biases associated with $N_{m\ell}$ and N_s cancel each other, and we are left only with the problem of determining the corrections to the observed number of good events in the desired channels. Values for a as a function of incident momentum are shown in Table IV.

B. Scanning Corrections

The scanning corrections considered here are of three types--topological, fiducial, and accidental. Topological biases occur because scanners have a greater difficulty in finding events of certain configurations than they do others. Charged or neutral particles that decay very near the production vertex are more readily missed than those which decay some distance away. Plots of the number of events versus the proper time of decay show the proper exponential behavior beyond a minimum value. In the analysis, therefore, only events with decays beyond a length of 0.5 cm were used.

Decaying Σ^+ and Σ^- for which the direction of the charged secondary makes a small angle with the direction of the primary itself are also preferentially missed. Cross-section biases from this effect were easily corrected by examining the decay distribution in the Σ rest frame, which should be isotropic, but in fact has a depletion of events for the charged secondary decaying along the direction of the Σ. For the Σ^+, decaying via $p\pi^0$, a significant number of events at all decay angles were not recorded by scanners because they looked very much like p-p scatters with invisible recoils. The decay mode $n\pi^+$ was not biased in this way, since the ionization density of the outgoing π^+ was in general less than that of the Σ^+. We determined the cross sections for final states containing a Σ^+, therefore, using only the $n\pi^+$ decay mode and multiplying the number of events by two.

When the scanning instructions were written, only general loose criteria were provided for elimination of zero-opening-angle vees that were electron pairs. A later analysis of the expected distribution of opening angles revealed that a negligible percentage of all K^0 and Λ decays should have a zero opening angle in the laboratory. Events with acceptable fits and vees with zero opening angles were most likely to be electron pairs with poor momentum determinations. To eliminate all bias from this source, events with vees were accepted only if the opening angle in the laboratory was greater than 1.5 deg.

The three cameras which view the bubble chamber look down with a line of sight roughly in the z (vertical) direction in the laboratory. Decays for which the normal to the decay plane is perpendicular to this direction might more readily be missed than those with a normal parallel to this direction. The "perpendicular" vees would appear

to have a small opening angle and might be discarded as electron pairs by the scanners, whereas the "parallel" vees are in a optimum orientation for viewing. In order to investigate the possibility of a bias from this effect, the quantity $\cos^{-1}\{[(\underset{\sim}{N}\times\underset{\sim}{P}_1)\cdot(\underset{\sim}{P}_1\times\underset{\sim}{P}_2)]/(|\underset{\sim}{N}\times\underset{\sim}{P}_1||\underset{\sim}{P}_1\times\underset{\sim}{P}_2|)\}$ was plotted for all K^0 and Λ decays, where $\underset{\sim}{P}_1$ is the laboratory momentum of the neutral, $\underset{\sim}{P}_2$ is the laboratory momentum of a charged secondary, and $\underset{\sim}{N}$ is a unit vector along the z (vertical) axis. This quantity, which measures the isotropy of the decay normal about the neutral direction, would not be flat if a bias existed for detecting vee decays of certain orientations. In this experiment the distribution was consistent with isotropy, and no corrections were necessary.

The probability of finding events is lower near the boundaries of the chamber than in the center. Interactions near the far end of the chamber are likely to produce tracks that are relatively short, the measurement errors will be greater for these events, and the possibility of misidentification is enhanced. Turbulence is greater near the chamber boundaries and measured values of momenta may be poor in these regions. For these reasons, only events in a restricted fiducial volume were accepted for analysis. These events were properly weighted for cross-section determinations to take into account the different volumes used in the cross-section scan and the analysis that follows. This criterion reduces the number of usable events by about 15%. We have also removed another 1% of the events by demanding that the beam track dip less than ±2% away from the horizontal plane. This procedure is necessary to ensure a monochromatic beam.

By restricting ourselves to the subsample defined by the criteria above, we have arrived at a collection of events for which the scanning efficiency is constant, but not necessarily equal to unity. Scanners miss a surprisingly large fraction of events that are in plain sight in the center of the chamber and have good topological features. These "accidental" oversights are presumably caused by monotony, carelessness, or fatigue and are not expected to bias the data in any significant way except to cause cross-section estimates to be systematically low. To find the magnitude of this effect we scanned the entire exposure of film a second time and prepared a second-scan master list in the same manner as the first-scan master list. The two master lists were compared, and a conflict list was compiled of all events which were found on (a) scan 1 but no scan 2, (b) scan 2 but not scan 1, and (c) both scans but assigned to different topologies. One is tempted to take the number of events in categories a and b, and the number of events on the masterlists that agree, and from these compute the scanning efficiency for each topology. In a complicated scan such as this one, however, such a technique would be in error. Both scans and hence the data from the "conflict" analysis contain nonvalid events. In fact, such events preferentially appear on one scan and not the other because of the varying abilities of the scanners to distinguish between electron pairs and vees, charged decays and scatters, etc. Also, only part of an event might be missed--one of two vees in a zero-prong, two-vee event, for example. The following procedure was adopted, therefore, to take into account the complications present for this experiment.

A scanner looked at the events on the conflict list a third time, decided between different topology assignments, and rejected obvious nonstrange particle events found on the second scan but not on the first. All nonrejected second-scan events that were not on the first master list were then processed through the primary data-analysis system used for the first scan. A sample of 5000 conflict events were then selected, and the events of this sample for each topology were divided into eight classes:

1. Good event found by scan 1 but not by scan 2.
2. Good event found by scan 2 but not by scan 1.
3. Good event found and wrong topology assigned by scan 1; not found by scan 2.
4. Good events found and wrong topology assigned by scan 2; not found by scan 1.
5. Good event found by both scan 1 and scan 2, wrong topology assigned by scan 2.
6. Good event found by both scan 1 and scan 2, wrong topology assigned by scan 1.
7. Reject event found by scan 1 but not by scan 2.
8. Reject event found by scan 2 but not by scan 1.

These eight clases are related as shown in Table V.

We assume that the topological and fiducial errors already discussed are strongly correlated between the two scans, but that the accidental errors are entirely uncorrelated and can be characterized by independent probabilities for each scan:

P_{ci} = probability of finding and correctly assigning an event on scan i

P_{mi} = probability of finding but incorrectly assigning an event on scan i

P_{bi} = probability of finding a nonvalid event on scan i.

We also define:

T_g = total number of good events in the film

T_b = total number of nonvalid events in the film.

The quantities P_{b1}, P_{b2}, and T_b are not of interest, but serve as Lagrangian multipliers in the problem. With these definitions we can then write expressions for the number of events observed in each of our eight categories and on the masterlists:

$$
\begin{aligned}
N_1 &= P_{c1}(1 - P_{c2} - P_{m2})\, T_g \\
N_2 &= P_{c2}(1 - P_{c1} - P_{m1})\, T_g \\
N_3 &= P_{m1}(1 - P_{c2} - P_{m2})\, T_g \\
N_4 &= P_{m2}(1 - P_{c1} - P_{m1})\, T_g \\
N_5 &= P_{c1} P_{m2} T_g \\
N_6 &= P_{c2} P_{m1} T_g \\
N_7 &= P_{b1}(1 - P_{b2})\, T_b \\
N_8 &= P_{b2}(1 - P_{b1})\, T_b \\
N_{m\ell 1} &= (P_{c1} + P_{m1})\, T_g + P_{b1} T_b \\
N_{m\ell 2} &= (P_{c2} + P_{m2})\, T_g + P_{b2} T_b,
\end{aligned}
\tag{4}
$$

where $N_{m\ell i}$ is the number of events recorded on masterlist i. For each topology we now have ten observed quantities with eight unknown parameters to fit them. A χ^2 was formed for these quantities and minimized. The results are shown in Table VI. As we expected, vee-four-prong events have the best chance of being found and two-prong positive decays the least. The percentage of misidentified events in some categories is nonnegligible. These efficiencies were taken into account in cross-section computations.

C. Measurement Corrections

Unmeasured and unmeasurable events were allocated in a manner proportional to the events that did proceed through the primary data-reduction system. An average weight was assigned to each event placed in the passing category.

The number of events in specific channels were corrected for the cross-contaminations with other reactions in accordance with the conclusions obtained from the hypothesis separation analysis described in Section II.

D. Detection Corrections

To correct for the loss of events due to (a) imposing the minimum-length cutoff on decaying particles, and (b) their escape from the finite fiducial volume, we used the following procedure. For each observed decaying particle an event was weighted by a factor

$$W_1 = [\exp(-L/\eta c\tau) - \exp(-\ell/\eta c\tau)]^{-1}. \quad (5)$$

For each unseen neutral an event was weighted by

$$W_2 = \{1 + [b_1/(1 - b_1)] \exp(-\ell/\eta c\tau)\}^{-1} \quad (6)$$

where ℓ is the distance from the production vertex to the edge of the decay fiducial volume, L is the minimum length cutoff (0.5 cm), η is the ratio of the momentum of the particle to the mass of the particle, c is the velocity of light, τ is the liefetime, and b_1 is the branching fraction into charged decay products ($\pi^+\pi^-$ for K^0, $p\pi^-$ for Λ). The values of W_1 and W_2 are normally close to 1.0. Typical values are 1.10 for W_1 and 0.99 for W_2. Only extremely rarely does W_1 exceed 1.5. For cross section calculations the numbers of weighted events must still be scaled by the branching fractions.

We have determined the lifetimes for Σ^+, Σ^-, Λ^0, and K^0 from our data, and find these values to be consistent with world averages.

E. Results

In Table VII are tabulated the total cross sections and errors for the final states studied here. Figures 7 through 10 illustrate the variation of cross section with momentum. We believe that the systematic errors are most likely less than 5%. Cross sections from $\pi 72$ determined by Schwartz and from other experiments are also shown in Figs. 7 through 10 and Table VII. In the following sections data from the two parts of the exposure $\pi 72$ and $\pi 63$ are combined.

IV. THREE-BODY FINAL STATES

A. Mass Distributions

Three-body final states are dominated by resonance production in the momentum range covered by this experiment. Any search of the effective mass distributions for the existence of new states is complicated by the presence of well-established resonances which distort the predictions of unmodified phase space. To facilitate analysis of the data, we examined to what extent a simple phenomenological description of well-known resonance states could provide a satisfactory explanation for the distributions we observe.

We assumed that resonant processes can be represented by simple Breit-Wigner matrix elements with constant widths, that all processes add incoherently, and all decays are isotropic in their respective centers of mass. Three ranges of incident pion momentum were selected for the analysis -- 1.8 to 2.2, 2.9 to 3.3, and 3.8 to 4.2 BeV/c -- and the relative strength of each process was assumed constant over each of these intervals.[38]

The values for the mass, width, and relative amount of each resonance were fit by a maximum-likelihood program, SUPERFIT.[39] The variation in center-of-mass energy over each interval was taken into account by the program. The values for the mass and width of each resonance obtained from different states and at different momenta were consistent with one another. These values were averaged and the program run again with only the relative amounts of processes allowed to vary.

With the relative amounts of each process determined from the fit, the effective mass distributions expected from these effects were calculated. The variation in incident momentum was taken into account by dividing each interval into eight subintervals, computing the distributions for each subinterval, and summing these distributions properly weighted according to the numbers of events in the subintervals.

Table VIII gives the number of events for each final state.[40]

The Dalitz plots and mass projections are presented in Fig. 11 through 19. The left, middle, and right columns contain data from the low, middle, and high momentum intervals respectively. The curves on the histograms correspond to the masses, widths, amounts, and corresponding cross sections of resonances given in Tables IX and X. Numbers without errors have been fixed in the fit. In Fig. 18 the nK_1^0 effective mass distributions contain two points per event. The fits are quite good, and the data are well explained by the resonant states expected to be present. The resolutions in the mass histograms are everywhere less than 15 MeV, and in the lower mass regions they are typically 5 to 10 MeV.

The experimental width of the K^{*+} as shown in Table IX is wider than that of the K^{*0} because of the poorer resolution in the $\Sigma^-(K\pi)^+$ final states. The difference in mass between charge states of the $Y_1^*(1385)$ and the $K^*(890)$ in the table are not to be interpreted as the result of a serious attempt to measure these quantities. No effort has been made to carefully investigate systematic differences between the various channels producing these states. Such investigations are more fruitfully carried out in final states from other reactions. The results should be viewed as empirical values that best describe the presence of resonant processes in our data.

B. Coordinate Frames and Conventions

The following conventions are used for the presentation of all angular distributions. We define the four vectors $\underset{\sim}{P}_1$, $\underset{\sim}{P}_2$, $\underset{\sim}{P}_3$, and $\underset{\sim}{P}_4$ as the momenta of the beam, target, meson resonance (meson), and baryon (baryon resonance) respectively.

Production angular distributions are calculated in the overall center of mass with $\cos\theta_{prod} = \hat{\underset{\sim}{P}}_1 \cdot \hat{\underset{\sim}{P}}_3 = \hat{\underset{\sim}{P}}_2 \cdot \hat{\underset{\sim}{P}}_4$ (see Fig. 20). Defined in this way both peripherally produced meson and baryon systems will have $\cos\theta_{prod} \simeq +1$. The production normal is given by $\hat{\underset{\sim}{n}} = (\underset{\sim}{P}_1 \times \underset{\sim}{P}_3)/|\underset{\sim}{P}_1 \times \underset{\sim}{P}_3| = (\underset{\sim}{P}_2 \times \underset{\sim}{P}_4)/|\underset{\sim}{P}_2 \times \underset{\sim}{P}_4|$ evaluated in the overall center of mass. In the rest frame of a meson resonance (meson) we use the coordinate system (see Fig. 20 b) defined by $(\hat{\underset{\sim}{x}}, \hat{\underset{\sim}{y}}, \hat{\underset{\sim}{z}}) = [(\hat{\underset{\sim}{n}} \times \hat{\underset{\sim}{P}}_1)/|\underset{\sim}{n} \times \underset{\sim}{P}_1|, \hat{\underset{\sim}{n}}, \hat{\underset{\sim}{P}}_1]$, and in the rest frame of a baryon (baryon resonance) the coordinate system (see Fig. 20 c) defined by $(\hat{\underset{\sim}{x}}, \hat{\underset{\sim}{y}}, \hat{\underset{\sim}{z}}) = [(\underset{\sim}{n} \times \underset{\sim}{P}_2)/|\underset{\sim}{n} \times \underset{\sim}{P}_2|, \hat{\underset{\sim}{n}}, \hat{\underset{\sim}{P}}_2]$. The angles θ and ϕ are the usual spherical coordinates with $\phi = 0$ in the xz plane. Defined in this way, ϕ is the Treiman-Yang angle. For meson decays we measure the

angles for the final state K; for baryon decays we measure the angles for the final-state baryon relative to the coordinate systems we have defined. For the weak decays we choose our conventions such that the decay of a spin projection +1/2 yields the decay distribution for the nucleon of $1 + \alpha \cos\theta$, where α is the decay asymmetry parameter. With these conventions we have $\alpha = +0.66$ for lambda decay.

Weighted events are used for all angular distributions (Sec. IIID). The unweighted numbers of events used in each final state in each interval are shown in Figs. 11-19.

C. $Y_0^*(1405) \rightarrow \Sigma\pi$

Although the fits to the three-body final states are generally quite good, the fits to the $Y_0^*(1405)$ in both the $\Sigma^+\pi^-$ and $\Sigma^-\pi^+$ channels are poor. The asymmetric nature of the peak with rapid falloff of events on the high side is not well-fitted by the Breit-Wigner shape (The best fit gives a central value of 1387 MeV for the mass of the reasonance). These distributions are much better explained by the interpretation of the $Y_0^*(1405)$ as a $\bar{K}$-N S-wave bound state. The K-matrix formalism of Dalitz and Tuan,[41] as applied by Alexander et al.,[14] adequately describes the behavior of the data with a three-parameter fit. The decay distributions of the $\Sigma^\pm$ from $Y_0^*(1405)$ in the final states $\Sigma^\pm K^0 \pi^\mp$ at 1.8 to 2.2 BeV/c are shown in Fig. 21. The distributions are consistent with the S-wave bound-state interpretation of this effect. Although 1.8 to 2.2 BeV/c is not far from threshold for the reaction $\pi^- p \rightarrow Y^* K$, the angular distribution for $Y_0^*(1405)$ production is very peripheral. Corresponding plots for $Y_0^*(1520)$ and $Y_1^*(1385)$ in Fig. 22 also show forward peaking, but it is not nearly so severe as for the $Y_0^*(1405)$. If one accepts the view that absorptive effects are primarily

responsible for the observed angular distributions, then these data imply that the final-state Y^*K elastic scattering is stronger for the $Y_0^*(1405)$ than for the other two states.

Rather than use the Breit-Wigner fitted values to determine the cross sections for $Y_0^*(1405)K^0$, we estimated the numbers of events above smooth backgrounds and used them in the calculations. The branching ratio into the states $\Sigma^+\pi^-$ and $\Sigma^-\pi^+$ is consistent with unity. The exact form of this resonant peak has little effect on the other projections of the $\Sigma^\pm K^0\pi^\mp$ Dalitz plots.

D. $Y_0^*(1520) \rightarrow \Sigma\pi, \Lambda\pi\pi, N\bar{K}$

Besides decaying into $\Sigma^+\pi^-$ and $\Sigma^-\pi^+$, the $Y_0^*(1520)$ decays into $\Lambda\pi\pi$ and $N\bar{K}$. The numbers of events above background in each channel were estimated, and branching ratios were computed. The results are shown in Table XI. The values we obtain are not consistent with those that Tripp et al. obtained from the reaction $K^-p \rightarrow Y_0^*(1520)$ $\rightarrow$ decay products.[42] More data are being collected for this process, however, and the revised values will probably be consistent with ours.[43]

The production and decay angular distributions for the $Y_0^*(1520)$ from the final states $\Sigma^+K^0\pi^-$ and pK^0K^- at 1.8 to 2.2 BeV/c are presented in Fig. 22. Events from $\Sigma^-K^0\pi^+$ were not used because of the K^* formation in that final state. The background events, which constitute about 30% of the sample, were not subtracted.

The decay distributions of weighted events in $\cos\theta$ and ϕ have been fit by a maximum-likelihood method to the density-matrix parameters appropriate for the strong decay of a spin-3/2 state. (The density-matrix formalism is discussed in Appendix A.) The values of the parameters and the selection criteria for the events are presented in

Table XII. As shown in Fig. 22, the correlation with the beam direction exhibits a $\cos^2\theta$ character with possibly some S-wave interference, and the ϕ distribution is reasonably flat.

Because the process $\pi^- p \rightarrow Y^* K$ cannot proceed through single K exchange, $K^*(890)$ is the lightest particle to contribute. The ρ-photon analogy of Stodolsky and Sakurai[44,45] assumes that the exchanged vector particle couples to the baryon vertex in much the same way as does a photon in reactions such as $\gamma + N \rightarrow N^*$. If one assumes further that a single multipole transition dominates the process, one can predict specific decay distributions for the baryon resonance. The predictions for $3/2^+$ and $3/2^-$ states expressed in terms of density-matrix parameters are shown in Table XIII. Our data favor the longitudinal dipole transition for $Y_0^*(1520)$ production. The production angular distribution for this state shows the characteristics of peripheral production.

E. $Y_1^*(1660)$

The 1.8- to 2.2-BeV/c region just includes threshold for the production of $Y_1^*(1660)$, but there is no strong evidence for its production in the final states $\Sigma^\pm K^0 \pi^\mp$ and $NK\bar{K}$. The likelihood-function fit to these final states was insensitive to the amount of this resonance present, and no quantitative value was obtained. The $\Sigma K\pi$ data with incident momentum between 2.2 and 2.4 BeV/c show a peak at 1660 MeV in the $\Sigma\pi$ channel. The cross section for $\pi^- p \rightarrow Y_1^{*0}(1660)K^0$, $Y_1^*(1660) \rightarrow \Sigma\pi$ at 2.3 BeV/c is estimated to be ~12 μb. No compelling evidence exists for the production of $Y_1^*(1660)$ at the higher momentum intervals in the three-body final states.

F. $Y_1^*(1385) \rightarrow \Lambda\pi$

Both the Y^{*0} and Y^{*-} are strongly produced in three-body final states at 1.8 to 2.2 BeV/c. At higher momenta the production of Y^{*0} falls off significantly, and the Y^{*-} is virtually not produced.

Production and decay angular distributions for the Y^{*0} are presented in Fig. 22. We performed a background subtraction on the data by taking events on either side of the Y^* mass.

The model of the ρ-photon analogy is also applicable to $Y_1^*(1385)$ production. For this case, in addition to prescribing the form of the decay angular distribution for the three possible dominant multipoles, the model selects the magnetic-dipole transition in particular. The process $\gamma + N \rightarrow N^*(1238)$ seems to proceed through this process, and the analogy predicts the same for ρ exchange in $\pi^- p \rightarrow N^*\pi$. Since the ρ and K^* as well as $N^*(1238)$ and $Y_1^*(1385)$ are in the same SU_3 multiplet, one might expect K^* exchange to behave in the same way also. Our experimental determinations of density-matrix parameters from subtracted weighted events are presented in Table XII, and the theoretical predictions in Table XIII. The agreement is best for the magnetic-dipole transition, but the fit could be much better.

For magnetic-dipole transitions the production differential cross section should vanish in both the forward and backward directions. Our data instead show the characteristic forward-peaked distribution.

Analysis of the Y^{*-} state is extremely difficult in this experiment. The rapid decrease in cross sections with increasing momentum limits our investigation to 1.8 to 2.2 BeV/c. Here we are faced with untangling the effects in the reaction $\pi^- p \rightarrow \Lambda K^+\pi^-$ of the Y^* and the strongly produced $K^{*0}(890)$. Decay angular distributions are critically

influenced by the presence of the other resonance. In the case of the Y^{*0}, in the reaction $\pi^- p \rightarrow \Lambda K^0 \pi^0$ we were able to make subtractions that yielded physically tenable distributions. But for the Y^{*-} and K^{*0}, such a procedure would have doubtful validity.

G. $Y_0^*(1815) \rightarrow N\bar{K}$

The $Y_0^*(1815)$ appears to be produced in the 3.8- to 4.2-BeV/c region as shown in the pK^- effective mass histogram of Fig. 17 f. The bump on the curve of Fig. 18 c is the corresponding amount expected in the nK_1^0 system.

H. Search for Other Y_0^* States

To investigate the possible existence of I = 0 hyperon states, we have plotted the effective mass of Λ + mm from the ΛK^0 + mm final state. The events are predominantly from the reactions $\pi^- p \rightarrow \Sigma^0 K^0 \pi^0$ and $\pi^- p \rightarrow \Lambda K^0 \pi^0 \pi^0$. In each instance the isotopic spin of the Λ + mm mass system ($\Sigma^0 \pi^0$ or $\Lambda \pi^0 \pi^0$) must be even. In Fig. 23 where we combined the data from all momenta, we see clear evidence for the production of the I = 0 states $Y_0^*(1405)$ and $Y_0^*(1520)$, but no strong indication of any other resonant phenomena. In particular, we see no evidence for the proposed $Y_0^*(1660)$ to complete the hypothesized octet of $3/2^-$ particles to be composed of $N_{1/2}^*(1518)$, $\Xi^*(1816)$, $Y_1^*(1660)$, and $Y_0^*(1660)$.

I. $K^*(890)$

Both the positive and neutral charge states of $K^*(890)$ are produced in three-body final states. The production cross section for the K^{*+} falls rapidly with increasing incident momentum, whereas for the K^{*0} it remains at a relatively high value. Branching ratios of K^{*+}

decay into $K^0\pi^+$ and $K^+\pi^0$ as well as K^{*0} decays into $K^+\pi^-$ and $K^0\pi^0$ obtained from the fitting program are consistent with the expectations from isotopic-spin conservation.

Production of K^* states has been extensively analyzed in Kp reactions.[46-50] The experimental quantities that can be determined from these analyses are the production differential cross sections and three density-matrix parameters that characterize the decay of the K^*. In our experiment we observe the decay of the final-state fermion also, and deduce the parameters for the joint density matrix of the hyperon and K^*. Instead of three parameters, the most general decay is characterized by a sum of eleven independent terms. The details of the formulation are discussed in Appendix A, and the most general decay distribution is given by Eq. (A14).

Weighted events from the reaction $\pi^-p \rightarrow \Sigma^0K^{*0}$ at 1.8 to 2.2 BeV/c and 2.9 to 3.3 BeV/c and from $\pi^-p \rightarrow \Lambda K^{*0} \rightarrow \Lambda K^+\pi^-$ at 2.9 to 3.3 BeV/c and 3.8 to 4.2 BeV/c were fit to this general decay distribution by means of a maximum-likelihood method; the results along with selection criteria are presented in Table XIV. Although data are plentiful at 1.8 to 2.2 BeV/c for the process $\pi^-p \rightarrow \Lambda K^{*0}$, we were unable to satisfactorily compensate for the presence of the competing process $\pi^-p \rightarrow Y_1^{*-}K^+$ and have thus not presented results here. At 1.8 to 2.2 BeV/c the Σ^0K^{*0} events, although they show a peripheral character, are distributed over all production angles, and the statistics allow us to determine density-matrix parameters in three intervals of production angle. Background subtractions for these parameters in all three intervals of production angle were less than the statistical errors; there are no important competing processes in this final state. At 2.9 to

3.3 BeV/c we found parameters for events in the forward direction ($0.5 \leq \cos\theta_{prod} \leq 1.0$) only. The highest momentum data were insufficient to determine fitted distributions.

Since Y_1^{*-} production is negligible and K^* production is extremely forward-peaked at the higher momenta, data are presented for the $\Lambda K^+\pi^-$ events in the forward direction also. Background subtractions for the density-matrix parameters were less than the statistical errors.

The subtracted angular distributions for production and decay of the K^* with the selections discussed above are presented in Figs. 24 through 26, along with the curves obtained from the maximum-likelihood fits to the density-matrix parameters.

The predictions of the simple one-particle exchange model for the density matrix of the fermion and K^* final state are well known. The K-exchange model predicts a $\cos^2\theta$ decay with respect to the beam in the K^* rest frame and no other correlations. All eleven parameters, defined in Appendix A, should be identically zero at all production angles. For K^* exchange or any other member of the "normal" spin-parity series, ($J^P = 1^-, 2^+, 3^-, \cdots$), term one should equal 0.5 and only term four (Re ρ_{+++-}) of the rest is allowed to be nonzero. The K^* decay distribution is of the form $\sin^2\theta(1 + a\cos 2\phi)$. Combined K and K^* exchange yield no new nonzero terms; the quantity $1 - 2(\rho_{++++} + \rho_{+-+-})$ measures the fractional amount of K exchange present.

Taken at face value, terms one and four for this experiment indicate that K^* exchange dominates the production of both $\Sigma^0 K^{*0}$ and ΛK^{*0}. For each set of density-matrix parameters, we formed a

χ^2 for the hypothesis that the nine unallowed parameters are consistent with zero. For forward, intermediate, and backward production angles for $\Sigma^0 K^{*0}$, we obtained χ^2 values of 12.9, 17.1, and 19.3 for nine degrees of freedom. At 2.9 to 3.3 BeV/c in the forward direction, we obtained a χ^2 value of 18.1. For ΛK^{*0} production at 2.9 to 3.3 BeV/c and 3.8 to 4.2 BeV/c, we obtained 64.3 and 38.2, respectively. The correlations between these parameters were properly taken into account. We conclude that on the basis of decay correlations alone, simple one-particle exchange is not definitely ruled out for $\Sigma^0 K^{*0}$ but is certainly inconsistent with the data for ΛK^{*0}.

The differential cross sections predicted for either K or K^* exchange are in gross disagreement with the experimental distributions presented in Figs. 24 through 26. Simple one-particle exchange does not satisfactorily explain the differential cross sections for the processes $\pi^- p \rightarrow \Sigma^0 K^{*0}$ and $\pi^- p \rightarrow \Lambda K^{*0}$.

The failure of the one-particle exchange model here is of course not unique. Many reactions have deviated significantly from the model's predictions, in particular, in the production angular distribution. To overcome this deficiency, several authors have proposed an approach that leads to the absorption model.[51] The ideas that they present seem intuitively plausible, but the formulation in a quantitative fashion requires many brutal approximations. For an experiment with low statistics, the theory is flexible enough that reasonable fits to all aspects of the data can be obtained. For experiments with sufficient statistical accuracy to test the validity of the model in detail, one must decide to what extent a bad fit is due to the approximations and to what extent to the inaccuracies of the theory. Detailed analyses of the absorption

model have been discussed elsewhere;[52-54] such an undertaking is too ambitious for the data available here.

Rather we shall ask the question: Given the absorption model, to what extent is our conclusion about the dominance of vector exchange modified for $\pi^- p \to Y K^{*0}$? We use Huff's formulation of the absorption model[55] which is outlined in Appendix B. The production angular distribution and density matrices appropriate to a given reaction and momentum interval were fit to the theory, and the values of the unknown parameters that minimized χ^2 were determined. In general there was more than one minimum corresponding to different choices of relative sign between the fitted coupling constants. For all three data sets fitted, however, the characteristics of all minima were the same. Results of the fitting are also given in Appendix B. We conclude that even when we allow for the presence of absorptive effects, vector exchange processes are strongly present. Such an observation is somewhat surprising, because we expect the $K^*K^*\pi$ coupling to be suppressed, since it does not conserve A parity.[56]

Density-matrix parameters were also obtained for the process $\pi^- p \to \Sigma^- K^{*+}$ from the final state $\Sigma^- K^+ \pi^0$. Here $\Sigma^- K^0 \pi^+$ events were not used because of the presence of the several Y_0^* states in that channel. Only the terms that remain after integrating over the decay distribution of the Σ^- are presented, since strong scanning biases are associated with that distribution. Background for K^{*+} events is rather significant, but the K^{*+} decay distribution does not possess features very different from those of the background control region. Consequently the subtraction changed parameters slightly for this state. Angular distributions are presented in Fig. 24.

The production distribution is not peaked backwards as one might expect from a baryon-exchange model; absorptive effects would serve only to increase this peaking. Therefore some more complicated mechanism is responsible for the production of this state at the low momentum.

J. $K^*(1440) \rightarrow K\pi$

The $K^*(1440)$ is definitely produced only at 3.8 to 4.2 BeV/c in the final state $\Lambda K^+\pi^-$. The best fits to the mass and width, given in Table IX, are in disagreement with the values obtained from K^-p experiments.[57, 58] Fits were attempted with Breit-Wigner matrix elements of higher angular momentum, but the results were within errors of the quoted values. An examination of possible biases that might produce a shift in the mass of $K\pi$ systems was undertaken.

The effective-mass distribution for the $K\pi$ projection calculated with measured (unfitted) values for the momenta was examined, but no significant shift was noted in either the $K^*(890)$ or $K^*(1440)$ region. The fact that the fit to the mass of the $K^*(890)$ gives a value of 892 ± 3 MeV indicates that there is no overall displacement in the $K\pi$ spectrum. The unfitted values of the momenta of the incident pion and the outgoing K and π were used to calculate the mass of the "missing" lambda. The distributions in lambda mass for $K\pi$ effective mass higher and lower than 1 BeV were examined separately, but no significant shift was found in either of the two plots. Since our measurements give correct values for the $K\pi$ mass in the vicinity of the $K^*(890)$ and we detect no systematic variations with increasing $K\pi$ effective mass, we conclude that if we are observing the same state as in the K^-p experiments, then increased statistics would yield consistent values for the resonance mass.

The differential production cross section and decay angular distribution for the $K^*(1440)$ are shown in Fig. 27. The production is peripheral, but not so much as that of the $K^*(890)$ at this momentum. The decay distribution in $\cos\theta$ was fit by the two distributions: (1) $a + b\cos^2\theta$ and (2) $a + b\cos^4\theta$. (No $\cos^2\theta$ term was needed for the second distribution.) Using weighted events, we find that the ratio of likelihoods for these two distributions is $L_1/L_2 = 1/6.3$. The expected distributions for various exchanged particles and spin-parity assignments are discussed in more detail in Ref. 24. As reported there, the assignment 2^+ is favored by our data, but the assignment 1^- is not excluded.

Several experimenters report the possible existence of other decay modes for the $K^*(1440)$.[57, 58] Figure 28, a through f, shows the effective-mass plots for $K\pi\pi$ combinations from the final states $\Lambda K^+\pi^0\pi^-$ and $\Lambda K^0\pi^+\pi^-$; where we have selected the mass of either the appropriate $K\pi$ combinations to be in the K^* interval or $\pi\pi$ combinations in the ρ interval. Also shown are $K^0 + mm$ from the final-state $\Lambda K^0 + mm$ with the missing mass in the η region ($0.5 \leq mm \leq 0.6$ BeV), and $K^0\pi^+\pi^0\pi^-$ from the final state $\Lambda K^0\pi^+\pi^0\pi^-$ with the three-pion mass in the ω region ($0.75 \leq M(\pi^+\pi^0\pi^-) \leq 0.81$ BeV). We see no definite evidence for $K^*(1440)$ decay into any of these modes. Upper limits for the branching ratios of $K^*(1440)$ into these channels are presented in Ref. 26.

K. $\kappa(725) \rightarrow K\pi$

Evidence for the kappa was first reported by Alexander et al. in the final state $\Sigma^-K^+\pi^0$ from the $\pi 72$ exposure.[14] These data are included in Fig. 13g. The final data are not conclusive evidence for the existence of this state. After removal of events with the $\Sigma^-\pi^+$ effective

mass in the regions of $Y_0^*(1405)$, $Y_0^*(1520)$, and $Y_1^*(1660)$, the final state shows no evidence for this enhancement. No effect is observed at other momenta or in the neutral $K\pi$ charge state. We must therefore conclude that our data from $\pi^- p$ interactions do not in themselves constitute independent evidence for the existence of the kappa.

The deviation from the calculated distribution in the $\Sigma^-\pi^0$ spectrum is entirely associated with the $K^*(890)$ and is a reflection of its nonisotropic decay distribution ($\sim\cos^2\theta$ along the K^* direction).

L. $A_2 \to K^0K^-$, $K_1^0K_1^0$

The $K\bar{K}$ decay mode of the A_2 as observed in our data has been discussed before.[21,26,59] Our best values for the mass and width of the A_2^- are $M = 1317.2 \pm 4.0$ MeV and $\Gamma = 47 \pm 18$ MeV. The mass and width of the A_2^0 are more difficult to determine because there are fewer events, but the values of $M = 1315.7 \pm 10.8$ MeV and $\Gamma = 80.5 \pm 36.5$ MeV given by the program SUPERFIT are consistent with the mass and width of the A_2^-. The width for which the curves are drawn on Figs. 17 and 18 is $\Gamma = 50$ MeV. This width is smaller than the value of 80 ± 20 MeV reported by Chung[60] and the value of 100 MeV reported in Ref. 61. Both these determinations come from observations of the $\rho\pi$ decay mode of the A_2. The possibility that the enhancements in the $\pi\rho$ and $K\bar{K}$ mass spectra are caused by different resonant processes still seems remote to us.

Figure 29 shows the Chew-Low plots for the two final states at the three momentum intervals. The most striking feature of these data is the tendency for events in the A_2 mass region to be produced with low values of Δ^2. Figure 30 presents the angular correlations for those events with a $K\bar{K}$ effective mass in the interval 1267 to 1367 MeV.

We have used weighted events but have not indicated errors since the average weight is about 1.1 for the K^0K^- events and 1.2 for the $K_1^0K_1^0$ events.

There were enough events at 2.9 to 3.3 BeV/c in the $pK_1^0K^-$ final state to make a fit to the elements of the density matrix. The conventions used for the density matrix are discussed in Appendix A. With these conventions and the assumption that $J^P = 2^+$, the decay angular distribution in the A_2 rest frame is given by

$$\frac{dN}{d\Omega} = (1 - 2\rho_{11} - 2\rho_{22})\left[\frac{5}{16\pi}(3\cos^2\theta - 1)^2\right] + \rho_{22}\left[\frac{15}{16\pi}\sin^4\theta\right]$$

$$+ \rho_{11}\left[\frac{15}{4\pi}\sin^2\theta\cos^2\theta\right] + \mathrm{Re}(\rho_{20})\left[\frac{15}{8\pi}\sqrt{\frac{2}{3}}(3\cos^2\theta - 1)\sin^2\theta\cos 2\phi\right]$$

$$+ \rho_{2-2}\left[\frac{15}{16\pi}\sin^4\theta\cos 4\phi\right] + \rho_{1-1}\left[-\frac{15}{4\pi}\sin^2\theta\cos^2\theta\cos 2\phi\right]$$

$$+ \mathrm{Re}(\rho_{21})\left[-\frac{15}{4\pi}\sin^3\theta\cos\theta\cos\phi\right] + \mathrm{Re}(\rho_{2-1})\left[\frac{15}{4\pi}\sin^3\theta\cos\theta\cos 3\phi\right]$$

$$+ \mathrm{Re}(\rho_{10})\left[-\frac{15}{4\pi}\sqrt{\frac{2}{3}}(3\cos^2\theta - 1)\sin\theta\cos\theta\cos\phi\right], \qquad (7)$$

where θ and ϕ are defined in Fig. 20b. The fit was a maximum-likelihood fit to the weighted events. We subtracted background by taking events on each side of the A_2 region. The results of such a fit are given in Table XV. All parameters except ρ_{11} and $1 - 2\rho_{11} - 2\rho_{22}$ are consistent with being zero. The production angular distribution strongly suggests production of the A_2^- by some exchange mechanism. The fact that the dominant decay mode of the A_2 is $\pi\rho$ makes the ρ meson a prime candidate for the particle exchanged. Note that the relative rates of production for A_2^0 and A_2^- are consistent with the ratio of 2 to 1 predicted on the basis of ρ exchange. Pure ρ exchange

would predict that ρ_{11} is 1/2 and all other coefficients but ρ_{1-1} are zero. The data are inconsistent with pure ρ exchange. Possible explanations for this behavior are (a) modification of the angular distribution by absorption effects or (b) background interference. The angular distribution for ω decay in the reaction $\pi^+ n \rightarrow p\omega$ (which we expect to be mediated by ρ exchange) is known to be significantly modified by absorption.[53] Our data are not plentiful enough to warrant the laborious calculation involved in predicting the effects of absorption in the production of a 2^+ particle by ρ exchange.

The curves on the angular distributions of Fig. 30 b and c are for the values of the density matrix elements given in Table XV. The distributions are for unsubtracted data because the fit is adequate. The asymmetry in the distribution of the decay cosine is, in part, due to the overlapping region of the A_2 and $Y_0^*(1520)$ (see Fig. 17 k).

We can determine the possible quantum numbers of the A_2 from the decay angular distributions (Fig. 30). Two points have been plotted in the A_2^0 histograms, since the K_1^0's are indistinguishable. The $K_1^0 K_1^0$ decay mode tells us immediately that $J^{P(C)}$ is even$^{+(+)}$ for the A_2. Since the $K^0 K^-$ decay insures that I = 1, we know $I^G = 1^-$. The decay angular distributions at 2.9 to 3.3 BeV/c are inconsistent with isotropy, so that J = 0 is ruled out. The lowest set of quantum numbers consistent with the data is $I^G J^P = 1^- 2^+$.

The curve on Fig. 30 e is what one would expect for pseudoscalar exchange with a small S-wave background. However, no known pseudoscalar particle is capable of mediating the reaction. An exchanged π^+ meson fails to conserve G parity at the $\pi^+ \pi^- A_2^0$ vertex, and an exchanged η meson fails to conserve charge at either vertex. Rho exchange modified by absorption may explain A_2^0 production.

Least-squares fits of Legendre polynomials have been made to the angular distributions in Fig. 30 b, e, h, and k. The values of the fitted parameters are given in Table XVI. In all cases a fourth-order fit is adequate, and for A_2^0 decay at 2.9 to 3.3 BeV/c it is preferred.

The branching ratio

$$R_1 = \frac{\Gamma(A_2^- \to K\bar{K})}{\Gamma(A_2^- \to \pi\rho)} = 0.053 \pm 0.021$$

has been reported in a previous communication.[59] This value is of particular interest because it represents the extent to which A parity is violated in A_2 decay.[56]

M. $A_1^- \to K^0K^-$

A search for the K^0K^- decay mode of the A_1^- was made in this experiment. Our data are consistent with no decay of the A_1^- into K^0K^-, so we have calculated upper limits to the cross sections for the process $\pi^-p \to A_1^-p$, $A_1^- \to K^0K^-$.[62] At 2.0 BeV/c the one-standard-deviation upper limit is 1.4 μb, at 3.1 BeV/c it is 0.9 μb, and at 4.0 BeV/c it is 0.7 μb.

By using the data of Chung[60] at 4.2 BeV/c, we can report an upper limit for the branching ratio of

$$\frac{\Gamma(A_1^- \to K^0K^-)}{\Gamma(A_1^- \to \pi\rho)} < 0.0025.$$

The preferred quantum numbers for the A_1 ($J^P = 1^+$ or 2^-) rule out decay into $K\bar{K}$.

N. $B^- \to K^0 K^-$

Since the B meson decays into $\pi\omega$ by strong interactions, it has quantum numbers $I^G = 1^+$. For a $K\bar{K}$ system we know that[63]

$$G = (-)^{J+I}$$

and

$$P = (-)^J.$$

We can therefore see that $K_1^0 K_1^0$ decay is forbidden for the B^0, and that the B meson will decay into $K\bar{K}$ only if its spin-parity is odd$^-$. Doubt has recently been cast on the nature of the enhancement observed in this experiment.[64] Nevertheless we may calculate the branching ratio

$$R_2 = \frac{\Gamma(B^- \to K^0 K^-)}{\Gamma(B^- \to \pi\omega)},$$

assuming that a genuine resonance is seen in the $\pi\omega$ channel with the production cross section determined by Chung.[60] The B meson is produced extremely peripherally [$\Delta^2 \leq 0.35$ (BeV/c)^2] in the energy range of this experiment.[64] The Chew-Low plot of Fig. 29b shows no enhancement in the low-Δ^2 region for $1.35 \leq M^2_{K\bar{K}} \leq 1.65$ BeV^2. We get an upper limit of 0.02 for R_2 by assigning all eight K^-K^0 events in this region to B decay. We shall discuss the $\pi\phi$ decay mode of the B in Sec. V.

O. $f \to K_1^0 K_1^0$, $f'(1500) \to K_1^0 K_1^0$

The branching ratio

$$R_3 = \frac{\Gamma(f \to K\bar{K})}{\Gamma(f \to \pi\pi)}$$

has been reported in a previous paper.[26] Since most events over background come from A_2^0 decay, it is difficult to assign an accurate value to R_3, so we have calculated an upper limit to this fraction by using

10 events in the interval of $K\bar{K}$ mass between 1200 and 1300 MeV on the histogram of Fig. 18e. Using our final data and the data of Jacobs,[36] we get an upper limit of 0.025 for R_3. Our data are certainly consistent with $R_3 = 0$.

We find no evidence for the production of the f'(1500) reported by Barnes et al.[65] We have calculated one-standard-deviation upper limits to the cross sections for the processes $\pi^- p \to nf'$, $f' \to K\bar{K}$[66] and $\pi^- p \to nf'$, $f' \to K\bar{K}\pi$. The results are

	2.9 to 3.3 BeV/c	3.8 to 4.2 BeV/c
$(f' \to K\bar{K})$	< 4.0 μb	< 5.5 μb
$(f' \to K^0 K^{\pm}\pi^{\mp})$	< 1.0 μb	< 1.5 μb

P. $K_1^0 K_1^0$ Threshold Enhancements

Several authors have reported a strong I = 0, $J^P = 0^+$ enhancement at low $K\bar{K}$ mass.[67-69] We observe this effect at extremely low Δ^2, as shown in Figs. 31a and b. This aspect suggests production by pion exchange, in which case Bose statistics demands I = 0 for the threshold enhancement. A quantitative test of the isotopic spin may be made with the triangle inequality for production of an I = 1 particle (here called T):

$$(2\sigma_{\pi^- p \to T^0 n})^{1/2} \leq (\sigma_{\pi^+ p \to T^+ p})^{1/2} + (\sigma_{\pi^- p \to T^- p})^{1/2}. \quad (8)$$

If we use the data of Lander et al.,[70] who have studied the reaction $\pi^+ p \to p\bar{K}^0 K^+$ at 3.5 BeV/c, and our data at 3.2 BeV/c, relation (8) becomes

$$(60 \pm 20\ \mu b)^{1/2} \leq (6.0 \pm 6.0\ \mu b)^{1/2} + (1.4 \pm 1.4\ \mu b)^{1/2}. \quad (9)$$

Since relation (9) is not well-satisfied we have a further indication that

the effect has $I = 0$. Figures 31 c and d show the decay angular distribution and the Treiman-Yang angular distribution for events at all momenta with $M_{K\bar{K}} \leq 1.075$ BeV. They are consistent with the isotropic distributions expected for the decay of a $J^P = 0^+$ state.

In a study of πp interactions above 5 BeV/c, Crennell et al.[68] and Beusch et al.[69] have observed an enhancement, which they interpret as a resonant state [$S^*(1068)$] that decays into $K_1^0 K_1^0$. The enhancement in our data is more naturally interpreted as the manifestation of a large scattering length in the $I = 0$ $K\bar{K}$ system. If we use the zero-effective-range approximation[71] and define the complex scattering length $A = a_0 + ib_0$, we get the cross section

$$\sigma(\pi^-\pi^+ \to K_1^0 K_1^0) = \frac{1}{6}\left(\frac{4\pi k_K}{k_\pi^2}\right)\frac{b_0}{[(1+b_0k_K)^2 + (a_0k_K)^2]} \quad ,$$

where k_K and k_π are respectively the K and π momentum in the $K\bar{K}$ center of mass. If we further use the Chew-Low formula,[72] the mass spectrum is given by

$$\frac{d\sigma}{dM} = \frac{f^2}{\pi}\frac{M^2 k_\pi}{M_\pi^2 p_\pi^2}\left[\int \frac{\Delta^2\, d\,\Delta^2}{(\Delta^2 + M_\pi^2)^2}\right]\sigma(\pi^+\pi^- \to K_1^0 K_1^0)$$

$$= \frac{2}{3} f^2 \frac{M^2 k_\pi}{M_\pi^2 p_\pi^2}\left[\int \frac{\Delta^2\, d\Delta^2}{(\Delta^2 + M_\pi^2)^2}\right]\frac{b_0}{[(1+b_0k_K)^2 + (a_0k_K)^2]}, \quad (10)$$

where M is the $K_1^0 K_1^0$ effective mass, $f^2 (= 0.16)$ is twice the square of the πN coupling constant, p_π is the laboratory beam momentum, Δ^2 is the square of the 4-momentum transfer, and M_π is the pion mass. An accurate determination of a_0 and b_0 is impossible with the few data at hand. We calculated curves for various values of a_0 and b_0 to see how well they reproduced the cross section and the shape

of the distribution.[73] We plotted two of these curves on Fig. 31 a along with a resonance shape for the S^* ($M = 1068$ MeV and $\Gamma = 80$ MeV). Figure 31 b shows the Δ^2 distribution for events with $M_{K\bar{K}} \leq 1.075$ BeV. The curve on the histogram is what we expect for one-pion exchange without any correction for absorption effects.[74] We also calculated the expected mass spectrum and momentum-transfer distribution with phenomenological form factors.[27] The qualitative features of the fit remained unchanged, except that we had to increase b_0 by a factor of about 5.

The data of Fig. 31 are from all the momenta of this experiment. The data for the separate beam-momentum intervals have been examined and are all adequately explained by a constant scattering length. (Fig. 18, d through f.) The events at higher momenta are produced more peripherally than those at lower momenta. This behavior is predicted by the one-pion-exchange model and is consistent with a continuous transition to the data of Crennell et al.[68] at 6.0 BeV/c.

On the assumption that the enhancement above phase space is entirely due to the threshold effect, we calculated the cross sections given in Table X.

One might attempt at this point to use the two-channel K-matrix formalism[71] and the $I = 0$, $K\bar{K}$ scattering length to compare the data presented with the $K_1^0 K_1^0$ mass spectrum from the reaction $K^- p \rightarrow \Lambda K_1^0 K_1^0$. Although some data are available on this last reaction,[75] a direct comparison is difficult because the absorption in the initial and final states will distort the spectra. If we neglect absorption and simply use the Chew-Low formula,[72] we find

$$\frac{\frac{d\sigma}{dM}(K^- p \to \Lambda K_1^0 K_1^0)}{\frac{d\sigma}{dM}(\pi^- p \to n K_1^0 K_1^0)} = \frac{3g^2}{8f^2} \frac{p_\pi^2 M_\pi^2 k_\pi}{p_K^2 M_K^2} \frac{\int \frac{\Delta_K^2 d\Delta_K^2}{(\Delta_K^2 + M_K^2)^2} \cdot \frac{a_0^2 + b_0^2}{b_0}}{\int \frac{\Delta_\pi^2 d\Delta_\pi^2}{(\Delta_\pi^2 + M_\pi^2)^2}}, \quad (5)$$

The ratio g^2/f^2 is not well known. We obtain reasonable agreement with the data of Lindsey and Smith[75] if we use $a_0 \sim 3.3$ F, $b_0 \sim 0.2$ F, and

$$\frac{g^2 \int \frac{\Delta_K^2 d\Delta_K^2}{(\Delta_K^2 + M_K^2)^2}}{f^2 \int \frac{\Delta_\pi^2 d\Delta^2_\pi}{(\Delta_\pi^2 + M_\pi^2)^2}} \approx \frac{1}{10} .$$

Q. K^0K^- Threshold Enhancement

Recent papers on $p\bar{p}$ annihilations give evidence for the production of an I = 1 state of mass 1000 MeV observed to decay into K^0K^-.[76-78] Our data are consistent with no production of such a state. The five events we observe over background at this mass in the K^0K^- system at 2.9 to 3.3 BeV/c correspond to a cross section of 1.4 ± 1.4 μb. Similarly at 1.8 to 2.2 BeV/c we get 0.25 ± 0.50 μb and at 3.8 to 4.2 BeV/c we get 0.7 ± 0.7 μb (Fig. 17, g through i).

R. $\phi \rightarrow K^+K^-$

From studies of the reactions $K^-p \rightarrow \Lambda K^+K^-$, $K^-p \rightarrow \Lambda K_1^0 K_2^0$ and $K^-p \rightarrow \Lambda K_1^0 K_1^0$, it is well known that the ϕ meson has $J^P = 1^-$ and decays into K^+K^- and $K_1^0 K_2^0$ but not into $K_1^0 K_1^0$.[79] We investigated ϕ production in π^-p interactions by studying the nK^+K^- final state.

The separation of the nK^+K^- final state from other final states is difficult and is discussed in Sec. II. C. Figure 19 g shows the K^+K^- effective-mass histogram for the events that unambiguously fit nK^+K^- with a beam momentum of 1.5 to 2.3 BeV/c. The most striking feature of the data is the enhancement in the region of K^+K^- effective mass centered around 1020 MeV. We interpret these data as evidence for production and decay of the ϕ meson.

A fit to the data gives the mass and width of the ϕ as $M = 1021 \pm 4$ MeV and $\Gamma = 10 \pm 3$ MeV. These values are consistent with the accepted values of 1019.5 MeV and 3.3 MeV if we take into account the 5-MeV resolution in the K^+K^- effective mass. The curve of Fig. 19 g is for 40% ϕ production (with $M = 1021$ MeV, $\Gamma = 10$ MeV), 40% phase space, and 20% $K\bar{K}$ threshold enhancement. This 20% is our best estimate of the amount we would expect on the basis of the effect we see in the $nK_1^0 K_1^0$ final state.

The angular distributions for the events in the 1.005- to 1.035-BeV K^+K^- effective mass interval are shown in Fig. 32, b, d, and f. For comparison we show in Fig. 32, a, c, and e the corresponding distributions for the $nK_1^0 K_1^0$ data in the same interval of beam momentum.

To determine the biases in our data and a value for the detection efficiency, we generated a number of Monte Carlo events of the type $\pi^-p \rightarrow n\phi$ with the program FAKE.[33]

The curves on Fig. 32, b, d, and f, are the distributions we would expect for isotropic production and decay angular distributions as determined by FAKE. The fact that the data are consistent with these curves verifies that the generated events are similar to the real events. That the production angular distributions for the $K^0_1K^0_1$ and K^+K^- systems are quite different is further evidence that the effect in the K^+K^- system is caused by a mechanism different from the S-wave threshold enhancement. To further illustrate this difference we show the Chew-Low plots for the K^+K^- and $K^0_1K^0_1$ systems in Fig. 33.

We corrected the angular distributions for detection efficiency and made a least-squares fit to the corrected data. Although the decay angular distribution is consistent with being isotropic, a slightly better fit is obtained if linear and quadratic terms in $\cos\theta$ are also included. Since the spin-parity of the ϕ is 1^-, we expect constant and quadratic terms. The S-wave background which is known to be present could interfere with the P-wave decay of the ϕ to give a linear term also. The model of ϕ production by ρ exchange predicts a $\sin^2\theta$ distribution for the decay angle. We do not observe such a correlation, but absorption effects are expected to modify the distribution significantly.[80] The angular distributions for ϕ production and decay are similar to the corresponding distributions reported by Kraemer et al. for the reaction $\pi^+n \to p\omega$.[81]

The detection efficiencies and cross sections for ϕ production are given in Table XVII. We have calculated the cross sections using the branching fraction of 0.48 ± 0.04 for $\phi \to K^+K^-$ determined by Lindsey and Smith.[75] We have displayed these cross sections in Fig. 34 along with the cross sections for the reaction $\pi^+n \to p\omega$ reported by

other experimenters.[81-84] One might expect the energy dependence to be related to $\pi^- p \to n\phi$ by SU_3 and charge symmetry. The abscissa is the center of mass momentum for the final state. The ordinate for the $\pi^+ n \to p\omega$ cross section is 50 times larger than the ordinate for the $\pi^- p \to n\phi$ cross section. Experimenters[85-87] with $\pi^+ p$ interactions have reported possible production of the ϕ meson through $\pi^+ p \to N^{*++}\phi$. The ratio of this cross section to the cross section for $\pi^+ p \to N^{*++}\omega$ is about 1/70.

We made a search for the $K_1^0 K_2^0$ decay of the ϕ. A rough calculation leads us to expect to find two events in which both the K_1^0 and the K_2^0 are observed to decay in the bubble chamber. A scan of the film yielded three events with visible K_1^0 and K_2^0 decays which fit $\pi^- p \to n K_1^0 K_2^0$. Of these three, one had a $K_1^0 K_2^0$ effective mass in the ϕ region.

S. $f \to K^+K^-$, $A_2 \to K^+K^-$

At the higher momenta where the f and the A_2 are produced, the nK^+K^- events could contain a large contamination. Even so it is interesting to check for possible decay of these states. If we use the detection efficiencies quoted in Table XVII and the cross sections for A_2^0 production given in Table X, we find that we expect about six events above background in the A_2 region at 2.9 to 3.3 BeV/c, and about one event above background at 3.8 to 4.2 BeV/c. The data in Fig. 19, h and i, are consistent with these numbers and with no decay of the f into K^+K^-.

V. FOUR- AND FIVE-BODY FINAL STATES

A. Four-Body Final States

In Table XVIII we give the number of events observed in each of the four-body final states. The numbers of events in the $\Sigma K\pi\pi$ and $NK\bar{K}\pi$ final states at low momentum are too small to warrant any further analysis.

1. $\pi^- p \to \Lambda K\pi\pi$

At 1.8 through 2.2 BeV/c the $\Lambda K^+\pi^0\pi^-$ and $\Lambda K^0\pi^+\pi^-$ final states are dominated by simultaneous production of $Y_1^*(1385)$ $K^*(890)$. At the higher momentum intervals the cross sections for Y^*K^* and nonresonant $\Lambda K\pi\pi$ have both risen. Figures 35 through 38 show the $\Lambda\pi$, $K\pi$, $\Lambda\pi\pi$, and $K\pi\pi$ mass projections with curves calculated from the fitted values for each resonant state present.[88] The fits are good in general and are given in Table XIX.

The effective-mass distribution for $K^+\pi^-$ at 3.8 to 4.2 BeV/c (Fig. 37d) shows deviations from the calculated distribution at low values for the $K\pi$ mass. This enhancement is entirely associated with events for which the mass of $\Lambda\pi^-$ falls in a band about 1385 MeV. Although such an enhancement might also be explained by a triangle diagram,[89] we believe this effect to be statistical.

The $K\pi\pi$ spectra were carefully examined for evidence of resonance states that are new or not yet firmly established.[90-97] The distributions with no selections are well explained by phase space with the possible exception of an excess of events in the vicinity of 1350 MeV in $K^0\pi^+\pi^-$ at 2.9 to 3.3 BeV/c. Figure 39 is a mass plot for $K\pi\pi$ at 2.9 to 3.3 BeV/c with $Y^*(1385)$ events removed,[98] and either (a) $K^+\pi^-$ or $K^+\pi^0$ from $\Lambda K^+\pi^0\pi^-$ or (b) $K^0\pi^+$ from $\Lambda K^0\pi^+\pi^-$ in the $K^*(890)$ region.[99] (There

is no evidence for ρ production in $\Lambda K\pi\pi$ final states.) No significant increase in deviation from calculated distributions is observed. In particular we see no evidence for a resonance at 1175, 1215 or 1275 MeV. Our data at 2.6, 2.8, 3.0, 3.1, and 3.2 BeV/c were separately examined, and no enhancement was observed whose cross section varied rapidly with momentum.

In Fig. 40, effective-mass distributions are plotted for $Y^*(1385)\pi$ at 2.9 to 3.3 BeV/c with K^* events excluded. We see no evidence for new resonance states.

The ΛK and $\Lambda K\pi$ effective mass distributions were also examined, and in no case do they show any significant deviation from phase space.

2. $\pi^- p \rightarrow \Sigma K\pi\pi$

The dominant features of these final states at the higher momenta are shown in Fig. 41, where the effective mass of $(\Sigma\pi)^0$ is plotted against the effective mass of $(K\pi)^0$. Many of the events proceed through Y^*K^* intermediate states. The $Y_0^*(1405)$, $Y_0^*(1520)$, and $Y_1^*(1660)$ are all definitely present and are produced in association with $K^*(890)$. Our estimates for the cross sections of these processes are shown in Table XIX. No enhancements are apparent in the $(K\pi\pi)^{\pm}$ distributions.

3. $\pi^- p \rightarrow NK\bar{K}\pi$

The effective mass histograms for the $NK\bar{K}\pi$ final states are shown in Figs. 42 through 45. The $pK^+K^-\pi^-$, $pK^0\bar{K}^0\pi^-$, and $pK^0K^-\pi^0$ final states as well as the $nK^{\pm}K^0\pi^{\mp}$ final states have been grouped together. The curves on the data are not computer fits but represent our best estimates for the amounts and corresponding cross sections for resonance production shown in Table XIX. Production of the D and E mesons is observed in the $K^{\pm}K^0\pi^{\mp}$ system.

Our best estimates for the mass and width of the D are $M = 1283 \pm 5$ MeV and $\Gamma = 35 \pm 10$ MeV. The parameters for the E are more difficult to estimate, but $M = 1420 \pm 20$ MeV and $\Gamma = 60 \pm 20$ MeV give a satisfactory fit.

a. $\pi^- p \rightarrow nD$, $\pi^- p \rightarrow nE$. The D and E mesons have been observed by other experimenters[100, 101] and have been discussed in previous papers on these data.[22, 25] Figure 46 presents a comparison of the four-body final states containing a proton with those containing a neutron. Figures 46 a and b show the contrast in the $K\bar{K}\pi$ effective mass distributions due to E and D production in the final states containing a neutron. Those events with low $K\bar{K}$ effective mass have been shaded to accentuate the difference. Figures 46 c and d, are scatter plots with two points per event. The accumulation of events in the region of Fig. 46 d where the E and $K^*(890)$ bands cross is evidence that the E meson decays predominantly by $K^*\bar{K}$ and $\bar{K}^*K$ intermediate states. The Chew-Low plots of Fig. 46 e and f further show the difference in structure between the charged and neutral $K\bar{K}\pi$ systems.

The I spins of both the D and the E are most likely zero. These assignments have been favored by other authors.[100, 101] Our strongest argument against $I = 1$ is the lack of any enhancement in the negatively charged states of the $K\bar{K}\pi$ system. Although the production mechanisms of the D and E mesons are unknown, the hypothesis of production by exchange of an $I = 1$ particle would lead to the predictions presented in Table XX if the D and the E had $I = 1$. Since the numbers of events observed disagree with the numbers predicted, this model is inconsistent with the D and E mesons having $I = 1$. Although the D appears to be produced at all momenta of this experiment above its

threshold of 2140 MeV/c (as shown in Table XIX), the cross section for the production of the E meson falls sharply between the momentum intervals at 2.9 to 3.3 BeV/c and 3.8 to 4.2 BeV/c. Figure 47 a and b show how the scatter plots differ at the two momenta.

Figure 47 c and d show the production angular distributions for the D and E mesons. For the D meson we have taken events with $1245\ \text{MeV} \leq M_{K\bar{K}\pi} \leq 1325\ \text{MeV}$. For the E meson we have taken events with $1360\ \text{MeV} \leq M_{K\bar{K}\pi} \leq 1480\ \text{MeV}$ and with either one of the two $K\pi$ systems in the 841 to 941-MeV mass interval. The E and D mesons appear to be produced peripherally.

The G parities of the D and E could best be determined by observation of a $K_1^0K_1^0\pi^0$ or $K_1^0K_2^0\pi^0$ decay mode, indicating a G parity of + and - respectively. Unfortunately the presence of the neutron usually makes it impossible to fit the $nK^0\bar{K}^0\pi^0$ final states. We looked at events fitting $K_1^0K_1^0$ + mm and searched the film for cases where the neutron momentum could be determined from a $np \rightarrow np$ scatter. We found only seven cases with an acceptable fit to $\pi^-p \rightarrow nK_1^0K_1^0\pi^0$. This number of events was too small to serve as a conclusive test of the G parities of either the D or the E mesons.

We have attempted to determine the J^{PG} quantum numbers of the D and E mesons by analyzing their decays into $K\bar{K}\pi$. Figures 48 a and b give the Dalitz plots for D and E decay. We have demanded that $1245\ \text{MeV} \leq M_{K\bar{K}\pi} \leq 1325\ \text{MeV}$ for the D events and that $1360\ \text{MeV} \leq M_{K\bar{K}\pi} \leq 1480\ \text{MeV}$ for the E events. The D mesons tend to decay in such a way that the $K\bar{K}$ effective mass is small. We cannot determine whether this effect comes from an $I = 1$ $K\bar{K}$ enhancement or a

constructive interference of the $K^*(890)$ with the $\bar{K}^*(890)$. The Dalitz plot for the E meson shows the crossing $K^*(890)$, and $\bar{K}^*(890)$ bands. Matrix elements for D and E decay have been calculated which take into account the $K^*(890)$ resonance. They are discussed in detail in Appendix C.

We have chosen to describe the decays in terms of the $K\bar{K}$ effective mass and the internal decay angle ($\theta_{K\bar{K}}$) shown in Fig. 20. The weighted distributions of these quantities are shown in Fig. 48 c through f. We have used the same events that appear in the Dalitz plots and have plotted two points per event in the angular distributions.

The curves on the distributions from the D meson are the three best fits to the angular distribution. Of these three cases the $J^{PG} = 1^{++}$ case is the best fit to the $K\bar{K}$ effective mass distribution. If we consider how well the different J^{PG} assignments fit the two distributions simultaneously, we favor the 1^{++} assignment, with 2^{-+}, 0^{-+}, and 1^{+-} being the next most likely.

The curves on the distributions from the E meson are for $J^{PG} = 1^{++}$ and 0^{-+}. The large amount of background in these distributions makes a definite determination of the quantum numbers impossible, but on the basis of the curves we favor 1^{++}, with 2^{-+} and 0^{-+} being the next most likely.

For both the D and E mesons the angular distributions show no tendency toward dropping at $|\cos \theta_{K\bar{K}}| = 1.0$. This rules out the $J^P = 1^-$ and 2^+ assignments because such assignments predict no events at $|\cos \theta_{K\bar{K}}| = 1.0$.

Note that the strong decay modes are quite restricted for particles with $M \leq 1450$ MeV, $I^G = 0^+$, and $J^P = 0^-$, 1^+, or 2^-. The only two

particle decays allowed are $K\bar{K}^*$, $\bar{K}K^*$, and $A_1\pi$. Allowed three particle decays are $K\bar{K}\pi$, $\pi\pi\rho$, and $\pi\pi\eta$. The fact that the D and E mesons have been observed only in the $K\bar{K}\pi$ channel can be considered additional weak evidence in favor of the 1^{++}, 2^{-+}, or 0^{-+} assignments.

The production angular distributions suggest production of the D and E by some exchange mechanism. The favored quantum numbers of the D and E rule out π, ρ, η, and ω exchange. The only remaining single-particle candidates are the heavier A_1 (if $J^P = 1^+$) and A_2 mesons.

The possibility that the E meson could be a kinematical enhancement has been discussed by Month.[89] The fact that the $K^*(890)$ has a width as large as 50 MeV makes a verification of the model difficult. Our data are consistent with the model, but by no means give proof of its validity.

We might expect the D and E mesons to decay into four pions via $\pi\pi\rho$ decay. Chung has studied the $n\pi^+\pi^+\pi^-\pi^-$ final states in this film and reports an effective mass distribution consistent with no decay into $\pi\pi\rho$ for both the D and E mesons.[60] On the basis of his data we can give one-standard-deviation upper limits on the branching ratios of

$$\frac{\Gamma\,(D \text{ or } E \rightarrow \pi\pi\rho)}{\Gamma\,(D \text{ or } E \rightarrow K^0 K^{\pm}\pi^{\mp})} < 2.0 .$$

We are unable to investigate the $\pi\pi\eta$ decay modes of the D and E mesons in this experiment.

The D and E mesons have not yet been unambiguously assigned to SU_3 multiplets, but the similarity of their favored quantum numbers tempts one to hypothesize that they are the mixing I = 0 members of an SU_3 nonet. If we assume that the A_1 meson (M = 1072 MeV) is the I = 1 member of such a nonet, then we expect the strange member to have a

mass between 1233 MeV and 1341 MeV. Possible candidates have been reported at masses 1215 MeV[96,97] and 1320 MeV.[93-95]

b. Other Resonances. There is also evidence in the $nK^+\bar{K}^0\pi^-$, $pK^0K^-\pi^0$, and $pK^+K^-\pi^-$ final states for the simultaneous production of $Y_0^*(1520)$ and $K^*(890)$ observed in the $\Sigma K\pi\pi$ final states. There are no significant enhancements in any of the histograms other than those due to well-known resonances. The $N\bar{K}\pi$ effective-mass distributions show no evidence of Y^* decay into $N\bar{K}\pi$, the NK and $NK\pi$ distributions show no evidence of a B = 1, S = 1 resonance, and the $N\pi$ histograms show no evidence of N^* production with $K\bar{K}$ pairs.

A search was made for the possible decay mode $B \to \pi\phi$ by assuming the following production and decay sequence:

$$\pi^- p \to pB^-$$
$$\hookrightarrow \pi^- \phi$$
$$\hookrightarrow K_1^0 K_2^0$$
$$\hookrightarrow K^+K^- .$$

Figure 49 is a scatter plot of the $K\bar{K}$ effective mass against the $K\bar{K}\pi$ effective mass for those events which fit either $pK^+K^-\pi^-$ or $pK^0\bar{K}^0\pi^-$ (only one K_1^0 decay in the chamber). There is only one event (where we expect a background of one event) in the rectangle defined by 1005 MeV $\leq M_{K\bar{K}} \leq$ 1035 MeV and 1160 MeV $\leq M_{K\bar{K}\pi} \leq$ 1280 MeV. This is a $pK^+K^-\pi^-$ event. If we assume 0 ± 5 events in the $pK_1^0K_2^0\pi^-$ (K_1^0 seen) channel and use the data of Chung,[60] we find an upper limit for the branching ratio of

$$\frac{\Gamma(B \to \pi\phi)}{\Gamma(B \to \pi\omega)} < 0.015.$$

This result agrees with the prediction of zero made by several authors.[102,103]

B. Five-Body Final States

In Table XXI we give the number of events observed in each of the five-body final states. These numbers are too small to allow a meaningful analysis of any single final state; we have, however, determined cross sections for them. In the $YK\pi\pi\pi$ final states there is some evidence for the production of $Y_0^*(1405)$, $Y_0^*(1520)$, $Y_1^*(1385)$, and $K^*(890)$. In addition, in the $\Lambda K^0\pi^+\pi^-\pi^0$ final state we observe production of ω, as shown in Fig. 50. The effective-mass plots for $\Lambda\omega$ and $K^0\omega$ are shown in Fig. 50 b and c. The curves in these plots are for an incident pion momentum of 3.2 BeV/c, but the data are from events at all momenta. Statistics are quite limited; no striking effects are seen. All the effective-mass distributions from the final states $NK\bar{K}\pi\pi$ have been examined and are consistent with phase space. In Fig. 51 we show the $K\bar{K}\pi\pi$ effective-mass distribution from all the five-body final states at 3.8 to 4.2 BeV/c.

VI. PRODUCTION OF Ξ HYPERONS

A. Experimental Procedure

Xi production is not copious in π^-p interactions. Cross contamination between Ξ production and other hypotheses has little effect upon the analysis presented in the previous sections but can produce strong biases in the sample of Ξ events. Consequently the analysis of Ξ reactions was not included in the general data system described in Section II, but was treated separately. In the regular scan of the film, events that indicated possible Ξ production (e.g., a topology with a lambda decay pointing to a kink in a negative track) were compiled into a list of Ξ candidates. To this list were added regularly processed events that were failures, rejects, or did not have an acceptable four-constraint fit. These candidates were

processed through a special version of the kinematic fitting program which tried to fit Ξ production hypotheses. The hypotheses attempted for Ξ^- production involved either an observed Λ decay from the Ξ or four constraints at the production vertex. These requirements insure the purity of the sample of events obtained. Only Ξ^0 hypotheses that involved the observed decays of the Λ and all K^0's were attempted. The reactions tried and topologies sought are shown in Table XXII. Other reactions or topologies are in general ambiguous with non-Ξ production hypotheses. Passing events were all examined on a scanning table to ensure consistency with observed bubble densities and to resolve ambiguities. In the final sample there was a single ambiguous event between two Ξ production reactions. This was assigned to the hypothesis with the higher confidence level.

The K^- contamination in our π^- beam (judging from the one τ decay observed) is too small to be an important source of background.

B. Results and Discussion

In Table XXII are shown the numbers of events found and our estimates for total cross sections in the vicinity of 3 and 4 BeV/c, assuming 100% scanning efficiency. The scanning efficiency is expected to be high, since the topologies considered are easily recognizable.

In Fig. 52 we present the Dalitz plot for the reaction $\pi^- p \rightarrow \Xi^- K^+ K^0$. The c.m. angular distribution of the final-state particles is shown on Fig. 53. The K^0 is seen to be produced preferentially along the beam direction.

In the reaction $\pi^- p \rightarrow \Xi^- K^0 K^0 \pi^+$ we see evidence for the production of $\Xi^*(1530)$. For six out of the nine events in our sample the $\Xi^- \pi^+$ mass

is in the interval $1520 < M(\Xi\pi) < 1540$ MeV. The cross section for $\Xi^*(1530)$ production is (0.25 ± 0.18) μb at 3.2 BeV/c and (1.4 ± 0.7) μb at 4 BeV/c.

From the small cross sections, and the lack of semi-two-body final states that characterize our results, we conclude that

(a) If there exist strangeness-2 mesons,[104] they are not strongly coupled to the $\Xi\bar{N}$ system;

(b) No strangeness-1 hyperons with mass below 2.3 BeV and a large partial width for decay into ΞK or $\Xi K\pi$ are observed in the present experiment.

It is interesting to note that the cross section for the reaction $\pi^- p \to \Xi^*(1530)\, KK$ is of the same order of magnitude as the cross section for $K^- p \to \Omega^- K^0 K^+$.[105] Both reactions involve a strangeness change of two units for the production of a member of the same SU_3 decuplet.

In the course of the experiment we have found no event with three or more V's. The lack of such events indicates that the cross section for the reactions $\pi^- p \to \Lambda KK\bar{K}$ and $\Sigma KK\bar{K}$ is below the level of sensitivity of this experiment.

VII. SUMMARY

The general pattern that emerges from the study of strange-particle final states in $\pi^- p$ interactions in the 1.5 to 4.2 BeV/c range can be summarized as follows:

1. Reactions involving strange particles in the final state account for about 5% of the total cross section.

2. Here, as in the case of the final states without strange particles, the peripheral production of resonant states is the outstanding feature of

this energy range. As a consequence, two-body or semi-two-body reactions of the form $\pi^- p \rightarrow YK$, YK^*, Y^*K, or Y^*K^* account for most events observed.

3. Among these resonant states we find that in general the lower-lying states are more copiously produced than higher-mass states in the same channels. The cross sections for resonant-state production in general fall with increasing beam momentum. From these observations we can draw the tentative conclusion that resonance production does not play such a central part in characterizing strange-particle final states at higher energies.

4. Simple one-particle exchange models are fairly successful in describing the decay distributions of $Y_1^{*-}(1385)K^+$, $Y_0^*(1520)K^0$, and $\Sigma^0 K^{*0}(890)$ but fail for $\Lambda K^{*0}(890)$. The absorption model is able to fit the production-angular distributions for ΛK^{*0} and $\Sigma^0 K^{*0}$ states, and in a qualitative fashion explain all the decay correlations. K^* exchange appears to dominate over K exchange in the processes $\pi^- p \rightarrow YK^{*0}$.

5. Reactions involving $K\bar{K}$ pairs are rich in nonstrange mesons. Production of the ϕ, the A_2, the D, and the E have been observed in addition to the enhancement in the $K_1^0 K_1^0$ system near threshold. We have presented evidence for the assignment $I^G J^P = 1^- 2^+$ for the A_2 and reasons for favoring $I^G J^P = 0^+ 1^+$ for both the D and the E.

6. Cross sections for two-body final states fall monotonically with increasing beam momentum in the range of this experiment. For three-body final states, we see a rise up to about 2 BeV/c, and a fall

above that momentum. Cross sections for four- and-more-body final states all rise up to the highest momenta available to us.

7. Production of Ξ hyperons accounts for a fraction of about 10^{-4} of the $\pi^- p$ total cross section.

8. We have no evidence for the decay of nucleon isobars into strange particles.

VIII. ACKNOWLEDGMENTS

Many people have contributed to the experimental program that forms the subject of this report. We wish to thank first Professor Luis W. Alvarez for his continued encouragement, interest, and support. Many members of the Alvarez group have contributed valuable suggestions, and useful criticism on countless occasions. Mr. William Nolan has attended to the problems of administration and organization.

Many of the ideas contained in this work, and much of the data-analysis system used have originated with Dr. Gideon Alexander, Dr. George R. Kalbfleisch, Dr. Joseph A. Schwartz, and Professor Gerald A. Smith, who have participated in the first phases of this effort. We had the pleasure of collaborating with Dr. Suh Urk Chung and Dr. Laurance D. Jacobs, who have analyzed other aspects of the same exposure.

Of the two beams used for collecting the film, the first one was built by Professor Harold K. Ticho and Professor Donald Stork from UCLA, and Dr. George R. Kalbfleisch and Professor Janice B. Shafer from Berkeley. The second was built as a collaborative effort between the Goldhaber-Trilling and Alvarez groups, with Dr. John A.

Kadyk, Dr. Joseph J. Murray, Professor Janice B. Shafer, Dr. Benjamin Shen, and Professor George H. Trilling taking responsibility for the design and construction. We received much help and cooperation from the Bevatron operations group, under the direction of Dr. Edward J. Lofgren, and the 72-inch bubble chamber crew under the direction of Mr. Robert Watt.

Much of the task of computer programming was performed by the programming group under Dr. Robert Harvey.

We have received invaluable help from our scanning and measuring staff. Mr. Edward Hoedemaker has provided overall supervision. Mr. Joseph Requa, Mr. Werner O. Koellner, Mr. Arthur Wang, and Mr. Walter Hendricks have at different times coordinated the effort for this experiment. The bookkeeping and library operations over the years were in the charge of Miss Judith Allen, Mrs. Cathy Bowers, Mrs. Sharon Villacorta, Mrs. Ruth Good, and finally Mrs. Betty Armstrong. The actual task of scanning and measuring was performed by too many devoted people to list here. Outstanding contributions were made by Mr. Carl Dukatz, Mr. Alex Emerson, Mrs. Doris Jensen, Mr. James Neufeld, and Mr. Arthur Pedreira.

Finally we wish to thank Mrs. Ann McLellan and Miss Karlyn Shepler for performing all secretarial and many administrative tasks with patience, competence, and devotion.

APPENDICES

A. The Density Matrix

We first discuss the density matrix for the decay of a spin-J particle into two spin-zero particles. We use the coordinate system shown in Fig. 20 b and quantize angular-momentum projections along the beam direction (z-axis).

The density-matrix formalism is discussed briefly by Williams[106] and in detail by Fano.[107] The initial state may be described as a statistical mixture of pure states ψ_i, with statistical weights w_i. When the particle decays, its spin is transformed into orbital angular momentum. If the particle starts in a single pure state ψ_i, then the decay amplitude is described by

$$\phi_i = \sum_{m=-J}^{+J} a_{im} \, Y_J^m(\theta, \phi), \tag{A1}$$

where $Y_J^m(\theta, \phi)$ is the spherical harmonic with magnetic quantum number m. The decay distribution is then

$$\langle \phi_i | \phi_i \rangle = \sum_{m=-J}^{+J} \sum_{j=-J}^{+J} a_{im} \, Y_J^m(\theta, \phi) \, a_{ij}^* \, [Y_J^j(\theta, \phi)]^* \tag{A2}$$

If we now imagine that the particle starts as a statistical mixture, the decay distribution becomes

$$I(\theta, \phi) = \sum_i \sum_m \sum_j w_i \, a_{im} \, Y_J^m(\theta, \phi) \, a_{ij}^* [Y_J^j(\theta, \phi)]^* . \tag{A3}$$

We can define the density matrix elements

$$\rho_{mj} = \sum_i w_i \, a_{im} \, a_{ij}^* \tag{A4}$$

to get

$$I(\theta,\phi) = \sum_m \sum_j \rho_{mj}\, Y_J^m(\theta,\phi)\, [Y_J^j(\theta,\phi)]^* . \tag{A5}$$

From the definition of ρ_{mj} it is clear that

$$\rho_{mj} = \rho^*_{jm} . \tag{A6}$$

We further normalize by imposing the condition

$$\sum_m \rho_{mm} = 1. \tag{A7}$$

Conservation of parity in the production and the decay tells us that $I(\theta,\phi) = I(\theta,-\phi)$. Imposition of this condition requires the relation

$$\rho_{-m,-j} = (-1)^{m+j}\, \rho_{mj} . \tag{A8}$$

For the process $A_2 \to K\bar{K}$, it is convenient to define the matrix

$$A = [Y_2^{\,2}(\theta,\phi),\ Y_2^{\,1}(\theta,\phi),\ Y_2^{\,0}(\theta,\phi),\ Y_2^{\,-1}(\theta,\phi),\ Y_2^{\,-2}(\theta,\phi)]. \tag{A9}$$

Then the decay angular distribution becomes

$$I(\theta,\phi) = A\,\rho\,A^{\dagger}, \tag{A10}$$

where the density matrix is given by[108]

$$\rho = \begin{pmatrix} \rho_{22} & \rho_{21} & \rho_{20} & \rho_{2-1} & \rho_{2-2} \\ \rho^*_{21} & \rho_{11} & \rho_{10} & \rho_{1-1} & -\rho^*_{2-1} \\ \rho^*_{20} & \rho^*_{10} & 1-2(\rho_{11}+\rho_{22}) & -\rho^*_{10} & \rho^*_{20} \\ \rho^*_{2-1} & \rho_{1-1} & -\rho_{10} & \rho_{11} & -\rho^*_{21} \\ \rho_{2-2} & -\rho_{2-1} & \rho_{20} & -\rho_{21} & \rho_{22} \end{pmatrix} \tag{A11}$$

Evaluation of Eq. (A10) gives Eq. (7) in the text.

For the process $\pi^- p \to Y K^*$, we have in the final state a spin 1/2 and a spin-1 particle. Quantizing along the beam direction yields

the 6×6 density matrix shown in Table XXIII, where the first and third indices refer to the fermion spin states, and the second and fourth indices refer to the vector particle. Here our density-matrix parameters are constrained by

$$\rho_{-m-j-n-\ell} = (-1)^{m+j+n+\ell+1}\,\rho_{mjn\ell}\,. \tag{A12}$$

If we use θ and ϕ for the K^* rest frame and θ' and ϕ' for the baryon, the most general decay distribution is given by

$$I(\theta,\phi,\theta',\phi') = \sum_{mjn\ell} \rho_{mjn\ell}\; Y_1^j(\theta,\phi)\,\Lambda^m(\theta',\phi')\,[Y_1^\ell(\theta,\phi)\Lambda^n(\theta',\phi')]^*, \tag{A13}$$

where

$$\Lambda^{\pm1/2}(\theta',\phi')\,[\Lambda^{\pm1/2}(\theta',\phi')]^* = (1 \pm \alpha\cos\theta')/4\pi$$

and

$$\Lambda^{\pm1/2}(\theta',\phi')\,[\Lambda^{\mp1/2}(\theta',\phi')]^* = (\alpha\sin\theta'\,e^{\pm i\phi'})/4\pi.$$

Performing the sums we find

$$\begin{aligned}
I(\theta,\phi,\theta',\phi') = {} & \frac{3}{16\pi^2}\,(\rho_{++++} + \rho_{+-+-})\sin^2\theta \\
& + [1 - 2(\rho_{++++} + \rho_{+-+-})]\cos^2\theta \\
& - \sqrt{2}\,\mathrm{Re}(\rho_{+++0} - \rho_{+0+-})\sin2\theta\cos\phi \\
& + \sqrt{2}\,\mathrm{Im}(\rho_{+++0} - \rho_{+0+-})\sin2\theta\sin\phi\,\alpha\cos\theta' \\
& - 2\,\mathrm{Re}\,\rho_{+++-}\sin^2\theta\cos2\phi \\
& + 2\mathrm{Im}\,\rho_{+++-}\sin^2\theta\sin2\phi\,\alpha\cos\theta' \\
& - 2\mathrm{Im}\,\rho_{++-+}\sin^2\theta\,\alpha\sin\theta'\sin\phi' \\
& + \sqrt{2}\,\mathrm{Im}\,\rho_{++-0}\sin^2\theta\,\alpha\sin\theta'(\sin\phi'\cos\phi + \cos\phi'\sin\phi) \\
& + \sqrt{2}\,\mathrm{Im}\,\rho_{+0-+}\sin2\theta\,\alpha\sin\theta'(\sin\phi'\cos\phi - \cos\phi'\sin\phi) \\
& + \rho_{++--}\sin^2\theta\,\alpha\sin\theta'(\sin\phi'\cos2\phi + \cos\phi'\sin2\phi) \\
& - 2\,\rho_{+0-0}\cos^2\theta\,\alpha\sin\theta'\sin\phi' \\
& + \rho_{+--+}\sin^2\theta\,\alpha\sin\theta'(\sin\phi'\cos2\phi - \cos\phi'\sin2\phi),
\end{aligned} \tag{A14}$$

where α is the fermion decay-asymmetry parameter. This distribution is characterized by 11 parameters that we can experimentally determine: $\rho_{++++} + \rho_{+-+-}$, $\mathrm{Re}(\rho_{+++0} - \rho_{+0+-})$, $\mathrm{Im}(\rho_{+++0} - \rho_{+0+-})$, $\mathrm{Re}\,\rho_{+++-}$, $\mathrm{Im}\rho_{+++-}$, $\mathrm{Im}\rho_{++-+}$, $\mathrm{Im}\rho_{++-0}$, $\mathrm{Im}\rho_{+0-+}$, ρ_{++--}, ρ_{+0-0}, and ρ_{+--+}. These are related by a linear transformation to the 11 correlation coefficients of Berman and Oakes.[109] For convenience, these 11 quantities are referred to as terms 1 through 11, respectively.

If we choose to ignore the information from the fermion decay and integrate over θ' and ϕ', we are left with three variables describing the decay of the K^*. These are the parameters used in the literature for the analysis of $K^-p \to K^*N$;

$$\rho_{11} = \rho_{++++} + \rho_{+-+-} \qquad \text{(term 1)}$$

$$\rho_{1-1} = 2\,\mathrm{Re}\,\rho_{+++-} \qquad \text{(term 4)}$$

$$\mathrm{Re}\rho_{10} = \mathrm{Re}(\rho_{+++-} - \rho_{+0+-}) \qquad \text{(term 2)}$$

$$\rho_{00} = 1 - 2\rho_{11}. \qquad \text{(A15)}$$

For electromagnetic Σ^0 decay, no polarization information can be obtained from observation of the isotropic γ-ray decay distribution. It can be shown, however, that the average polarization in the subsequent Λ decay is equal to -1/3 that of the Σ^0,[110] if we average over all Λ decay angles in the Σ^0 rest frame. We can use the formalism developed here, therefore, if we evaluate θ' and ϕ' from the proton decay of the Λ in the Λ rest frame and use a value of $\alpha = -0.22$. Here we must be careful to transform pertinent vectors from the center-of-mass to the Σ rest frame and then to the Λ rest frame to avoid complications from coordinate rotation effects.

For the reaction $\pi p \rightarrow Y^* K$, we consider only the states $Y_0^*(1520)$ and $Y_1^*(1385)$ and the initial strong decay of these states. For particles of spin 3/2, the decay distribution is given by

$$I(\theta,\phi) = \frac{3}{4\pi}\{\rho_{33}\sin^2\theta + (1/2 - \rho_{33})(1/3 + \cos^2\theta)$$

$$- \frac{2}{\sqrt{3}} \mathrm{Re}\rho_{3-1} \sin^2\theta\cos 2\phi - \frac{2}{\sqrt{3}}\mathrm{Re}\rho_{31}\sin 2\theta\cos\phi\}, \qquad \text{(A16)}$$

where the indices refer to twice the magnetic quantum numbers of Y^* states.

B. The Absorption Model

The basic formula from which absorption calculations proceed comes from a nonrelativistic approach to the problem. The validity of extending the formalism to processes at high energy is not certain, but the fact that it works is motivation enough to investigate its consequences. The basic statement is that the matrix element for a process between given initial and final spin states is given by

$$M = S_f^{1/2}\, B S_i^{1/2}, \qquad \text{(B1)}$$

where $S_i(S_f)$ is the elastic-scattering matrix element for the initial (final) state, B is the "raw" Feynman-diagram matrix element, and M is the final absorbed element. Jackson[51] has outlined the decomposition of B into angular-momentum components, and the calculation of M. In this report we used instead Huff's formulation,[55] which casts the matrix elements in a linear-momentum representation. This approach is computationally convenient, since the usual calculation of B is in this representation. We need not decompose B into partial waves, perform the absorption calculation in each angular momentum

state, and then convert the results back to the linear representation.

Properly stated, Eq. (B1) is

$$\langle f\Omega\,\lambda_1\lambda_2\,|M|\,i\,O\,\lambda_3\lambda_4\rangle$$

$$= \sum_{\lambda_i'} \int d\Omega_f\, d\Omega_i\, \langle f\Omega\,\lambda_1\lambda_2\,|S_f^{1/2}|f\Omega_f\lambda_1'\lambda_2'\rangle\langle f\Omega_f\lambda_1'\lambda_2'\,|B|\,i\Omega_i\lambda_3'\lambda_4'\rangle$$

$$\times \langle i\Omega_i\lambda_3'\lambda_4'\,|S_i^{1/2}\,|\,i\,O\,\lambda_3\lambda_4\rangle\,, \qquad \text{(B2)}$$

where i and f indicate the initial and final states, λ_i the helicity states of the particles involved, Ω the production angle of the final state, and λ_i', Ω_f, and Ω_i the helicities and angular distribution variables of the intermediate states that are to be summed and integrated over. Expressions are cast in a helicity representation because manipulative formulae are particularly easy to express. By means of these formulae, expression (B2) is converted to

$$\langle f\theta\lambda_1\lambda_2\,|M|\,iO\,\lambda_3\lambda_4\rangle = \int d\Omega_f\, d\Omega_i \sum \langle f\theta\lambda_1\lambda_2\,|S_f^{1/2}|f\Omega_f\lambda_1'\lambda_2'\rangle$$

$$\times\ (-1)^{\mu-\mu'}\langle f\theta_i\lambda_1'\lambda_2'\,|B|\,iO\lambda_3'\lambda_4'\rangle\exp[i\phi_i(\mu'-\lambda')]$$

$$\times\ \langle i\Omega_i\lambda_3'\lambda_4'\,|S_i^{1/2}\,|\,i\Omega_f\lambda_3\lambda_4\rangle, \qquad \text{(B3)}$$

where $\lambda = \lambda_1 - \lambda_2$, $\mu = \lambda_3 - \lambda_4$, $\lambda' = \lambda_1' - \lambda_2'$, and $\mu' = \lambda_3' - \lambda_4'$. Here we have the quantity $\langle f\theta_i\lambda_1'\lambda_2'\,|B|\,iO\lambda_3'\lambda_4'\rangle$, which is just the unmodified one-particle-exchange matrix element for scattering into an angle θ_i.

We now expand $S^{1/2}$ as $1 - T/2$ and keep terms at most linear in T. Since elastic scattering is largely confined to the forward direction, we restrict ourselves to no helicity changes for these processes.

After some manipulation and trivial integration and summation, we obtain

$$\langle f\theta\lambda_1\lambda_2 \,|M|\, i0\lambda_3\lambda_4\rangle = \langle f\theta\lambda_1\lambda_2 \,|B|\, i0\lambda_3\lambda_4\rangle$$

$$- \int_{-1}^{+1} d\cos\theta' \int_0^{\pi} d\phi' \langle f\theta'\lambda_1\lambda_2 \,|B|\, i0\lambda_3\lambda_4\rangle$$

$$\times \left(\langle\theta''\lambda_3\lambda_4 \,|T_i|\, 0\lambda_3\lambda_4\rangle \, \mathrm{Re}\, \{\eta^{2\mu} \exp[-i\phi'(\mu-\lambda)]\} \right.$$

$$\left. + \langle\theta''\lambda_1\lambda_2 \,|T_f|\, 0\lambda_1\lambda_2\rangle \, \mathrm{Re}\, \{\eta^{2\lambda} \exp[i\phi'(\mu-\lambda)]\} \right) ,$$

where $\eta = [\cos(\theta'/2)\cos(\theta/2) + \sin(\theta'/2)\sin(\theta/2)\exp(i\phi')]/\cos(\theta''/2)$

$$\cos\theta'' = \cos\theta' \cos\theta + \sin\theta' \sin\theta \cos\phi' . \qquad \text{(B4)}$$

To compare with experiment we must now rotate the final amplitudes from the helicity directions to the coordinate directions we have selected, and form the density matrix as outlined in Appendix A.

The matrix element T is related to the elastic-scattering cross-section distribution by

$$\frac{d\sigma}{d\Omega} = \left(\frac{2\pi}{K}\right)^2 |T|^2 . \qquad \text{(B5)}$$

Experimentally, elastic differential cross sections can be well approximated at least in the forward direction by the expression

$$\frac{d\sigma}{d\Omega} = \frac{K^2}{16\pi^2} \sigma_{\text{total}}^2 \exp(-A\Delta^2) \qquad \text{(B6)}$$

where Δ is the absolute value of the four-momentum transfer. This gives us the magnitude of the matrix element T but not its phase. Since we have no knowledge of the phase of T, we assume that it is constant over all production angles and that it is the same for the

initial and final states. If we arbitrarily set this phase to zero, then our matrix element will be real and we will have no fermion polarization. Consequently terms three and five through eleven of the YK^* density matrix must of necessity be zero. We choose to let the value of this common phase be a free parameter to be determined by the fitting program. This, of course, is only an expediency to cover our ignorance of the situation and has no direct physical significance. Although the introduction of this parameter allows for nonzero values for all density-matrix parameters, large deviations from zero cannot be fit by the theory. To achieve the extreme peripheral character of production distributions, the second term in Eq. (B4) must be mostly in phase with the first. The out-of-phase component adds to the differential cross section rather than subtracts from it.

From the observed width of decay of the K^*, we know the $K^*K\pi$ coupling constant but we have no information about the $pK\Lambda$ vertex. Information at both vertices for K^* exchange is lacking. Although we know the characteristics of elastic scattering over the range of energies considered here, the quantities characterizing the final-state interactions are completely unknown. Finally, we have no value for the phase parameter which we call ζ. In the fitting program, χ^2 was minimized, with six parameters allowed to vary: σ_f, A_f, ζ, g_p^2, g_V, and g_T. The last three coupling constants are defined in terms of the coupling constants presented in Ref. 111 by the relationships:

$$g_p = g(Kp\Lambda)$$

$$g_V = g(K^*K^*\pi)\, g_V(pK^*\Lambda)$$

$$g_T = g(K^*K^*\pi)\, g_T(pK^*\Lambda).$$

We find $g_p^2/4\pi \approx 1$ for ΛK^{*0} at the two higher momentum intervals; g_p^2 was of necessity set equal to zero to get convergence for $\Sigma^0 K^{*0}$ at 1.8 to 2.2 BeV/c. The vector coupling g_V and tensor coupling g_T were large and of the same order of magnitude for all cases

$$|g_V| \approx |g_T| \approx 10.$$

The parameters characterizing the final-state YK^* interaction, (a) σ_f, the total cross section, and (b) A_f, the slope of the differential elastic cross section, were not determined with any sensitivity by the fitting procedure. The angle ζ was small in all cases. As an example, the best fit for ΛK^{*0} at 2.9 to 3.3 BeV/c is shown in Fig. 54. Also shown in Fig. 54a is the prediction for the variation of term one with the best-fit coupling constants but with no absorption. Except in the extreme forward direction (the vector particle exchange contribution must decrease near $\theta_{prod} = 0$), $|g_V|$ and $|g_T|$ on the order of 10 and $g_p^2/4\pi$ on the order of 1 corresponds to dominance of vector exchange over pseudoscalar exchange ($[1 - 2(\rho_{++++} + \rho_{+-+-})]$ is small.) We conclude that vector exchange dominates pseudoscalar exchange for these reactions and that absorption calculations give a good qualitative explanation for the data.

C. Matrix Elements for the Decay of an I = 0 State into $K\bar{K}^*$ and $\bar{K}K^*$

We have constructed the matrix elements for the decay of an I = 0 state into $K\bar{K}^*$ and $\bar{K}K^*$, using the approach discussed by Zemach.[112] The total system is in an eigenstate of G, so that the matrix element must be of the form

$$\mathcal{M} = M(K\bar{K}^*) + G\, M(\bar{K}K^*), \tag{C1}$$

where $G = \pm 1$ and $M(K\bar{K}^*)$ are functional forms depending on the assumed spin and parity. The forms for $M(K\bar{K}^*)$ are given in Table XXIV as a function of

(a) the relative $K, \bar{K}^*$ angular momentum, ℓ,

and

(b) the ampltude for $\bar{K}^*$ decay into $\bar{K} + \pi$,

$$\bar{f} = \frac{\Gamma\, M_0^3/M_{\bar{K}\pi}^2}{(M_0^2 - M_{\bar{K}\pi}^2) + i\Gamma\, M_0^3/M_{\bar{K}\pi}^2 (p/p_0)^3} .$$

Here we have Γ = 50 MeV, M_0 = 890 MeV, $M_{\bar{K}\pi}$ is the $\bar{K}\pi$ effective mass, p is the $\bar{K}\pi$ relative momentum in the $\bar{K}\pi$ rest frame, p_0 = 576 MeV/c, and the four-vectors are[113]

(c) $W_\mu = K_\mu - \bar{K}_\mu - \pi_\mu$ (relative $\bar{K}^*$, K momentum),

(d) $T_\mu = \bar{K}_\mu - \pi_\mu$ (relative $\bar{K}$, π momentum),

(e) $D_\mu = K_\mu + \bar{K}_\mu + \pi_\mu$ (total momentum),

(f) $\bar{e}_\mu$ (polarization vector of the $\bar{K}^*$),

(g) $\mathcal{E}_\mu$, $\mathcal{E}_{\mu\nu}$ (polarization tensor for the whole system),[114]

(h) $R_\mu = -W_\mu + (W_\nu D^\nu / D_\lambda D^\lambda) D_\mu$ ($R_0 = 0$ in the overall rest frame).

We also have

(i) the tensor $\delta_{\mu\nu} = -g_{\mu\nu} + D_\mu D_\nu / D_\lambda D^\lambda$,

and

(j) the completely antisymmetric symbol $\epsilon_{\mu\nu\lambda\sigma}$.

The matrix elements were integrated over an S-wave Breit-Wigner shape for the $E^{\cdot}$ meson (mass = 1420 MeV, Γ = 70 MeV) and the D meson (mass = 1285 MeV, Γ = 35 MeV) to give the curves of Figs. 55 and 56.

FOOTNOTES AND REFERENCES

*This work was done under the auspices of the U. S. Atomic Energy Commission.

†Part of this paper forms the subject of a thesis submitted to the Graduate Division of the University of California, Berkeley, in partial fulfillment of the requirements for the degree of Doctor of Philosophy.

‡Present address: TRW Systems, Inc., 1 Space Park, Redondo Beach, Calif.

**Present address: Logicon, Inc., 205 Avenue I, Redondo Beach, Calif.

1. L. J. Curtis, C. T. Coffin, D. I. Meyer, and K. M. Terwilliger, Phys. Rev. 132, 1771 (1963) (1.508 BeV/c).
2. O. Goussu, M. Sené, B. Ghidini, S. Mongelli, A. Romano, P. Waloschek, and V. Alles-Borelli, Nuovo Cimento 42, A606 (1966) (1.59 BeV/c).
3. A. R. Erwin, R. H. March, and W. D. Walker, Nuovo Cimento 24, 237 (1962), Phys. Letters 3, 99 (1962) (1.89, 2.1 BeV/c).
4. D. Colley, N. Gelfand, U. Nauenberg, J. Steinberger, S. Wolf, H. R. Brugger, P. R. Kramer, and R. J. Plano, Phys. Rev. 128, 1930 (1962) (2.0 BeV/c).
5. D. H. Miller, A. Z. Kovacs, R. McIlwain, T. R. Palfrey, and G. W. Tautfest, Phys. Rev. 140, B360 (1965) (2.7 BeV/c).
6. O. Goussu, G. Smadja, and G. Kayas, Nuovo Cimento (to be published) (2.75 BeV/c).
7. T. P. Wangler, A. R. Erwin, and W. D. Walker, Phys. Rev. 137, B414 (1965) (3.0 BeV/c).

8. J. Bartsch et al., Aachen-Hamburg-London-MünchenCollaboration, Nuovo Cimento 43, A 1010 (1966) (4 BeV/c).

9. L. Bertanza, B. B. Culwick, K. W. Lai, I. S. Mittra, N. P. Samios, A. M. Thorndike, S. S. Yamamoto, and R. M. Lea, Phys. Rev. 130, 786 (1963) (4.65 BeV/c).

10. V. A. Belyakov, V. I. Veksler, N. M. Viryasov, E. N. Kladnitskaya, G. I. Kopylov, V. N. Penev, and M. I. Solov'ev, J. Nucl. Phys. (USSR) 1, 240 and 249 (1965) (7.5 BeV/c).

11. R. Ehrlich, W. Selove, and H. Yuta, Phys. Rev. 152, 1194 (1966). (7.91 BeV/c).

12. A. Bigi, S. Brandt, A. deMarco-Trabucco, Ch. Peyrou, R. Sosnowski, and A. Wróblewski, Nuovo Cimento 33, 1249 (1964) (10 BeV/c).

13. G. Alexander, L. Jacobs, G. R. Kalbfleisch, D. H. Miller, G. A. Smith, and J. Schwartz, in Proceedings of the 1962 International Conference on High-Energy Physics at CERN (CERN Scientific Information Service, Geneva, Switzerland, 1962), p. 320.

14. G. Alexander, G. R. Kalbfleisch, D. H. Miller, and G. A. Smith, Phys. Rev. Letters 8, 447 (1962).

15. G. Alexander, O. I. Dahl, L. D. Jacobs, G. R. Kalbfleisch, D. H. Miller, A. Rittenberg, J. Schwartz, and G. A. Smith, Phys. Rev. Letters 9, 460 (1962).

16. G. R. Kalbfleisch, G. Alexander, O. I. Dahl, D. H. Miller, A. Rittenberg, and G. A. Smith, Phys. Letters 4, 225 (1963).

17. G. A. Smith, J. Schwartz, D. H. Miller, G. R. Kalbfleisch, R. W. Huff, O. I. Dahl, and G. Alexander, Phys. Rev. Letters 10, 138 (1963).

18. D. H. Miller, G. Alexander, O. I. Dahl, L. Jacobs, G. R. Kalbfleisch, and G. A. Smith, Physics Letters 5, 279 (1963).

19. G. Alexander, O. Dahl, L. Jacobs, D. H. Miller, G. Kalbfleisch, J. Schwartz, and G. A. Smith, in Proceedings of the International Conference on Nucleon Structure, Stanford University, June 24-27, 1963, R. Hofstadter, Editor (Stanford University Press, Stanford, California, 1964), p. 390.

20. Gerald A. Smith, in Proceedings of the Athens Topical Conference on Recently Discovered Resonant Particles (Ohio University, Athens, Ohio, 1963), p. 67.

21. S. U. Chung, O. I. Dahl, L. M. Hardy, R. I. Hess, G. R. Kalbfleisch, J. Kirz, D. H. Miller, and G. A. Smith, Phys. Rev. Letters 12, 621 (1964).

22. R. I. Hess, S. U. Chung, O. I. Dahl, L. M. Hardy, J. Kirz, and D. H. Miller, Proceedings of the XII International Conference on High Energy Physics, Dubna, 1964, (Atomizdat, Moscow, 1966), p. 422.

23. L. M. Hardy, S. U. Chung, O. I. Dahl, R. I. Hess, J. Kirz, and D. H. Miller, in Proceedings of the XII International Conference on High Energy Physics, Dubna, 1964 (Atomizdat, Moscow, 1966), p. 705.

24. L. M. Hardy, S. U. Chung, O. I. Dahl, R. I. Hess, J. Kirz and D. H. Miller, Phys. Rev. Letters 14, 401 (1965).

25. D. H. Miller, S. U. Chung, O. I. Dahl, R. I. Hess, L. M. Hardy, J. Kirz, and W. Koellner, Phys. Rev. Letters 14, 1074 (1965).

26. S. U. Chung, O. I. Dahl, L. M. Hardy, R. I. Hess, L. D. Jacobs, J. Kirz, and D. H. Miller, Phys. Rev. Letters 15, 325 (1965).

27. R. I. Hess, O. I. Dahl, L. M. Hardy, J. Kirz, and D. H. Miller, Phys. Rev. Letters 17, 1109 (1966).

28. Joseph A. Schwartz, (Ph.D. thesis), Lawrence Radiation Laboratory report UCRL-11360, June 1964, (unpublished).

29. Joseph A. Schwartz, Strange Particle Cross Sections in $\pi 72$, Alvarez Group Internal Note No. 526, September 1964 (unpublished).

30. O. I. Dahl, L. M. Hardy, R. I. Hess, J. Kirz, D. H. Miller, and J. Schwartz, Phys. Rev. (following paper); Lawrence Radiation Laboratory report UCRL-17217, January 1967 (unpublished).

31. A. H. Rosenfeld and W. E. Humphrey, Ann. Rev. Nucl. Sci. 13, 103 (1963).

32. These events were not used for the study of the $\Sigma^0 K^0$ final state.

33. G. R. Lynch, Lawrence Radiation Laboratory Report UCRL-10335, July 1962 (unpublished).

34. A. N. Diddens, E. W. Jenkins, T. F. Kycia, and K. F. Riley, Phys. Rev. Letters 10, 262 (1963).

35. A. Citron, W. Galbraith, T. F. Kycia, B. A. Leontić, R. H. Phillips, and A. Rousset, Phys. Rev. Letters 13, 205 (1964). See also Phys. Rev. 144, 1101 (1966).

36. L. Jacobs (Ph. D. thesis), Lawrence Radiation Laboratory Report UCRL-16877, August 1966 (unpublished).

37. For details see R. I. Hess, (Ph. D. Thesis) UCRL-16832, June 1966 (unpublished).

38. In order to improve statistics, for the $NK\bar{K}$ final states we expanded the lowest momentum interval to 1.6 to 2.4 BeV/c for $nK_1^0K_1^0$ and pK^0K^-, and to 1.5 to 2.3 BeV/c for nK^+K^-.

39. J. Friedman and R. Ross, Maximum Likelihood Estimate of Resonant State Production in Multiparticle Final States, Alvarez Group Internal Note No. P-102, October 1964 (unpublished).

40. The $\Sigma^0K^+\pi^-$ and $\Lambda K^+\pi^-$ final states were used only if a $\Lambda \rightarrow p\pi^-$ decay was observed; the pK^0K^- final states were used only if a $K_1^0 \rightarrow \pi^+\pi^-$ decay was observed.

41. R. H. Dalitz and S. F. Tuan, Phys. Rev. Letters 2, 425 (1959).

42. R. D. Tripp, M. B. Watson and M. Ferro-Luzzi, Phys. Rev. Letters 8, 175 (1962); M. B. Watson, M. Ferro-Luzzi, and R. D. Tripp, Phys. Rev. 131, 2248 (1963).

43. R. D. Tripp (Lawrence Radiation Laboratory), private communication.

44. L. Stodolsky and J. J. Sakurai, Phys. Rev. Letters 11, 90 (1963).

45. L. Stodolsky, Phys. Rev. 134, B1099 (1964).

46. H. DeStaebler Jr., E. F. Erickson, A. C. Hearn, and C. Schaerf, Phys. Rev. 140, B336 (1965).

47. G. R. Lynch, M. Ferro-Luzzi, R. George, Y. Goldschmidt-Clermont, V. P. Henri, B. Jongejans, D. W. G. Leith, F. Muller, and J. M. Perreau, Phys. Letters 9, 359 (1964).

48. R. Barloutaud, A. Leveque, C. Louedec, J. Meyer, P. Schlein, A. Verglas, J. Badier, M. Demoulin, J. Goldberg, B. P. Gregory, P. Krejbich, C. Pelletier, M. Ville, E. S. Gelesema, J. Hoogland, J. C. Kluyver, and A. G. Tenner, Phys. Letters 12, 352 (1964).

49. J. H. Friedman and R. R. Ross, Phys. Rev. Letters 16, 485 (1966).

50. For a recent review see J. D. Jackson, Peripheral Collisions at Intermediate Energies in Proceedings of the XIIIth International Conference on High Energy Physics Berkeley, 1966 (University of California Press, Berkeley, 1967).

51. See for example J. D. Jackson, Rev. Mod. Phys. 37, 484 (1965).

52. K. Gottfried and J. D. Jackson, Nuovo Cimento 34, 735 (1964).

53. J. D. Jackson, J. T. Donohue, K. Gottfried, R. Keyser, and B. E. Y. Svensson, Phys. Rev. 139, B428 (1965).

54. S. M. Flatté (Ph. D. thesis), Lawrence Radiation Laboratory Report UCRL-16648, March 1966 (unpublished).

55. R. Huff (Department of Physics, University of California at Los Angeles), private communication.

56. J. B. Bronzan and F. E. Low, Phys. Rev. Letters 12, 522 (1964).

57. N. Haque et al., Birmingham-Glasgow-London (I. C.), -Oxford-Rutherford Laboratory Collaboration, Phys. Letters 14, 338 (1965); S. Forcardi, A. Minguzzi-Ranzi, P. Serra, L. Monari, S. Herrier, and A. Verglas, Phys. Letters 16, 351 (1965).

58. For a recent review see G. Goldhaber, Boson Resonances in Proceedings of the XIIIth International Conference on High Energy Physics Berkeley, 1966 (University of California Press, Berkeley, 1967).

59. S. U. Chung, O. I. Dahl, L. M. Hardy, R. I. Hess, J. Kirz, and D. H. Miller, Phys. Rev. Letters 18, 100 (1967).

60. S. U. Chung (Ph. D. thesis), Lawrence Radiation Laboratory Report UCRL-16881, July 1966 (unpublished)

61. Aachen-Berlin-Birmingham-Bonn-Hamburg-London (I. C.)-München Collaboration, Phys. Letters 10, 226 (1964).

62. We have used a mass of 1080 MeV and a width of 125 MeV for the A_1.

63. M. Goldhaber, T. D. Lee, and C. N. Yang, Phys. Rev. 112, 1796 (1958).

64. S. U. Chung, M. Neveu-René, O. I. Dahl, J. Kirz, D. H. Miller, and Z. G. T. Guiragossian, Phys. Rev. Letters 16, 481 (1966).

65. V. E. Barnes, B. B. Culwick, P. Guidoni, G. R. Kalbfleisch, G. W. London, R. B. Palmer, D. Radojičić, D. C. Rahm, R. R. Rau, C. R. Richardson, N. P. Samios, J. R. Smith, B. Goz, N. Horwitz, T. Kikuchi, J. Leitner, and R. Wolfe, Phys. Rev. Letters 15, 322 (1965).

66. We have used a mass of 1500 MeV and a width of 80 MeV for the f'.

67. A. R. Erwin, G. A. Hoyer, R. H. March, W. D. Walker, and T. P. Wangler, Phys. Rev. Letters 9, 34 (1962).

68. D. J. Crennell, G. R. Kalbfleisch, K. W. Lai, J. M. Scarr, T. G. Schumann, I. O. Skillicorn, and M. S. Webster, Phys. Rev. Letters 16, 1025 (1966).

69. W. Beusch et al., ETH Zurich-CERN Collaboration, Resonances in the K_1K_1 System Produced in $\pi^- p \to K^0\overline{K^0}n$ at 5, 7, and 12 GeV/c, presented at the XIII International Conference on High-Energy Physics, Berkeley, 1966. (Proceedings to be published

by University of California Press, Berkeley).

70. L. Lander, M. Abolins, D. D. Carmony, T. Hendricks, N-h Xuong, and P. M. Yager, Phys. Rev. Letters 13, 346 (1964).

71. For a review on this formalism see R. H. Dalitz, Strange Particles and Strong Interactions (Oxford University Press, London, 1962), p. 60.

72. G. F. Chew and F. E. Low, Phys. Rev. 113, 1640 (1959).

73. We find that between $a_0 = 1.5$ fermis and $a_0 = 10.0$ fermis we get a reasonable fit to the data if b_0 is chosen so that $(a_0^2 - 4.65\, a_0 + 16.7)/b_0$ is between 50 and 100 fermis.

74. The slope of this curve is insensitive to the choice of a_0 and b_0. We have used $a_0 = 2.0$ fermis and $b_0 = 0.12$ fermis for the curve which is shown. The structure in the curve comes from combining data at several momenta.

75. J. S. Lindsey and G. A. Smith, Phys. Rev. 147, 914 (1966).

76. R. Armenteros, D. N. Edwards, T. Jacobsen, L. Montanet, J. Vandermeulen, Ch. D'Andlau, A. Astier, P. Baillon, J. Cohen-Ganouna, C. Defoix, J. Siaud, and P. Rivet, Phys. Letters 17, 344 (1965).

77. C. Baltay, J. Lach, J. Sandweiss, H. D. Taft, N. Yeh, D. L. Stonehill, and R. Stump, Phys. Rev. 142, 932 (1966).

78. A compilation is made by A. H. Rosenfeld, in Supplement to the Proceedings of the Oxford International Conference on Elementary Particles, Sept. 19-25, 1965, (Rutherford High-Energy Laboratory, Chilton, England, 1966). See also Lawrence Radiation Laboratory Report UCRL-16462, September 1965.

79. The ϕ meson has not been previously observed in $\pi^- p$ interactions because the $nK_1^0K_2^0$ final state is rarely analyzable, and the nK^+K^- final state is difficult to identify due to the long mean lives of the K_2^0 and $K^\pm$ respectively.

80. It is known that ρ exchange is considerably modified by absorption in the reaction $\pi^+ n \rightarrow p\omega$. A discussion and references are given in Ref. 53.

81. R. Kraemer, L. Madansky, M. Meer, M. Nussbaum. A. Pevsner, C. Richardson, R. Strand, R. Zdanis, T. Fields, S. Orenstein, and T. Toohig, Phys. Rev. 136, B496 (1964).

82. T. C. Bacon, W. J. Fickinger, D. G. Hill, H. W. K. Hopkins, D. K. Robinson, and E. O. Salant, in Proceedings of the Second Topical Conference on Resonant Particles, Athens, Ohio, 1965 (University of Ohio, Athens, Ohio, 1965) p. 129.

83. H. O. Cohn, W. M. Bugg, and G. T. Condo, Phys. Letters 15, 344 (1965).

84. A. Forino et al., Bologna-Bari-Firenze-Orsay-Saclay Collaboration, Phys. Letters 19, 68 (1965).

85. G. H. Trilling, J. L. Brown, G. Goldhaber, S. Goldhaber, J. A. Kadyk, and J. Scanio, Phys. Letters 19, 427 (1965).

86. M. Abolins, R. L. Lander, W. A. W. Mehlhop, N-h. Xuong, and P. M. Yager, Phys. Rev. Letters 11, 381 (1963).

87. Y. Y. Lee, W. D. C. Moebs, Jr., B. P. Rose, D. Sinclair, and J. C. Vander Velde, Phys. Rev. Letters 11, 508 (1963).

88. The fitting procedure is explained in Sec. IV A.

89. M. Month, Phys. Letters 18, 357 (1965).

90. T. P. Wangler, A. R. Erwin, and W. D. Walker, Phys. Letters 9, 71 (1964).

91. D. H. Miller, A. Z. Kovacs, R. L. McIlwain, T. R. Palfrey, and G. W. Tautfest, Phys. Letters 15, 74 (1965).

92. R. Böck, B. R. French, J. B. Kinson, V. Šimak, J. Badier, M. Bazin, B. Equer, A. Rougé, and P. Grieve, Phys. Letters 12, 65 (1964).

93. S. P. Almeida, H. W. Atherton, T. A. Byer, P. J. Dornan, A. G. Forson, J. H. Scharenguivel, D. M. Sendall, and B. A. Westwood, Phys. Letters 16, 184 (1965).

94. B. C. Shen, I. Butterworth, C. Fu, G. Goldhaber, S. Goldhaber, and G. H. Trilling, Phys. Rev. Letters 17, 726 (1966).

95. M. Derrick, W. A. Cooper, L. Hyman, J. Loken, T. Fields, F. Schweingruber, R. Ammar, R. Davis, W. Kropac, and J. Mott, Bull. Am. Phys. Soc. 11, 76 (1966).

96. R. Armenteros, D. N. Edwards, T. Jacobsen, L. Montanet, A. Shapira, J. Vandermeulen, Ch. D'Andlau, A. Astier, P. Baillon, J. Cohen-Ganouna, C. Defoix, J. Siaud, C. Ghesquiere, and P. Rivet, Phys. Letters 9, 207 (1964).

97. N. Barash, J. Steinberger, T. H. Tan, L. Kirsch, and P. Franzini, in Proceedings of the Twelfth International Conference on High Energy Physics, Dubna, 1964 (Atomizdat, Moscow, 1966) p. 587.

98. The $Y_1^*(1385)$ band is defined by $1350 \leq M(\Lambda\pi) \leq 1410$ MeV.

99. The $K^*(890)$ band is defined by $861 \leq M(K\pi) \leq 921$ MeV.

100. R. Armenteros, D. N. Edwards, T. Jacobsen, L. Montanet, J. Vandermeulen, Ch. d'Andlau, A. Astier, P. Baillon, J. Cohen-Ganouna, C. Defoix, J. Siaud, and P. Rivet, Proceedings of the International Conference on High Energy Physics, Dubna, 1964

(Atomizdat, Moscow, 1966) p. 577; also CERN - College de France-Institut du Radium Collaboration, Further Study of the E. Meson In Antiproton-Proton Annihilations at Rest, presented at the XIII International Conference on High-Energy Physics Berkeley, 1966; proceedings to be published by University of California Press, Berkeley.

101. Ch. D'Andlau, A. Astier, M. Dall Negra, L. Dobrzynski, S. Wojcicki, J. Barlow, T. Jacobsen, L. Montanet, L. Tallone, M. Thomas, A-M. Adamson, M. Baubillier, J. Duboc, M. Goldberg, E. Levy, D. N. Edwards and J. E. A. Lys, Phys. Letters 17, 347 (1965).

102. E. Abers, Phys. Rev. Letters 12, 55 (1964).

103. R. H. Capps and J. G. Koerner, Phys. Rev. Letters 15, 320 (1965).

104. M. Ferro-Luzzi, R. George, Y. Goldschmidt-Clermont, V. P. Henri, B. Jongejans, D. W. G. Leith, G. R. Lynch, F. Muller, and J. M. Perreau, Phys. Letters 17, 155 (1965). Evidence against S = 2 mesons has been presented by A. R. Erwin, W. D. Walker, and A. Weinberg, Phys. Rev. Letters 16, 1063 (1966) and T. Joldersma, R. B. Palmer, and N. P. Samios, Phys. Rev. Letters 17, 716 (1966).

105. C. R. Richardson, V. E. Barnes, D. J. Crennell, B. B. Culwick, W. B. Fowler, N. Horwitz, J. Leitner, G. W. London, R. B. Palmer, D. Radojicic, D. C. Rahm, N. P. Samios, and J. R. Smith, Bull. Am. Phys. Soc. 10, 115 (1965).

106. W. S. C. Williams, Introduction to Elementary Particles (Academic Press, New York, 1961) p. 172.

107. U. Fano, Rev. Mod. Phys. 29, 74 (1957).

108. It should be borne in mind that the elements of the density matrix depend on the production variables. We have made a fit only to the averages of these elements.

109. S. M. Berman and R. J. Oakes, Phys. Rev. 135, B1034 (1964).

110. N. Byers and H. Burkhardt, Phys. Rev. 121, 281 (1961).

111. J. D. Jackson and H. Pilkuhn, Nuovo Comento 33, 906 (1964).

112. C. Zemach, Phys. Rev. 133, B1201 (1964).

113. Here we use the notation $V_\mu = (V_0, \underset{\sim}{V})$ and $V^\mu = \sum_0^3 g^{\mu\nu} V_\nu$, where

$$g_{\mu\nu} = g^{\mu\nu} = \begin{pmatrix} 1 & 0 & 0 & 0 \\ 0 & -1 & 0 & 0 \\ 0 & 0 & -1 & 0 \\ 0 & 0 & 0 & -1 \end{pmatrix}$$

Any repeated indices are summed over $A_\mu B^\mu = A_0 B_0 - \underset{\sim}{A} \cdot \underset{\sim}{B}$. Here we also let the name of the particle stand for its 4-momentum.

114. $\mathcal{E}_\mu$ is used when we assume spin one, and $\mathcal{E}_{\mu\nu}$ is used when we assume spin two for the decaying particle.

Table I. Number of events of each topology found at momentum intervals covered by this experiment.

Topology[a]	Incident-pion momentum (BeV/c)		
	1.4 to 2.4	2.5 to 3.4	3.7 to 4.3
a	9166	4458	1264
b	4512	5417	2499
c	0	127	180
d	3327	1597	430
e	139	579	312
f	493	458	151
g	0	8	11
h	915	607	179
i	0	11	21
j	923	523	588
k	13	228	189
l	6363	2340	657
m	58	452	339
Total	25909	16805	6820

a See Fig. 1.

Table II. Hypotheses we attempted to fit.

Final state	Topology[a]	Production constraint class	Total constraint class
Two body			
$\Sigma^0 K^0; K^0 \to \pi^+\pi^-$	a	1	4
$\Sigma^0 K^0, \Sigma^0 \to \Lambda+\gamma; K^0 \to \pi^+\pi^-, \Lambda \to p\pi^-$	d	2	8
$\Sigma^- K^+, \Sigma^- \to n\pi^-$	l	4	4
$\Lambda K^0, K^0 \to \pi^+\pi^-, \Lambda \to p\pi^-$	d	4	10
$\Lambda K^0; \Lambda \to p\pi^-$	a	1	4
$\Lambda K^0; K^0 \to \pi^+\pi^-$	a	1	4
Three body			
$\Sigma^+ K^0 \pi^-, \Sigma^+ \to \begin{matrix} p\pi^0 \\ n\pi^+ \end{matrix}; K^0 \to \pi^+\pi^-$	f	4[b]	7
$\Sigma^+ K^0 \pi^-, \Sigma^+ \to \begin{matrix} p\pi^0 \\ n\pi^+ \end{matrix}$	j	1	1
$\Sigma^0 K^+ \pi^-, \Sigma^0 \to \Lambda+\gamma; \Lambda \to p\pi^-$	b, f	2	5
$\Sigma^0 K^+ \pi^-$	j	1	1
$\Sigma^- K^+ \pi^0, \Sigma^- \to n\pi^-$	l	1	1
$\Sigma^- K^0 \pi^+, \Sigma^- \to n\pi^-; K^0 \to \pi^+\pi^-$	h	4	7
$\Sigma^- K^0 \pi^+, \Sigma^- \to n\pi^-$	l	1	1
$\Lambda K^+ \pi^-; \Lambda \to p\pi^-$	b	4	7
$\Lambda K^+ \pi^-$	j	1	1
$\Lambda K^0 \pi^0; \Lambda \to p\pi^-, K^0 \to \pi^+\pi^-$	d	1	7
$\Lambda mm^c; \Lambda \to p\pi^-$	a	0	3
$K^0 mm; K^0 \to \pi^+\pi^-$	a	0	3

Table II. (continued)

Final state	Topology[a]	Production constraint class	Total constraint class
Three body (cont)			
$pK^0K^-;K^0\to\pi^+\pi^-$	b, h	4	7
pK^0K^-	l	1	1
nK^+K^-	j, l	1	1
$nK^0\overline{K}^0;K^0\to\pi^+\pi^-,\overline{K}^0\to\pi^+\pi^-$	d	1	7
Four body			
$\Sigma^+K^+\pi^-\pi^-,\Sigma^+\to\begin{cases}p\pi^0\\n\pi^+\end{cases}$	k	4	4
$\Sigma^+K^0\pi^0\pi^-,\Sigma^+\to\begin{cases}p\pi^0\\n\pi^+\end{cases}$ $K^0\to\pi^+\pi^-$	f	1	4
$\Sigma^0K^0\pi^+\pi^-,\Sigma^0\to\Lambda\gamma;$ $\Lambda\to p\pi^-,K^0\to\pi^+\pi^-$	e	2	8
$\Sigma^0K^0\pi^+\pi^-;K^0\to\pi^+\pi^-$	b	1	4
$\Sigma^-K^+\pi^+\pi^-,\Sigma^-\to n\pi^-$	m	4	4
$\Sigma^-K^0\pi^+\pi^0,\ \Sigma^-\to n\pi^-;K^0\to\pi^+\pi^-$	h	1	4
$\Sigma^+\pi^-mm;\Sigma^+\to\begin{cases}p\pi^0\\n\pi^+\end{cases}$	j	0	1
$\Sigma^-\pi^+mm;\Sigma^-\to n\pi^-$	l	0	1
$\Sigma^-K^+mm;\ \Sigma^-\to n\pi^-$	l	0	1
$\Lambda K^+\pi^0\pi^-;\Lambda\to p\pi^-$	b, f	1	4
$\Lambda K^0\pi^+\pi^-;\Lambda\to p\pi^-,K^0\to\pi^+\pi^-$	e	4	10
$\Lambda K^0\pi^+\pi^-;\Lambda\to p\pi^-$	b	1	4
$\Lambda K^0\pi^+\pi^-;K^0\to\pi^+\pi^-$	b	1	4

Table II. (continued)

Final state	Topology[a]	Production constraint class	Total constraint class
Four body (cont)			
$\Lambda K^0 mm; \Lambda \to p\pi^-, K^0 \to \pi^+\pi^-$	e	0	6
$K^+\pi^- mm$	j	0	0
$K^-\pi^+ mm$	l	0	0
$pK^+K^-\pi^-$	k, m	4	4
$pK^0\bar{K}^0\pi^-; K^0 \to \pi^+\pi^-, \bar{K}^0 \to \pi^+\pi^-$	e	4	10
$pK^0\bar{K}^0\pi^-; K^0 \to \pi^+\pi^-$	b	1	4
$pK^0K^-\pi^0; K^0 \to \pi^+\pi^-$	b, h	1	4
$nK^+\bar{K}^0\pi^-; \bar{K}^0 \to \pi^+\pi^-$	b, f	1	4
$nK^0K^-\pi^+; K^0 \to \pi^+\pi^-$	b, h	1	4
$pK^- mm$	l	0	0
$K^+K^- mm$	j, l	0	0
$K^0\bar{K}^0 mm; K^0 \to \pi^+\pi^-; \bar{K}^0 \to \pi^+\pi^-$	e	0	6
Five body			
$\Sigma^+K^+\pi^0\pi^-\pi^-, \Sigma^+ \to \begin{cases} p\pi^0 \\ n\pi^+ \end{cases}$	k	1	1
$\Sigma^+K^0\pi^+\pi^-\pi^-; \Sigma^+ \to \begin{cases} p\pi^0 \\ n\pi^+ \end{cases}, K^0 \to \pi^+\pi^-$	g	4	8
$\Sigma^+K^0\pi^+\pi^-\pi^-; \Sigma^+ \to \begin{cases} p\pi^0 \\ n\pi^+ \end{cases}$	k	1	2
$\Sigma^0K^+\pi^+\pi^-\pi^-; \Sigma^0 \to \Lambda\gamma, \Lambda \to p\pi^-$	c, g	1	5
$\Sigma^0K^+\pi^-\pi^-\pi^-$	k	1	1
$\Sigma^-K^+\pi^+\pi^0\pi^-; \Sigma^- \to n\pi^-$	m	1	2
$\Sigma^-K^0\pi^+\pi^+\pi^-; K^0 \to \pi^+\pi^-, \Sigma^- \to n\pi^-$	i	4	8

Table II. (continued)

Final state	Topology[a]	Production constraint class	Total constraint class
Five body (cont)			
$\Sigma^- K^0 \pi^+ \pi^+ \pi^-; \Sigma^- \to n\pi^-$	m	1	2
$\Sigma^+ K^0 \pi^- mm; \Sigma^+ \to \begin{cases} p\pi^0 \\ n\pi^+ \end{cases}, K^0 \to \pi^+\pi^-$	f	0	4
$\Sigma^- K^0 \pi^+ mm; \Sigma^- \to n\pi^-, K^0 \to \pi^+\pi^-$	h	0	4
$\Lambda K^+ \pi^+ \pi^- \pi^-; \Lambda \to p\pi^-$	c	4	7
$\Lambda K^+ \pi^+ \pi^- \pi^-$	g, k	1	1
$\Lambda K^0 \pi^+ \pi^- \pi^0; \Lambda \to p\pi^-, K^0 \to \pi^+\pi^-$	e	1	7
$\Lambda K^+ \pi^- mm; \Lambda \to p\pi^-$	b, f	0	3
$K^+ K^0 \pi^- mm; K^0 \to \pi^+\pi^-$	b, f	0	3
$\Lambda \pi^+ \pi^- mm; \Lambda \to p\pi^-$	b	0	3
$K^0 K^- \pi^+ mm; K^0 \to \pi^+\pi^-$	b, h	0	3
$pK^+ K^0 \pi^- \pi^-; K^0 \to \pi^+\pi^-$	c, g	4	7
$pK^+ K^0 \pi^- \pi^-$	k, m	1	1
$pK^+ K^- \pi^0 \pi^-$	k, m	1	1
$pK^0 K^- \pi^+ \pi^-; K^0 \to \pi^+\pi^-$	c, j	4	7
$pK^0 \bar{K}^0 \pi^0 \pi^-; K^0 \to \pi^+\pi^-, \bar{K}^0 \to \pi^+\pi^-$	e	1	7

Table II. (continued)

Final state	Topology[a]	Production constraint class	Total constraint class
Five body (continued)			
$pK^0\pi^-mm; K^0 \rightarrow \pi^+\pi^-$	b	0	3
$pK^0K^-mm; K^0 \rightarrow \pi^+\pi^-$	b, h	0	3
$nK^+K^-\pi^+\pi^-$	k, m	1	1
$nK^0\overline{K^0}\pi^+\pi^-; K^0 \rightarrow \pi^+\pi^-, \overline{K^0} \rightarrow \pi^+\pi^-$	e	1	7
Six body			
$\Lambda K^0\pi^+\pi^-mm; \Lambda \rightarrow p\pi^-, K^0 \rightarrow \pi^+\pi^-$	e	0	6

[a]See Fig. 1.

[b]Measured momentum of Σ not used.

[c]mm indicates two or more unobserved neutrals.

Table III. Final status of strange-particle events.

	Unmeasured	Rejected	Failing	Passing
Fraction	0.04	0.18	0.04	0.74

Table IV. The amount of film analyzed in units of microbarns per event for each momentum interval.

Momentum interval (BeV/c)	μb per event
The π 63 exposure	
1.590 to 1.640	0.411 ± 0.053
1.915 to 1.960	0.260 ± 0.020
1.960 to 2.015	0.352 ± 0.055
2.015 to 2.080	0.200 ± 0.016
2.080 to 2.190	1.19 ± 0.13
2.580 to 2.630	0.339 ± 0.029
2.825 to 2.895	0.959 ± 0.081
2.960 to 3.065	0.387 ± 0.036
3.065 to 3.175	0.287 ± 0.020
3.175 to 3.245	0.148 ± 0.008
3.840 to 3.930	0.398 ± 0.040
4.130 to 4.190	0.323 ± 0.028
The π 72 exposure[a]	
1.45 to 1.55	0.664
1.62 to 1.76	0.457
1.80 to 1.90	0.522
1.90 to 2.00	0.441

The π 72 exposure (continued)	
2.00 to 2.10	0.947
2.10 to 2.20	0.354
2.20 to 2.31	0.333
2.31 to 2.41	0.683

[a]Ref. 28.

Table V. Assignment of events from conflict analysis.[a]

	Scan 1				
Scan 2	Good event	Good event, wrong topology assigned	Good event, not found	Reject event	Reject event, not found
Good event	X	6	2	X	X
Good event, wrong topology assigned	5	X	4	X	X
Good event, not found	1	3	X	X	X
Reject event	X	X	X	X	8
Reject event, not found	X	X	X	7	X

[a]Numbers given for classes are described in text.

Table VI. Scanning efficiencies for each topology.

Topology[a]	Scan 1		Scan 2	
	Correct (P_{c1})	Misidentified (P_{m1})	Correct (P_{c2})	Misidentified (P_{m2})
a	0.918 ± 0.005	0.012 ± 0.002	0.921 ± 0.005	0.016 ± 0.002
b	0.924 ± 0.005	0.010 ± 0.002	0.921 ± 0.005	0.014 ± 0.002
c	0.924 ± 0.025	0.035 ± 0.016	0.944 ± 0.021	0.029 ± 0.015
d	0.936 ± 0.008	0.047 ± 0.007	0.926 ± 0.009	0.055 ± 0.008
e	0.898 ± 0.021	0.089 ± 0.020	0.881 ± 0.023	0.096 ± 0.021
f	0.871 ± 0.027	0.102 ± 0.023	0.817 ± 0.031	0.119 ± 0.025
g[b]	- -	- -	- -	- -
h	0.905 ± 0.016	0.072 ± 0.015	0.868 ± 0.014	0.120 ± 0.013
i[b]	- -	- -	- -	- -
j	0.849 ± 0.016	0.008 ± 0.004	0.875 ± 0.014	0.011 ± 0.004
k	0.932 ± 0.022	0.006 ± 0.008	0.919 ± 0.026	0.011 ± 0.004
l	0.881 ± 0.008	0.005 ± 0.002	0.897 ± 0.008	0.010 ± 0.002
m	0.972 ± 0.010	0.023 ± 0.009	0.937 ± 0.018	0.022 ± 0.014

[a] See Fig. 1.

[b] There were too few events with these topologies to obtain statistically significant values. For cross-section calculations the values for topologies k and m were used.

Table VII. Cross sections for strange-particle production.

A. Two-, three-, and four-body final states

Final state	Incident-beam momentum[a] (BeV/c)																							
	1.50[b]			1.59[c]			1.615			1.69[b]			1.85[b]			1.94			1.95[b]			1.98		
	σ	dσ	Events	σ	dσ	Events	σ	dσ	Events	σ	dσ	Events	σ	dσ	Events	σ	dσ	Events	σ	dσ	Events	σ	dσ	Events
ΛK^0	334	19	308	214	21	106	208	25	286	199	12	263	181	12	215	185	15	436	182	11	255	184	20	299
$\Sigma^0 K^0$	167	22	59	178	22	65	111	20	70	110	14	58	140	17	66	126	15	127	94	13	53	116	15	87
$\Sigma^- K^+$	242	14	293	262	16	285	180	22	319	153	9	266	99	8	153	98	10	281	99	7	182	90	10	191
$\Sigma^+ K^0 \pi^-$	3.4	1.9	3	10	3	10	17.2	5.3	13	19.3	3.9	25	34	5	39	41	7	51	31	5	42	44	9	39
$\Sigma^0 K^+ \pi^-$	7.1	2.9	6	15	4	13	13.8	3.5	22	11.1	3.0	14	30	5	32	62	7	146	67	7	86	56	10	105
$\Sigma^- K^+ \pi^0$	8.9	2.7	11	15	4	15	13.2	3.1	21	21	3	37	38	5	61	51	6	147	44	5	83	50	9	107
$\Sigma^- K^0 \pi^+$	11.5	3.2	13	21	5	22	22	4	38	52	6	87	63	7	94	110	9	308	94	7	161	100	13	206
$\Lambda K^+ \pi^-$	64	9	54	75	10	61	86	13	127	76	8	95	96	10	103	140	13	317	104	9	133	143	23	248
$\Lambda K^0 \pi^0$	56	16	12	180	26	49	91	22	35	123	20	39	192	27	52	155	26	97	171	23	58	163	36	77
$pK^0 K^-$	-	-	-	2	2	1	1.6	1.6	1	11.8	5.3	5	42	10	16	30	6	30	38	9	18	31	8	24
$nK^+ K^-$	-	-	-	11	6	3	-	(e)	-	-	-	-	-	-	-	-	(e)	-	-	-	-	39	10	86
$nK^0_1 K^0_1$	-	-	-	10	4	6	4.3	2.6	3	12.9	5.0	7	7.1	3.5	4	10.8	3.1	13	15.6	5.0	10	21	6	19
$\Sigma^+ K^+ \pi^- \pi^-$	-	-	-	-	-	-	-	-	-	-	-	-	-	-	-	-	-	-	-	-	-	-	-	-
$\Sigma^+ K^0 \pi^0 \pi^-$	-	-	-	-	-	-	-	-	-	-	-	-	-	-	-	-	-	-	-	-	-	-	-	-
$\Sigma^0 K^0 \pi^+ \pi^-$	-	-	-	-	-	-	-	-	-	-	-	-	-	-	-	-	-	-	-	-	-	-	-	-
$\Sigma^- K^+ \pi^+ \pi^-$	-	-	-	-	-	-	-	-	-	-	-	-	-	-	-	-	-	-	-	-	-	-	-	-
$\Sigma^- K^0 \pi^+ \pi^0$	-	-	-	-	-	-	-	-	-	-	-	-	-	-	-	-	-	-	-	-	-	-	-	-
$\Lambda K^+ \pi^0 \pi^-$	-	-	-	-	-	-	1.4	1.4	1	0.8	0.8	1	7.2	2.6	8	8.0	2.0	17	7.6	2.4	10	10.1	2.9	16
$\Lambda K^0 \pi^+ \pi^-$	-	-	-	-	-	-	1.1	1.1	1	1.7	1.2	2	5.3	2.2	6	9.9	2.3	24	15.7	3.4	21	11.6	3.1	19
$nK^+ \bar{K}^0 \pi^-$	-	-	-	-	-	-	-	-	-	-	-	-	-	-	-	-	-	-	-	-	-	1.3	1.3	1
$nK^0 K^- \pi^+$	-	-	-	-	-	-	-	-	-	-	-	-	-	-	-	-	-	-	-	-	-	-	-	-
$pK^0_1 K^0_1 \pi^-$	-	-	-	-	-	-	-	-	-	-	-	-	-	-	-	-	-	-	-	-	-	-	-	-
$pK^0_1 K^0_2 \pi^-$	-	-	-	-	-	-	-	-	-	-	-	-	-	-	-	-	-	-	-	-	-	-	-	-
$pK^0 K^- \pi^0$	-	-	-	-	-	-	-	-	-	-	-	-	-	-	-	-	-	-	-	-	-	-	-	-
$pK^+ K^- \pi^-$	-	-	-	-	-	-	-	-	-	-	-	-	-	-	-	-	-	-	-	-	-	-	-	-

UCRL-16978

Final state	Incident-beam momentum (BeV/c)																							
	2.05[b]			2.05			2.14			2.15[b]			2.25[b]			2.35[b]			2.61			2.70[f]		
	σ	dσ	Events	σ	dσ	Events	σ	dσ	Events	σ	dσ	Events	σ	dσ	Events	σ	dσ	Events	σ	dσ	Events	σ	dσ	Events
ΛK^0	182	17	119	179	15	515	162	20	78	192	11	334	172	10	319	174	14	157	106	12	182	120	11	
$\Sigma^0 K^0$	123	21	33	113	18	153	100	20	23	114	13	82	105	12	80	113	18	41	81	12	66	85	12	
$\Sigma^- K^+$	70	9	60	87	8	327	39	10	25	65	5	148	57	5	138	53	7	63	30	5	67	31	5	
$\Sigma^+ K^0 \pi^-$	41	8	26	39	6	63	33	14	6	52	6	88	62	6	113	65	9	58	39	7	40	51	7	
$\Sigma^0 K^+ \pi^-$	68	11	40	66	7	213	63	13	38	78	7	123	87	7	147	82	10	68	53	8	94	75	9	
$\Sigma^- K^+ \pi^0$	51	8	44	52	6	196	44	10	28	51	5	118	56	5	141	59	7	71	35	5	81	40	6	
$\Sigma^- K^0 \pi^+$	120	12	97	123	9	452	110	16	70	133	8	286	144	8	337	138	11	158	65	7	149	118	10	
$\Lambda K^+ \pi^-$	170	17	101	152	14	442	116	20	55	118	9	187	106	8	176	145	14	116	115	13	203	97	10	
$\Lambda K^0 \pi^0$	182	34	29	164	26	139	88	28	13	174	21	73	131	17	61	187	29	42	91	18	47	132	18	
$pK^0 K^-$	40	13	9	35	6	46	30	12	7	33	8	20	70	11	44	77	16	23	52	9	43	81	13	
$nK^+ K^-$	-	-	-	-	(e)	-	-	(e)	-	-	-	-	-	-	-	-	-	-	-	-	-	84	47	
$nK^0_1 K^0_1$	23	9	7	16.1	3.5	26	28	11	8	21	5	17	33	7	27	38	9	16	30	6	29	33	7	
$\Sigma^+ K^+ \pi^- \pi^-$	-	-	-	3.2	1.4	6	-	-	-	-	-	-	-	-	-	-	-	-	7.5	2.8	8	14	3	
$\Sigma^+ K^0 \pi^0 \pi^-$	-	-	-	-	-	-	-	-	-	-	-	-	-	-	-	-	-	-	8.2	3.8	5	17	6	
$\Sigma^0 K^0 \pi^+ \pi^-$	-	-	-	3.9	2.3	3	-	-	-	-	-	-	-	-	-	-	-	-	9.9	4.5	12	32	7	
$\Sigma^- K^+ \pi^+ \pi^-$	-	-	-	2.6	0.8	11	4.2	2.5	3	-	-	-	-	-	-	-	-	-	10.3	2.2	26	12	3	
$\Sigma^- K^0 \pi^+ \pi^0$	-	-	-	1.7	1.2	2	-	-	-	-	-	-	-	-	-	-	-	-	11.5	4.2	8	22	7	
$\Lambda K^+ \pi^0 \pi^-$	19	6	11	12.4	2.4	38	10.5	4.8	5	21	4	32	38	5	66	40	7	33	57	8	96	77	9	
$\Lambda K^0 \pi^+ \pi^-$	21	6	13	22	3	62	9.9	5.1	8	48	5	80	46	5	81	74	9	64	59	7	104	83	9	
$nK^+ \bar{K}^0 \pi^-$	-	-	-	.73	.73	1	-	-	-	-	-	-	-	-	-	-	-	-	16.6	4.8	13	20	7	
$nK^0 K^- \pi^+$	-	-	-	-	-	-	-	-	-	-	-	-	-	-	-	-	-	-	14.0	4.4	11	9	5	
$pK^0_1 K^0_1 \pi^-$	-	-	-	-	-	-	-	-	-	-	-	-	-	-	-	-	-	-	2.1	1.6	2	4	2	
$pK^0_1 K^0_2 \pi^-$	-	-	-	-	-	-	2.5	2.5	1	-	-	-	-	-	-	-	-	-	3.1	1.4	4	2	2	
$pK^0 K^- \pi^0$	-	-	-	1.5	1.1	2	4.6	4.6	1	-	-	-	-	-	-	-	-	-	5.2	2.6	4	12	5	
$pK^+ K^- \pi^-$	-	-	-	-	-	-	-	-	-	-	-	-	-	-	-	-	-	-	3.0	2.6	2	12	9	

Table VII (continued).

Final state	Incident-beam momentum (BeV/c)																							
	2.75[g]			2.86			3.00[h]			3.01			3.13			3.21			3.89			4.00[d]		
	σ	dσ	Events	σ	dσ	Events	σ	dσ	Events	σ	dσ	Events	σ	dσ	Events	σ	dσ	Events	σ	dσ	Events	σ	dσ	Events
ΛK^0	90	25	18	109	15	59	31	14	5	84	12	111	94	12	170	87	10	301	67	12	86	-	(i)	-
$\Sigma^0 K^0$	95	25	19	93	25	26	86	25	14	74	12	52	41	10	39	50	6	91	37	8	22	-	(i)	-
$\Sigma^- K^+$	32	10	15	22	7	18	15	5	12	22	4	43	15.5	3.0	41	14.5	2.0	76	8.5	2.5	16	5.0	3.0	2
$\Sigma^+ K^0 \pi^-$	39	10	13	37	11	14	44	11	30	50	9	44	47	7	55	43	5	102	42	8	36	21	7	9
$\Sigma^0 K^+ \pi^-$	50	10	30	56	11	40	-	(j)	-	54	8	88	46	6	101	41	4	184	43	7	68	-	(k)	-
$\Sigma^- K^+ \pi^0$	64	8	30	27	6	21	48	9	41	40	6	79	29	4	77	28	3	147	34	5	65	12	5	5
$\Sigma^- K^0 \pi^+$	84	20	25	73	11	58	91	14	80	86	9	174	69	6	183	75	5	388	60	7	126	69	22	10
$\Lambda K^+ \pi^-$	117	20	71	138	20	85	-	(j)	-	114	14	171	97	10	188	95	8	371	99	13	138	-	(k)	-
$\Lambda K^0 \pi^0$	180	40	36	128	32	23	-	(m)	-	121	24	53	76	15	46	97	15	111	98	21	41	-	(n)	-
$pK^0 K^-$	78	16	26	90	20	25	66	16	24	85	14	61	54	8	53	63	7	118	80	13	57	98	25	15
$nK^+ K^-$	250	90	5	-	(p)	-	56	29	4	-	(p)	-	195	60	90	-	(p)	-	370	130	48	124	72	3
$nK_1^0 K_1^0$	27	9	12	58	14	21	52	13	19	40	8	36	49	7	59	45	5	108	42	8	37	44	15	8
$\Sigma^+ K^+ \pi^- \pi^-$	4	4	2	-	-	-	15	6	10	13.8	4.1	13	8	3	11	16	3	40	24	6	21	7	4	3
$\Sigma^+ K^0 \pi^0 \pi^-$	36	11	6	17.8	9.1	4	41	17	9	38	10	17	23	6	17	27	5	38	34	9	18	8	8	1
$\Sigma^0 K^0 \pi^+ \pi^-$	20	6	15	-	-	-	86	19	26	41	11	29	30	8	38	17	4	64	38	11	55	-	(q)	-
$\Sigma^- K^+ \pi^+ \pi^-$	30	6	14	18.3	4.8	16	29	7	24	14.5	2.9	32	17	3	50	17	2	101	20	4	43	24	8	10
$\Sigma^- K^0 \pi^+ \pi^0$	10	5	3	25	10	6	33	11	10	29	8	18	32	7	25	30	5	47	30	8	19	71	25	8
$\Lambda K^+ \pi^0 \pi^-$	86	15	52	65	11	38	-	(r)	-	86	11	124	74	8	144	93	8	350	103	13	142	-	(s)	-
$\Lambda K^0 \pi^+ \pi^-$	97	15	71	93	15	57	72	17	61	113	12	167	84	8	166	104	8	403	122	14	181	-	(q)	-
$nK^+ K^0 \pi^-$	24	7	8	39	13	10	7	5	2	37	8	26	31	6	28	45	6	79	74	15	45	78	23	12
$nK^0 K^- \pi^+$	18	7	6	21	9	6	18	8	5	31	7	21	23	5	21	36	5	67	71	14	44	01	25	17
$pK_1^0 K_1^0 \pi^-$		u		-	-	-	10	5	8	6.1	2.8	5	3.9	2.0	4	8.6	2.1	19	12	4	11	16	9	3
$pK_1^0 K_2^0 \pi^-$	-	u	-	9.0	5.0	4	9	4	6	13.4	3.8	15	21	4	34	14.2	2.7	43	32	6	35	20	10	11
$pK^0 K^- \pi^0$	30	10	10	25	10	7	32	11	9	28	7	20	23	5	22	35	5	68	35	8	25	64	21	9
$pK^+ K^- \pi^-$	-	-	-	21	13	5	28	20	2	25	13	12	27	10	13	38	10	39	63	20	19	05	52	4

UCRL-16978

Final state	Incident-beam momentum = 4.16 BeV/c		
	σ	dσ	Events
ΛK^0	49	9	75
$\Sigma^0 K^0$	42	8	30
$\Sigma^- K^+$	4.5	1.5	10
$\Sigma^+ K^0 \pi^-$	40	7	40
$\Sigma^0 K^+ \pi^-$	32	5	66
$\Sigma^- K^+ \pi^0$	28	4	66
$\Sigma^- K^0 \pi^+$	44	5	103
$\Lambda K^+ \pi^-$	88	11	151
$\Lambda K^0 \pi^0$	68	15	35
$pK^0 K^-$	54	9	47
$nK^+ K^-$	-	(t)	-
$nK_1^0 K_1^0$	32	6	36
$\Sigma^+ K^+ \pi^- \pi^-$	25	5	28
$\Sigma^+ K^0 \pi^0 \pi^-$	36	8	24
$\Sigma^0 K^0 \pi^+ \pi^-$	46	11	59
$\Sigma^- K^+ \pi^+ \pi^-$	20	3	53
$\Sigma^- K^0 \pi^+ \pi^0$	55	11	23
$\Lambda K^+ \pi^0 \pi^-$	108	12	184
$\Lambda K^0 \pi^+ \pi^-$	96	10	180
$nK^+ \bar{K}^0 \pi^-$	64	12	48
$nK^0 K^- \pi^+$	69	13	52
$pK_1^0 K_1^0 \pi^-$	18	5	19
$pK_1^0 K_2^0 \pi^-$	14	5	19
$pK^0 K^- \pi^0$	75	20	41
$pK^+ K^- \pi^-$	13	4	26

Footnotes to Table VII A.

a. The momentum bite is typically between ±0.03 and ±0.05 BeV/c.
b. Refs. 28 and 29.
c. Ref. 2.
d. Ref. 8.
e. Cross section from threshold to 2.3 BeV/c tabulated at 1.98 BeV/c.
f. Ref. 5.
g. Ref. 6.
h. Ref. 7.
i. Ref. 8 gives $\sigma_{\Lambda K^0} + \sigma_{\Sigma^0 K^0} = 93 \pm 14$ μb.
j. Ref. 7 gives $\sigma_{\Sigma^0 K^+ \pi^-} + \sigma_{\Lambda K^+ \pi^-} = 136 \pm 21$ μb with 80 events.
k. Ref. 8 gives $\sigma_{\Lambda K^+ \pi^-} + \sigma_{\Sigma^0 K^+ \pi^-} = 133 \pm 21$ μb with 39 events.
m. Ref. 7 gives $\sigma_{\Lambda K^0 \pi^0} + \sigma_{\Sigma^0 K^0 \pi^0} = 141 \pm 33$ μb with 23 events.
n. Ref. 8 gives $\sigma_{\Lambda K^0 \pi^0} + \sigma_{\Sigma^0 K^0 \pi^0} = 88 \pm 33$ μb with 7 events.
p. Cross section from 2.9 to 3.3 BeV/c tabulated at 3.13 BeV/c.
q. Ref. 8 gives $\sigma_{\Lambda K^0 \pi^+ \pi^-} + \sigma_{\Sigma^0 K^0 \pi^+ \pi^-} = 195 \pm 21$ μb with 78 events.
r. Ref. 7 gives $\sigma_{\Lambda K^0 \pi^+ \pi^-} + \sigma_{\Sigma^0 K^0 \pi^+ \pi^-} = 91 \pm 16$ μb with 49 events.
s. Ref. 8 gives $\sigma_{\Lambda K^+ \pi^- \pi^0} + \sigma_{\Sigma^0 K^+ \pi^- \pi^0} = 93 \pm 17$ μb with 30 events.
t. Cross section from 3.8 to 4.2 BeV/c tabulated at 3.89 BeV/c.
u. Ref. 6 gives $\sigma_{pK_1^0 K_1^0 \pi^-} + \sigma_{pK_1^0 K_2^0 \pi^-} = 16 \pm 6$ μb with 9 events.

B. Five-body final states

Final state	Incident beam momentum (BeV/c)					
	2.9-3.3			3.8-4.2		
	σ	dσ	Events	σ	dσ	Events
$\Sigma^+ K^+ \pi^0 \pi^- \pi^-$	1.7	0.4	16	5.3	1.2	22
$\Sigma^0 K^+ \pi^+ \pi^- \pi^-$	2.1	0.6	19	7.3	1.6	30
$\Sigma^- K^+ \pi^+ \pi^0 \pi^-$	5.5	0.8	61	16.2	2.2	78
$\Sigma^+ K^0 \pi^+ \pi^- \pi^-$	0.8	0.3	8	3.7	1.0	15
$\Sigma^- K^0 \pi^+ \pi^+ \pi^-$	2.9	0.6	30	13.2	2.0	60
$\Lambda K^+ \pi^+ \pi^- \pi^-$	10.1	1.3	82	30	3.8	106
$\Lambda K^0 \pi^+ \pi^- \pi^0$	38	5	78	70	11	63
$pK^+ \bar{K}^0 \pi^- \pi^-$	2.0	0.75	12	9.7	2.6	23
$pK^0 K^- \pi^+ \pi^-$	2.3	0.80	19	15.8	3.4	49
$pK_1^0 K_1^0 \pi^0 \pi^-$	1.0	0.60	3	5.0	2.3	10
$nK_1^0 K_1^0 \pi^+ \pi^-$	0.64	0.46	3	6.0	2.5	13

UCRL-16978

Table VIII. Number of events for each three-body final state[a]

Final state	Observed decays	Momentum interval (BeV/c)		
		1.8 to 2.2	2.9 to 3.3	3.8 to 4.2
$\Sigma^+K^0\pi^-$	Σ^+, K^0	79	92	30
$\Sigma^+K^0\pi^-$	Σ^+	223	210	74
$\Sigma^0K^+\pi^-$	Λ	445	314	104
$\Sigma^0K^+\pi^-$	K^+	68	59	26
$\Sigma^-K^+\pi^0$	Σ^-	486	299	123
$\Sigma^-K^0\pi^+$	Σ^-, K^0	336	209	56
$\Sigma^-K^0\pi^+$	Σ^-	726	523	167
$\Lambda K^+\pi^-$	Λ	1031	689	263
$\Lambda K^+\pi^-$	K^+	68	42	9
$\Lambda K^0\pi^0$	Λ, K^0	336	208	72
pK^0K^-	K^0	113	228	95
pK^0K^-	K^-	42	44	17
nK^+K^-	K^+	40	48	29
nK^+K^-	K^-	44	111	62
$nK^0\bar{K}^0$	$K^0, \bar{K}^0$	68	201	68

[a]Events from the π 72 exposure are not included here. They contribute 1/3 of the combined data at 1.8 to 2.2 BeV/c, and none in the other intervals.

Table IX. Resonance fits in three-body final states.

Final state	Momentum interval (BeV/c)	Resonance system	Mass (MeV)	Width (MeV)	Amount (%)
$\Sigma^+ K^0 \pi^-$	1.8 - 2.2	$\Sigma^+\pi^-$	1386	53	42 ± 4
		$\Sigma^+\pi^-$	1517	18	17 ± 3
	2.9 - 3.3	$\Sigma^+\pi^-$	1386	53	29 ± 3
		$\Sigma^+\pi^-$	1517	18	14 ± 3
	3.8 - 4.2	$\Sigma^+\pi^-$	1386	53	28 ± 6
		$\Sigma^+\pi^-$	1517	18	11 ± 4
$\Sigma^0 K^+ \pi^-$	1.8 - 2.2	$K^+\pi^-$	891	44	56 ± 3
	2.9 - 3.3	$K^+\pi^-$	891	44	54 ± 4
	3.8 - 4.2	$K^+\pi^-$	891	44	42 ± 6
$\Sigma^- K^+ \pi^0$	1.8 - 2.2	$K^+\pi^0$	885	51	29 ± 3
	2.9 - 3.3	$K^+\pi^0$	885	51	24 ± 4
	3.8 - 4.2	$K^+\pi^0$	885	51	8 ± 4
$\Sigma^- K^0 \pi^+$	1.8 - 2.2	$\Sigma^-\pi^+$	1386	53	19 ± 2
		$\Sigma^-\pi^+$	1517	18	8 ± 1
		$K^0\pi^+$	885	51	29 ± 3
	2.9 - 3.3	$\Sigma^-\pi^+$	1386	53	13 ± 2
		$\Sigma^-\pi^+$	1517	18	5 ± 2
		$K^0\pi^+$	885	51	21 ± 3
	3.8 - 4.2	$\Sigma^-\pi^+$	1386	53	18 ± 3
		$\Sigma^-\pi^+$	1517	18	9 ± 3
		$K^0\pi^+$	885	51	12 ± 3

(cont.)

Table IX. (continued)

Final state	Momentum interval (BeV/c)	Resonance system	Mass (MeV)	Width (MeV)	Amount (%)
$\Lambda K^+\pi^-$	1.8 - 2.2	$\Lambda\pi^-$	1385	41	31 ± 2
		$K^+\pi^-$	891	44	49 ± 2
	2.9 - 3.3	$\Lambda\pi^-$	1385	41	5 ± 1
		$K^+\pi^-$	891	44	43 ± 3
	3.8 - 4.2	$\Lambda\pi^-$	1385	41	2 ± 2
		$K^+\pi^-$	891	44	48 ± 4
		$K^+\pi^-$	1446 ± 7.9	61 ± 24	17 ± 4
$\Lambda K^0\pi^0$	1.8 - 2.2	$\Lambda\pi^0$	1380	43	41 ± 4
		$K^0\pi^0$	891	44	17 ± 4
	2.9 - 3.3	$\Lambda\pi^0$	1380	43	29 ± 6
		$K^0\pi^0$	891	44	20 ± 4
	3.8 - 4.2	$\Lambda\pi^0$	1380	43	16 ± 6
		$K^0\pi^0$	891	44	19 ± 6
$pK^0_1K^-$	1.6 - 2.4	pK^-	1518.9	16	28 ± 4
	2.9 - 3.3	pK^-	1518.9	16	20 ± 3
		$K^0_1K^-$	1317	50	28 ± 5
	3.8 - 4.2	pK^-	1518.9	16	9 ± 4
		$K^0_1K^-$	1317	50	26 ± 7
		pK^-	1815	50	15 ± 6
	2.7 - 4.5	$K^0_1K^-$	1317.2 ± 4.0	47.0 ± 17.7	-

(cont.)

Table IX. (continued)

Final state	Momentum interval (BeV/c)	Resonance system	Mass (MeV)	Width (MeV)	Amount (%)
$nK_1^0K_1^0$	1.6 - 2.4	nK_1^0	1518.9	16	5 ± 2
		$K_1^0K_1^0$	982.1 + 6.0	32.5 ± 30.0	50 ± 11
	2.9 - 3.3	nK_1^0	1518.9	16	5 ± 2
		$K_1^0K_1^0$	982	30	20 ± 5
		$K_1^0K_1^0$	1317	50	20 ± 5
	3.8 - 4.2	nK_1^0	1518.9	16	2 ± 1
		$K_1^0K_1^0$	982	30	25 ± 5
		$K_1^0K_1^0$	1317	50	10 ± 3
		nK_1^0	1815	50	3
	2.7 - 4.5	$K_1^0K_1^0$	1315.7 ± 10.8	80.5 ± 36.5	-
nK^+K^-	1.5 - 2.3	K^+K^-	1021 ± 4	10 ± 3	40
		K^+K^-	982	30	20

Table X. Cross section for resonance production in 3-body final states.

Process	Momentum interval (BeV/c)	Cross section (μb)
$\pi^- p \to Y_0^*(1405) K^0$, $Y_0^*(1405) \to \Sigma\pi$	1.8 to 2.2	51.0 ± 4.7
	2.9 to 3.3	37.4 ± 3.7
	3.8 to 4.2	30.3 ± 4.6
$\pi^- p \to Y_0^*(1520) K^0$, $Y_0^*(1520) \to \Sigma\pi$	1.8 to 2.2	23.7 ± 2.7
	2.9 to 3.3	18.7 ± 2.1
	3.8 to 4.2	14.0 ± 3.6
$\pi^- p \to Y_0^*(1520) K^0$, $Y_0^*(1520) \to N\bar{K}$	1.8 to 2.2	20.8 ± 5.0
	2.9 to 3.3	24.2 ± 5.0
	3.8 to 4.2	12.2 ± 6.0
$\pi^- p \to Y_0^*(1815) K^0$, $Y_0^*(1815) \to N\bar{K}$	2.9 to 3.3	2.6 ± 2.0
	3.8 to 4.2	20.0 ± 8.0
$\pi^- p \to Y_1^{*-}(1385) K^+$, $Y_1^{*-}(1385) \to \Lambda\pi^-$	1.8 to 2.2	42.8 ± 4.0
	2.9 to 3.3	5.0 ± 1.0
	3.8 to 4.2	0.0 ± 1.9
$\pi^- p \to Y_1^{*0}(1385) K^0$, $Y_1^{*0}(1385) \to \Lambda\pi^0$	1.8 to 2.2	61.6 ± 10.0
	2.9 to 3.3	28.9 ± 7.0
	3.8 to 4.2	13.0 ± 5.4
$\pi^- p \to \Sigma^0 K^{*0}(890)$, $K^{*0}(890) \to K\pi$	1.8 to 2.2	49.4 ± 4.4
	2.9 to 3.3	36.4 ± 3.8
	3.8 to 4.2	23.1 ± 4.3
$\pi^- p \to \Sigma^- K^{*+}(890)$, $K^{*+}(890) \to K\pi$	1.8 to 2.2	45.3 ± 3.2
	2.9 to 3.3	23.1 ± 2.7
	3.8 to 4.2	8.8 ± 2.1
$\pi^- p \to \Lambda K^{*0}(890)$, $K^{*0}(890) \to K\pi$	1.8 to 2.2	98.4 ± 7.4
	2.9 to 3.3	63.0 ± 5.6
	3.8 to 4.2	63.1 ± 7.7

continued

Table X. (continued)

Process	Momentum interval (BeV/c)	Cross section (μb)
$\pi^- p \to p A_2^-$, $A_2^- \to K^0 K^-$	2.9 to 3.3	18.2 ± 4.0
	3.8 to 4.2	17.1 ± 4.7
$\pi^- p \to n + K\bar{K}$ threshold enhancement	1.8 to 2.2	7.9 ± 2.0
$K\bar{K}$ threshold enhancement $\to K_1^0 K_1^0$	2.9 to 3.3	7.5 ± 2.5
	3.8 to 4.2	9.0 ± 3.8
$\pi^- p \to n A_2^0$, $A_2^0 \to K\bar{K}$	2.9 to 3.3	36.2 ± 10.0
	3.8 to 4.2	17.6 ± 9.0
$\pi^- p \to n\phi$	1.58 to 1.71	29.0 ± 15.0
	1.8 to 2.2	30.0 ± 8.0
	2.58 to 2.63	0.0 ± 9.0
	2.9 to 3.3	6.0 ± 8.0
	3.8 to 4.2	15.0 ± 20.0

Table XI. Cros's sections and branching ratios for $Y_0^*(1520)$.

$\sigma[\pi^- p \rightarrow Y_0^*(1520)\ K^0]$	
Momentum	σ (μb)
1.8 to 2.2	49 ± 6
2.9 to 3.3	47 ± 7
3.8 to 4.2	28 ± 7

Branching ratios		
$\Sigma\pi$	$\Lambda\pi\pi$	$N\bar{K}$
0.45 ± 0.04	0.08 ± 0.02	0.47 ± 0.09

Table XII. Selection criteria and density-matrix parameters for $\pi p \rightarrow Y^* K$. [a]

Final state	Mass interval (BeV)	Incident momentum (BeV/c)	ρ_{33}	Re ρ_{3-1}	Re ρ_{31}
$Y_0^*(1520) K^0 \rightarrow \Sigma^+ \pi^- K^0$	1.493 to 1.537	1.8 to 2.2	0.073 ± 0.052	0.039 ± 0.050	0.057 ± 0.043
$Y_1^{*0}(1385) K^0 \rightarrow \Lambda \pi^0 K^0$	1.350 to 1.410	1.8 to 2.2	0.285 ± 0.048	0.262 ± 0.041	-0.104 ± 0.043

[a] Data at all production angles were included in the fit.

Table XIII. Predictions for density-matrix parameters of $3/2^+$ and $3/2^-$ states for various multipole interactions.

Resonant state	J^P	Interaction	ρ_{33}	Re ρ_{3-1}	Re ρ_{31}
$Y^{*0}(1385)$	$3/2^+$	M_1	3/8	$\sqrt{3/8} = 0.216$	0
		E_2	1/8	$-\sqrt{3/8}$	0
		L_2	0	0	0
$Y^{*0}(1520)$	$3/2^-$	M_2	1/8	$\sqrt{3/8}$	0
		E_1	3/8	$-\sqrt{3/8}$	0
		L_1	0	0	0

Table XIV. The YK^* selection criteria and density matrix elements.

Final state	Mass (BeV)	$\cos\theta_{prod}$	Incident momentum (BeV/c)	(1) $\rho_{++++} + \rho_{+-+-}$	(2) $\mathrm{Re}\{\rho_{+++0} - \rho_{+0+-}\}$	(3) $\mathrm{Im}\{\rho_{+++0} - \rho_{+0+-}\}$	(4) $\mathrm{Re}\,\rho_{+++-}$	(5) $\mathrm{Im}\,\rho_{+++-}$	(6) $\mathrm{Im}\,\rho_{++-+}$	(7) $\mathrm{Im}\,\rho_{++-0}$	(8) $\mathrm{Im}\,\rho_{+0-+}$	(9) ρ_{++--}	(10) ρ_{+0-0}	(11) ρ_{+--+}
$\Sigma^- K^{*+}$ $\hookrightarrow K^+\pi^0$	0.850 - 0.920	-1.0 - 1.0	1.8 - 2.2	0.310 ± 0.034	-0.084 ± 0.044		-0.068 ± 0.028							
$\Sigma^0 K^{*0}$	0.861 - 0.921	-1.0 - 0.0	1.8 - 2.2	0.336 ± 0.043	0.064 ± 0.046	-0.111 ± 0.461	0.094 ± 0.038	-0.344 ± 0.278	-0.156 ± 0.247	-0.021 ± 0.348	0.353 ± 0.308	-1.24 ± 0.486	0.639 ± 0.330	-0.563 ± 0.415
$\Sigma^0 K^{*0}$	0.861 - 0.921	0.0 - 0.5	1.8 - 2.2	0.438 ± 0.036	0.021 ± 0.043	1.21 ± 0.313	0.149 ± 0.030	0.228 ± 0.360	-0.077 ± 0.250	0.067 ± 0.274	-0.116 ± 0.259	-0.045 ± 0.461	0.170 ± 0.314	-0.062 ± 0.423
$\Sigma^0 K^{*0}$	0.861 - 0.921	0.5 - 1.0	1.8 - 2.2	0.368 ± 0.052	-0.076 ± 0.065	0.333 ± 0.519	0.080 ± 0.046	0.495 ± 0.417	-0.122 ± 0.345	-0.309 ± 0.409	-0.933 ± 0.406	-0.816 ± 0.580	-0.223 ± 0.529	-0.686 ± 0.607
$\Sigma^0 K^{*0}$	0.861 - 0.921	0.5 - 1.0	2.9 - 3.3	0.477 ± 0.055	0.009 ± 0.031	0.215 ± 0.379	0.149 ± 0.039	-0.578 ± 0.356	0.785 ± 0.273	0.048 ± 0.235	-0.771 ± 0.277	-0.291 ± 0.487	-1.81 ± 0.570	-0.131 ± 0.497
ΛK^{*0} $\hookrightarrow K^+\pi^-$	0.861 - 0.921	0.5 - 1.0	2.9 - 3.3	0.372 ± 0.035	0.052 ± 0.036	-0.339 ± 0.100	0.075 ± 0.027	-0.028 ± 0.075	0.151 ± 0.053	0.034 ± 0.061	-0.042 ± 0.061	0.430 ± 0.082	-0.072 ± 0.097	0.039 ± 0.086
ΛK^{*0} $\hookrightarrow K^+\pi^-$	0.861 - 0.921	0.5 - 1.0	3.8 - 4.2	0.367 ± 0.055	0.046 ± 0.082	-0.701 ± 0.198	0.082 ± 0.040	0.203 ± 0.114	0.050 ± 0.075	-0.110 ± 0.078	0.124 ± 0.086	0.377 ± 0.123	0.002 ± 0.108	0.078 ± 0.130

UCRL-16978

Table XV. Fits to the density-matrix elements for the A_2^- at 2.9 to 3.3 BeV/c.

Parameter	Best fit
$1 - 2\rho_{11} - 2\rho_{22}$	0.38 ± 0.15
ρ_{22}	0.10 ± 0.08
ρ_{11}	0.21 ± 0.07
$\mathrm{Re}\,[\rho_{20}]$	0.02 ± 0.06
ρ_{2-2}	-0.04 ± 0.09
ρ_{1-1}	-0.06 ± 0.10
$\mathrm{Re}\,[\rho_{21}]$	-0.06 ± 0.07
$\mathrm{Re}\,[\rho_{2-1}]$	-0.00 ± 0.07
$\mathrm{Re}\,[\rho_{10}]$	-0.05 ± 0.07

Table XVI. Decay angular distributions of the A_2 fit to $\sum_n A_n P_n(\cos\theta)$.

	Order	A_0	A_1	A_2	A_3	A_4	χ^2	Degrees of freedom	Confidence level (%)
	0	1.00 ± 0.21	--	--	--	--	35.5	9	0.0
	1	0.78 ± 0.13	1.09 ± 0.27	--	--	--	19.2	8	1.4
A_2^- at 3.2 GeV/c	2	1.04 ± 0.15	1.27 ± 0.28	1.27 ± 0.36	--	--	6.7	7	46.1
	3	1.07 ± 0.15	1.05 ± 0.31	1.10 ± 0.38	-0.57 ± 0.40	--	4.6	6	59.1
	4	1.10 ± 0.15	1.03 ± 0.31	1.29 ± 0.41	-0.39 ± 0.41	0.63 ± 0.50	3.1	5	68.8
	0	1.00 ± 0.26	--	--	--	--	34.5	4	0.0
A_2^0 at 3.2 GeV/c	2	3.36 ± 0.44	--	7.91 ± 1.18	--	--	11.7	3	0.9
	4	3.87 ± 0.46	--	10.61 ± 1.46	--	5.70 ± 1.83	6.9	2	3.2
	0	1.00 ± 0.34	--	--	--	--	9.3	9	41.1
A_2^- at 4.2 GeV/c	1	1.00 ± 0.34	0.00 ± 0.66	--	--	--	9.3	8	31.9
	2	1.13 ± 0.35	-0.36 ± 0.71	1.07 ± 0.78	--	--	7.4	7	38.8
	0	1.00 ± 0.33	--	--	--	--	6.5	4	16.5
A_2^0 at 4.2 GeV/c	2	1.82 ± 0.42	--	3.43 ± 1.04	--	--	1.1	3	77.7

Table XVII. Detection efficiencies and cross sections for $\pi^- p \rightarrow n\phi$.

Momentum (BeV/c)	No. ϕ's over background	Efficiency (%)	Events per μb	Cross section (μb)
1.6	7 ± 3	8.3 ± 1.0	2.91 ± 0.34	29 ± 15
2.0	25 ± 6	6.3 ± 0.7	13.38 ± 0.67	30 ± 8
2.6	0 ± 1	3.8 ± 1.9	2.99 ± 0.26	0 ± 9
3.1	2 ± 2	2.5 ± 0.6	12.8 ± 0.6	6 ± 8
4.0	1 ± 1	1.3 ± 0.4	5.6 ± 0.4	15 ± 20

Table XVIII. Number of events for each four-body final state.[a]

Final state	Observed decays	Momentum interval (BeV/c)		
		1.8 to 2.2	2.9 to 3.3	3.8 to 4.2
$\Sigma^+K^+\pi^-\pi^-$	Σ^+	7	63	47
$\Sigma^+K^0\pi^0\pi^-$	Σ^+, K^0	2	73	42
$\Sigma^0K^0\pi^+\pi^-$	Λ, K^0	4	53	37
$\Sigma^0K^0\pi^+\pi^-$	K^0	2	78	74
$\Sigma^-K^+\pi^+\pi^-$	Σ^-	17	182	93
$\Sigma^-K^0\pi^+\pi^0$	Σ^-, K^0	3	90	42
$\Lambda K^+\pi^0\pi^-$	Λ	78	617	312
$\Lambda K^0\pi^+\pi^-$	Λ, K^0	31	193	76
$\Lambda K^0\pi^+\pi^-$	Λ	84	538	270
$\Lambda K^0\pi^+\pi^-$	K^0	25	154	92
$pK^+K^-\pi^-$	K^+	0	31	21
$pK^+K^-\pi^-$	K^-	2	34	22
$pK^0\bar{K}^0\pi^-$	K^0 or $\bar{K}^0$	1	119	80
$pK^0\bar{K}^0\pi^-$	K^0, $\bar{K}^0$	0	27	30
$pK^0K^-\pi^0$	K^0	3	108	63
$nK^+\bar{K}^0\pi^-$	$\bar{K}^0$	2	128	89
$nK^0K^-\pi^+$	K^0	0	108	92

[a]Events from the π72 exposure are not included here. They contribute 1/3 of the combined sample at 1.8 to 2.2 BeV/c, and none in the other intervals.

Table XIX. Resonance fits in four-body final states

Process	Momentum (BeV/c)	Mass (MeV)	Width (MeV)	Amount (%)	Cross section (μb)
$\pi^- p \to Y_0^*(1520)K^0$, $Y_0^*(1520) \to \Lambda\pi\pi$	1.8 to 2.2			9 ± 3	2.8 ± 1.0
	2.9 to 3.3	1517	18	3 ± 1	4.4 ± 1.5
	3.8 to 4.2			2 ± 1	2.9 ± 1.6
$\pi^- p \to Y_1^{*+}(1385)K^0\pi^-$, $Y_1^{*+}(1385) \to \Lambda\pi^+$	1.8 to 2.2			19 ± 7	2.9 ± 1.1
	2.9 to 3.3	1385	41	15 ± 2	15.1 ± 2.2
	3.8 to 4.2			11 ± 3	11.9 ± 3.4
$\pi^- p \to Y_1^{*-}(1385)K^0\pi^+$, $Y_1^{*-}(1385) \to \Lambda\pi^-$	1.8 to 2.2			-	0.0 ± 1.1
	2.9 to 3.3	1385	41	16 ± 3	16.1 ± 3.2
	3.8 to 4.2			10 ± 3	10.8 ± 3.4
$\pi^- p \to Y_1^{*-}(1385)K^{*+}(890)$	1.8 to 2.2			38 ± 8	4.1 ± 1.0
$Y_1^{*-}(1385) \to \Lambda\pi^-$	2.9 to 3.3	1385	41	6 ± 2	5.5 ± 1.9
$K^{*+}(890) \to K^+\pi^0$	3.8 to 4.2	885	51	-	0.0 ± 3.3
$\pi^- p \to Y_1^{*-}(1385)K^{*+}(890)$	1.8 to 2.2			52 ± 7	7.9 ± 1.4
$Y_1^{*-}(1385) \to \Lambda\pi^-$	2.9 to 3.3	1385	41	10 ± 3	10.1 ± 3.1
$K^{*+}(890) \to K^0\pi^+$	3.8 to 4.2	885	51	-	0 ± 1.1
$\pi^- p \to Y_1^{*-}(1385)\, K^+\pi^0$, $Y_1^{*-}(1385) \to \Lambda\pi^-$	1.8 to 2.2			-	0.0 ± 1.1
	2.9 to 3.3	1385	41	6 ± 3	5.5 ± 2.8
	3.8 to 4.2			12 ± 3	13.5 ± 3.6

(cont.)

Table XIX. (cont.).

Process	Momentum (BeV/c)	Mass (MeV)	Width (MeV)	Amount (%)	Cross section (μb)
	1.8 to 2.2			-	0.0 ± 1.6
$\pi^- p \rightarrow K^{*+}(890)\Lambda\pi^-$, $K^{*+}(890) \rightarrow K^+\pi^0$	2.9 to 3.3	885	51	11 ± 3	10.1 ± 2.8
	3.8 to 4.2			8 ± 3	9.0 ± 3.5
	1.8 to 2.2			-	0.0 ± 1.1
$\pi^- p \rightarrow K^{*+}(890)\Lambda\pi^-$, $K^{*+}(890) \rightarrow K^0\pi^+$	2.9 to 3.3	885	51	11 ± 3	11.1 ± 3.1
	3.8 to 4.2			11 ± 4	11.9 ± 4.4
	1.8 to 2.2			12 ± 14	1.3 ± 1.5
$\pi^- p \rightarrow Y_1^{*0}(1385)K^+\pi^-$, $Y_1^{*0}(1385) \rightarrow \Lambda\pi^0$	2.9 to 3.3	1380	43	12 ± 3	11.0 ± 2.9
	3.8 to 4.2			8 ± 3	9.0 ± 3.5
$\pi^- p \rightarrow Y_1^{*0}(1385)\, K^{*0}(890)$	1.8 to 2.2			42 ± 14	6.8 ± 2.4
$Y_1^{*0}(1385) \rightarrow \Lambda\pi^0$	2.9 to 3.3	1380	43	18 ± 3	24.0 ± 4.5
$K^{*0}(890) \rightarrow K\pi$	3.8 to 4.2	891	44	14 ± 3	23.6 ± 5.6
	1.8 to 2.2			-	0.0 ± 1.6
$\pi^- p \rightarrow K^{*0}(890)\Lambda\pi^0$, $K^{*0}(890) \rightarrow K\pi$	2.9 to 3.3	891	44	16 ± 3	22.0 ± 4.4
	3.8 to 4.2			17 ± 4	28.6 ± 7.3
$\pi^- p \rightarrow Y_0^*(1405)K^{*0}(890)$	1.8 to 2.2			-	-
$Y_0^*(1405) \rightarrow \Sigma\pi$	2.9 to 3.3	1386	53	-	13 ± 2
$K^{*0}(890) \rightarrow K\pi$	3.8 to 4.2	891	44	-	16 ± 3

(cont.)

Table XIX. (cont.)

Process	Momentum (BeV/c)	Mass (MeV)	Width (MeV)	Amount (%)	Cross section (μb)
$\pi^- p \rightarrow Y_0^*(1520)\, K^{*0}(890)$	1.8 to 2.2			-	-
$Y_0^*(1520) \rightarrow \Sigma\pi$	2.9 to 3.3	1517	18	-	7 ± 1
$K^{*0}(890) \rightarrow K\pi$	3.8 to 4.2	891	44	-	6 ± 1
$\pi^- p \rightarrow Y_1^{*0}(1660)\, K^{*0}(890)$	1.8 to 2.2			-	-
$Y_1^{*0}(1660) \rightarrow \Sigma\pi$	2.9 to 3.3	1660	44	-	3 ± 1
$K^{*0}(890) \rightarrow K\pi$	3.8 to 4.2	891	44	-	3 ± 1
	2.5 to 2.63			-	7.5 ± 4.0
$\pi^- p \rightarrow nD,\ D \rightarrow K^{\pm}K^0\pi^{\mp}$	2.9 to 3.3	1283	35	10	7 ± 2
	3.8 to 4.2			7	10 ± 4
$\pi^- p \rightarrow nE,\ E \rightarrow K^{\pm}K^0\pi^{\mp}$	2.9 to 3.3	1420	60	17	17 ± 5
	3.8 to 4.2			5	3 ± 2
$\pi^- p \rightarrow nK\bar{K}^*$ or $n\bar{K}K^*$	2.9 to 3.3	891	50	30	32 ± 8
	3.8 to 4.2			15	15 ± 5
$\pi^- p \rightarrow pK\bar{K}^*$ or $p\bar{K}K^*$	2.9 to 3.3	891	50	17	22 ± 8
	3.8 to 4.2			10	20 ± 9
$\pi^- p \rightarrow Y_0^*(1520)\, K\pi,\ Y_0^*(1520) \rightarrow pK^-$	2.9 to 3.3	1518.9	16	15	9 ± 1
	3.8 to 4.2			10	11 ± 5

Table XX. Expected and observed numbers of events based on the assumption that I = 1 for the D and E mesons.

		$nK^0K^{\pm}\pi^{\mp}$ 1 K^0 decay	$pK^+K^-\pi^-$ 1 $K^{\pm}$ decay	$pK^0\bar{K}^0\pi^-$ 1 K^0 decay	$pK^0\bar{K}^0\pi^-$ 2 K^0 decays	$pK^0K^-\pi^0$ 1 K^0 decay
Observed events over background	D	35 ± 8	0 ± 1	0 ± 2	0 ± 1	1 ± 2
	E	50 ± 10	1 ± 6	9 ± 10	0 ± 4	2 ± 5
Expected numbers[a] for: Decay into $K\bar{K}^*$ and $\bar{K}K^*$	D	35	3 ± 1	11 ± 3	3 ± 1	9 ± 3
	E	50	5 ± 1	17 ± 4	4 ± 1	12 ± 3
Decay into $(K\bar{K})\pi$ with $I^G=1^-$ for $K\bar{K}$	D	35	2 ± 1	3 ± 1	3 ± 1	4 ± 1
	E	50	2 ± 1	4 ± 1	4 ± 1	12 ± 3
Decay into $(K\bar{K})\pi$ with $I^G=1^+$ for $K\bar{K}$	D	35	2 ± 1	17 ± 4	0	4 ± 1
	E	50	2 ± 1	25 ± 5	0	12 ± 3

[a] The number of events observed in the $nK^0K^{\pm}\pi^{\mp}$ final states is used for normalization.

Table XXI. Number of events for each five-body final state.

Final state	Observed decays	Momentum interval (BeV/c) 2.9 to 3.3	3.8 to 4.2
$\Sigma^+K^+\pi^0\pi^-\pi^-$	Σ^+	15	21
$\Sigma^+K^0\pi^+\pi^-\pi^-$	Σ^+, K^0	1	5
$\Sigma^+K^0\pi^+\pi^-\pi^-$	Σ^+	7	10
$\Sigma^0K^+\pi^+\pi^-\pi^-$	Λ	16	22
$\Sigma^0K^+\pi^+\pi^-\pi^-$	K^+	3	7
$\Sigma^-K^+\pi^+\pi^0\pi^-$	Σ^-	59	74
$\Sigma^-K^0\pi^+\pi^+\pi^-$	Σ^-, K^0	7	16
$\Sigma^-K^0\pi^+\pi^+\pi^-$	Σ^-	22	40
$\Lambda K^+\pi^+\pi^-\pi^-$	Λ	72	87
$\Lambda K^+\pi^+\pi^-\pi^-$	K^+	10	13
$\Lambda K^0\pi^+\pi^0\pi^-$	Λ, K^0	77	62
$pK^+K^-\pi^0\pi^-$	K^+	1	6
$pK^+K^-\pi^0\pi^-$	K^-	4	7
$pK^+\bar{K}^0\pi^-\pi^-$	K^+	5	6
$pK^+\bar{K}^0\pi^-\pi^-$	$\bar{K}^0$	7	17
$pK^0\bar{K}^0\pi^0\pi^-$	$K^0, \bar{K}^0$	3	10
$pK^0K^-\pi^+\pi^-$	K^0	12	32
$pK^0K^-\pi^+\pi^-$	K^-	7	17
$nK^+K^-\pi^+\pi^-$	K^+	1	11
$nK^+K^-\pi^+\pi^-$	K^-	11	32
$nK^0\bar{K}^0\pi^+\pi^-$	$K^0, \bar{K}^0$	3	13

Table XXII. Cross section for Ξ production reactions.

Final state	Production threshold (BeV/c)	Decays observed[a]	Fraction[b] expected for given topology	3.2 BeV/c		4.0 BeV/c	
				Number of events	σ (μb)	Number of events	σ (μb)
$\Xi^0 K^0 K^0$	2.36	Λ, K^0, K^0	2/27	0	$< 1^c$	0	$< 2.4^c$
$\Xi^- K^+ K^0$	2.37	Ξ^-, Λ, K^0	2/9	7		1	
		Ξ^-, Λ	4/9	9	1.9 ± 0.5	5	1.8 ± 0.9
		Ξ^-, K^0	1/9	2		0	
$\Xi^0 K^+ K^0 \pi^-$	2.70	Λ, K^0	2/9	0	$< 0.3^c$	0	$< 0.8^c$
$\Xi^- K^+ K^+ \pi^-$	2.71	Ξ^-, Λ	2/3	0	$< 0.08^c$	2	0.5 ± 0.4
		Ξ^-	1/3	0		0	
$\Xi^- K^+ K^0 \pi^0$	2.71	Ξ^-, Λ, K^0	2/9	0	0.2 ± 0.2	1	0.6 ± 0.5
		Ξ^-, Λ	4/9	1		1	
$\Xi^- K^0 K^0 \pi^+$	2.73	Ξ^-, Λ, K^0, K^0	2/27	0		0	
		Ξ^-, Λ, K^0	8/27	1	0.25 ± 0.18	2	2.3 ± 1.0
		Ξ^-, Λ	8/27	1		5	
		Ξ^-, K^0, K^0	1/27	0		0	

a. The particle symbols stand for visible two-body decays in the bubble chamber. The search for Ξ production was limited to the event topologies indicated.

b. Rounded decay branching ratios are used for simplicity. Escape corrections are not included.

c. The value given corresponds to one observed event.

Table XXIII. Density matrix for 1^- and $1/2^+$ particles.

Polarization states	Polarization states					
	++	+0	+-	-+	-0	--
++	ρ_{++++}	ρ_{+++0}	ρ_{+++-}	ρ_{++-+}	ρ_{++-0}	$i\rho_{++--}$
+0	ρ^*_{+++0}	$\frac{1}{2}-\rho_{++++}$ $-\rho_{+-+-}$	ρ_{+0+-}	ρ_{+0-+}	$i\rho_{+0-0}$	ρ^*_{++-0}
+-	ρ^*_{+++-}	ρ^*_{+0+-}	ρ_{+-+-}	$i\rho_{+--+}$	ρ^*_{+0-+}	$-\rho^*_{++-+}$
-+	ρ^*_{++-+}	ρ^*_{+0-+}	$-i\rho_{+--+}$	ρ_{+-+-}	$-\rho^*_{+0+-}$	ρ^*_{+++-}
-0	ρ^*_{++-0}	$-i\rho_{+0-0}$	ρ_{+0-+}	$-\rho_{+0+-}$	$\frac{1}{2}-\rho_{++++}$ $-\rho_{+-+-}$	$-\rho^*_{+++0}$
--	$-i\rho_{++--}$	ρ_{++-0}	$-\rho_{++-+}$	ρ_{+++-}	$-\rho_{+++0}$	ρ_{++++}

Table XXIV. Decay matrix elements.

J^P	ℓ	$M(K\bar{K}^*)$
0^-	1	$\bar{f}\,\bar{e}^{\mu}\bar{T}_{\mu}\bar{e}^{\nu}W_{\nu}$
1^-	1	$\bar{f}\,\bar{e}^{\mu}\bar{T}_{\mu}\bar{e}^{\nu}W^{\lambda}D^{\sigma}\mathcal{E}^{\rho}\epsilon_{\nu\lambda\sigma\rho}$
1^+	0	$\bar{f}\,\bar{e}^{\mu}\bar{T}_{\mu}\bar{e}^{\nu}\mathcal{E}_{\nu}$
1^+	2	$\bar{f}\,\bar{e}^{\mu}\bar{T}_{\mu}\bar{e}^{\nu}\mathcal{E}_{\lambda}[R_{\nu}R_{\lambda}-\frac{1}{3}R_{\sigma}R^{\sigma}\delta_{\nu\lambda}]$
2^+	2	$\bar{f}\,\bar{e}^{\mu}\bar{T}_{\mu}\bar{e}^{\alpha}W^{\beta}D^{\gamma}\mathcal{E}^{\delta\nu}W_{\nu}\epsilon_{\alpha\beta\gamma\delta}$
2^-	1	$\bar{f}\,\bar{e}^{\mu}\bar{T}_{\mu}\bar{e}^{\nu}W^{\lambda}\mathcal{E}_{\nu\lambda}$
2^-	3	$\bar{f}\,\bar{e}^{\mu}\bar{T}_{\mu}\bar{e}^{\nu}\mathcal{E}^{\lambda\sigma}[R_{\nu}R_{\lambda}R_{\sigma}-\frac{1}{5}R_{\alpha}R^{\alpha}(\delta_{\nu\lambda}R_{\sigma}+\delta_{\lambda\sigma}R_{\nu}+\delta_{\sigma\nu}R_{\lambda})]$

FIGURE LEGENDS

Fig. 1. Topologies sought in this experiment: (a) zero-prong with a vee; (b) two-prong with a vee; (c) four-prong with a vee; (d) zero-prong with two vees; (e) two-prong with two vees; (f) two-prong with a vee, positive decay; (g) four-prong with a vee, positive decay; (h) two-prong with a vee, negative decay; (i) four-prong with a vee, negative decay; (j) two-prong with a positive decay; (k) four-prong with a positive decay; (l) two-prong with a negative decay; (m) four-prong with a negative decay.

Fig. 2. Number of strange-particle events found in this experiment as a function of incident-pion momentum (a) in the $\pi 63$ exposure, (b) in the $\pi 72$ exposure, and (c) for the two samples combined.

Fig. 3. Angular distributions for γ rays from Σ^0 decay with respect to the normal to the production plane for the reaction $\pi^- p \rightarrow \Sigma^0 K^+ \pi^-$. (a) Events with an acceptable hypothesis for only Σ^0 production. (b) Events with the highest confidence level for Σ^0 production but also an acceptable $\pi^- p \rightarrow \Lambda K^+ \pi^-$ hypothesis. (c) Events with the highest confidence level for Λ production but also an acceptable Σ^0-production hypothesis.

Fig. 4. Scatter plots of the $(\text{missing mass})^2$ versus $M^2(\Lambda mm)$ for events with acceptable $\Sigma^0 K^+ \pi^-$ or $\Lambda K^+ \pi^- \pi^0$ hypotheses. (a) Events with only an acceptable Σ^0 hypothesis. (b) Events with only an acceptable $\Lambda\pi^0$ hypothesis. (c) Events with both Σ^0 - and $\Lambda\pi^0$ -production hypotheses and with a higher confidence level for Σ^0 production. (d) Events with both Σ^0 - and $\Lambda\pi^0$ -production hypotheses and with a higher confidence level for $\Lambda\pi^0$ production.

Fig. 5. Histogram of the missing mass for events in the "zero prong with one vee" class, where the vee is a $K^0 \rightarrow \pi^+\pi^-$ decay.

Fig. 6. Scatter plot of the confidence levels for events ambiguous between the production hypotheses $\Lambda K^+\pi^0\pi^-$ and $\Lambda K^0\pi^+\pi^-$.

Fig. 7. Total cross sections as a function of the beam momentum for $\Lambda K\pi$ and $\Lambda K\pi\pi$ final states. The arrow indicates the threshold for the reaction.

- ○ This experiment, π63
- ▽ This experiment, π72 (Ref. 29)
- ▲ O. Goussu et al., Ref. 2
- ■ D. Miller et al., Ref. 5
- ◆ O. Goussu et al., Ref. 6
- ● T. Wangler et al., Ref. 7
- △ J. Bartsch et al., Ref. 8
- □ L. Bertanza et al., Rev. 9

Fig. 8. Total cross sections as a function of beam momentum for $\Sigma K\pi$ final states. The symbols used are the same as on Fig. 7.

Fig. 9. Total cross sections as a function of the beam momentum for the $NK\bar{K}$ and the $NK\bar{K}\pi\pi$ final states. The symbols used are the same as on Fig. 7.

Fig. 10. Total cross sections as a function of the beam momentum for the $NK\bar{K}\pi$ final states. The symbols used are the same as on Fig. 7.

Fig. 11. Effective-mass histograms and Dalitz plots for $\Sigma^+K^0\pi^-$ at 1.8 to 2.2 BeV/c (a, d, g, j), 2.9 to 3.3 BeV/c (b, e, h, k), and 3.8 to 4.2 BeV/c (c, f, i, l). The curves are for phase

space and S-wave Breit-Wigner shapes with M = 1386 MeV, Γ = 53 MeV for the $Y_0^*(1405)$ and M = 1517 MeV, Γ = 18 MeV for the $Y_0^*(1520)$. The abscissae for the histograms are in units of BeV. The coordinates of the Dalitz plots are in units of BeV^2.

Fig. 12. Effective-mass histograms and Dalitz plots for $\Sigma^0 K^+ \pi^-$ at 1.8 to 2.2 BeV/c (a, d, g, j), 2.9 to 3.3 BeV/c (b, e, h, k), and 3.8 to 4.2 BeV/c (c, f, i, l). The curves are for phase space and an S-wave Breit-Wigner shape with M = 891 MeV, Γ = 44 MeV for the $K^*(890)$. The abscissae for the histograms are in units of BeV. The coordinates of the Dalitz plots are in units of BeV^2.

Fig. 13. Effective-mass histograms and Dalitz plots for $\Sigma^- K^+ \pi^0$ at 1.8 to 2.2 BeV/c (a, d, g, j), 2.9 to 3.3 BeV/c (b, e, h, k), and 3.8 to 4.2 BeV/c (c, f, i, l). The curves are for phase space and an S-wave Breit-Wigner shape with M = 885 MeV, Γ = 51 MeV for the $K^*(890)$. The abscissae for the histograms are in units of BeV. The coordinates of the Dalitz plots are in units of BeV^2.

Fig. 14. Effective-mass histograms and Dalitz plots for $\Sigma^- K^0 \pi^+$ at 1.8 to 2.2 BeV/c (a, d, g, j), 2.9 to 3.3 BeV/c (b, e, h, k), and 3.8 to 4.2 BeV/c (c, f, i, l). The curves are for phase space and S-wave Breit-Wigner shapes with M = 1386 MeV, Γ = 53 MeV for the $Y_0^*(1405)$, M = 1517 MeV, Γ = 18 MeV for the $Y_0^*(1520)$, and M = 885 MeV, Γ = 51 MeV for the $K^*(890)$. The abscissae for the histograms are in units of BeV. The coordinates of the Dalitz plots are in units of BeV^2.

Fig. 15. Effective-mass histograms and Dalitz plots for $\Lambda K^+\pi^-$ at 1.8 to 2.2 BeV/c (a, d, g, j), 2.9 to 3.3 BeV/c (b, e, h, k), and 3.8 to 4.2 BeV/c (c, f, i, l). The curves are for phase space and S-wave Breit-Wigner shapes with M = 1385 MeV, Γ = 41 MeV for the $Y_1^*(1385)$, M = 891 MeV, Γ = 44 MeV for the $K^*(890)$, and M = 1446 MeV, Γ = 61 MeV for the $K^*(1440)$. The abscissae for the histograms are in units of BeV. The coordinates of the Dalitz plots are in units of BeV^2.

Fig. 16. Effective-mass histograms and Dalitz plots for $\Lambda K^0\pi^0$ at 1.8 to 2.2 BeV/c (a, d, g, j), 2.9 to 3.3 BeV/c (b, e, h, k), and 3.8 to 4.2 BeV/c (c, f, i, l). The curves are for phase space and S-wave Breit-Wigner shapes with M = 1380 MeV, Γ = 43 MeV for the $Y_1^*(1385)$, and M = 891 MeV, Γ = 44 MeV for the $K^*(890)$. The abscissae for the histograms are in units of BeV. The coordinates of the Dalitz plots are in units of BeV^2.

Fig. 17. Effective-mass histograms and Dalitz plots for $pK_1^0K^-$ at 1.6 to 2.4 BeV/c (a, d, g, j), 2.9 to 3.3 BeV/c (b, e, h, k), and 3.8 to 4.2 BeV/c (c, f, i, l). The curves are for S-wave Breit-Wigner shapes with M = 1317 MeV, Γ = 50 MeV for the A_2, M = 1518.9 MeV, Γ = 16 MeV for the $Y_0^*(1520)$, and M = 1815 MeV, Γ = 50 MeV for the $Y_0^*(1815)$. The abscissae for the histograms are in units of BeV. The coordinates of the Dalitz plots are in units of BeV^2.

Fig. 18. Effective-mass histograms and Dalitz plots for $nK_1^0K_1^0$ at 1.6 to 2.4 BeV/c (a, d, g), 2.9 to 3.3 BeV/c (b, e, h), and 3.8 to 4.2 BeV/c (c, f, i). In (a, b, c, g, h, i) each event appears twice. The curves are for phase space and

S-wave Breit-Wigner shapes with M = 1317 MeV, Γ = 50 MeV for the A_2, M = 1518.9 MeV, Γ = 16 MeV for the $Y_0^*(1520)$, M = 1815 MeV, Γ = 50 MeV for the $Y_0^*(1815)$, and M = 982 MeV, Γ = 30 MeV for the $K\bar{K}$ threshold enhancement. The abscissae of the histograms are in units of BeV. The coordinates of the Dalitz plots are in units of BeV^2.

Fig. 19. Effective-mass histograms and Dalitz plots for nK^+K^- at 1.5 to 2.3 BeV/c (a, d, g, j), 2.9 to 3.3 BeV/c (b, e, h, k), and 3.8 to 4.2 BeV/c (c, f, i, l). The curves are for phase space and S-wave Breit-Wigner shapes with M = 1021 MeV, Γ = 10 MeV for the ϕ, and M = 982 MeV, Γ = 30 MeV for the $K\bar{K}$ threshold enhancement. The abscissae for the histograms are in units of BeV. The coordinates of the Dalitz plots are in units of BeV^2.

Fig. 20. Coordinate frames. (a) Production systems in the production center of mass. (b) Meson system in its center of mass. (c) Baryon system in its center of mass. (d) $K\bar{K}\pi$ system in the $K\bar{K}$ center of mass.

Fig. 21. Angular distributions for the $Y_0^*(1405)$ [$1346 \leq M(\Sigma\pi) \leq 1426$ MeV] from $\Sigma^{\pm}K^0\pi^{\mp}$ final states at 1.8 to 2.2 BeV/c. The angles are defined in Fig. 20. Each event has been weighted to correct for detection efficiency (see Section III D).

Fig. 22. Angular distributions (a-d) for the $Y_1^{*0}(1385)$ [$1346 \leq M(\Lambda\pi^0) \leq 1410$ MeV] (e-h) for the $Y_0^*(1520)$ [$1493 \leq M(\Sigma^+\pi^-, pK^-) \leq 1537$ MeV]. Data are from 1.8 to 2.2 BeV/c. Angles are defined in Fig. 20. Each event has been weighted to correct for detection efficiency (see Section III D).

Fig. 23. Effective-mass distribution of the lambda + missing mass from the final state ΛK^0 + mm. $\Lambda\pi^0\pi^0$ and $\Sigma^0\pi^0$ are the most likely contributors to this histogram.

Fig. 24. Angular distributions for (a-d) $K^{*0}(890)$ [$861 \leq M(K\pi) \leq 921$ MeV] from $\Sigma^0 K^{*0}$ and for (e-h) $K^{*+}(890)$ for $\Sigma^- K^{*+}$. Data are from 1.8 to 2.2 BeV/c. Angles are defined in Fig. 20. Each event has been weighted to correct for detection efficiency (see Section III D).

Fig. 25. Angular distributions for $K^{*0}(890)$ from $\Sigma^0 K^{*0}$ at (a-d) 2.9 to 3.3 BeV/c and (e-h) 3.8 to 4.2 BeV/c. Histograms of $\cos\theta$, $\cos\xi$, and ϕ are for events with $0.5 \leq \cos\theta_{prod} \leq 1.0$. Angles are defined in Fig. 20. Each event has been weighted to correct for detection efficiency (see Section IIID).

Fig. 26. Angular distributions for $K^{*0}(890)$ from ΛK^{0*} at (a-d) 2.9 to 3.3 BeV/c and (e-h) 3.8 to 4.2 BeV/c. Histograms of $\cos\theta$, $\cos\xi$, and ϕ are for events with $0.5 \leq \cos\theta_{prod} \leq 1.0$. Angles are defined in Fig. 20. Each event has been weighted to correct for detection efficiency (see Section III D).

Fig. 27. Angular distributions for the $K^*(1440)$ [$1400 \leq M(K^+\pi^-) \leq 1490$ MeV] from $\Lambda K^+\pi^-$ events at 3.8 to 4.2 BeV/c. Angles are defined in Fig. 20. Distributions (b) and (c) are folded. The events are weighted for detection efficiency (Section III D).

Fig. 28. Distribution of the effective mass recoiling against a Λ. (a) $K^+\pi^0\pi^-$ and $K^0\pi^+\pi^-$ with $861 \leq M(K^+\pi^0, K^0\pi^+) \leq 921$ MeV. (b) $K^+\pi^0\pi^-$ with $861 \leq M(K^+\pi^-) \leq 921$ MeV. (c) $K^+\pi^0\pi^-$ with $700 \leq M(\pi^0\pi^-) \leq 800$ MeV. (d) $K^0\pi^+\pi^-$ with $700 \leq M(\pi^+\pi^-) \leq 800$ MeV. (e) K^0 + mm with $500 \leq$ mm ≤ 600 MeV. (f) $K^0\pi^+\pi^0\pi^-$ with $750 \leq M(\pi^+\pi^0\pi^-) \leq 810$ MeV. Events at 3.8 to 4.2 BeV/c are used.

Fig. 29. Chew-Low plots for pK^0K^- and $nK_1^0K_1^0$ at 1.6 to 2.4 BeV/c (a, d), 2.9 to 3.3 BeV/c (b, e), and 3.8 to 4.2 BeV/c (c, f). Scales are in units of BeV^2 and $(BeV/c)^2$.

Fig. 30. Angular correlations for the A_2^- ($1267 \leq M(K\bar{K}) \leq 1367$ MeV) at 2.9 to 3.3 BeV/c (a, b, c), the A_2^0 at 2.9 to 3.3 BeV/c (d, e, f), the A_2^- at 3.8 to 4.2 BeV/c (g, h, i), and the A_2^0 at 3.8 to 4.2 BeV/c (j, k, l). The shaded events have $\Delta^2 \leq 0.96$ $(BeV/c)^2$. The curves on (b) and (c) are the best fits to the density-matrix elements. The curve on (e) is for 20% flat background plus 80% pseudoscalar exchange. Angles are defined in Fig. 20. The events are weighted for detection efficiency (Section III D). In (e, f, k, l) each event appears twice.

Fig. 31. Data from $nK_1^0K_1^0$ final states at all momenta. (a) $K_1^0K_1^0$ effective mass distribution. Curves compare the zero-effective-range approximation with a resonance shape at 1068 MeV. (b) Distribution of Δ^2 to the neutron for events with $M_{K\bar{K}} \leq 1075$ MeV. The curve is the prediction for one-pion-exchange. (c and d) Histograms of $\cos\theta$ and ϕ for events with $M_{K\bar{K}} \leq 1075$ MeV. Two points have been plotted for each event. Angles are defined in Fig. 20. Each event has been weighted to correct for detection efficiency (see Section III D).

Fig. 32. Angular correlations for the ϕ meson compared to those for the $K_1^0K_1^0$ system at 1.5 to 2.3 BeV/c. The curves on (b), (d), and (f) are Monte Carlo distributions for isotropic production and decay angular distributions. Angles are defined in Fig. 20. In (c) and (e) each event appears twice.

Fig. 33. Chew-Low plots for events with beam momentum less than 2.3 BeV/c. (a) $nK_1^0K_1^0$ events. (b) nK^+K^- events.

Fig. 34. Total cross sections for $\pi^+ n \rightarrow p\omega$ from Refs. 81-84. (solid symbols) and $\pi^- p \rightarrow n\phi$ from this experiment (open symbol). The abscissa is the c.m. momentum of the final-state particles. The ordinates differ by a factor of 50.

Fig. 35. Effective-mass histograms based on 617 events from the final state $\Lambda K^+ \pi^0 \pi^-$ at 2.9 to 3.3 BeV/c. (a) $\Lambda\pi^0$ (b) $\Lambda\pi^-$ (c) $K^+\pi^0$ (d) $K^+\pi^-$ (e) $\Lambda\pi^0\pi^-$ (f) $K^+\pi^0\pi^-$. The abscissae are in units of BeV.

Fig. 36. Effective-mass histograms based on 730 events from the final state $\Lambda K^0 \pi^+ \pi^-$ at 2.9 to 3.3 BeV/c. (a) $\Lambda\pi^+$ (b) $\Lambda\pi^-$ (c) $K^0\pi^+$ (d) $K^0\pi^-$ (e) $\Lambda\pi^+\pi^-$ (f) $K^0\pi^+\pi^-$. The abscissae are in units of BeV.

Fig. 37. Effective-mass histograms based on 312 events from the final state $\Lambda K^+ \pi^0 \pi^-$ at 3.8 to 4.2 BeV/c. (a) $\Lambda\pi^0$ (b) $\Lambda\pi^-$ (c) $K^+\pi^0$ (d) $K^+\pi^-$ (e) $\Lambda\pi^0\pi^-$ (f) $K^+\pi^0\pi^-$. The abscissae are in units of BeV.

Fig. 38. Effective-mass histograms based on 346 events from the final state $\Lambda K^0 \pi^+ \pi^-$ at 3.8 to 4.2 BeV/c. (a) $\Lambda\pi^+$ (b) $\Lambda\pi^-$ (c) $K^0\pi^+$ (d) $K^0\pi^-$ (e) $\Lambda\pi^+\pi^-$ (f) $K^0\pi^+\pi^-$. The abscissae are in units of BeV.

Fig. 39. Effective-mass histogram based on 218 events of $K\pi\pi$ from the final states $\Lambda K\pi\pi$ at 2.9 to 3.3 BeV/c. We have used events in which one of the $K\pi$ systems is in the $K^*(890)$ band [$861 \leq M(K\pi) \leq 921$ MeV] and in which neither of the $\Lambda\pi$ systems is in the $Y_1^*(1385)$ band [$1350 \leq M(\Lambda\pi) \leq 1410$ MeV]. The abscissa is in units of BeV.

Fig. 40. Effective-mass distributions of $\Lambda\pi\pi$ from the final states $\Lambda K\pi\pi$ at 2.9 to 3.3 BeV/c. We have used events in which one of the $\Lambda\pi$ systems is in the $Y_1^*(1385)$ band [$1350 \leq M(\Lambda\pi) \leq 1410$ MeV]. (a) $\Lambda\pi^+\pi^-$ (b) $\Lambda\pi^0\pi^-$. The abscissae are in units of BeV.

Fig. 41. Effective-mass histograms and scatter plot for $(\Sigma\pi)^0$ and $(K\pi)^0$ systems at 2.9 to 3.3 BeV/c. The scales are in units of BeV.

Fig. 42. Effective-mass histograms for the $nK\bar{K}\pi$ final states at 2.9 to 3.3 BeV/c. The abscissae are in units of BeV.

Fig. 43. Effective-mass histograms for the $nK\bar{K}\pi$ final states at 3.8 to 4.2 BeV/c. The abscissae are in units of BeV.

Fig. 44. Effective-mass histograms for the $pK^+K^-\pi^-$, $pK^0K^-\pi^0$, and $pK^0\bar{K}^0\pi^-$ final states at 2.9 to 3.3 BeV/c. a, b, i, and j contain events from the $pK^+K^-\pi^-$ and $pK^0K^-\pi^0$ final states. c and k use only the $PK^0\bar{K}^0\pi^-$ final state. The abscissae are in units of BeV.

Fig. 45. Effective-mass histograms for $pK\bar{K}\pi$ final states at 3.8 to 4.2 BeV/c. The format is the same as in Fig. 44.

Fig. 46. Data from $pK\bar{K}\pi$ final states (a, c, e) and $nK\bar{K}\pi$ final states (b, d, f) for all beam momenta. (a) and (b) Effective mass histograms of $K\bar{K}\pi$ (c) and (d) Scatter plots of the $K\pi$ and $\bar{K}\pi$ effective masses vs the $K\bar{K}\pi$ effective mass. Two points plotted per event. (e) and (f) Scatter plots of Δ^2 to the nucleon vs the $K\bar{K}\pi$ effective mass. The effective masses are in units of BeV, Δ^2 is in units of $(\text{BeV/c})^2$.

Fig. 47. Data from $nK\bar{K}\pi$ final states. (a) and (b) Scatter plots of the $K\pi$ and $\bar{K}\pi$ effective masses vs the $K\bar{K}\pi$ effective mass at 2.9 to 3.3 BeV/c and 3.8 to 4.2 BeV/c. (c) Production angular distribution for the D meson ($1.245 \text{ BeV} \leq M_{K\bar{K}\pi} \leq 1.325$ BeV). (d) Production angular distribution for the E meson ($1.360 \text{ BeV} \leq M_{K\bar{K}\pi} \leq 1.480$ BeV and the $\bar{K}\pi$ or $K\pi$ effective mass in the 0.841 to 0.941-

BeV interval). Effective masses are in units of BeV. Each event has been weighted to correct for detection efficiency (see Section III D). In (a) and (b) two points are plotted per event.

Fig. 48. Decay correlations for the D (a, c, e) and the E (b, d, f) mesons. Same mass intervals as those used in Fig. 47 except no restrictions on the $K\pi$ and $\bar{K}\pi$ effective masses. (a) and (b) Decay Dalitz plots. Arrows indicate the $K^*(891)$ and $\bar{K}^*(891)$ bands. The envelopes are for (a) 1.325 BeV and (b) 1.480 BeV. (c and d) $K\bar{K}$ effective-mass distributions. (e and f) Distribution in $\cos\theta_{K\bar{K}}$ (see Fig. 20); each event plotted twice. Curves represent predictions of the more likely J^P assignments. Coordinates of the Dalitz plots are in BeV^2. Each event has been weighted to correct for detection efficiency (see Section III D).

Fig. 49. Scatter plot of the $K\bar{K}\pi$ effective mass vs the $K\bar{K}$ effective mass for the $pK^0\bar{K}^0\pi^-$ (only one K_1^0 observed to decay) and $pK^+K^-\pi^-$ final states at all momenta. Arrows indicate the locations of the B and ϕ mesons. Scales are in units of BeV.

Fig. 50. Effective-mass histograms from the final-state $\Lambda K^0\pi^+\pi^0\pi^-$ at all momenta (a) $\pi^+\pi^0\pi^-$ (b) $K^0\pi^+\pi^0\pi^-$ for $[750 \leq M(\pi^+\pi^0\pi^-) \leq 810$ MeV]. (c) $\Lambda^0\pi^+\pi^0\pi^-$ for $[750 \leq M(\pi^+\pi^0\pi^-) \leq 810$ MeV]. Abscissae are in units of BeV. The curves are for phase space at 3.2 BeV/c.

Fig. 51. $K\bar{K}\pi\pi$ effective-mass histogram from the $NK\bar{K}\pi\pi$ final states at 3.8 to 4.2 BeV/c.

Fig. 52. Dalitz plot for the reaction $\pi^-p \rightarrow \Xi^-K^+K^0$. The 24 events shown are from all beam momenta. The envelope corresponds to 3.2 BeV/c.

Fig. 53. Center-of-mass angular distributions for (a) the Ξ^-, (b) the K^+ (c) the K^0 from the reaction $\pi^- p \rightarrow \Xi^- K^+ K^0$.

Fig. 54. Differential cross section for events with $0.5 \leq \cos\theta_{prod} \leq 1.0$; and (a to k) the 11 density-matrix parameters described in the text for $\pi^- p \rightarrow \Lambda K^{*0}$ at 2.9 to 3.3 BeV/c with theoretical curves from the absorption model. Best-fit parameters are $g_p^2/4\pi = 1.14$, $g_V = 11.7$, $g_T = -23.3$, $\sigma_f = 58.1$ μb, $A_f = 7.8$ (BeV/c)$^{-2}$, and $\zeta = 0.16$.

Fig. 55. Integrated matrix elements for the D meson. The functional forms are given in Table XXIV.

Fig. 56. Integrated matrix elements for the E meson. The functional forms are given in Table XXIV.

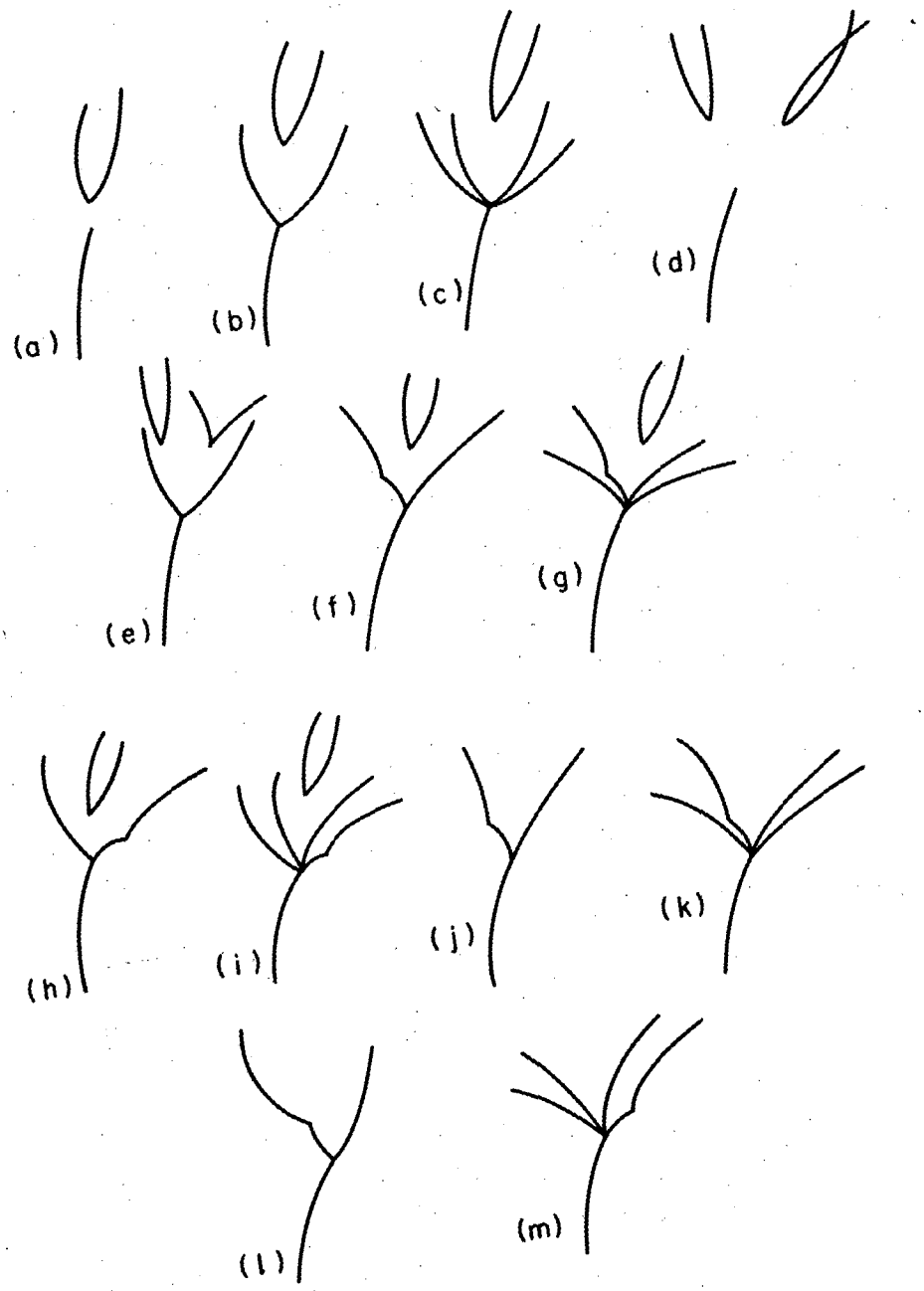

Fig. 1

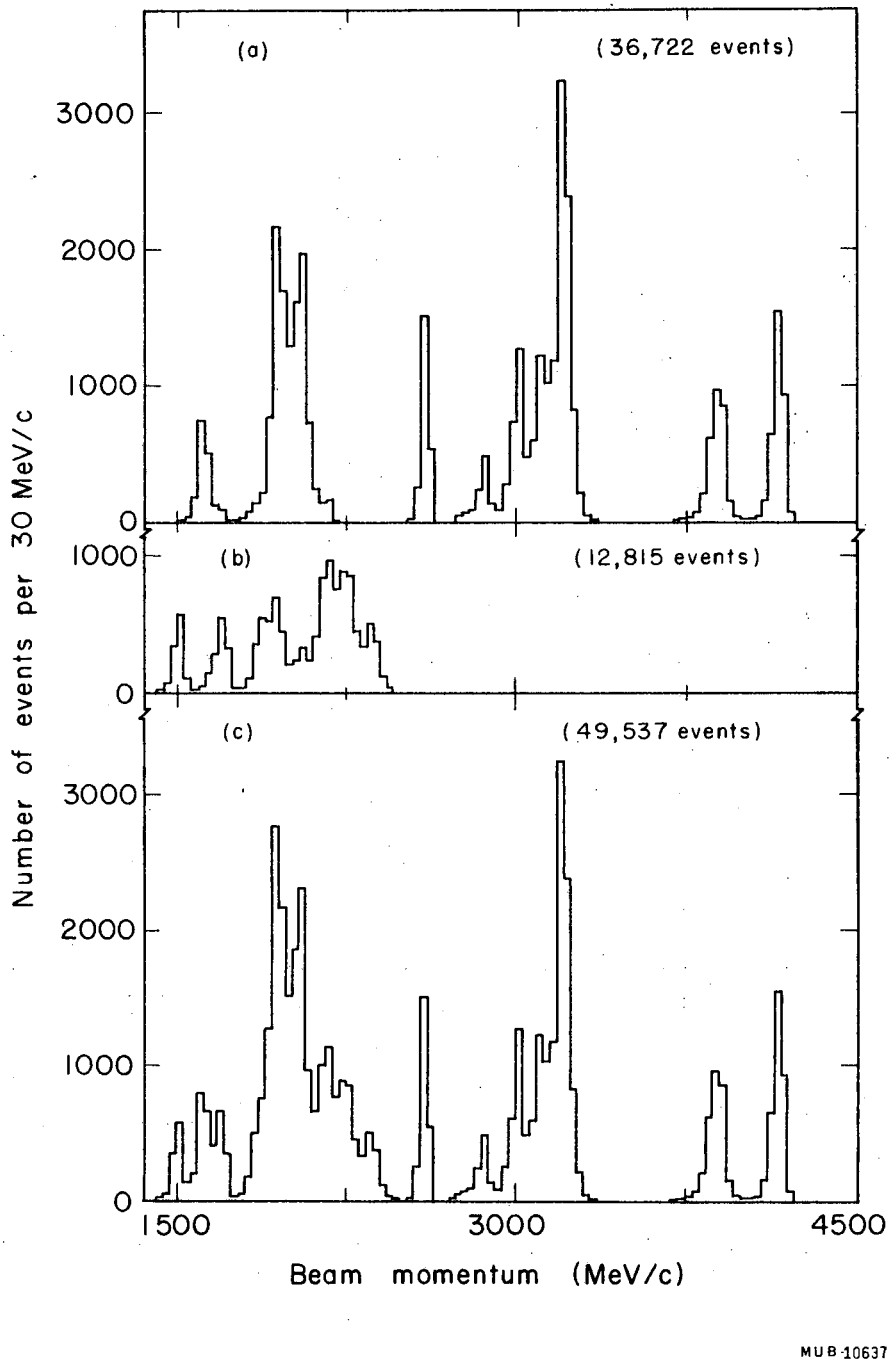
(a)
(36,722 events)
3000
2000
1000
0
(b)
(12,815 events)
1000
0
(c)
(49,537 events)
3000
2000
1000
0
Number of events per 30 MeV/c
1500
3000
4500
Beam momentum (MeV/c)
MUB-10637

Fig. 2

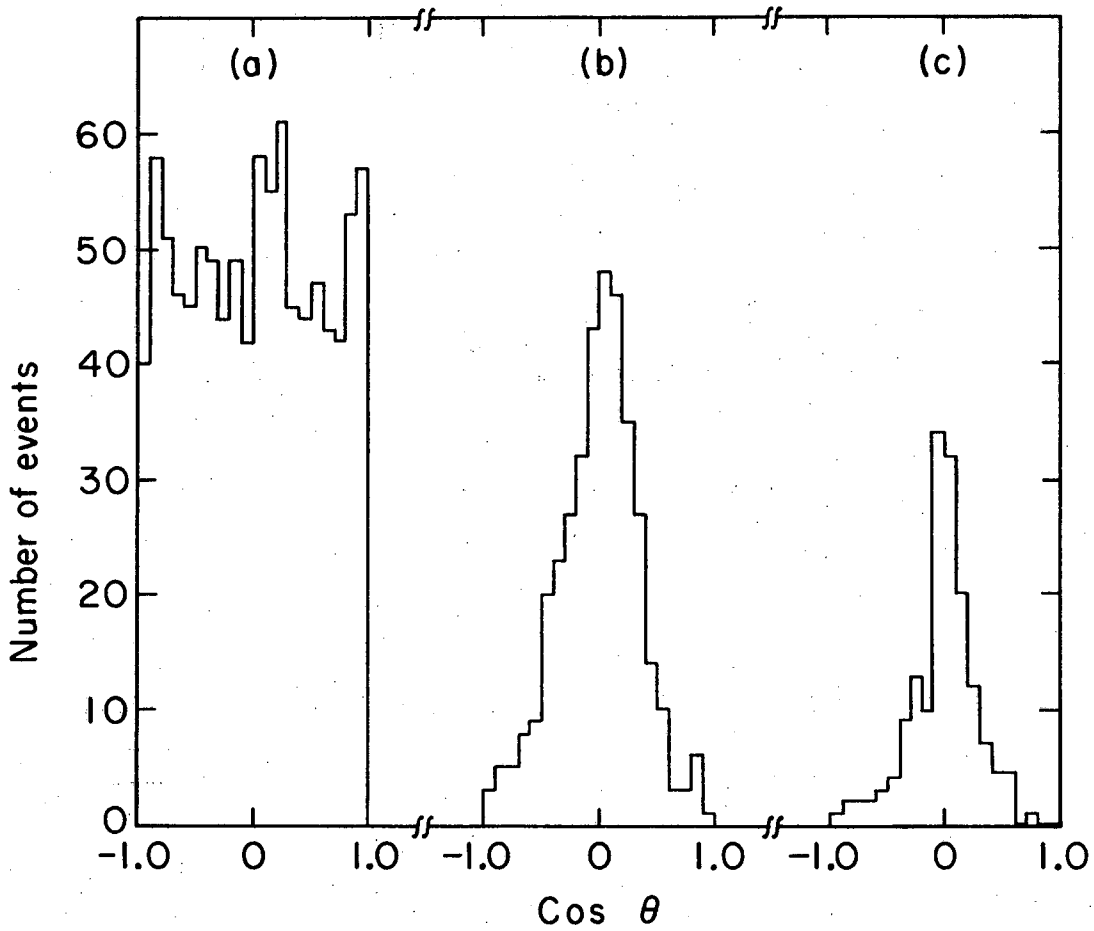
(a)
(b)
(c)
60
50
40
30
20
10
0
Number of events
-1.0
0
1.0
-1.0
0
1.0
-1.0
0
1.0
Cos θ
MUB-9841

Fig. 3

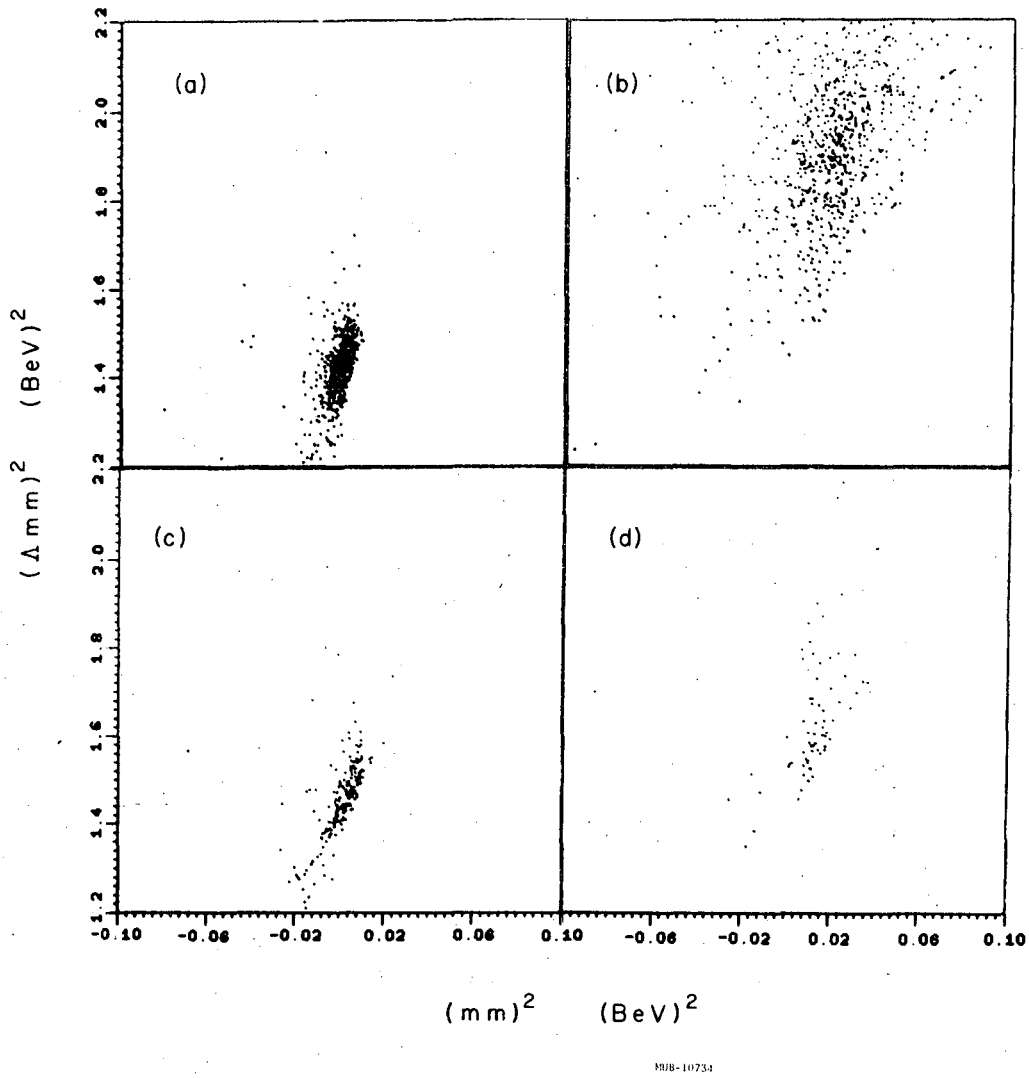
(a)
(b)
(c)
(d)
$(\Delta mm)^2$ (BeV)^2
$(mm)^2$ (BeV)^2
-0.10
-0.06
-0.02
0.02
0.06
0.10
1.2
1.4
1.6
1.8
2.0
2.2
MUB-10734

Fig. 4

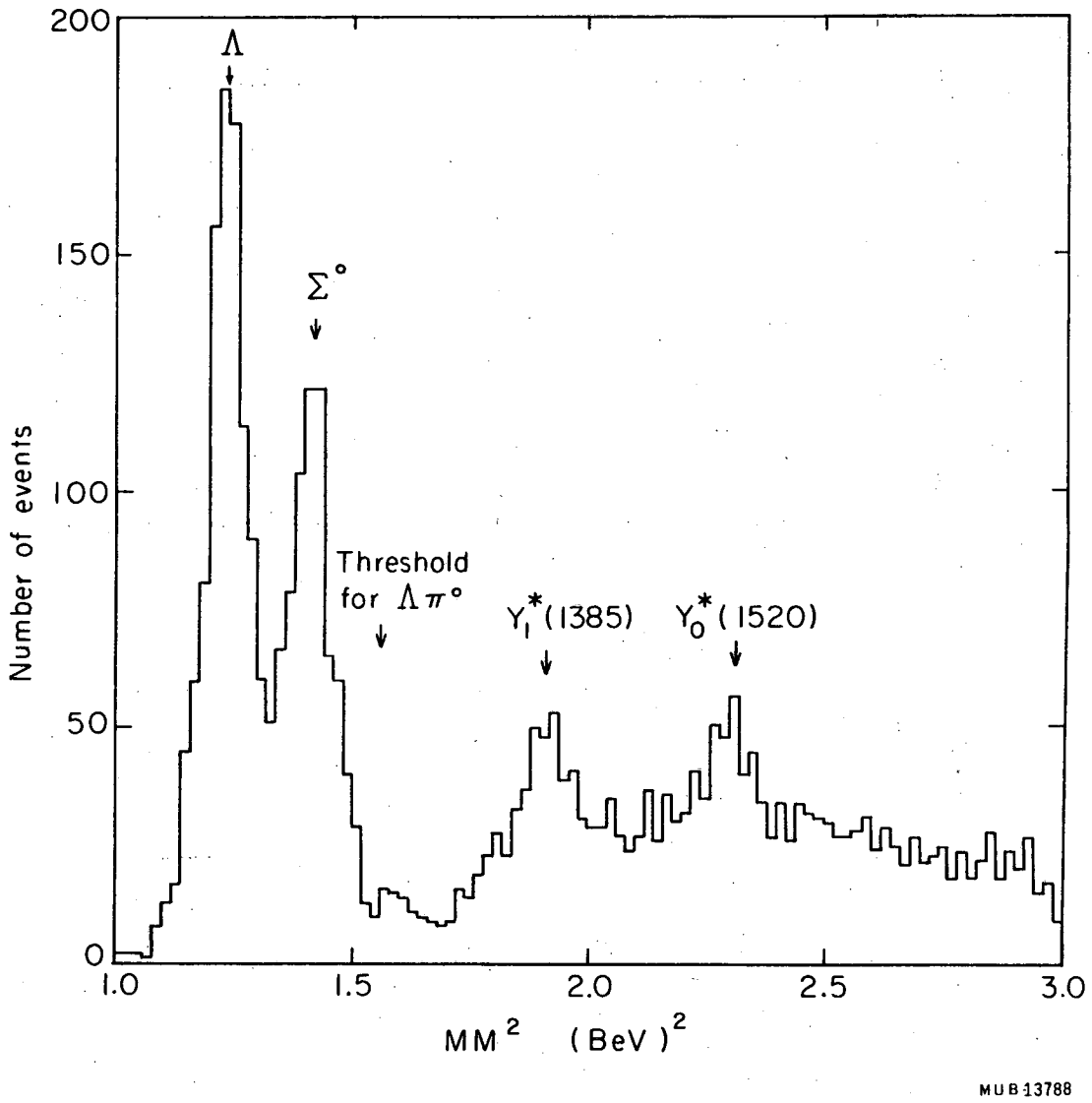
200
150
100
50
0
Number of events
Λ
Σ°
Threshold
for Λπ°
Y₁*(1385)
Y₀*(1520)
1.0
1.5
2.0
2.5
3.0
MM² (BeV)²
MUB-13788

Fig. 5

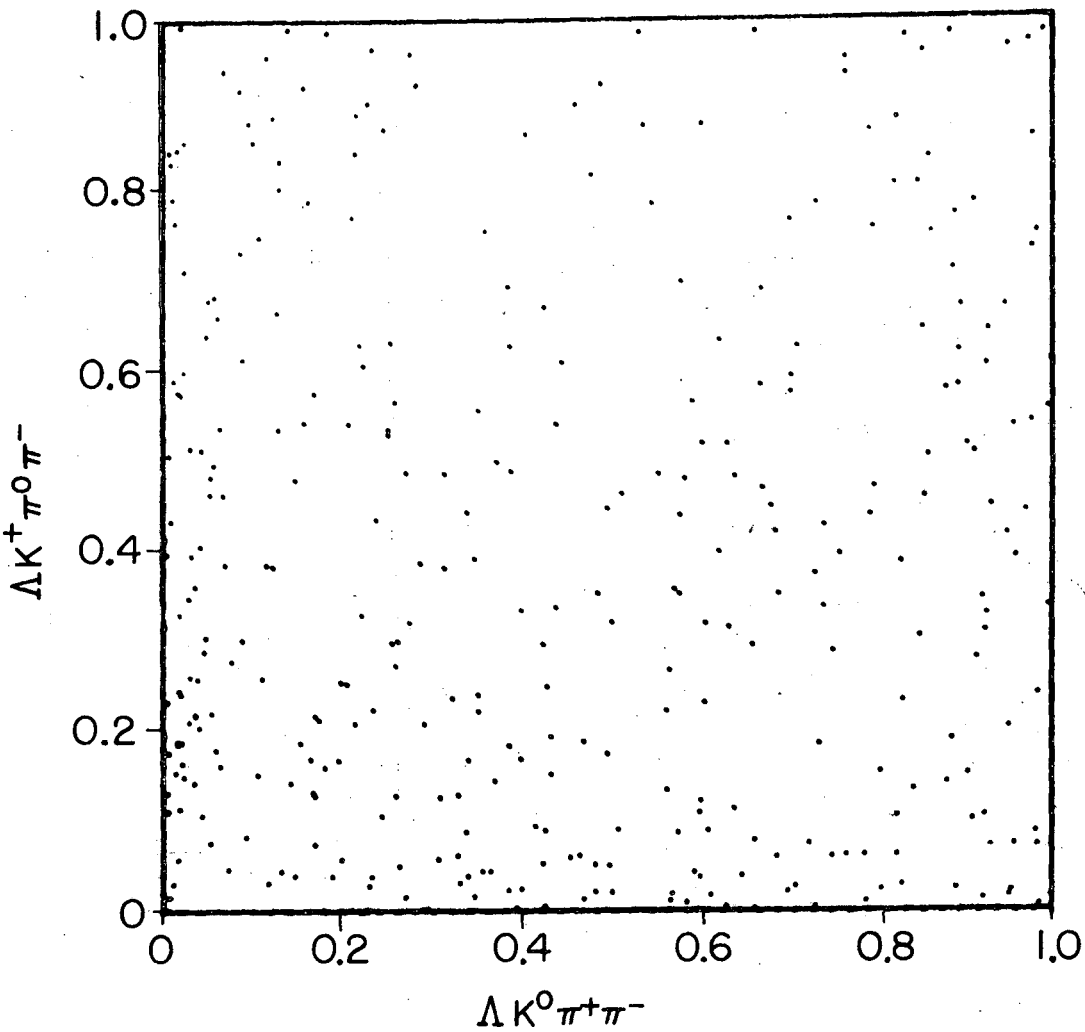

MUB-14128

Fig. 6

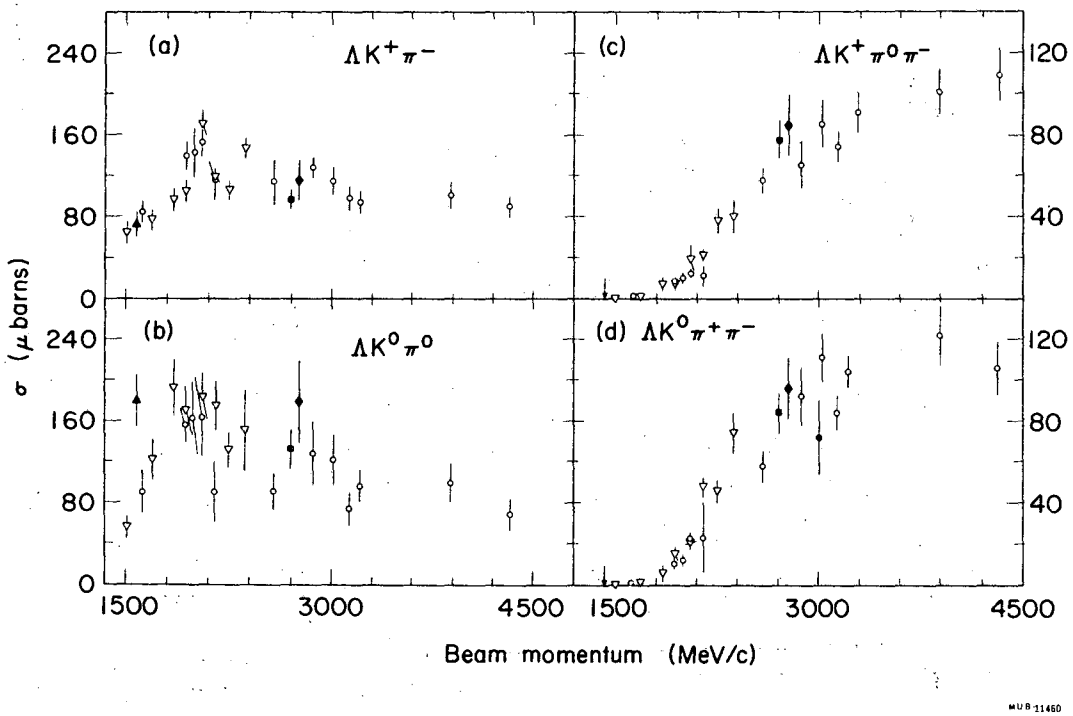
(a) ΛK+π−
(b) ΛK0π0
(c) ΛK+π0π−
(d) ΛK0π+π−
σ (μbarns)
240
160
80
0
120
40
1500
3000
4500
Beam momentum (MeV/c)
MUB-11460

Fig. 7

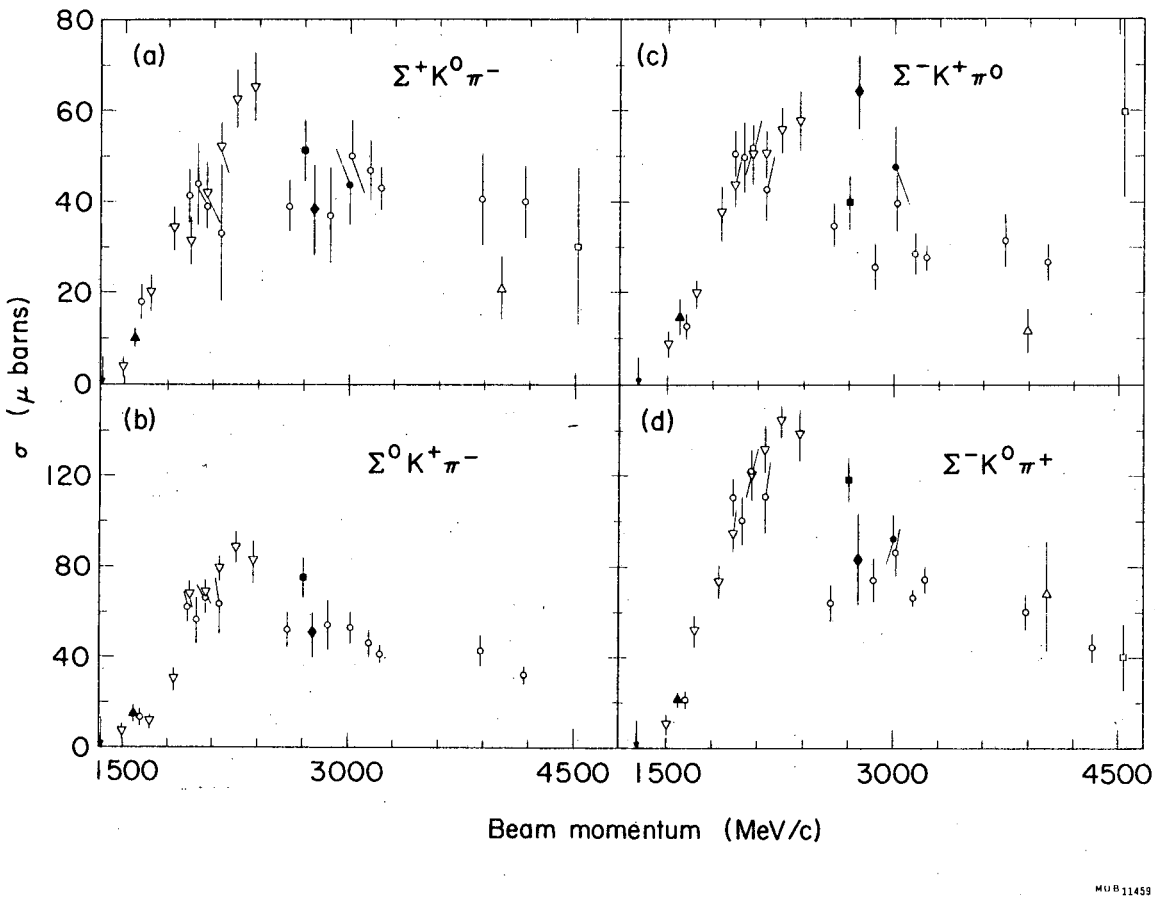
(a)
$\Sigma^+ K^0 \pi^-$
(c)
$\Sigma^- K^+ \pi^0$
(b)
$\Sigma^0 K^+ \pi^-$
(d)
$\Sigma^- K^0 \pi^+$
σ (μ barns)
Beam momentum (MeV/c)
MUB 11459

Fig. 8

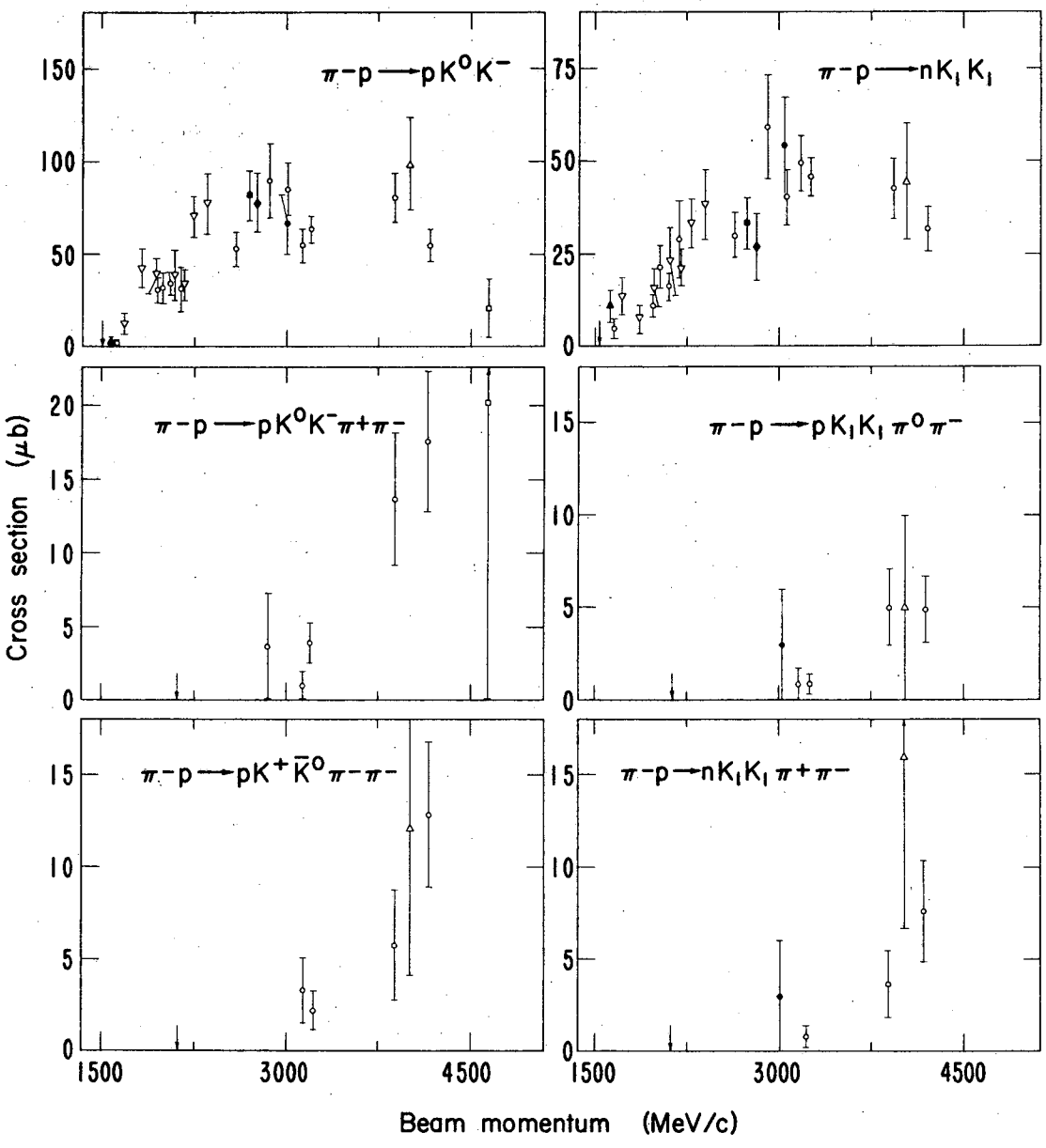
π⁻p → pK⁰K⁻
π⁻p → nK₁K₁
π⁻p → pK⁰K⁻π⁺π⁻
π⁻p → pK₁K₁π⁰π⁻
π⁻p → pK⁺K̄⁰π⁻π⁻
π⁻p → nK₁K₁π⁺π⁻
Cross section (μb)
Beam momentum (MeV/c)
1500
3000
4500
MUB-11233

Fig. 9

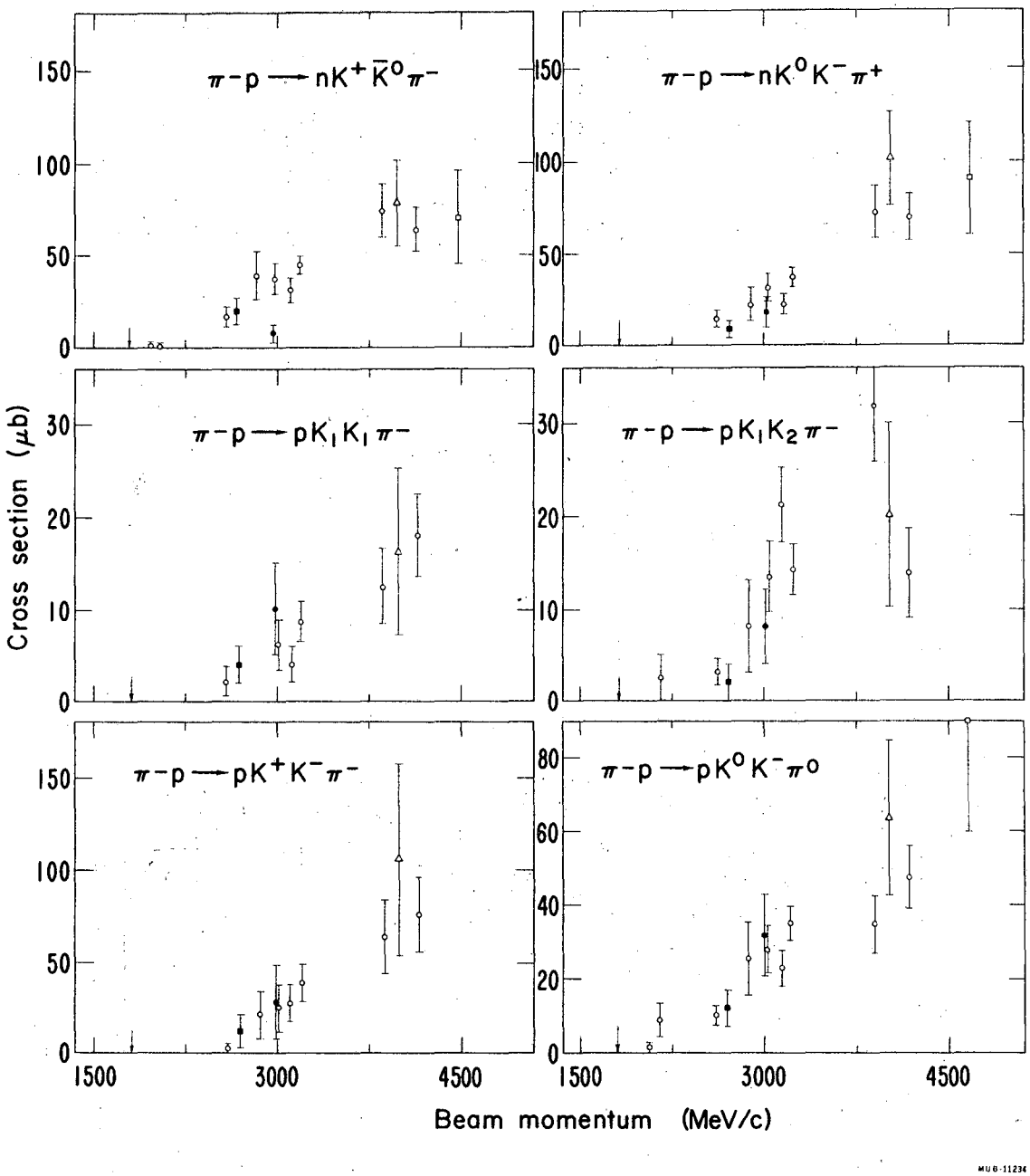
π⁻p → nK⁺K̄⁰π⁻
π⁻p → nK⁰K⁻π⁺
π⁻p → pK₁K₁π⁻
π⁻p → pK₁K₂π⁻
π⁻p → pK⁺K⁻π⁻
π⁻p → pK⁰K⁻π⁰
Cross section (μb)
Beam momentum (MeV/c)
1500
3000
4500
MU6-11234

Fig. 10

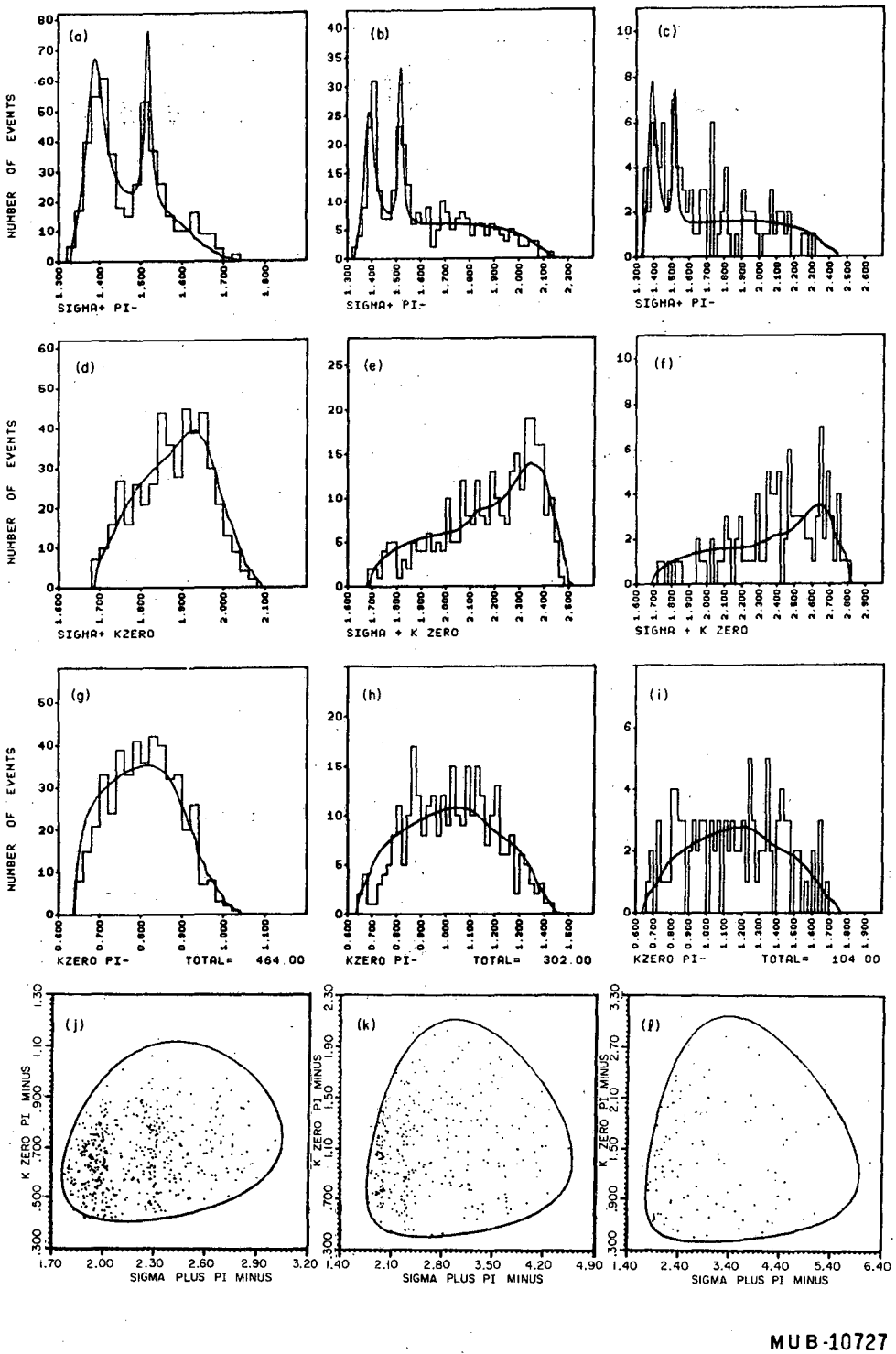
(a)
(b)
(c)
(d)
(e)
(f)
(g)
(h)
(i)
(j)
(k)
(l)
NUMBER OF EVENTS
SIGMA+ PI-
SIGMA+ KZERO
SIGMA + K ZERO
KZERO PI-
TOTAL= 464.00
TOTAL= 302.00
TOTAL= 104.00
K ZERO PI MINUS
SIGMA PLUS PI MINUS
MUB-10727

Fig. 11

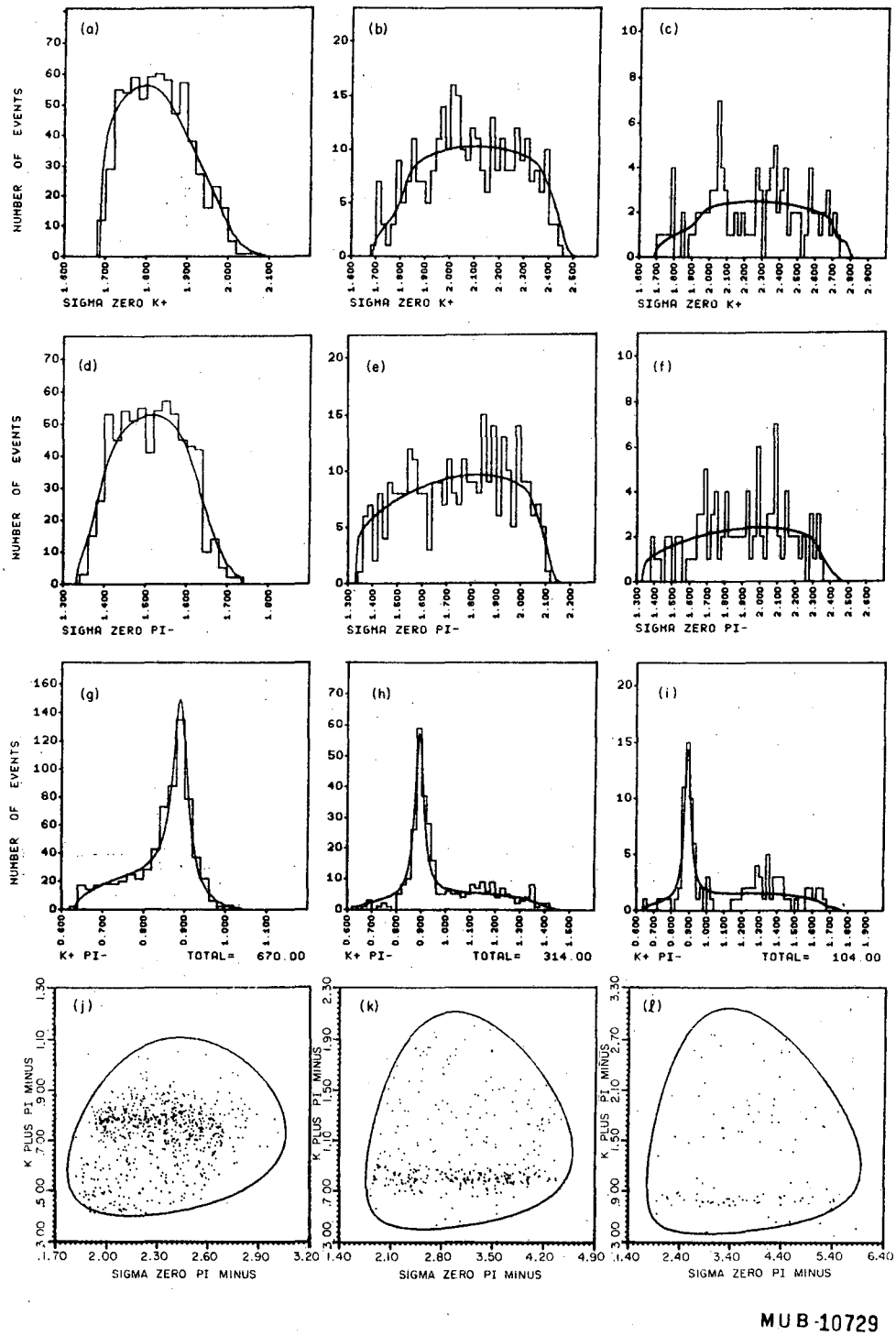
(a)
(b)
(c)
(d)
(e)
(f)
(g)
(h)
(i)
(j)
(k)
(l)
NUMBER OF EVENTS
SIGMA ZERO K+
SIGMA ZERO PI-
K+ PI-
TOTAL= 670.00
TOTAL= 314.00
TOTAL= 104.00
K PLUS PI MINUS
SIGMA ZERO PI MINUS
MUB-10729

Fig. 12

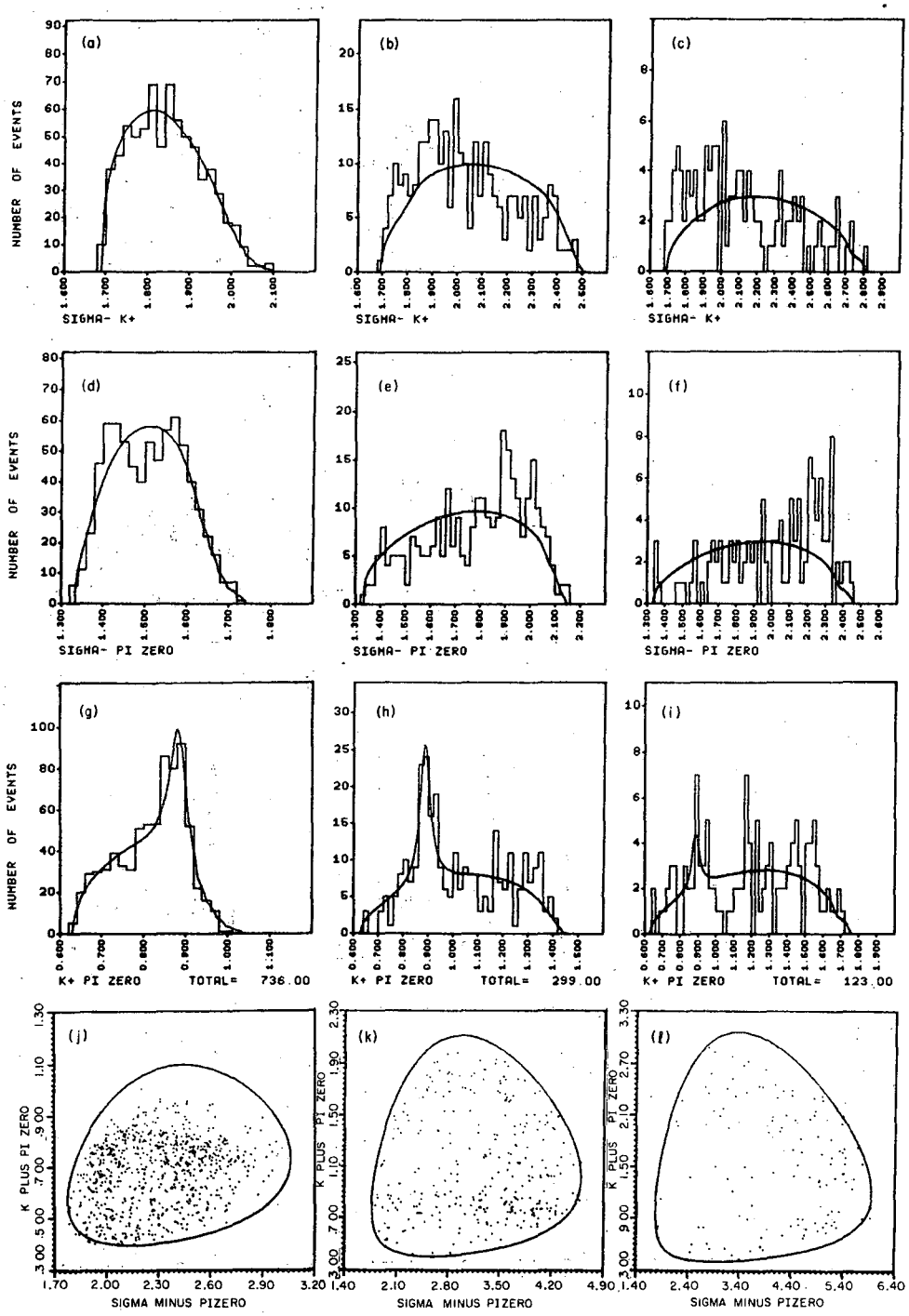
(a)
(b)
(c)
(d)
(e)
(f)
(g)
(h)
(i)
(j)
(k)
(l)
NUMBER OF EVENTS
SIGMA- K+
SIGMA- PI ZERO
K+ PI ZERO
TOTAL= 736.00
TOTAL= 299.00
TOTAL= 123.00
K PLUS PI ZERO
SIGMA MINUS PIZERO
MUB-10730

Fig. 13

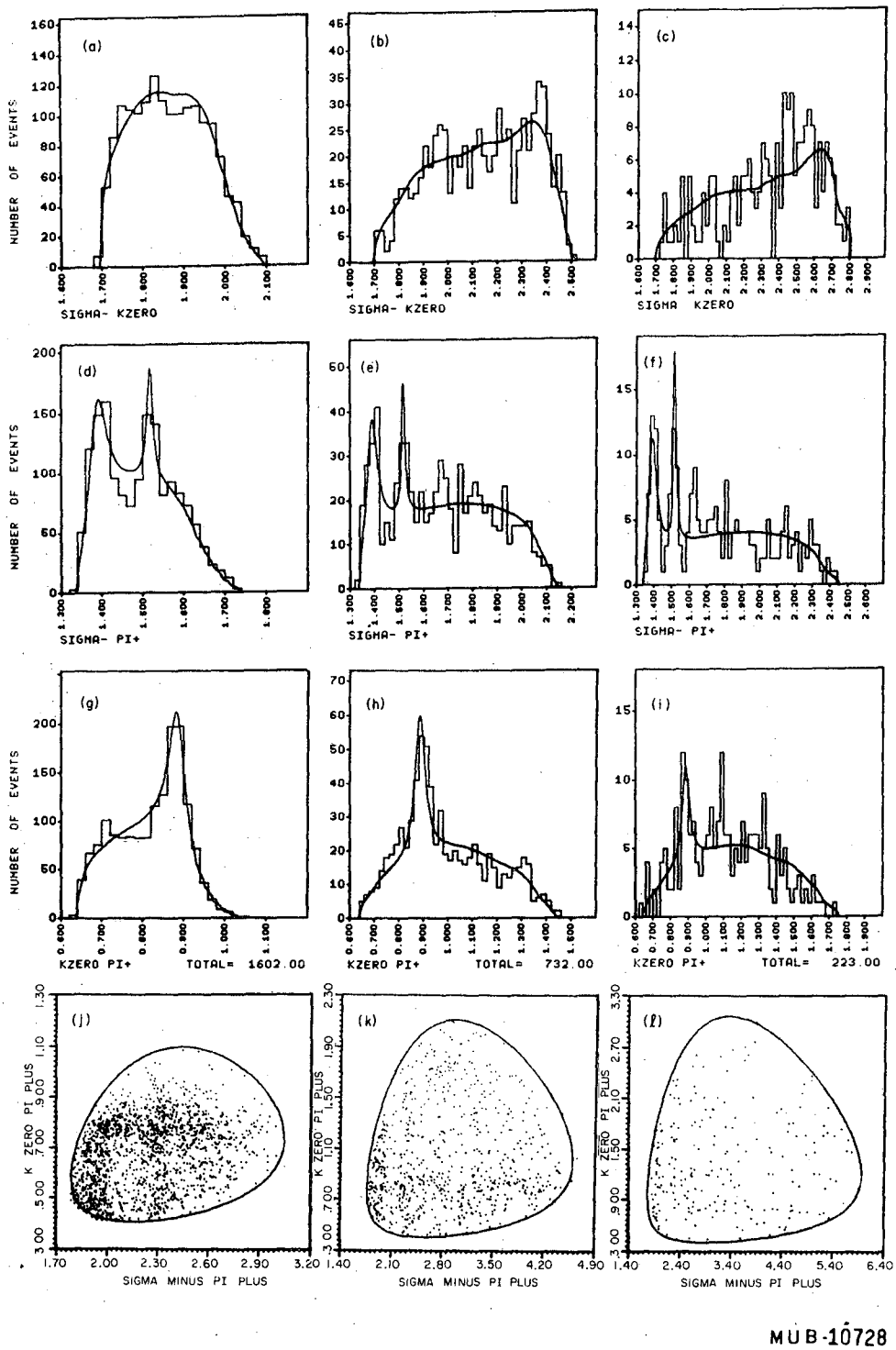
(a)
(b)
(c)
(d)
(e)
(f)
(g)
(h)
(i)
(j)
(k)
(l)
NUMBER OF EVENTS
SIGMA- KZERO
SIGMA KZERO
SIGMA- PI+
KZERO PI+
TOTAL= 1602.00
TOTAL= 732.00
TOTAL= 223.00
K ZERO PI PLUS
SIGMA MINUS PI PLUS
MUB-10728

Fig. 14

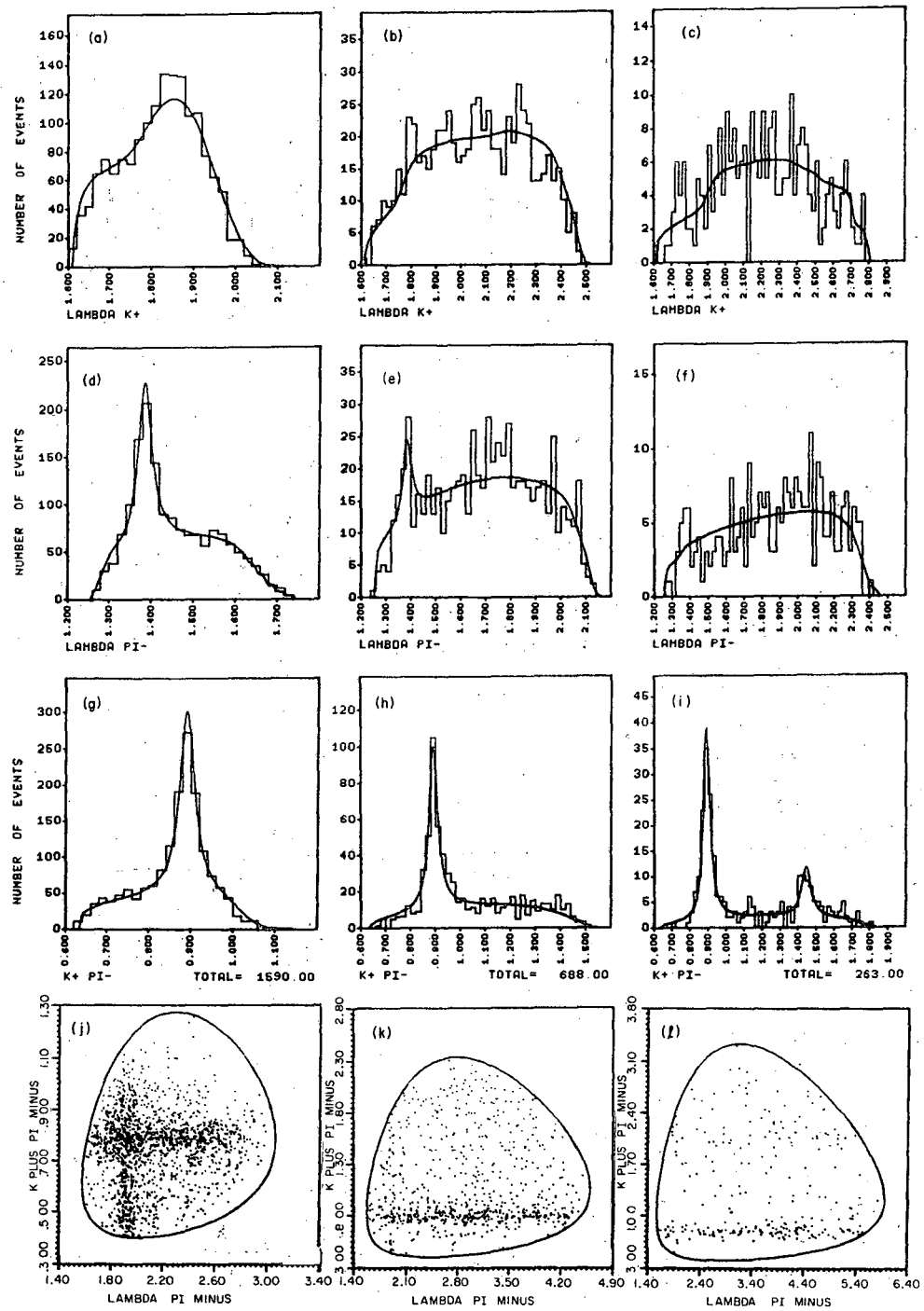
(a)
(b)
(c)
(d)
(e)
(f)
(g)
(h)
(i)
(j)
(k)
(l)
NUMBER OF EVENTS
LAMBDA K+
LAMBDA PI-
K+ PI-
TOTAL= 1590.00
TOTAL= 688.00
TOTAL= 263.00
K PLUS PI MINUS
LAMBDA PI MINUS
MUB-10726

Fig. 15

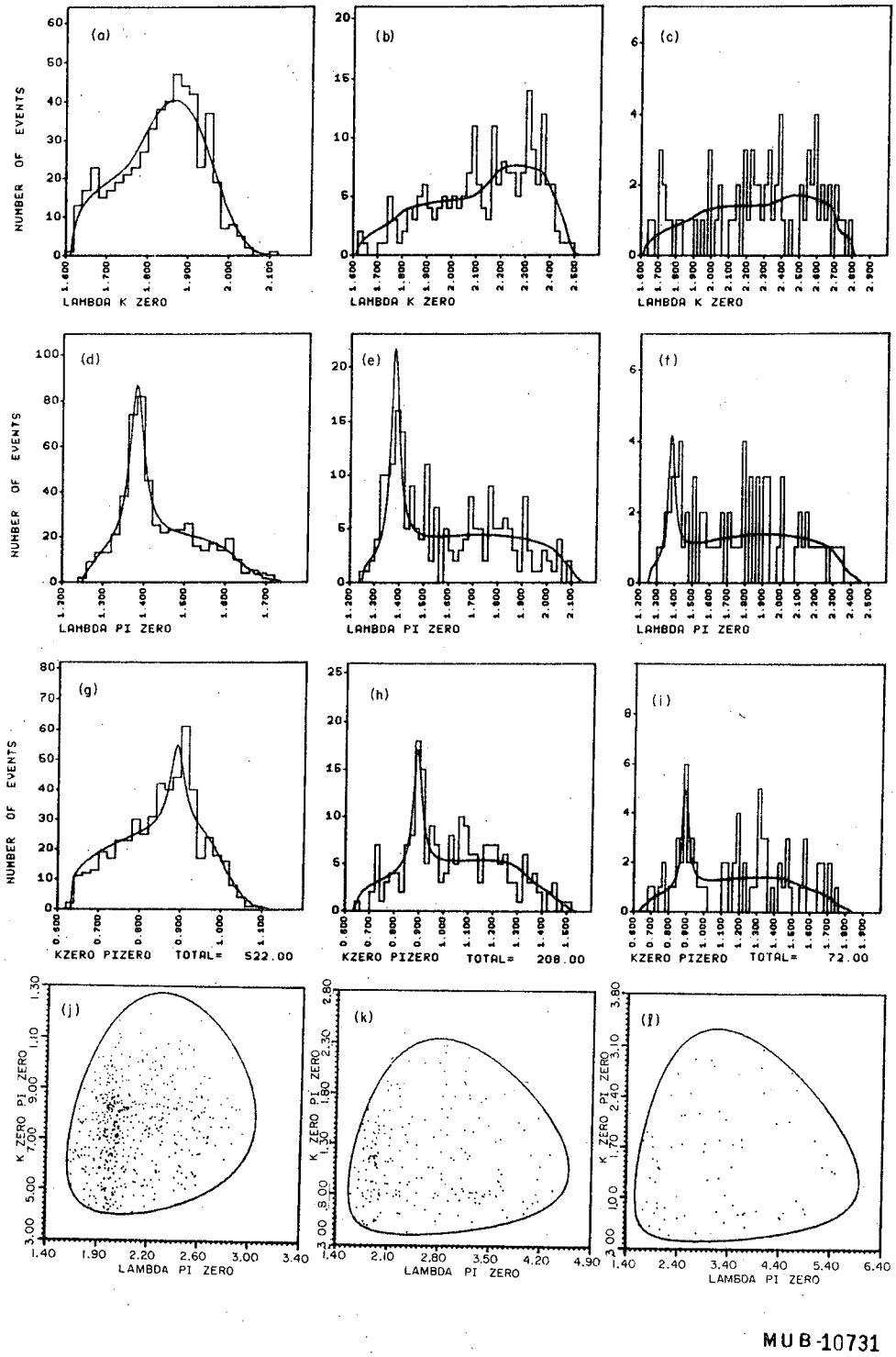
(a)
(b)
(c)
(d)
(e)
(f)
(g)
(h)
(i)
(j)
(k)
(l)
NUMBER OF EVENTS
LAMBDA K ZERO
LAMBDA PI ZERO
KZERO PIZERO TOTAL= 522.00
KZERO PIZERO TOTAL= 208.00
KZERO PIZERO TOTAL= 72.00
K ZERO PI ZERO
LAMBDA PI ZERO
MUB-10731

Fig. 16

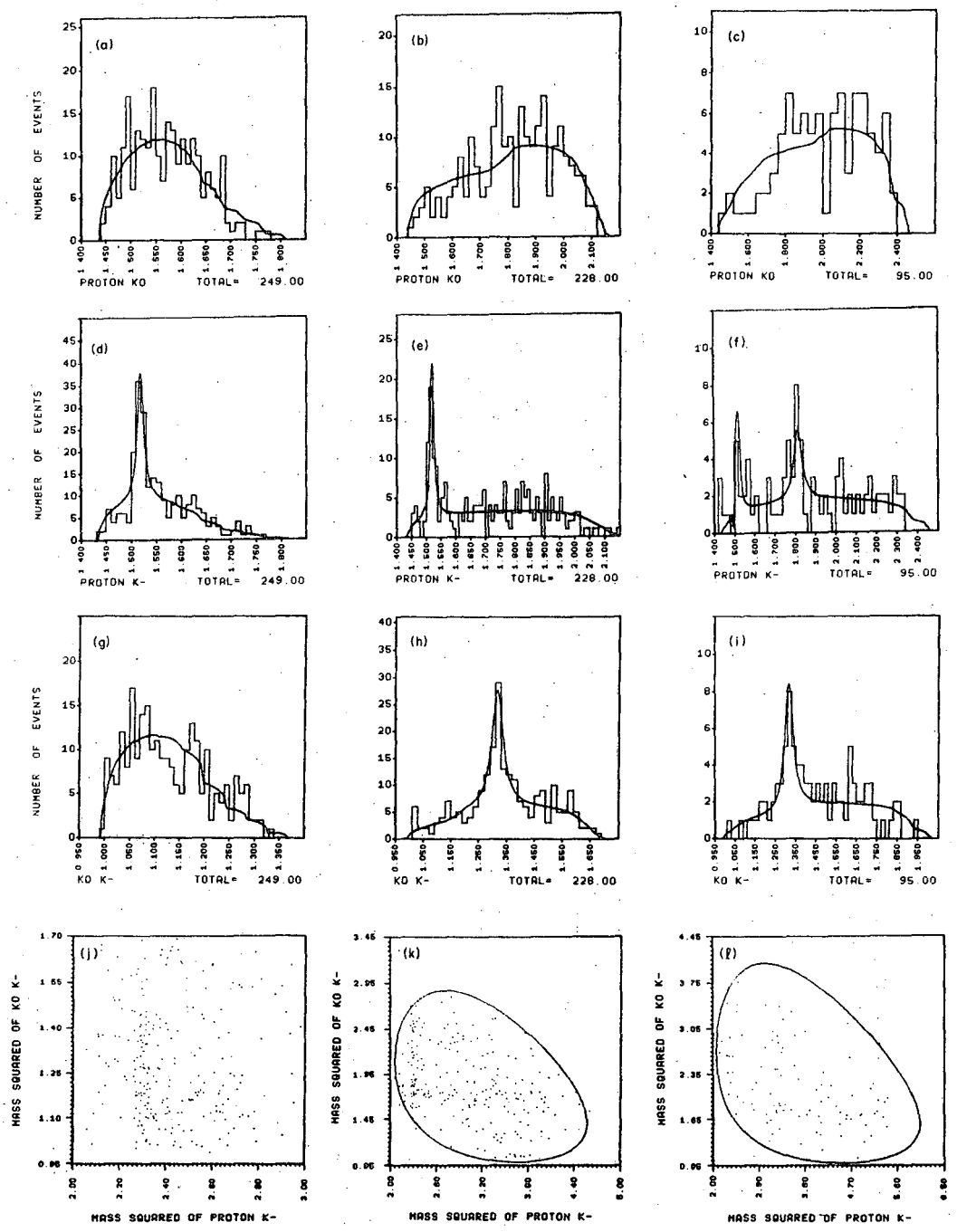

MUB 11453

Fig. 17

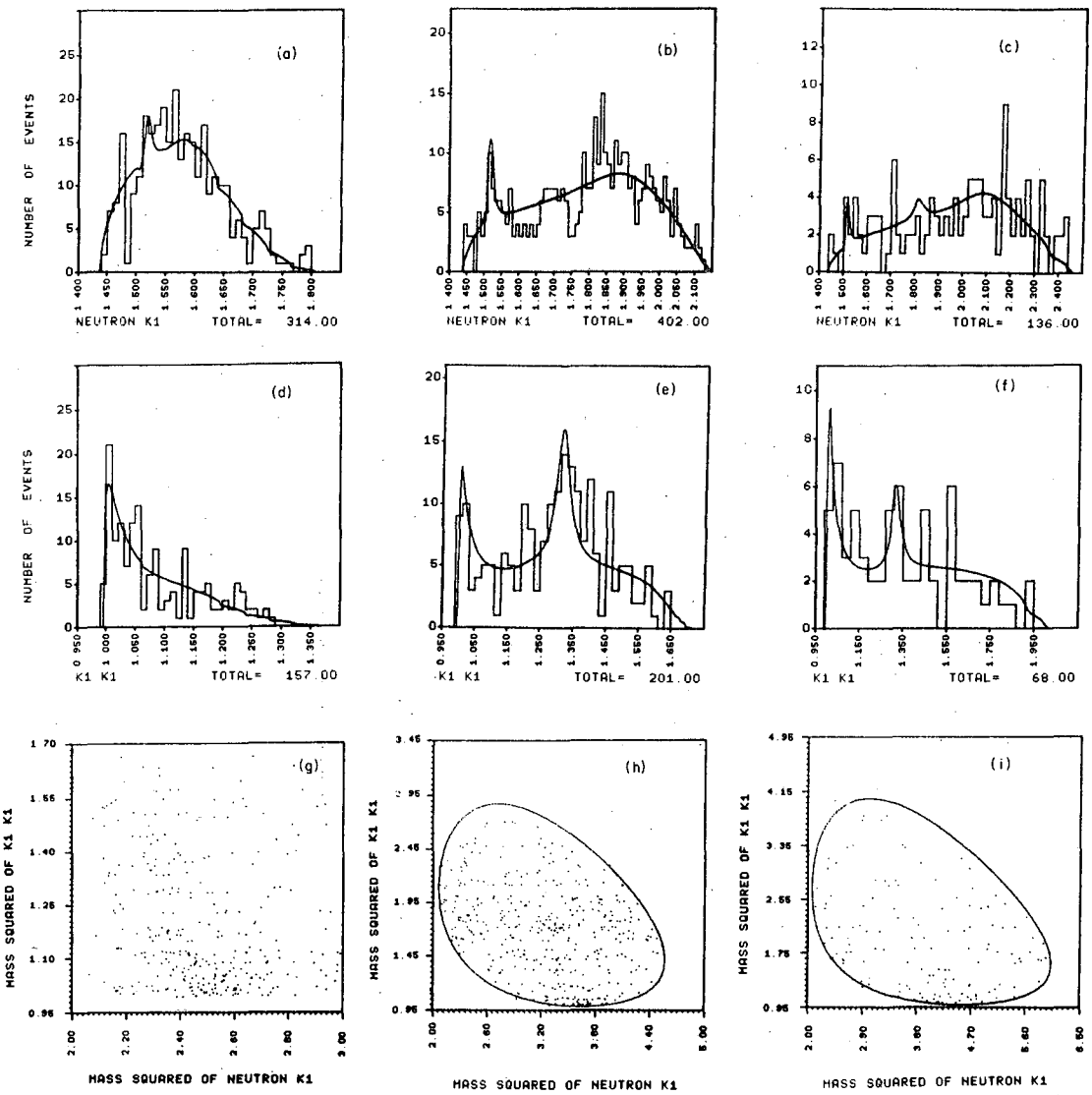

MUB-10774

Fig. 18

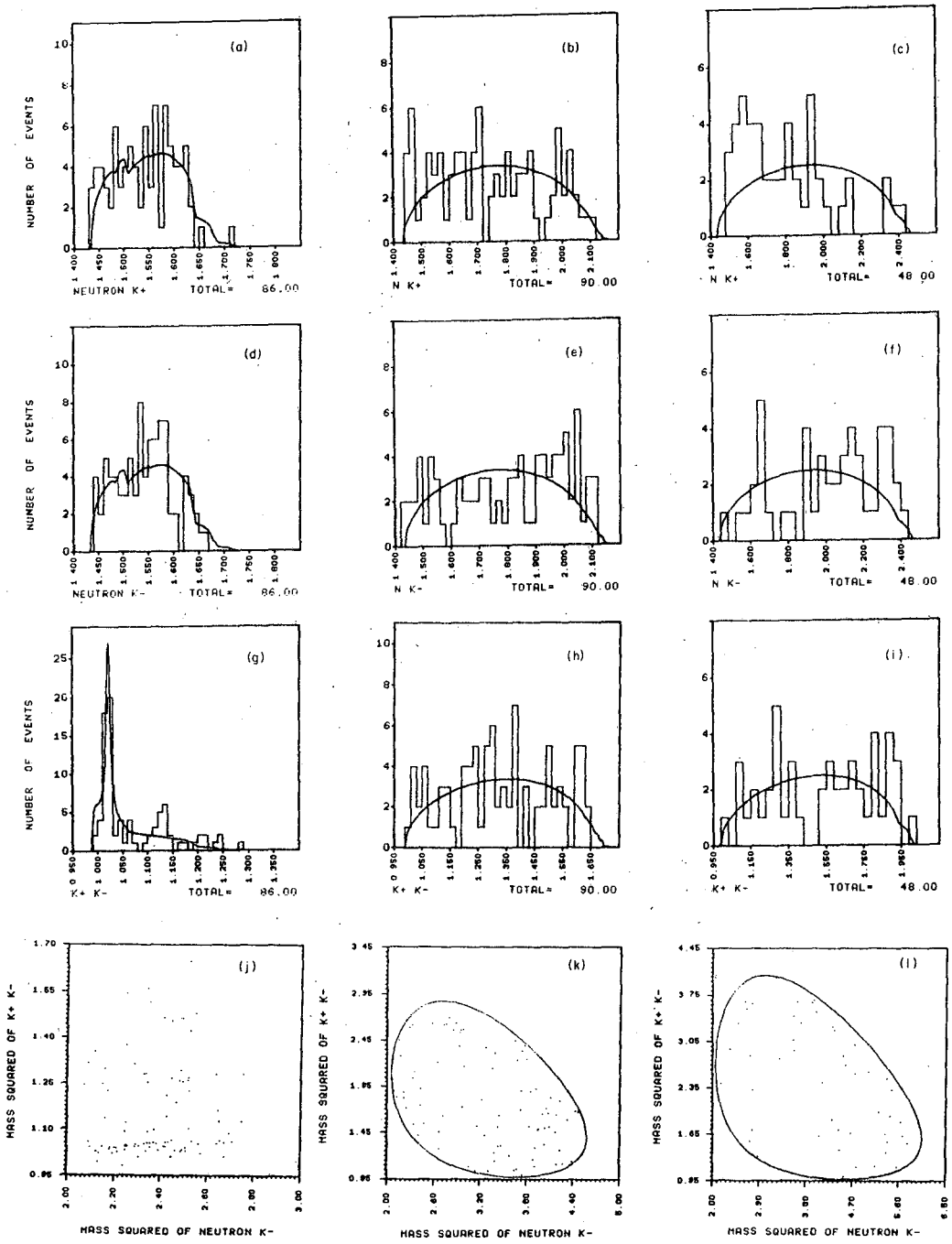

MUB-10769

Fig. 19

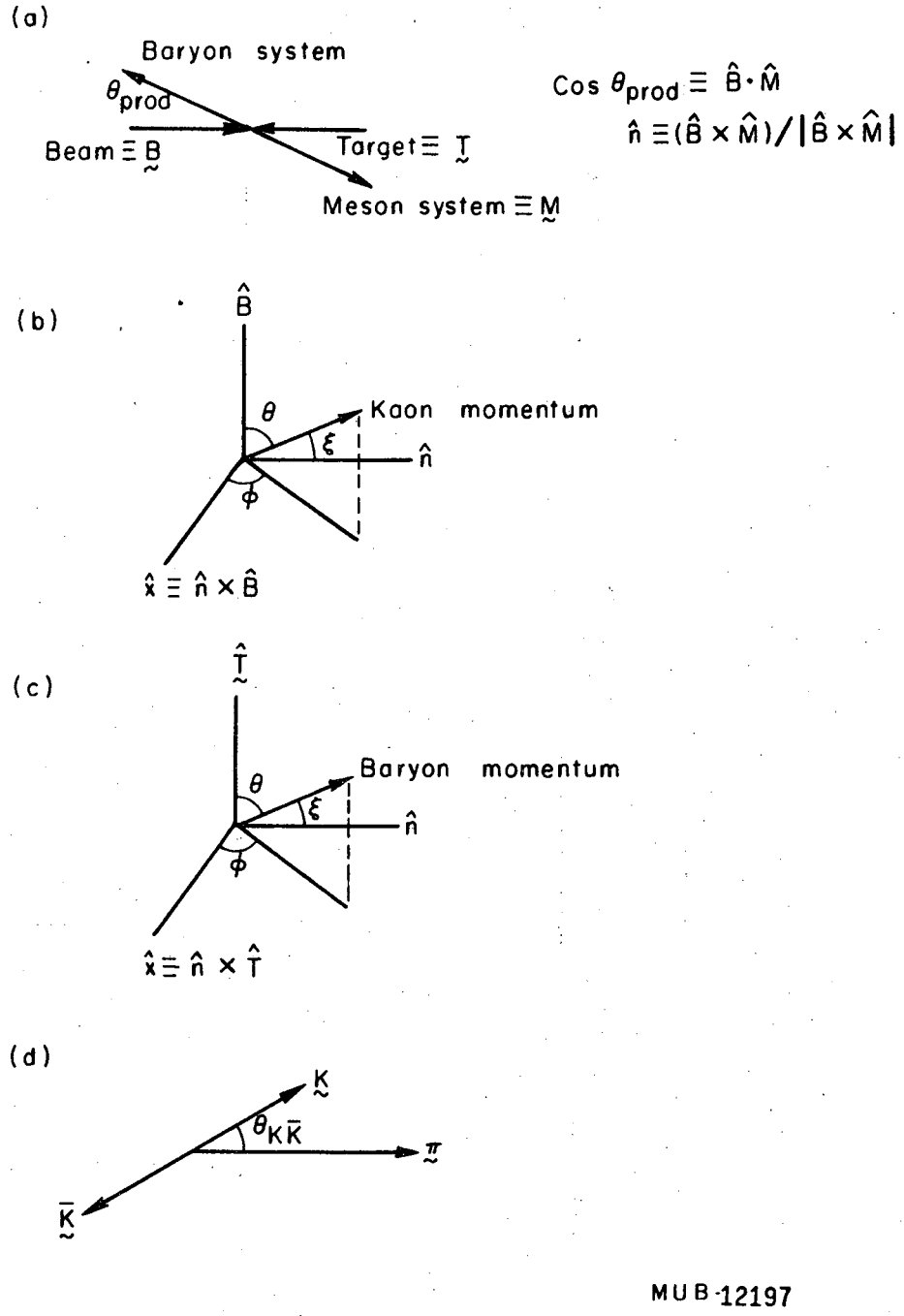
(a)
Baryon system
θ_{prod}
Beam $\equiv \underset{\sim}{B}$
Target $\equiv \underset{\sim}{T}$
Meson system $\equiv \underset{\sim}{M}$
$\text{Cos}\,\theta_{prod} \equiv \hat{B}\cdot\hat{M}$
$\hat{n} \equiv (\hat{B}\times\hat{M})/|\hat{B}\times\hat{M}|$
(b)
$\hat{B}$
θ
Kaon momentum
ξ
$\hat{n}$
ϕ
$\hat{x} \equiv \hat{n}\times\hat{B}$
(c)
$\hat{T}$
θ
Baryon momentum
ξ
$\hat{n}$
ϕ
$\hat{x} \equiv \hat{n}\times\hat{T}$
(d)
$\underset{\sim}{K}$
$\theta_{K\bar{K}}$
$\underset{\sim}{\pi}$
$\underset{\sim}{\bar{K}}$
MUB-12197

Fig. 20

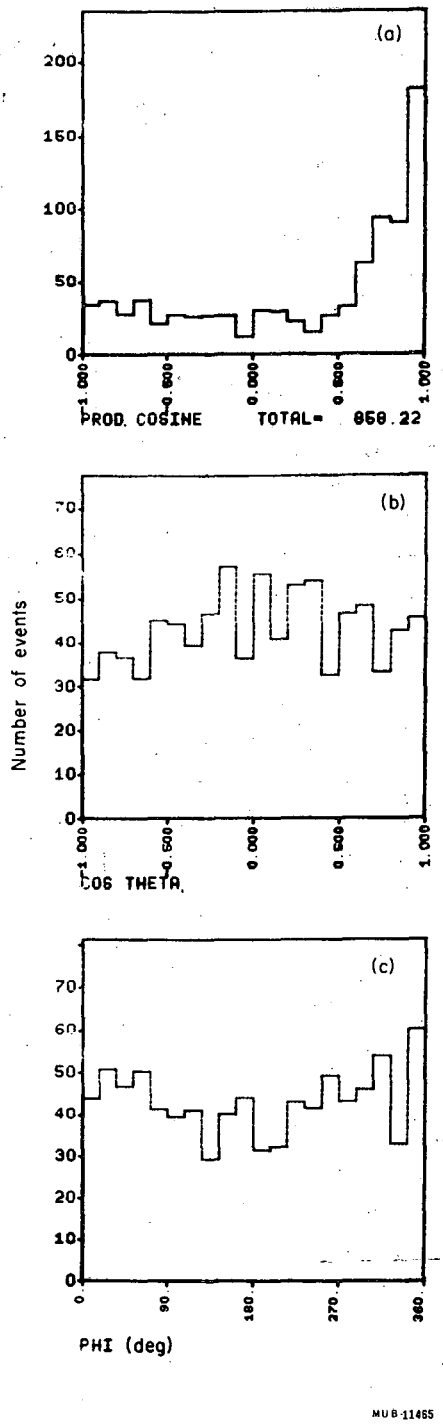
(a)
200
150
100
50
0
1.000
0.500
0.000
0.500
1.000
PROD. COSINE
TOTAL= 850.22
(b)
70
60
50
40
30
20
10
0
Number of events
1.000
0.500
0.000
0.500
1.000
COS THETA
(c)
70
60
50
40
30
20
10
0
0
90
180
270
360
PHI (deg)
MUB-11465

Fig. 21

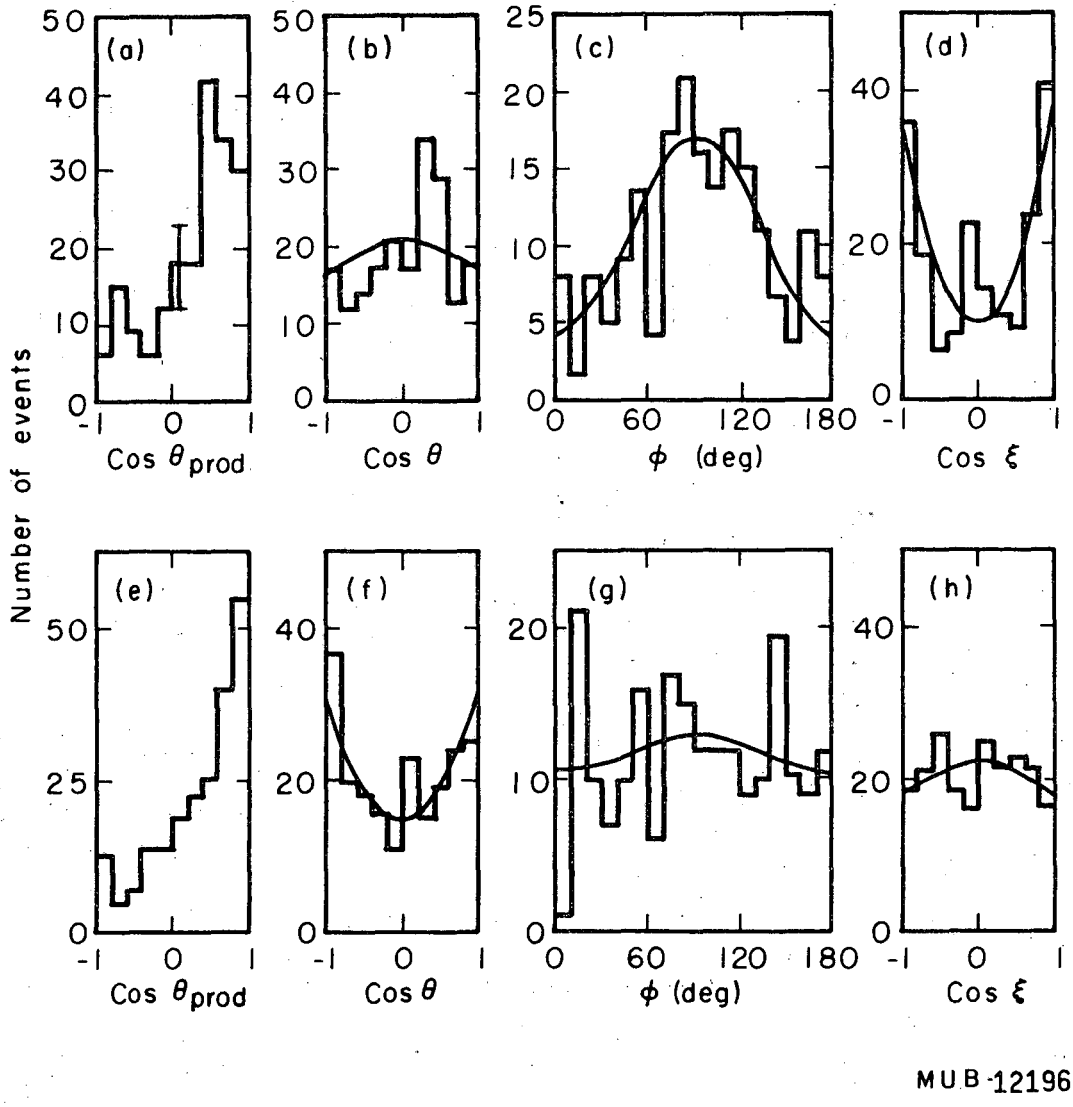
Number of events
(a)
(b)
(c)
(d)
(e)
(f)
(g)
(h)
Cos θprod
Cos θ
φ (deg)
Cos ξ
MUB-12196

Fig. 22

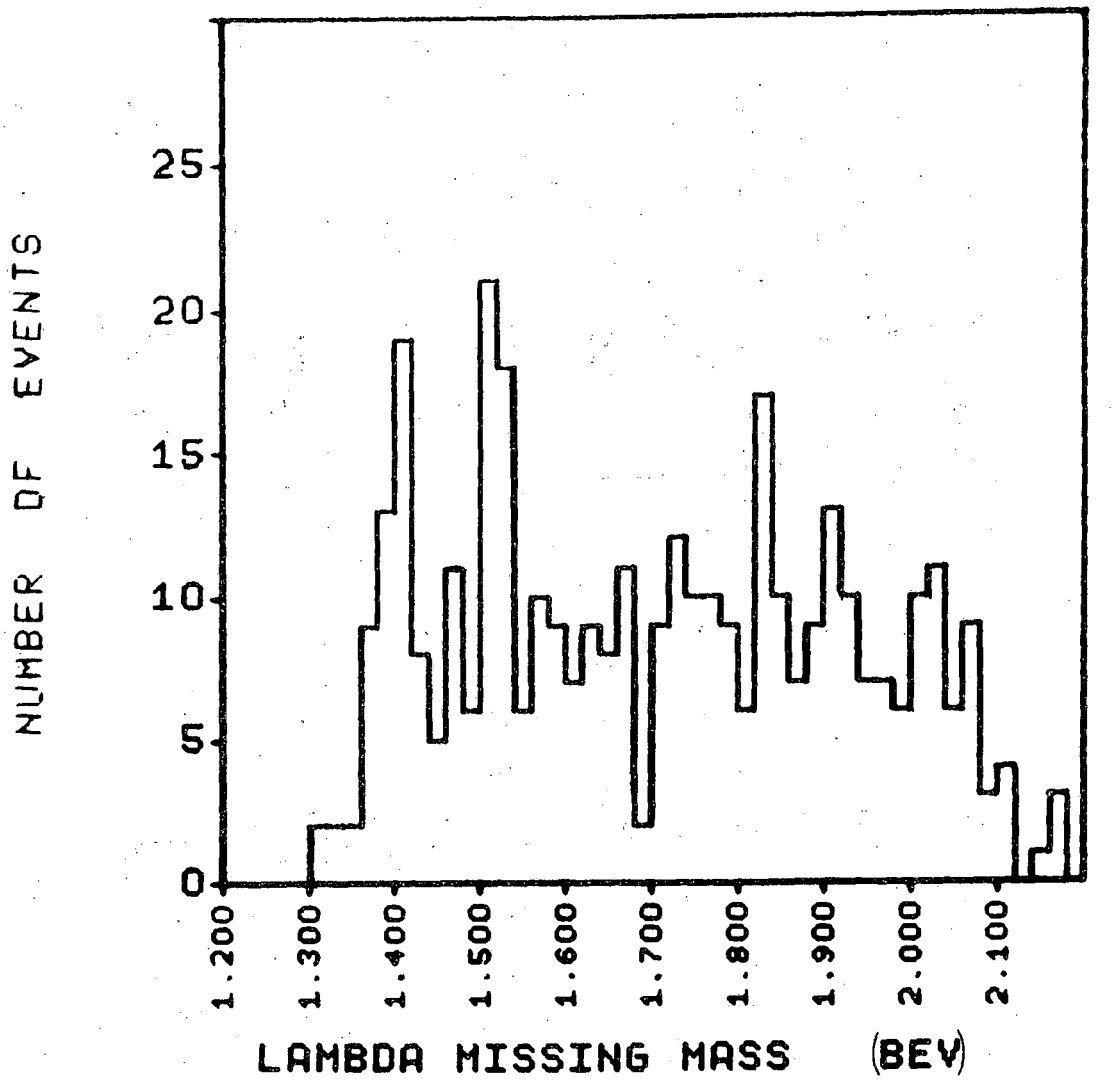
NUMBER OF EVENTS
0
5
10
15
20
25
1.200
1.300
1.400
1.500
1.600
1.700
1.800
1.900
2.000
2.100
LAMBDA MISSING MASS (BEV)
MUB-10733

Fig. 23

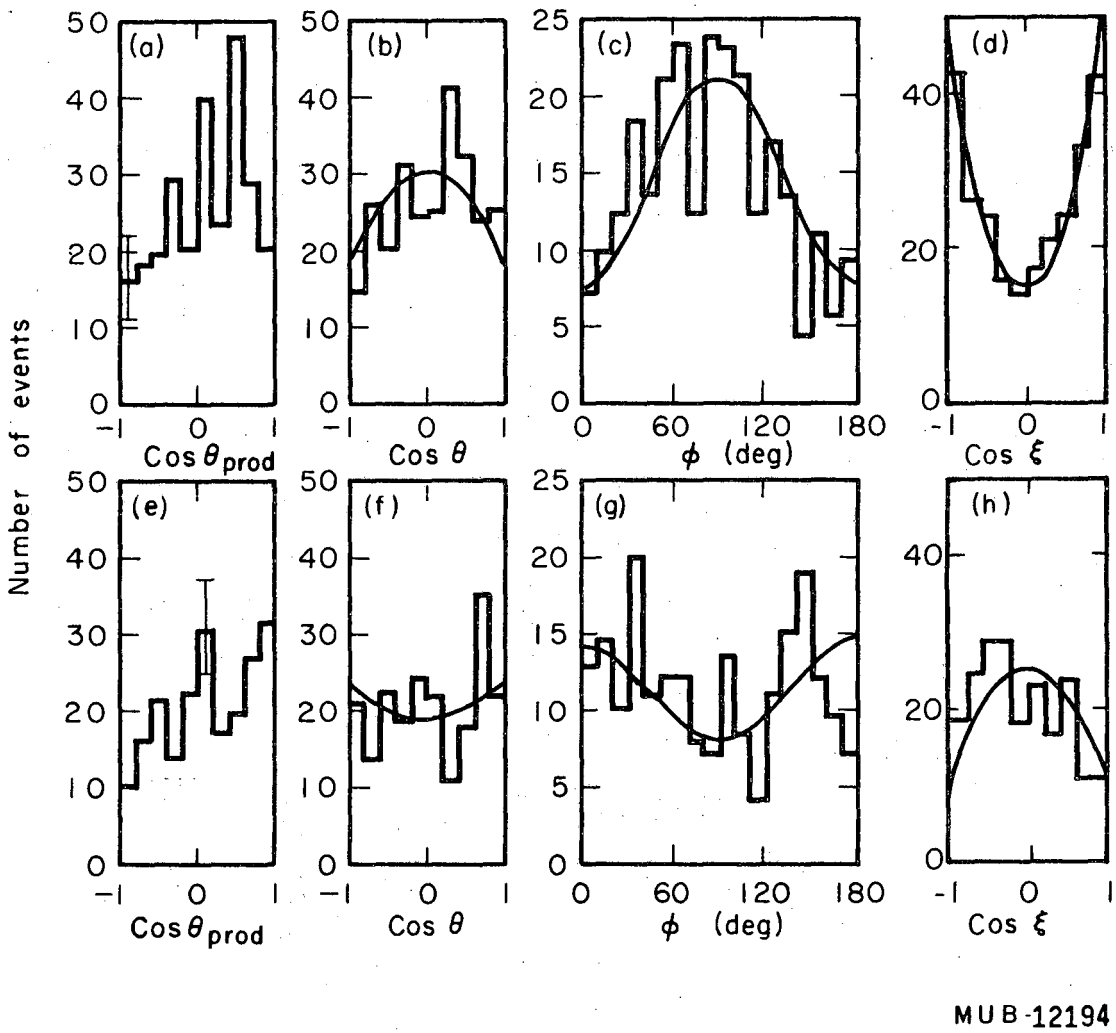
Number of events
(a)
(b)
(c)
(d)
(e)
(f)
(g)
(h)
Cos θprod
Cos θ
φ (deg)
Cos ξ
MUB-12194

Fig. 24

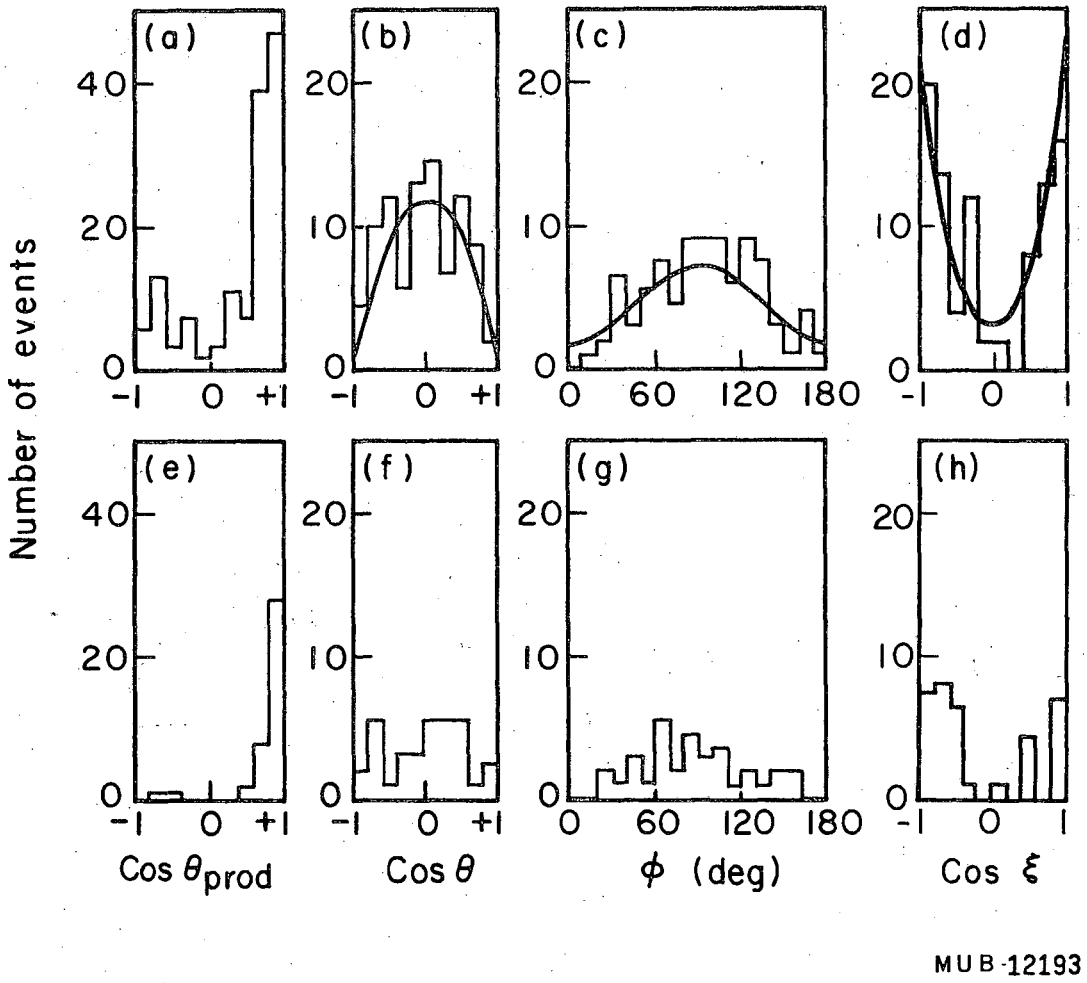
(a)
(b)
(c)
(d)
(e)
(f)
(g)
(h)
Number of events
Cos θ_{prod}
Cos θ
ϕ (deg)
Cos ξ
MUB-12193

Fig. 25

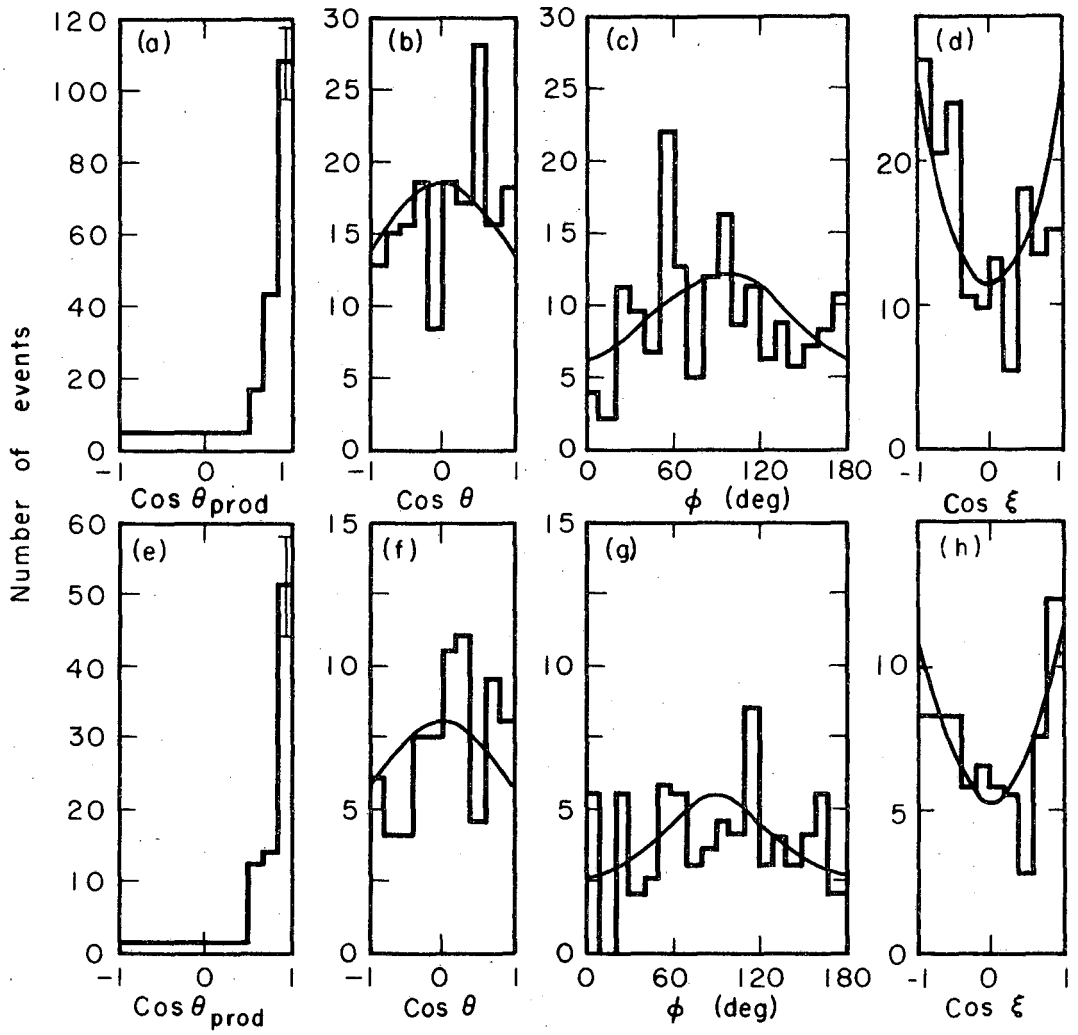
Number of events
(a)
Cos θ_{prod}
(b)
Cos θ
(c)
ϕ (deg)
(d)
Cos ξ
(e)
Cos θ_{prod}
(f)
Cos θ
(g)
ϕ (deg)
(h)
Cos ξ
MUB-12195

Fig. 26

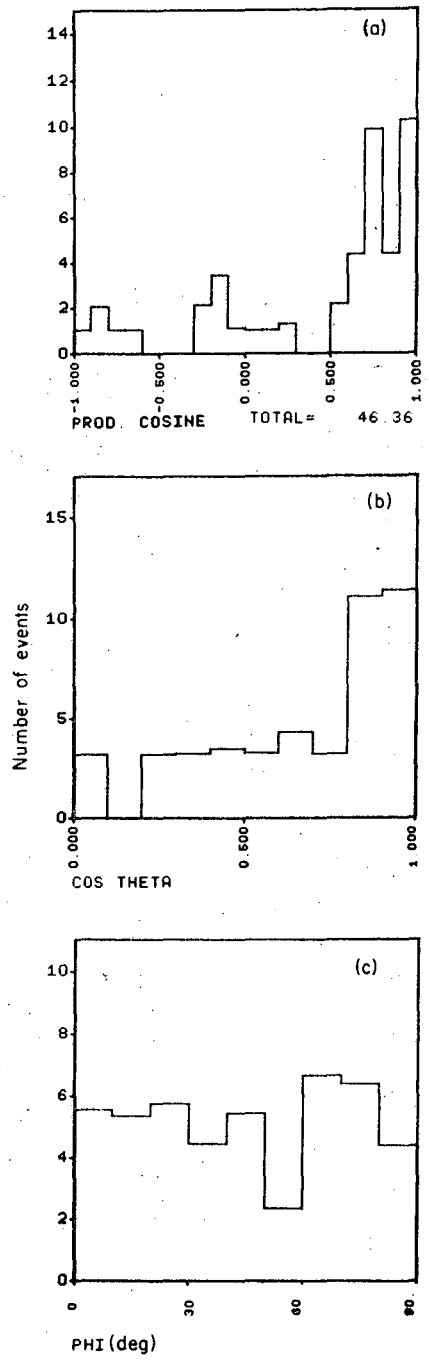

Fig. 27

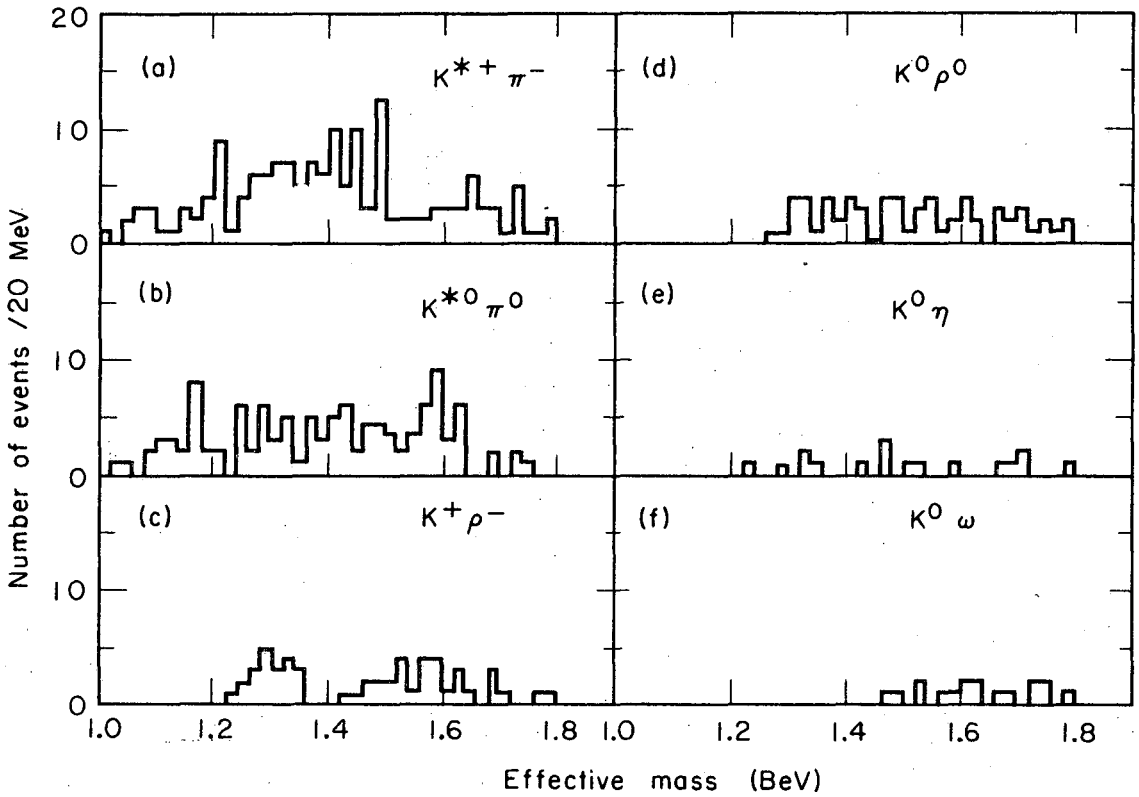
(a) $K^{*+}\pi^-$
(b) $K^{*0}\pi^0$
(c) $K^+\rho^-$
(d) $K^0\rho^0$
(e) $K^0\eta$
(f) $K^0\omega$
Number of events /20 MeV
Effective mass (BeV)
20
10
0
1.0
1.2
1.4
1.6
1.8
MUB-11462

Fig. 28

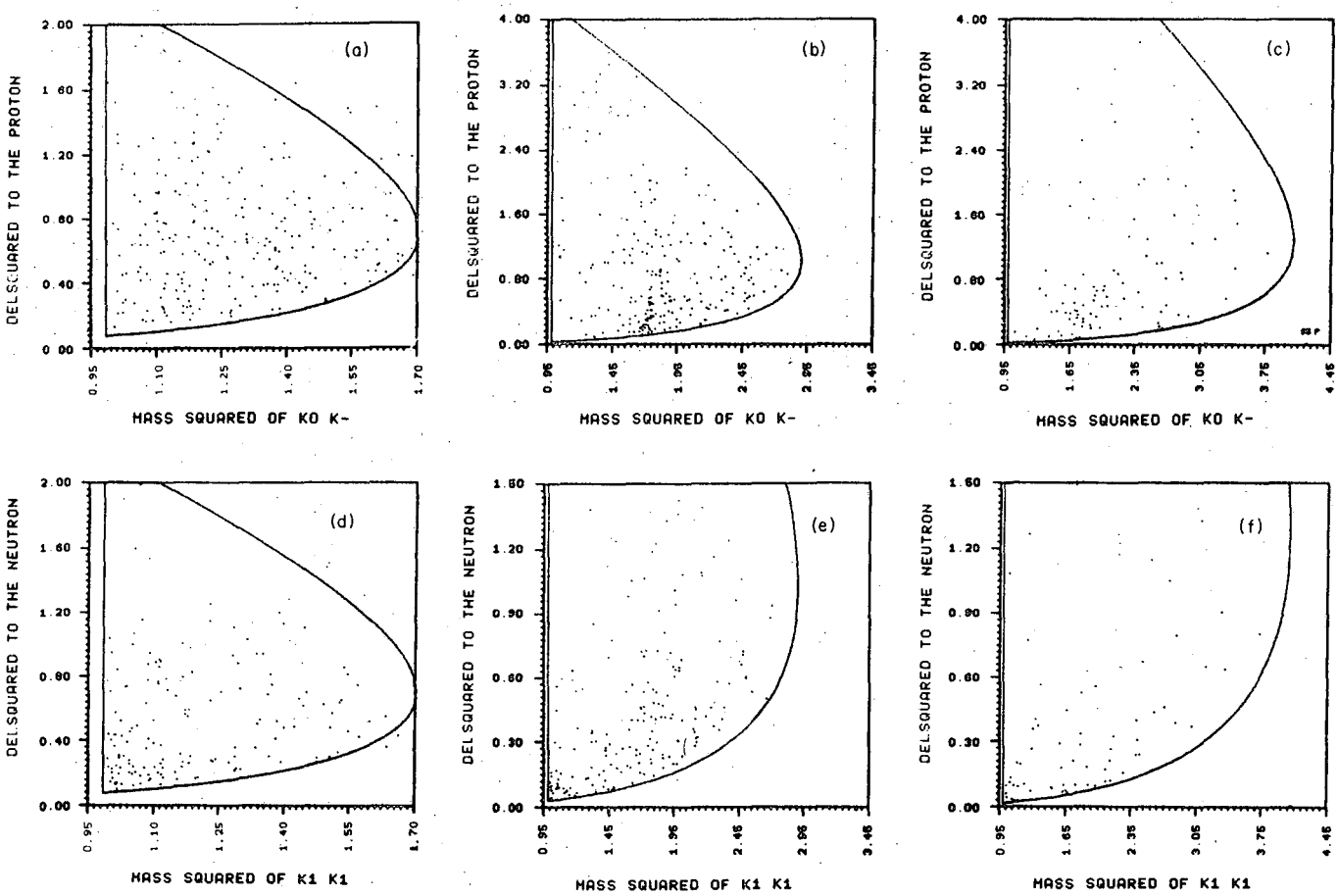

MUB 10772

Fig. 29

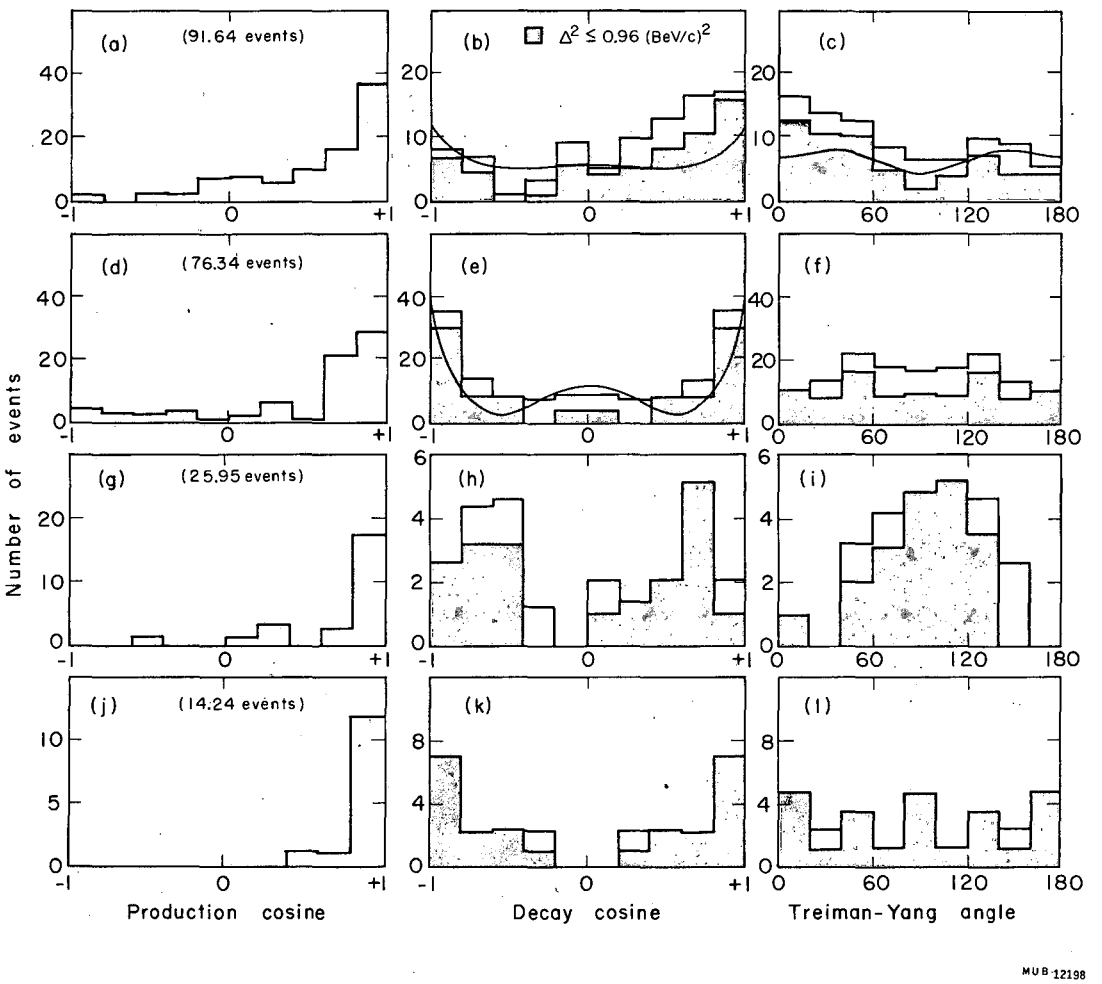
(a) (91.64 events)
(b) $\Delta^2 \leq 0.96$ (BeV/c)^2
(c)
(d) (76.34 events)
(e)
(f)
(g) (25.95 events)
(h)
(i)
(j) (14.24 events)
(k)
(l)
Number of events
Production cosine
Decay cosine
Treiman-Yang angle
MUB-12198

Fig. 30

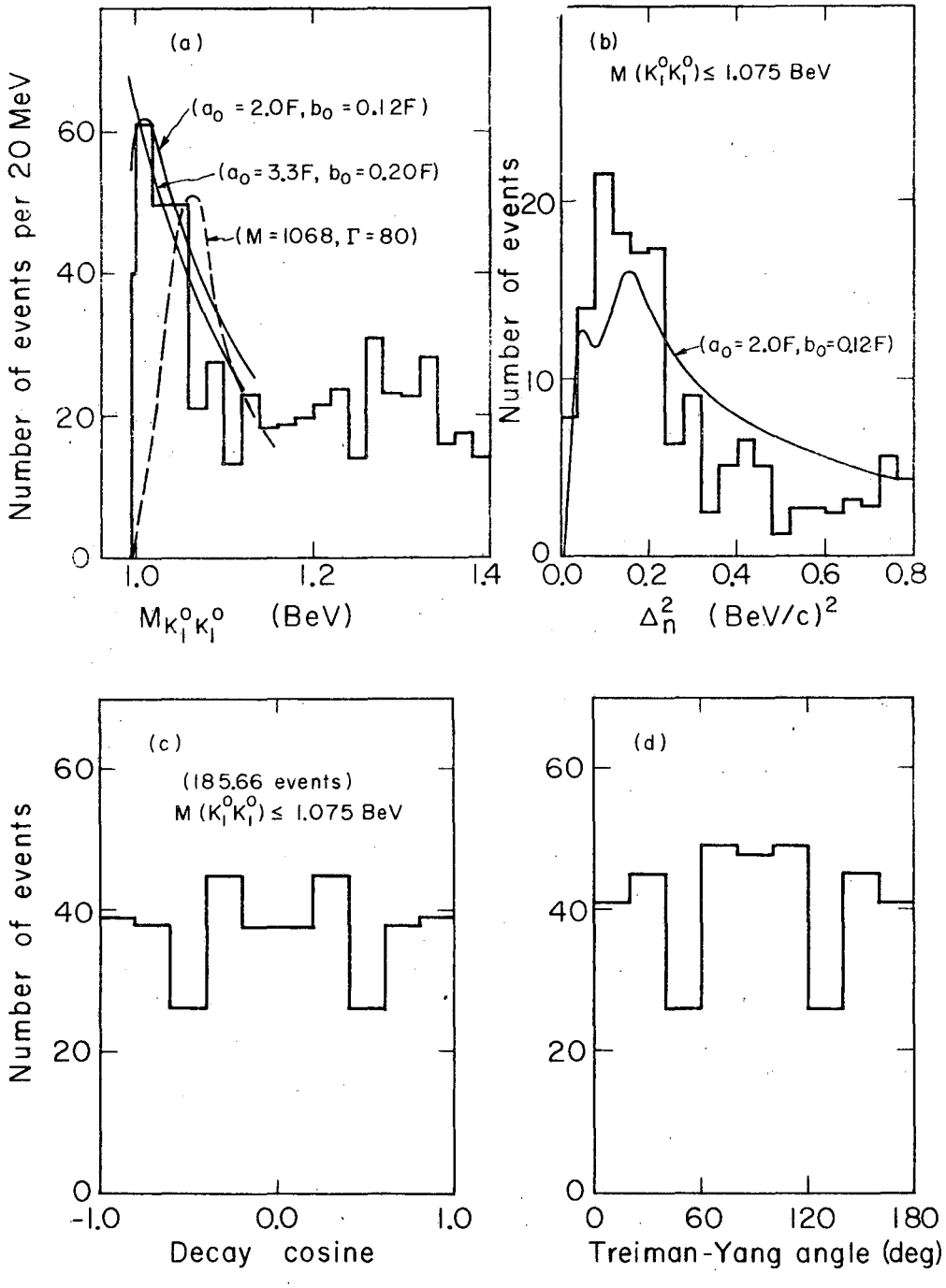
(a)
(a0 = 2.0F, b0 = 0.12F)
(a0 = 3.3F, b0 = 0.20F)
(M = 1068, Γ = 80)
Number of events per 20 MeV
MK0K0 (BeV)
(b)
M (K0K0) ≤ 1.075 BeV
(a0 = 2.0F, b0 = 0.12F)
Number of events
Δ2n (BeV/c)2
(c)
(185.66 events)
M (K0K0) ≤ 1.075 BeV
Number of events
Decay cosine
(d)
Treiman-Yang angle (deg)
MUB 11516

Fig. 31

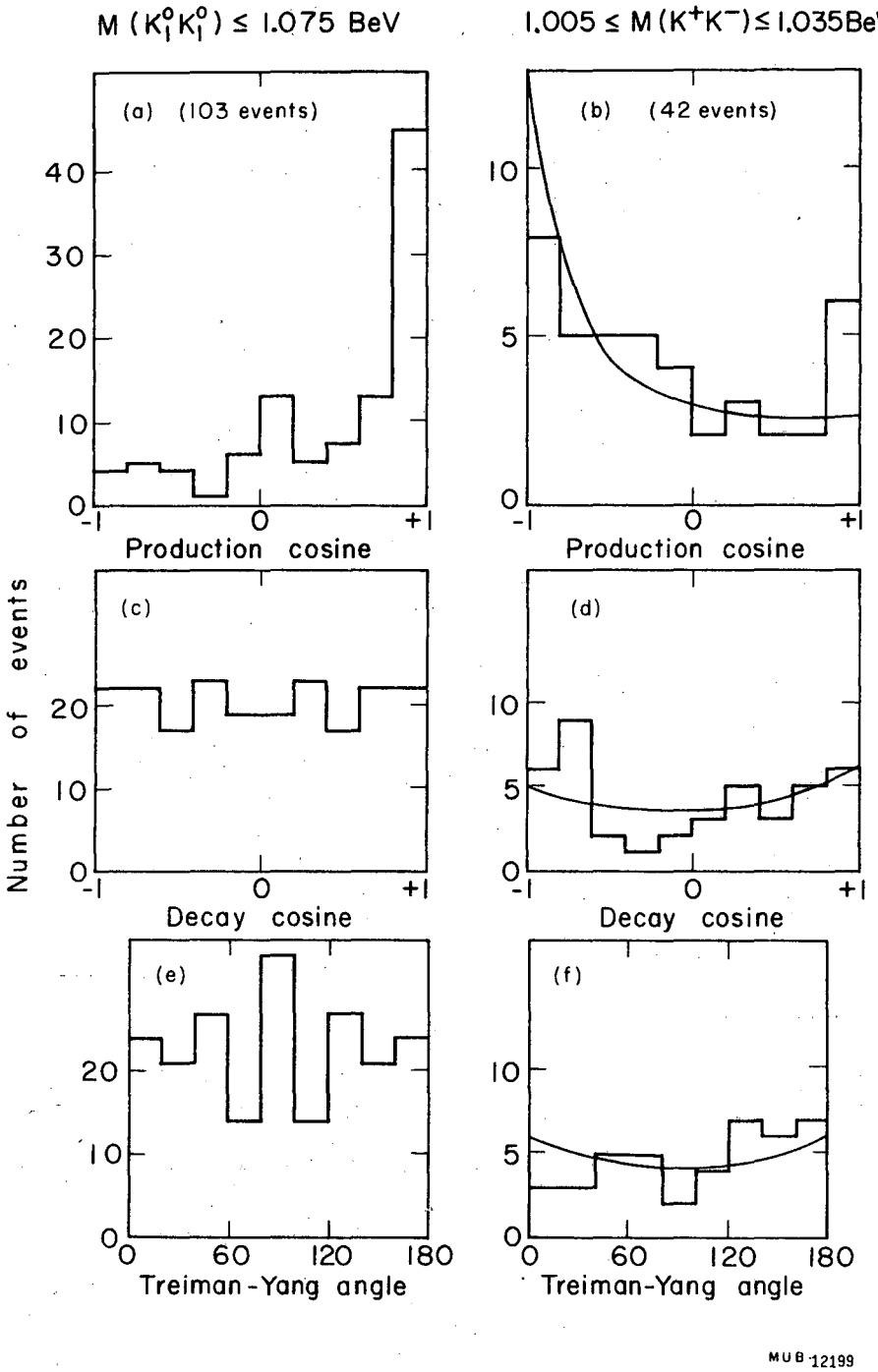
M ($K_1^0K_1^0$) ≤ 1.075 BeV
1.005 ≤ M (K^+K^-) ≤ 1.035BeV
(a) (103 events)
(b) (42 events)
(c)
(d)
(e)
(f)
Number of events
Production cosine
Decay cosine
Treiman-Yang angle
MUB-12199

Fig. 32

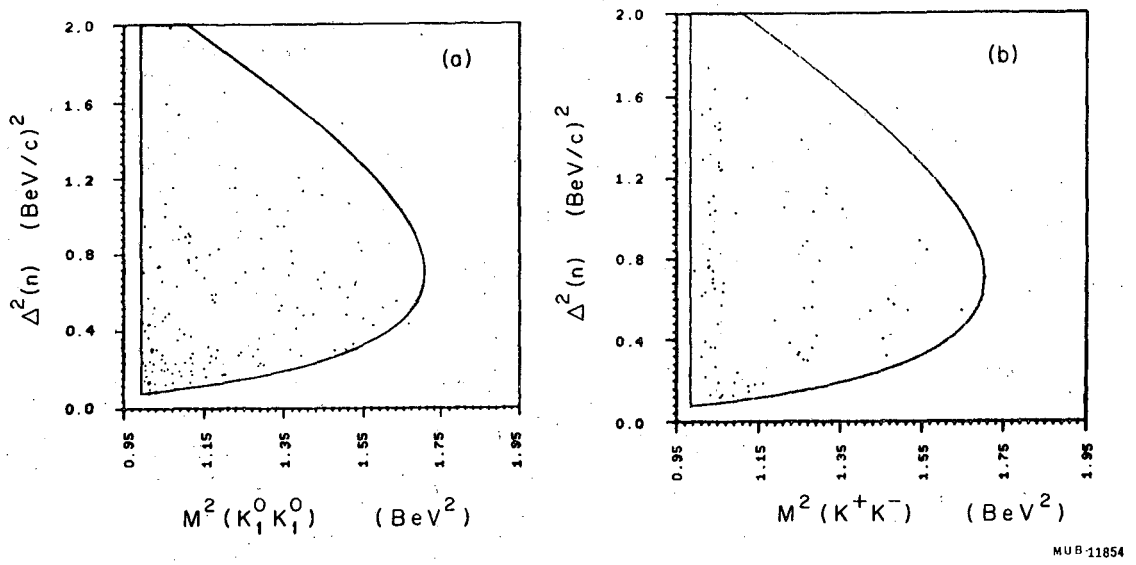
(a)
(b)
$\Delta^2(n)$ (BeV/c)^2
$M^2(K_1^0K_1^0)$ (BeV^2)
$M^2(K^+K^-)$ (BeV^2)
0.0
0.4
0.8
1.2
1.6
2.0
0.95
1.15
1.35
1.55
1.75
1.95
MUB-11854

Fig. 33

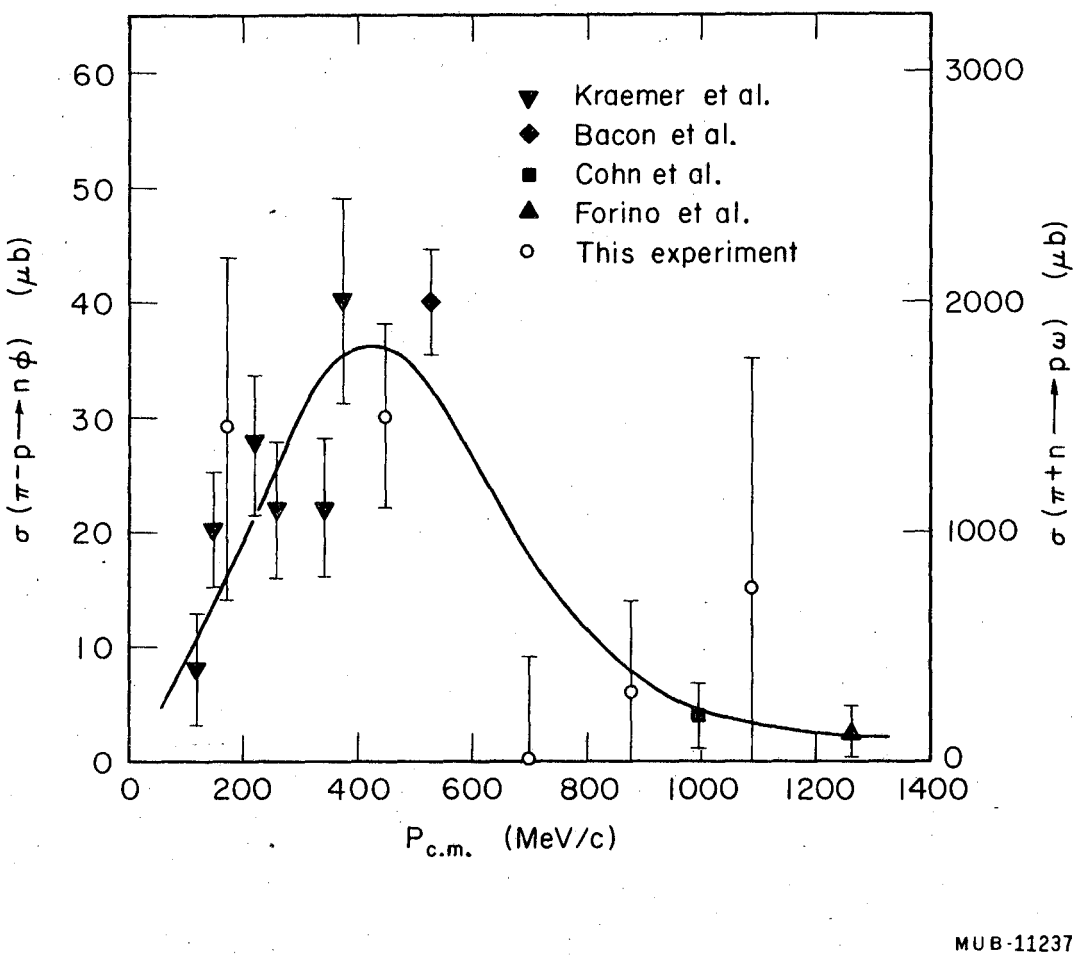
Kraemer et al.
Bacon et al.
Cohn et al.
Forino et al.
This experiment
σ (π⁻p → nφ) (μb)
σ (π⁺n → pω) (μb)
P c.m. (MeV/c)
0
10
20
30
40
50
60
1000
2000
3000
200
400
600
800
1200
1400
MUB-11237

Fig. 34

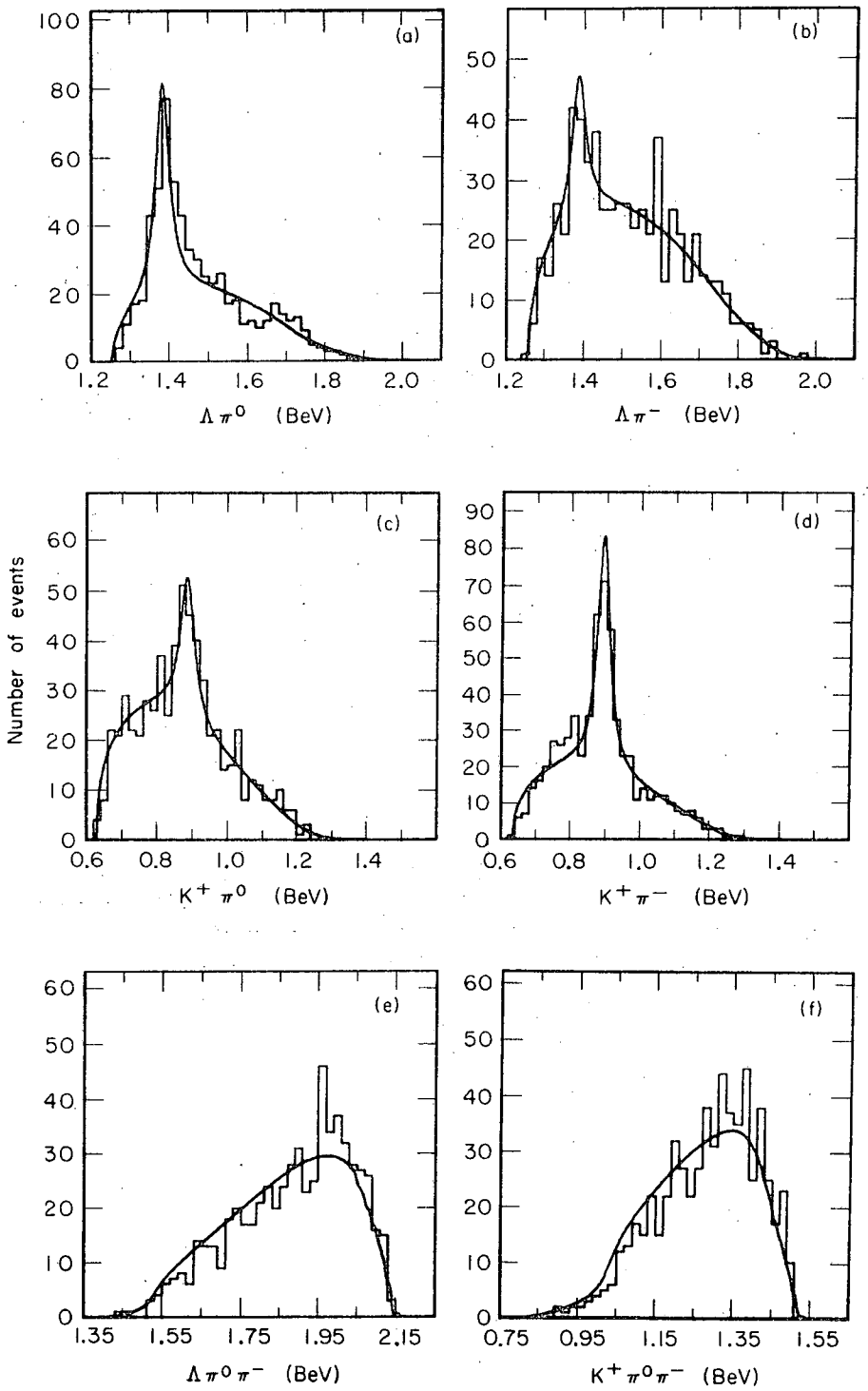

MUB-11551

Fig. 35

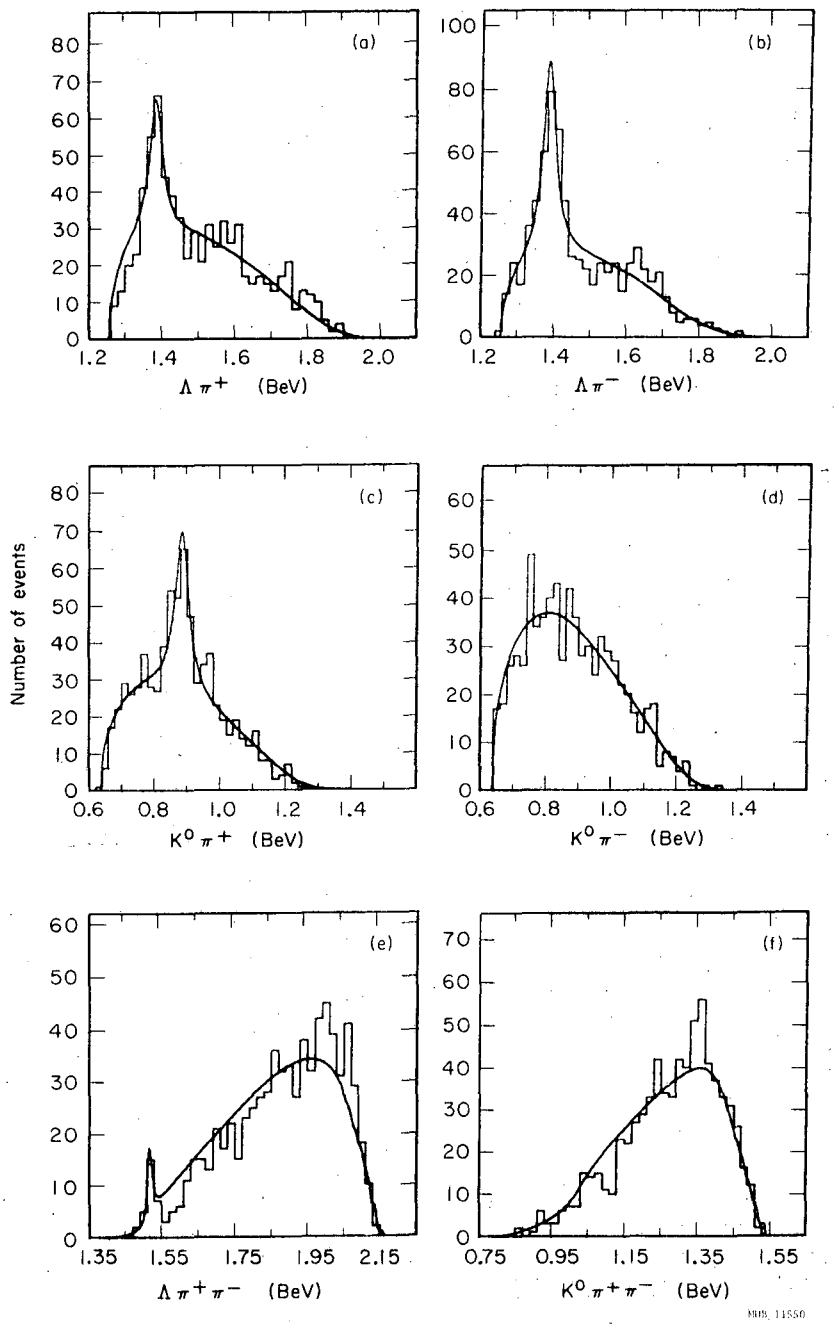
(a)
(b)
(c)
(d)
(e)
(f)
Number of events
Λ π+ (BeV)
Λ π− (BeV)
K0 π+ (BeV)
K0 π− (BeV)
Λ π+ π− (BeV)
K0 π+ π− (BeV)
MUB. 11550

Fig. 36

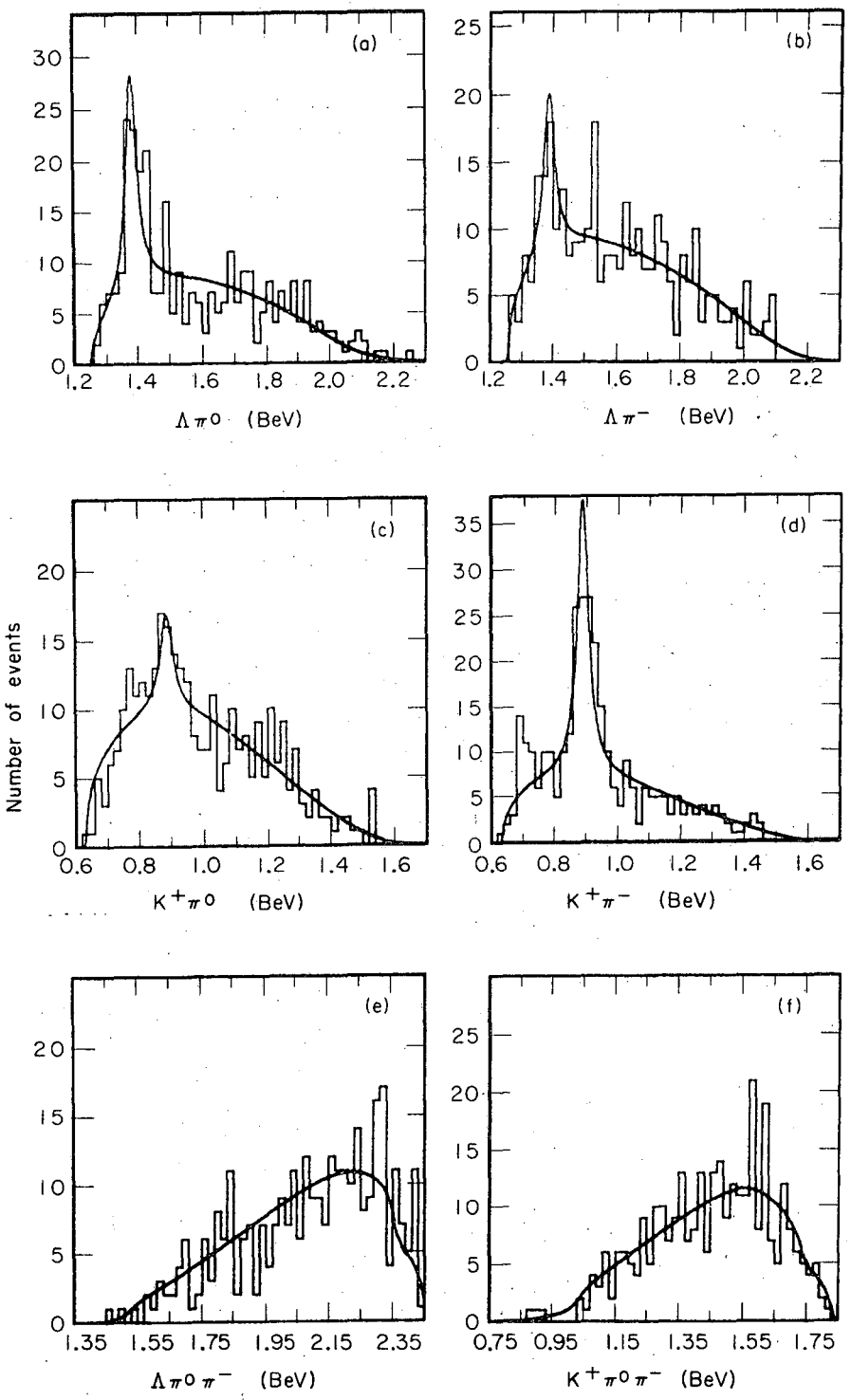

MUB-11548

Fig. 37

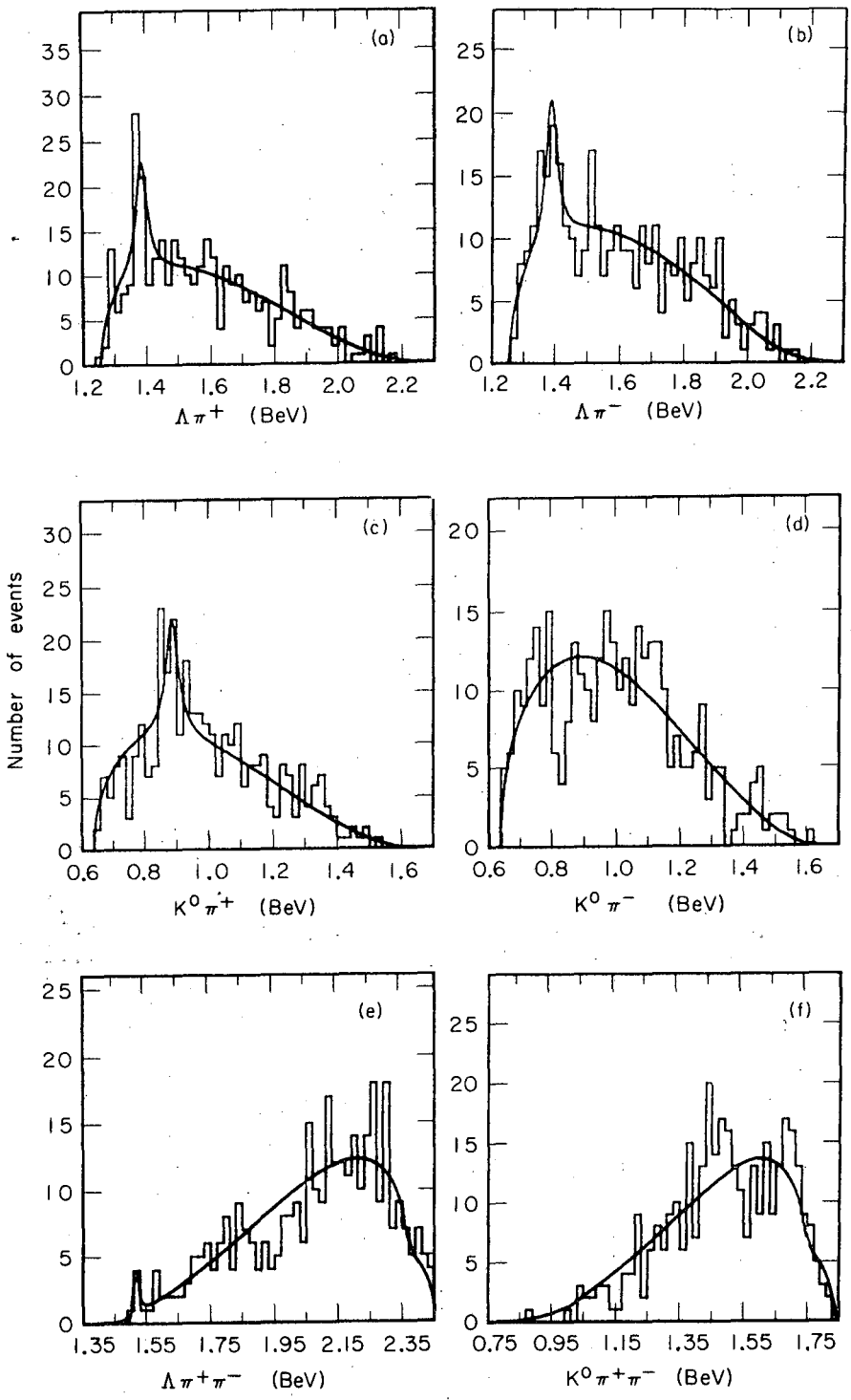

MUB-11547

Fig. 38

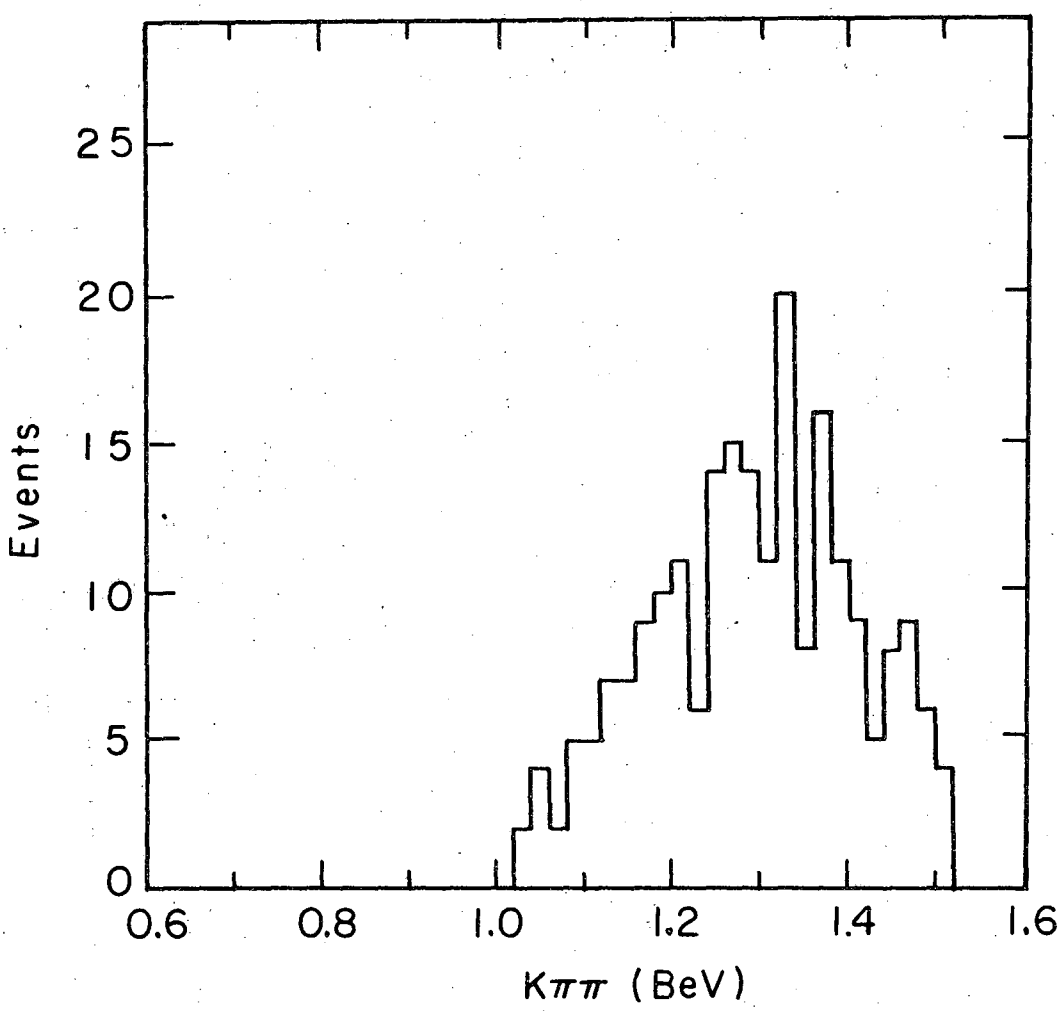

Fig. 39

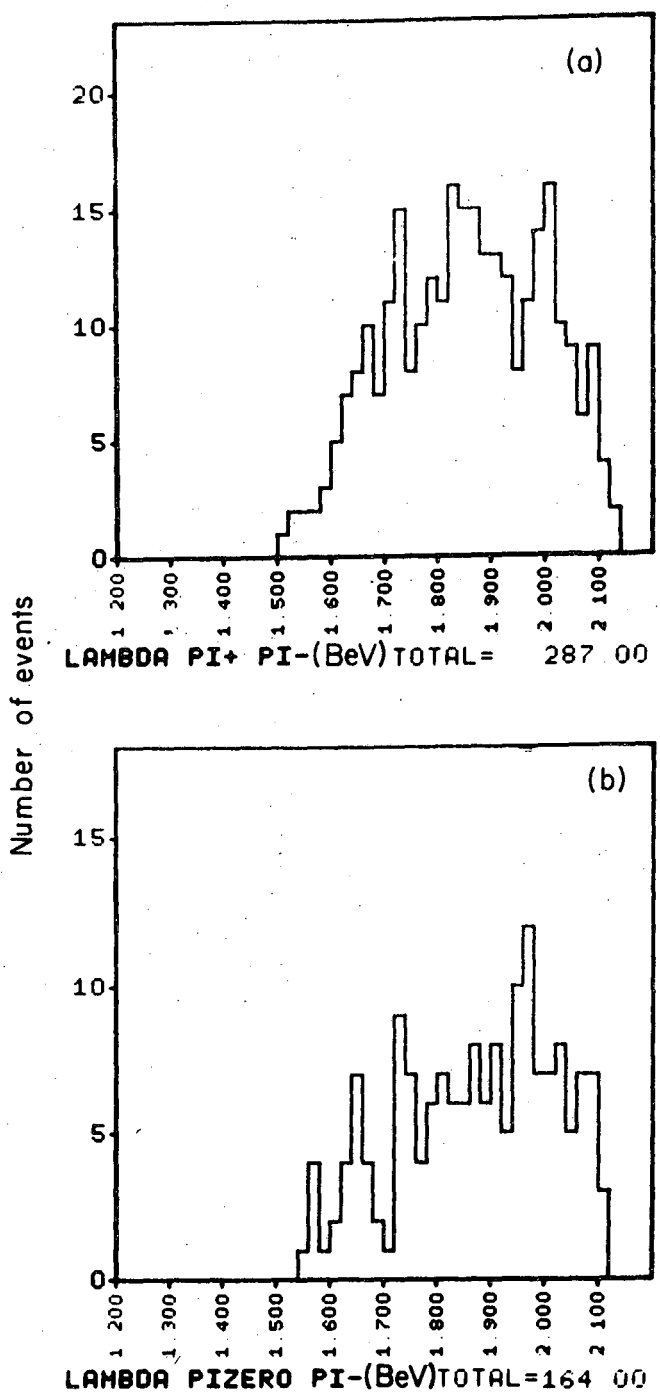

MUB-11545

Fig. 40

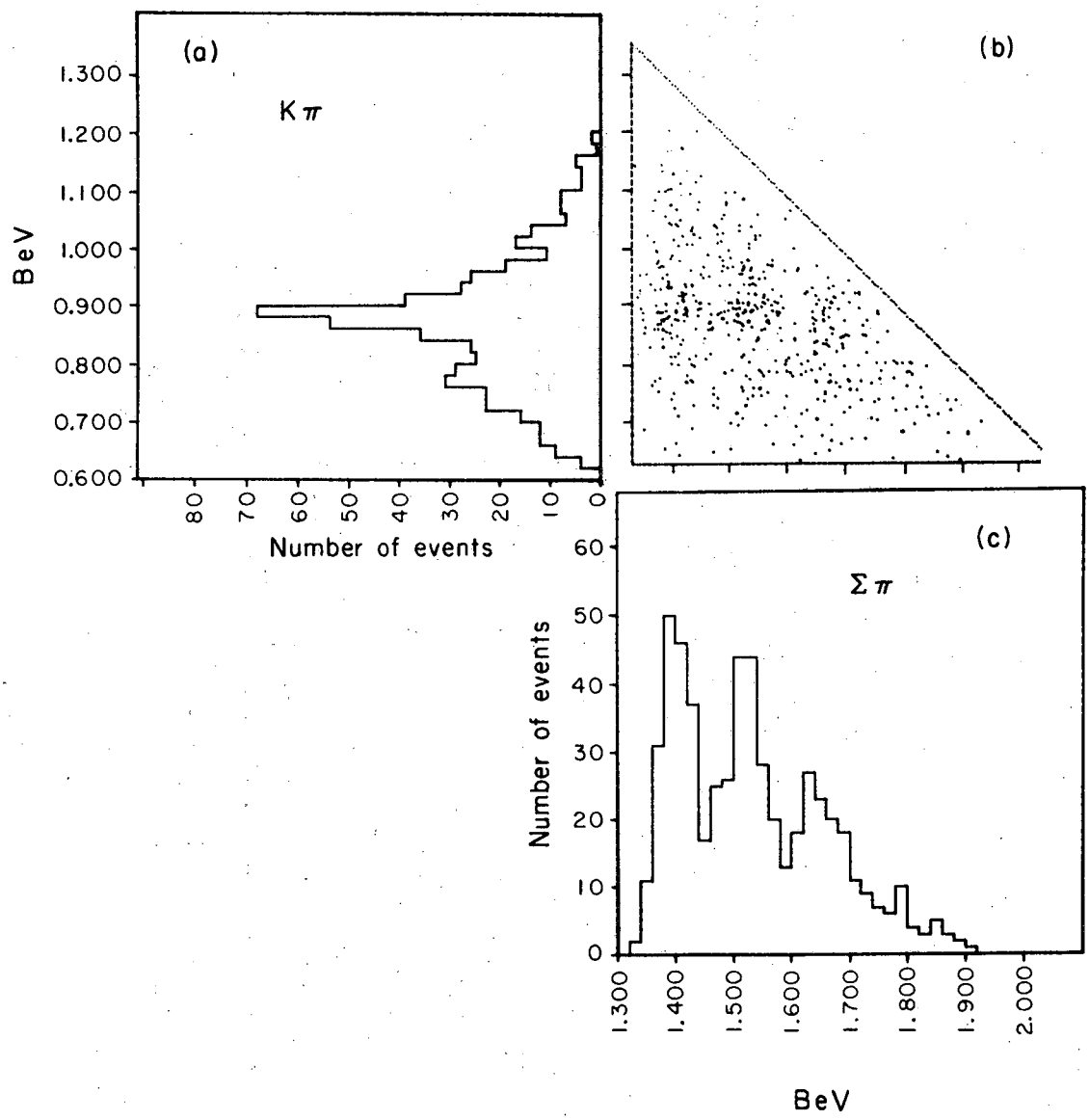
(a)
Kπ
BeV
1.300
1.200
1.100
1.000
0.900
0.800
0.700
0.600
80
70
60
50
40
30
20
10
0
Number of events
(b)
(c)
Σπ
Number of events
60
50
40
30
20
10
0
1.300
1.400
1.500
1.600
1.700
1.800
1.900
2.000
BeV
MUB-11788

Fig. 41

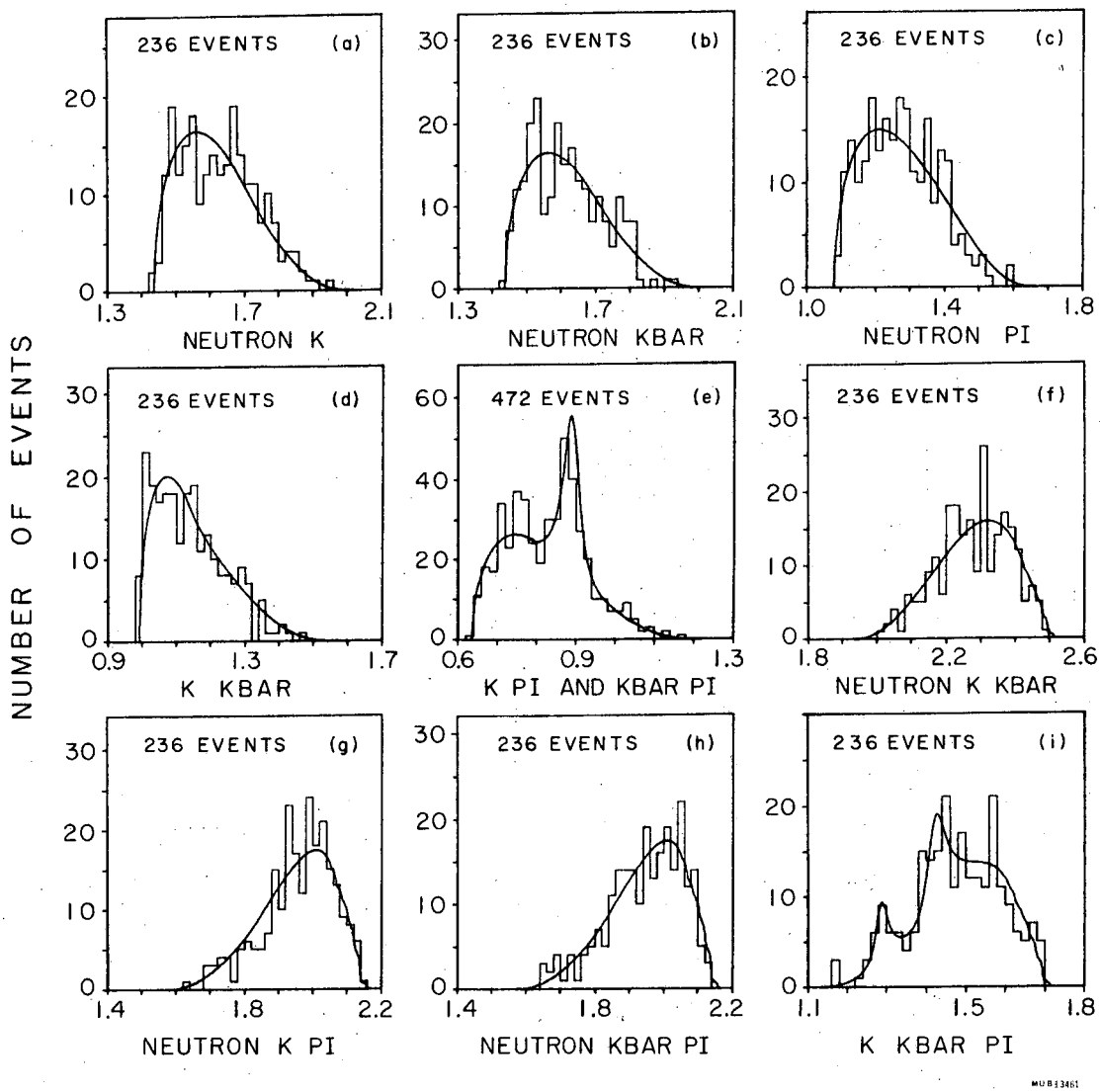
NUMBER OF EVENTS
236 EVENTS (a)
NEUTRON K
236 EVENTS (b)
NEUTRON KBAR
236 EVENTS (c)
NEUTRON PI
236 EVENTS (d)
K KBAR
472 EVENTS (e)
K PI AND KBAR PI
236 EVENTS (f)
NEUTRON K KBAR
236 EVENTS (g)
NEUTRON K PI
236 EVENTS (h)
NEUTRON KBAR PI
236 EVENTS (i)
K KBAR PI

Fig. 42

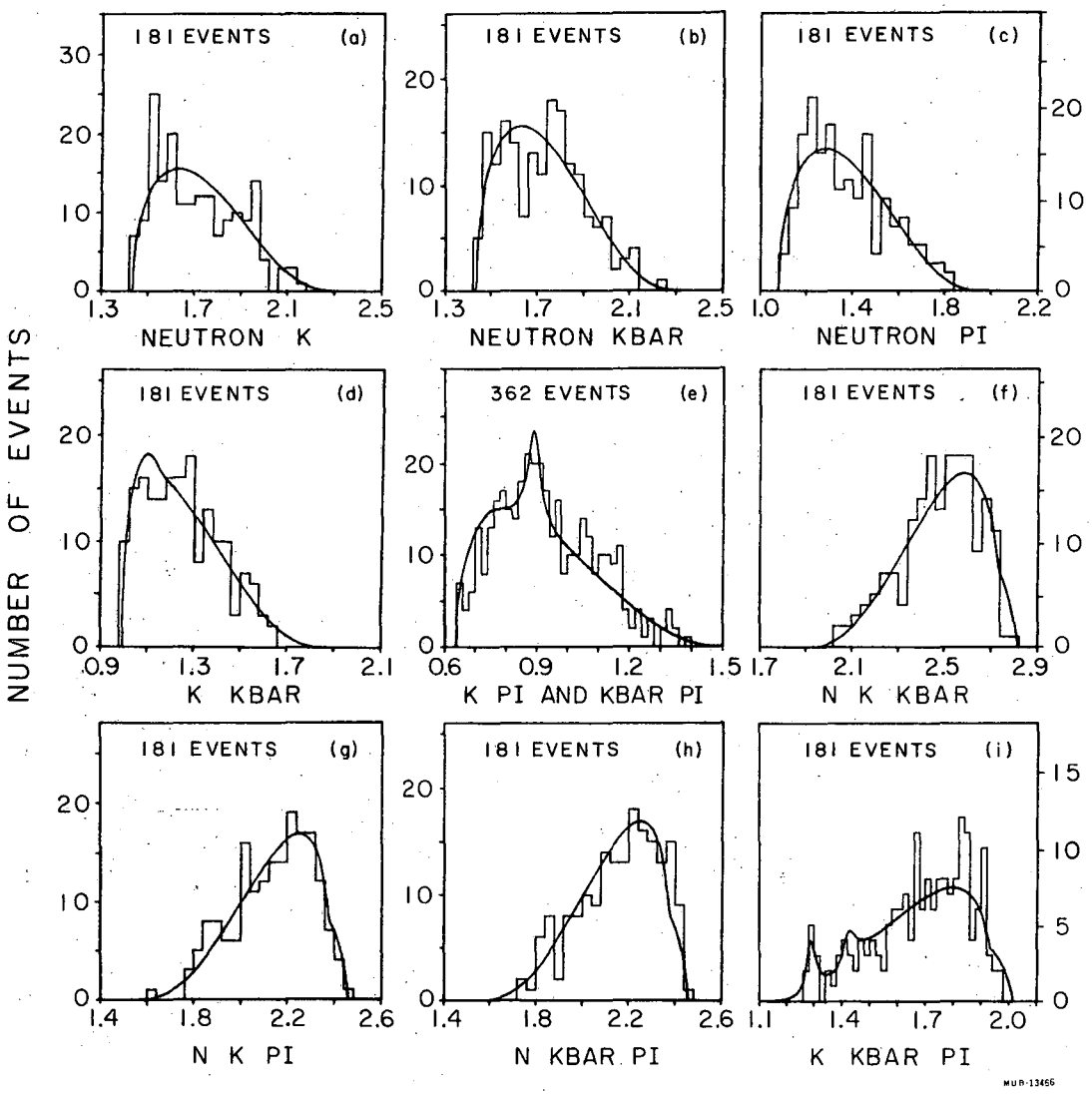
NUMBER OF EVENTS
181 EVENTS (a)
NEUTRON K
181 EVENTS (b)
NEUTRON KBAR
181 EVENTS (c)
NEUTRON PI
181 EVENTS (d)
K KBAR
362 EVENTS (e)
K PI AND KBAR PI
181 EVENTS (f)
N K KBAR
181 EVENTS (g)
N K PI
181 EVENTS (h)
N KBAR PI
181 EVENTS (i)
K KBAR PI
MUB-13466

Fig. 43

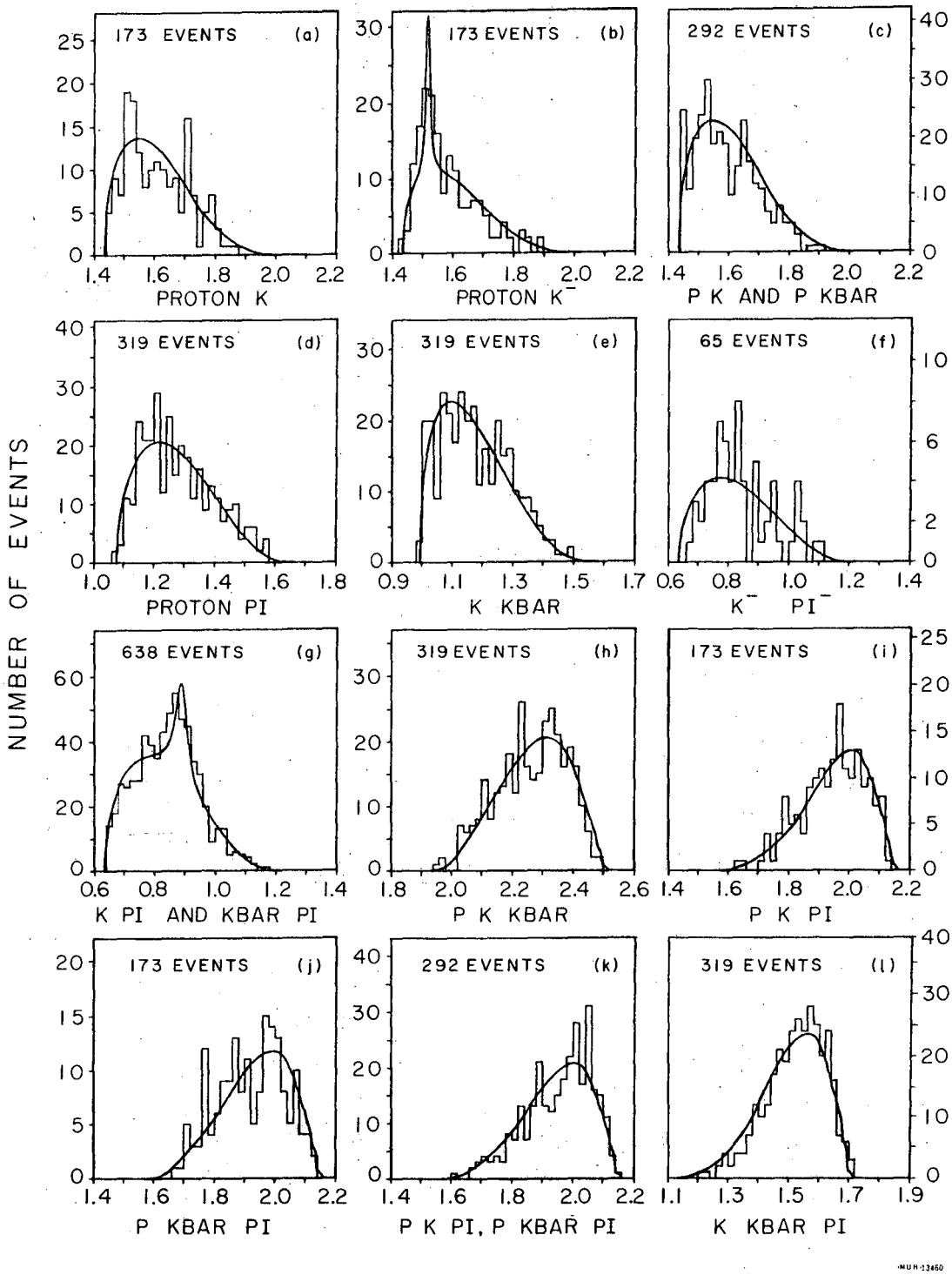
NUMBER OF EVENTS
173 EVENTS (a)
PROTON K
173 EVENTS (b)
PROTON K⁻
292 EVENTS (c)
P K AND P KBAR
319 EVENTS (d)
PROTON PI
319 EVENTS (e)
K KBAR
65 EVENTS (f)
K⁻ PI⁻
638 EVENTS (g)
K PI AND KBAR PI
319 EVENTS (h)
P K KBAR
173 EVENTS (i)
P K PI
173 EVENTS (j)
P KBAR PI
292 EVENTS (k)
P K PI, P KBAR PI
319 EVENTS (l)
K KBAR PI

Fig. 44

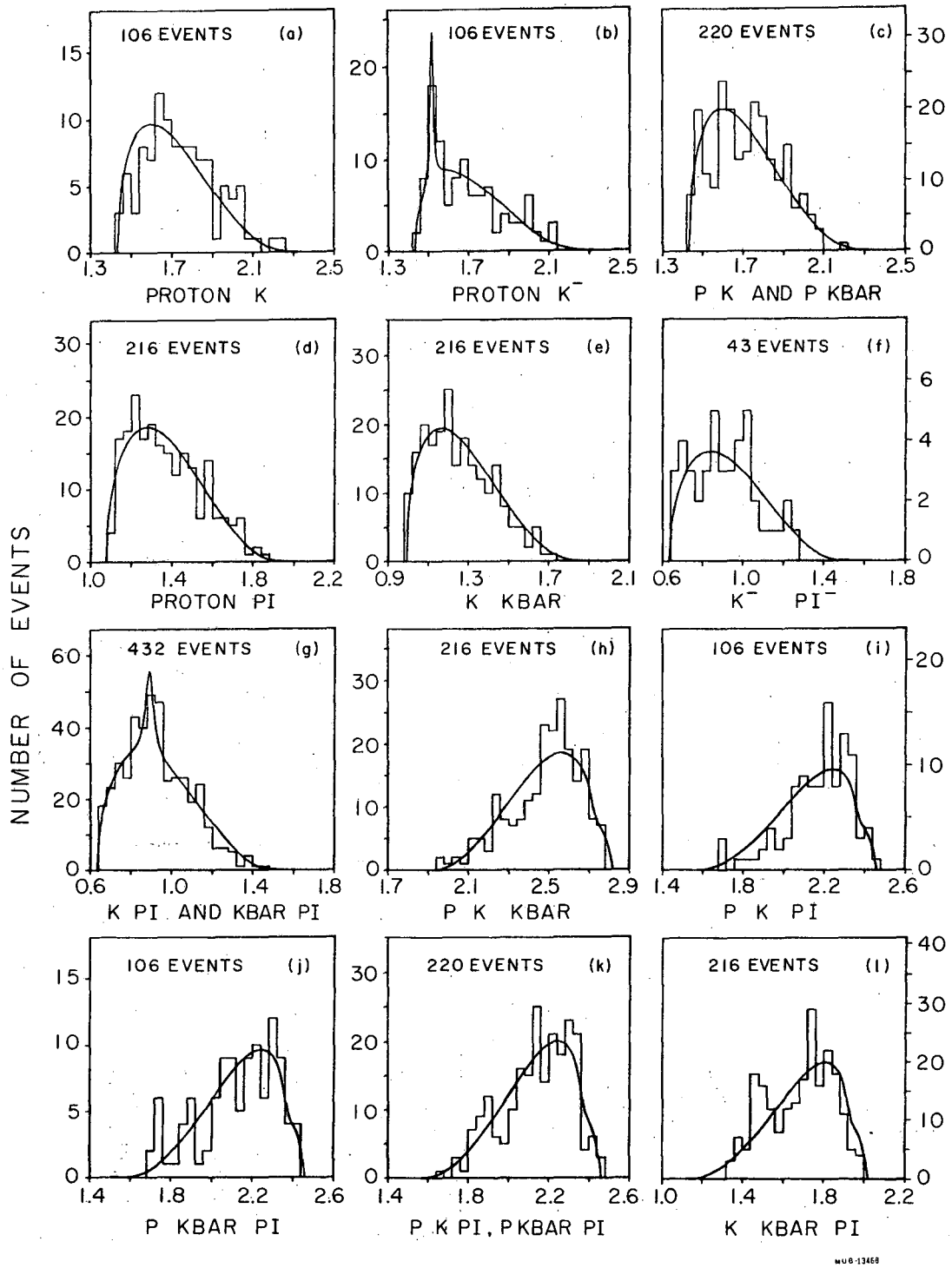
106 EVENTS (a)
PROTON K
106 EVENTS (b)
PROTON K⁻
220 EVENTS (c)
P K AND P KBAR
216 EVENTS (d)
PROTON PI
216 EVENTS (e)
K KBAR
43 EVENTS (f)
K⁻ PI⁻
NUMBER OF EVENTS
432 EVENTS (g)
K PI AND KBAR PI
216 EVENTS (h)
P K KBAR
106 EVENTS (i)
P K PI
106 EVENTS (j)
P KBAR PI
220 EVENTS (k)
P K PI, PKBAR PI
216 EVENTS (l)
K KBAR PI

Fig. 45

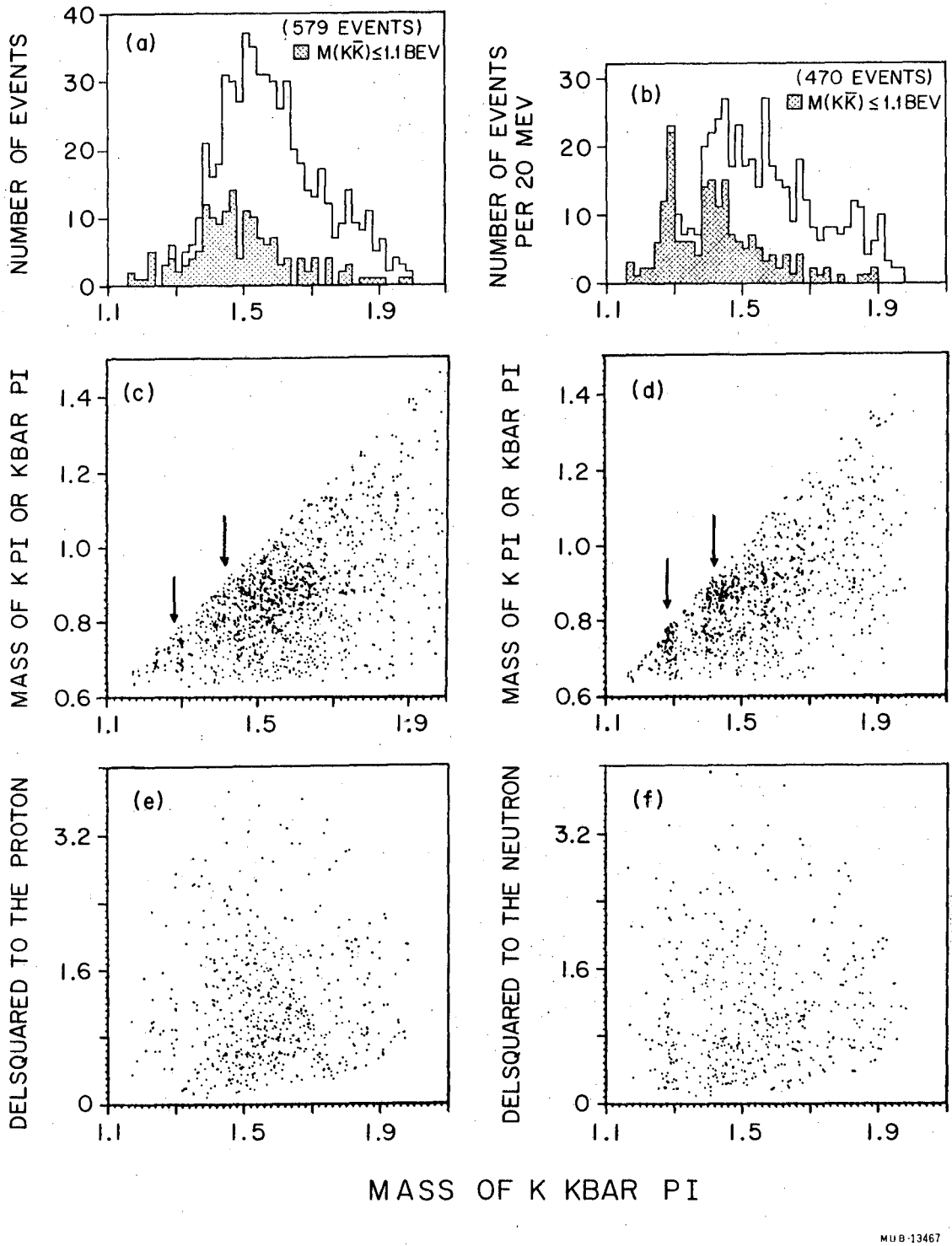
(a)
(579 EVENTS)
M(KK̄)≤1.1 BEV
NUMBER OF EVENTS
(b)
(470 EVENTS)
M(KK̄) ≤ 1.1 BEV
NUMBER OF EVENTS PER 20 MEV
(c)
MASS OF K PI OR KBAR PI
(d)
MASS OF K PI OR KBAR PI
(e)
DELSQUARED TO THE PROTON
(f)
DELSQUARED TO THE NEUTRON
MASS OF K KBAR PI
MUB-13467

Fig. 46

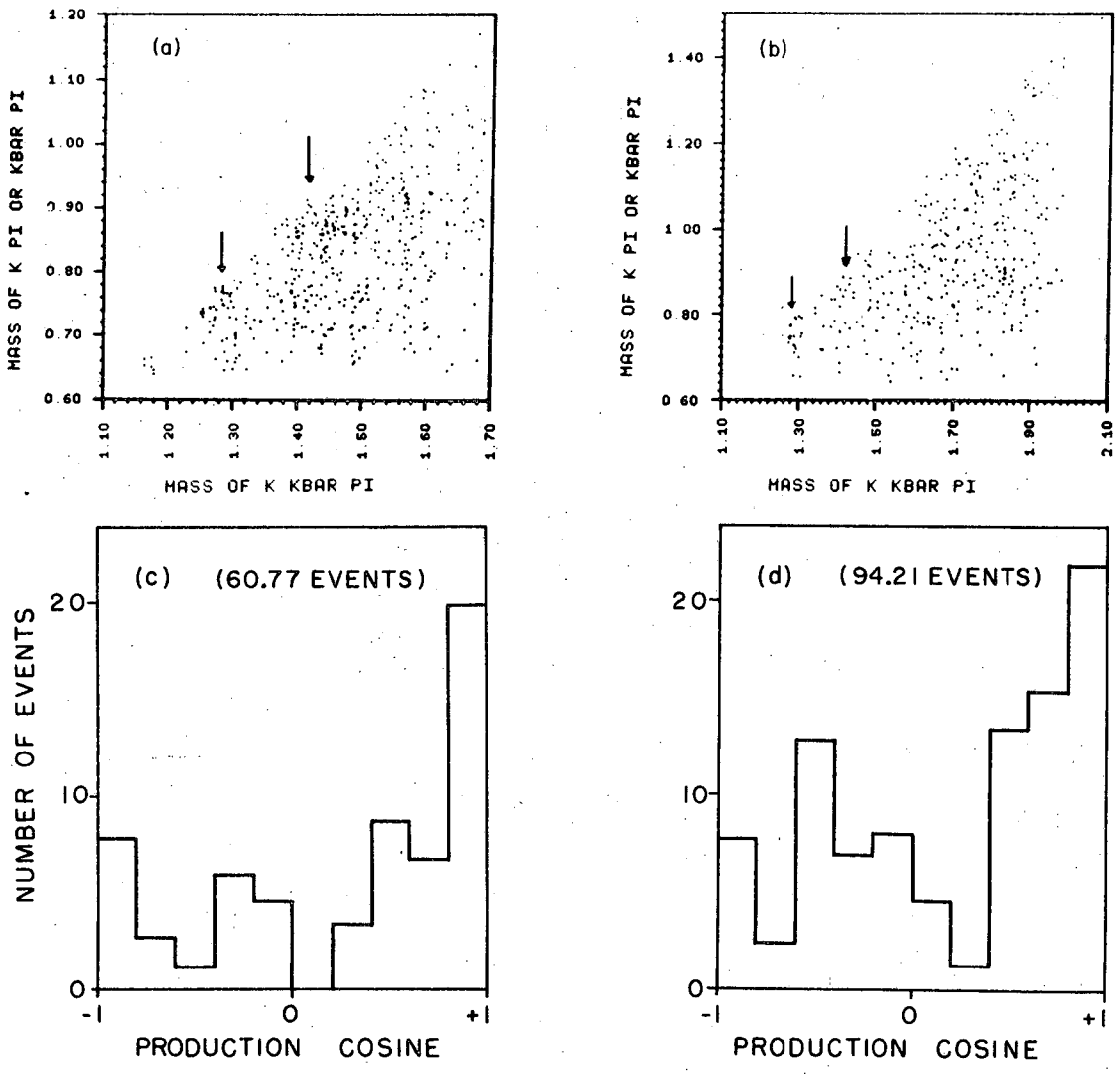

MUB 10869

Fig. 47

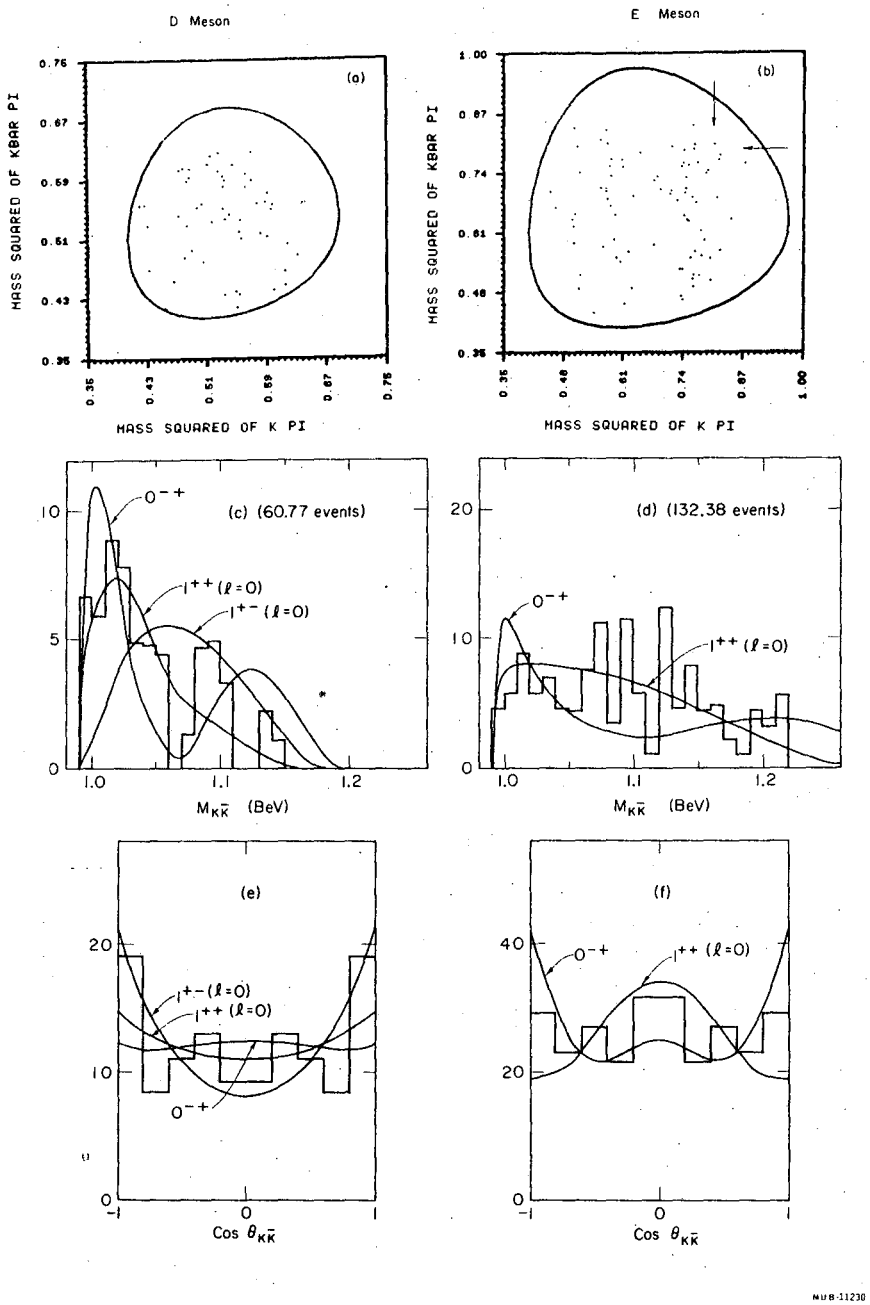
D Meson
E Meson
(a)
(b)
MASS SQUARED OF KBAR PI
MASS SQUARED OF K PI
(c) (60.77 events)
(d) (132.38 events)
0^{-+}
$1^{++}(\ell=0)$
$1^{+-}(\ell=0)$
$M_{K\bar{K}}$ (BeV)
(e)
(f)
Cos $\theta_{K\bar{K}}$
MUB-11230

Fig. 48

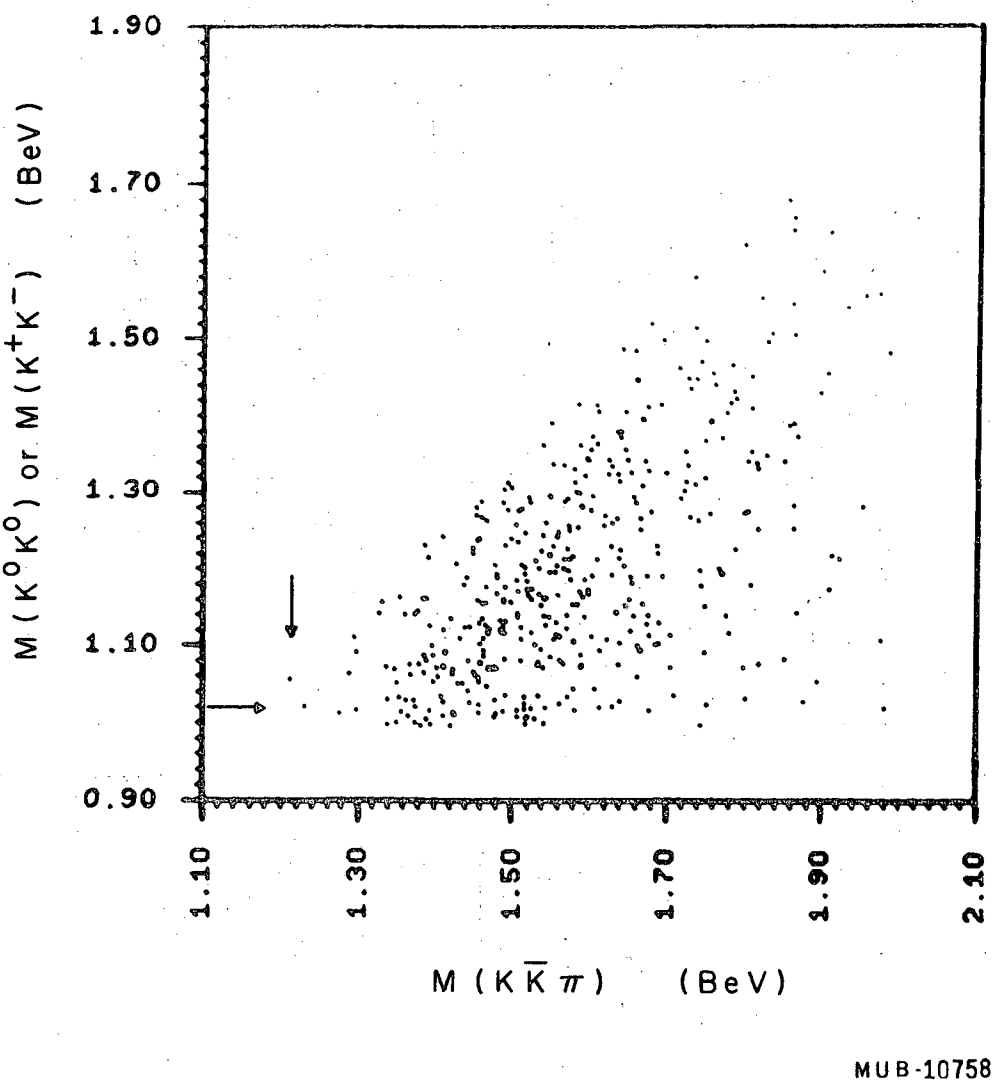
1.90
1.70
1.50
1.30
1.10
0.90
M (K⁰K̄⁰) or M (K⁺K⁻) (BeV)
1.10
1.30
1.50
1.70
1.90
2.10
M (K K̄ π) (BeV)
MUB-10758

Fig. 49

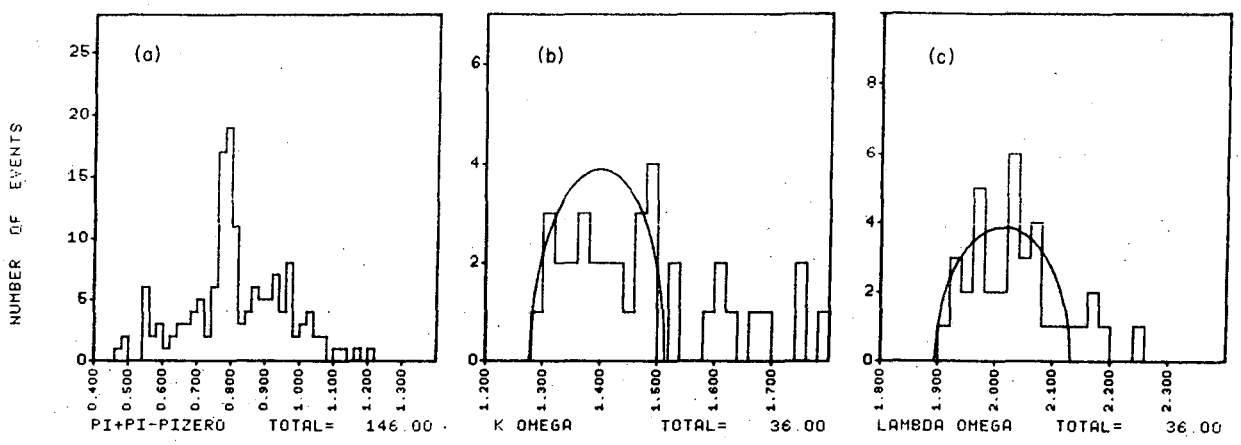
NUMBER OF EVENTS
(a)
PI+PI-PIZERO TOTAL= 146.00
(b)
K OMEGA TOTAL= 36.00
(c)
LAMBDA OMEGA TOTAL= 36.00
MUB-10725

Fig. 50

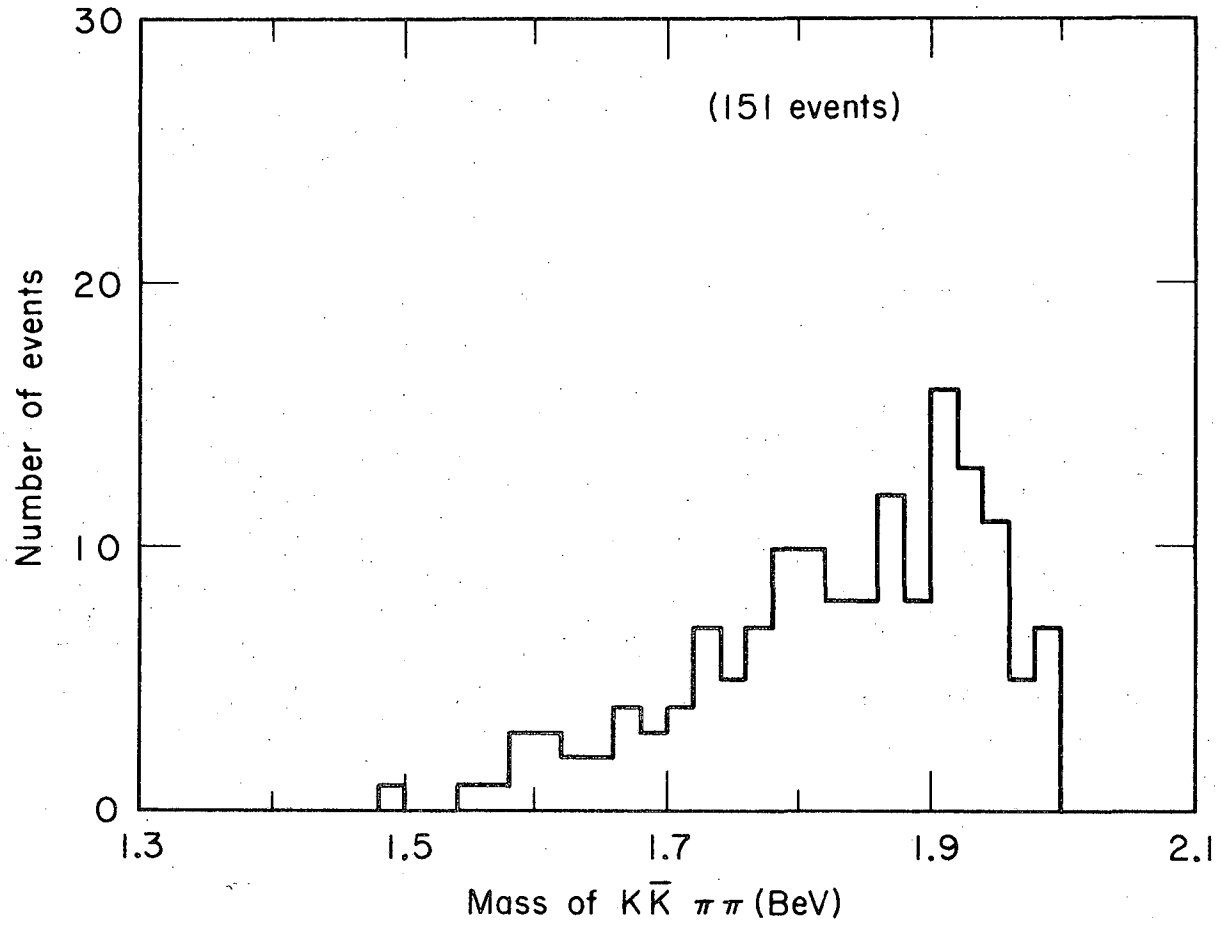

MUB-11235

Fig. 51

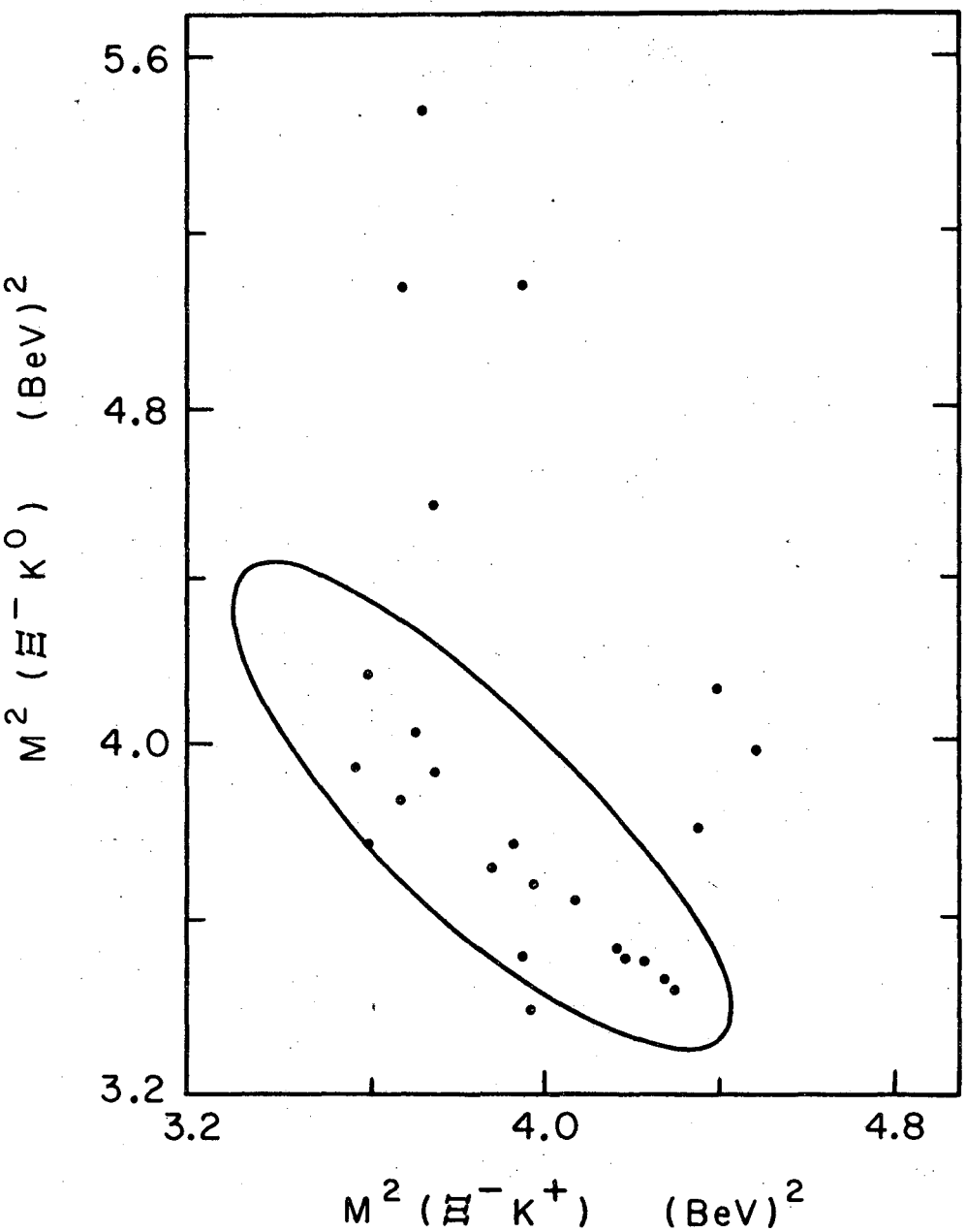

Fig. 52

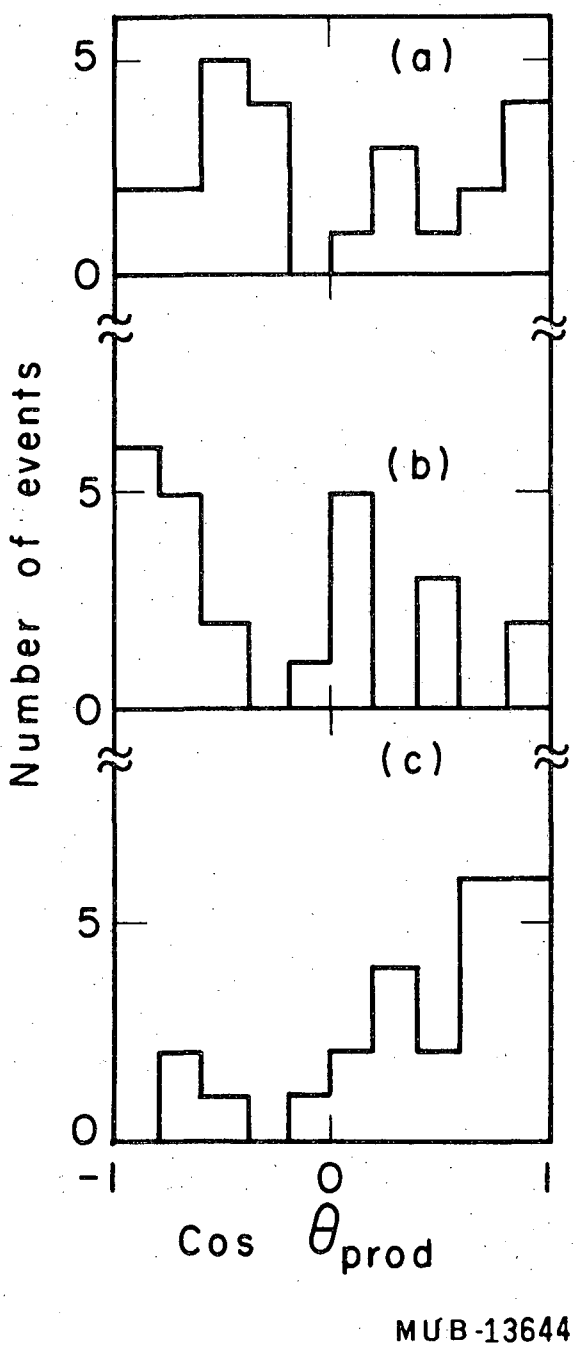

Fig. 53

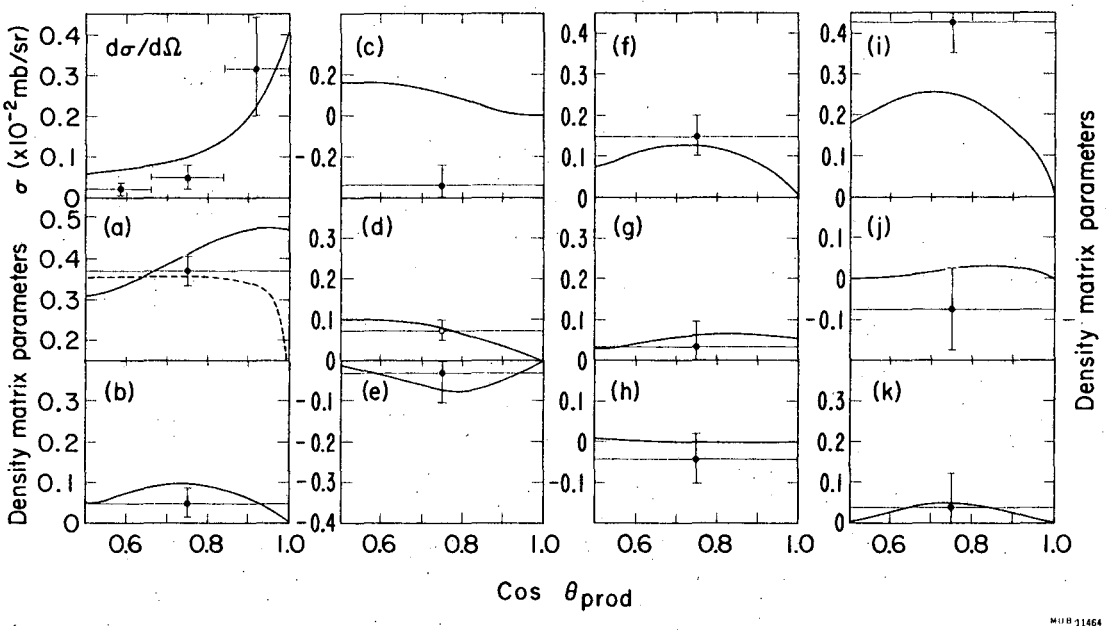
dσ/dΩ
σ (x10⁻²mb/sr)
(a)
(b)
(c)
(d)
(e)
(f)
(g)
(h)
(i)
(j)
(k)
Density matrix parameters
Density matrix parameters
Cos θprod
0.6
0.8
1.0
MUB 11464

Fig. 54

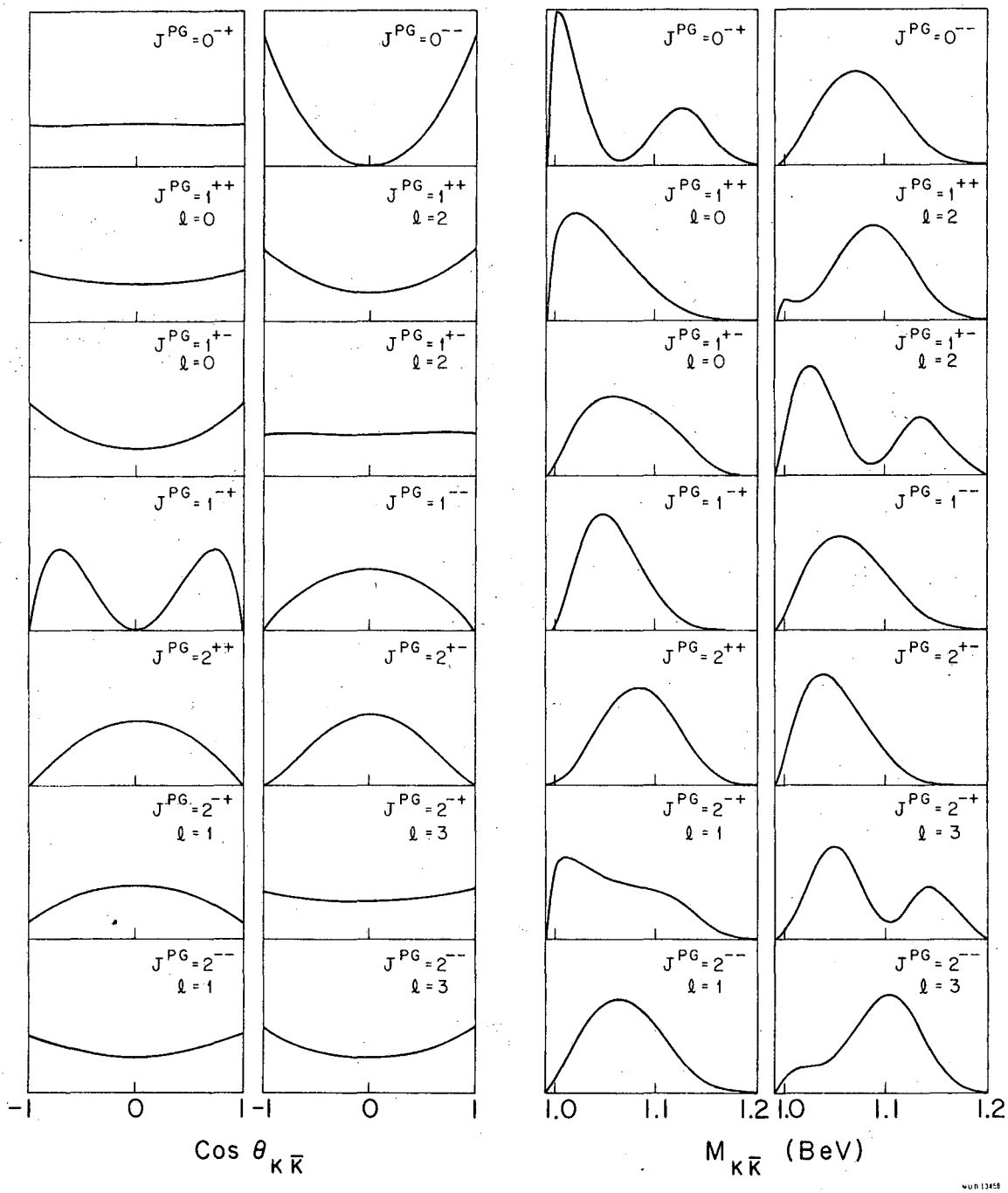
$J^{PG}=0^{-+}$
$J^{PG}=0^{--}$
$J^{PG}=1^{++}$ $\ell=0$
$J^{PG}=1^{++}$ $\ell=2$
$J^{PG}=1^{+-}$ $\ell=0$
$J^{PG}=1^{+-}$ $\ell=2$
$J^{PG}=1^{-+}$
$J^{PG}=1^{--}$
$J^{PG}=2^{++}$
$J^{PG}=2^{+-}$
$J^{PG}=2^{-+}$ $\ell=1$
$J^{PG}=2^{-+}$ $\ell=3$
$J^{PG}=2^{--}$ $\ell=1$
$J^{PG}=2^{--}$ $\ell=3$
-1 0 1
Cos $\theta_{K\bar{K}}$
1.0 1.1 1.2
$M_{K\bar{K}}$ (BeV)

Fig. 55

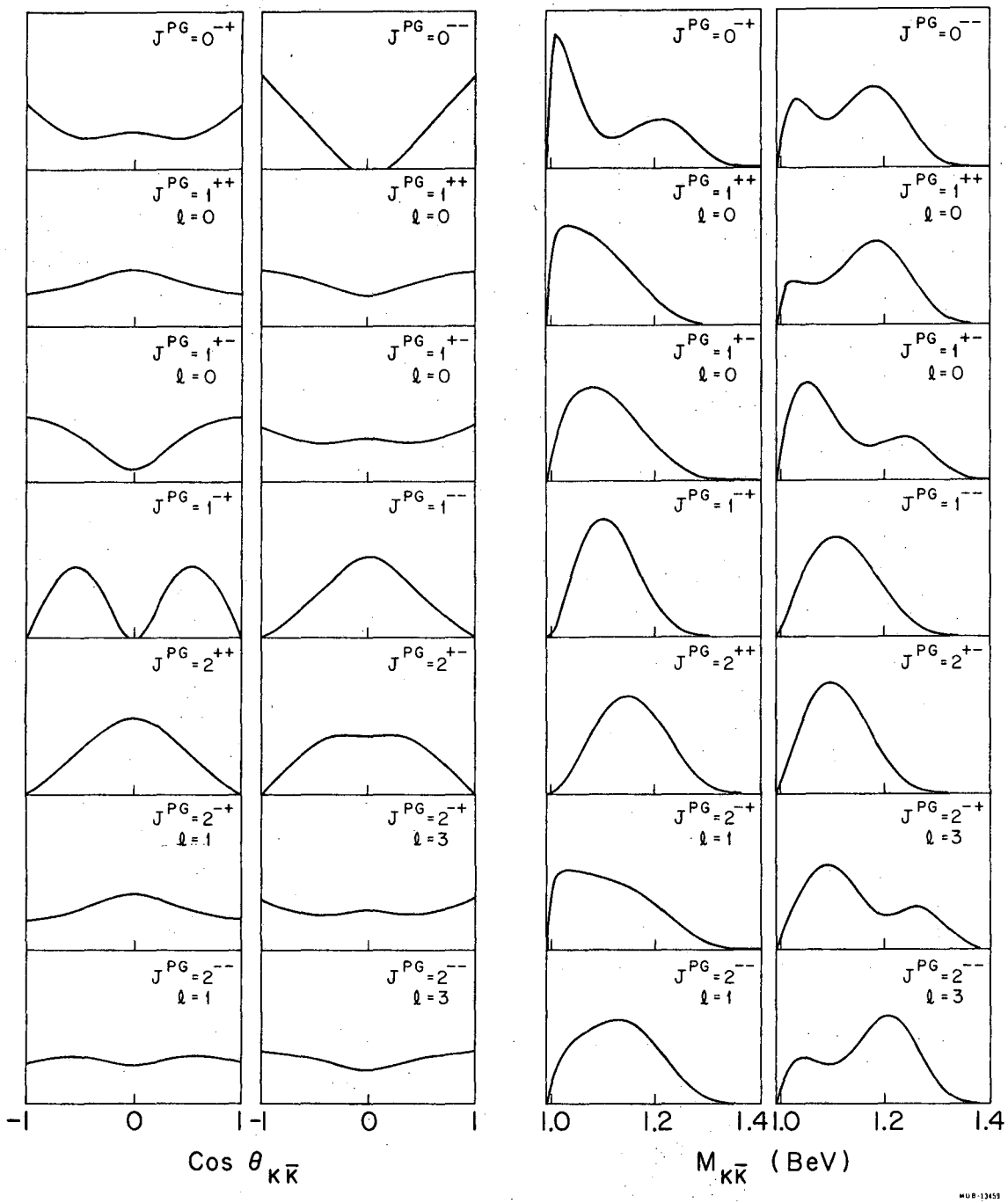
$J^{PG}=0^{-+}$
$J^{PG}=0^{--}$
$J^{PG}=1^{++}$ $\ell=0$
$J^{PG}=1^{+-}$ $\ell=0$
$J^{PG}=1^{-+}$
$J^{PG}=1^{--}$
$J^{PG}=2^{++}$
$J^{PG}=2^{+-}$
$J^{PG}=2^{-+}$ $\ell=1$
$J^{PG}=2^{-+}$ $\ell=3$
$J^{PG}=2^{--}$ $\ell=1$
$J^{PG}=2^{--}$ $\ell=3$
-1 0 1
Cos $\theta_{K\bar{K}}$
1.0 1.2 1.4
$M_{K\bar{K}}$ (BeV)

Fig. 56